UNIVERSITY OF SOUTHAMPTON
FACULTY OF ENGINEERING, SCIENCE AND MATHEMATICS
SCHOOL OF ELECTRONICS AND COMPUTER SCIENCE

Closed-Loop Multiple Antenna Aided Wireless Communications Using Limited Feedback

by

Du YANG

A thesis for the degree of
Doctor of Philosophy

2010

SUPERVISOR:
Professor Lajos Hanzo, Professor Lie-liang Yang

University of Southampton
Southampton SO17 1BJ
United Kingdom

Dedicated to my family

UNIVERSITY OF SOUTHAMPTON

ABSTRACT

Faculty of Engineering, Science and Mathematics
School of Electronics and Computer Science

A thesis submitted in partial fulfilment of the
requirements for the award of Doctor of Philosophy

Closed-Loop Multiple Antenna Aided Wireless Communications Using Limited Feedback

by Du YANG

The aim of this thesis is to study the design of closed-loop multiple antenna aided wireless communications relying on limited feedback. Multiple antennas may be employed either/both at the transmitter or/and at the receiver, where the latter periodically feeds back some information about the time-varying wireless channel using a limited number of bits. Furthermore, the transmitter then pre-processes the signals to be transmitted according to the received feedback information. This closed-loop multiple antenna aided communication scheme is capable of significantly improving the attainable system performance in terms of increasing the transmission rate or enhancing the transmission integrity.

The goal of our research is the efficient acquisition and exploitation of the Channel State Information at the Transmitter (CSIT), with the aid of different transmit preprocessing algorithms. The transmission schemes investigated in this thesis include the Transmit Matched Filter (TxMF), the Transmit Eigen-Beamformer (TxEBF), the linear Multi-User Transmitter (MUT) and a recently proposed MIMO scheme called Spatial Modulation (SM).

The entire process of CSIT acquisition is investigated in this thesis, which includes pilot assisted CSI estimation, CSI quantisation at the receiver, as well as CSI reconstruction at the transmitter. A number of novel designs are proposed in order to increase the CSI acquisition efficiency. A range of different CSI quantisers are detailed in Chapter 2, and their performances are evaluated throughout Chapter 3 to Chapter 6. Moreover, a pilot overhead reduction scheme is proposed for pilot assisted CSI estimation in Chapter 3 for rapidly fading channels. A pilot symbol assisted rateless code is also proposed in Chapter 3, which exploits the available pilot symbols not only for channel estimation but also for channel decoding. Furthermore, an Extrinsic Information Transfer (EXIT) Chart optimised Channel Impulse Response (CIR) Quantizer is proposed in Chapter 5, which assists the system in maintaining the lowest possible CSI feedback overhead, while ensuring that an open EXIT-tunnel is still attainable for the sake of achieving an infinitesimally low BER. A soft decoding assisted MIMO CIR recovery scheme is proposed in Chapter 5, which minimises the CIRs' reconstruction error at the transmitter for noise contaminated feedback. Last but not least, a CSI feedback scheme using channel prediction and predictive vector quantization is also proposed in Chapter 5 for delayed feedback channels.

Given feedback CSIT, a number of algorithms are proposed in order to efficiently exploit it. In Chapter 4 a novel Linear Dispersion Code (LDC) aided TxEBF scheme is proposed, which is capable of striking the required trade-off between the maximum attainable diversity gain and the capacity for an arbitrary number of transmit and receive antennas. In the same chapter, an application example using a novel scheme referred to as a TxEBF aided video transmission scheme is proposed, where the encoded video source bits are transmitted through different eigen-beams according to their error sensitivity, so as to improve the decoded video quality at the receiver by employing unequal error protection. Moreover, a feedback-aided phase rotation and a feedback-aided power allocation scheme are proposed in Chapter 6,

which achieves beneficial transmit diversity and enhances the robustness of a SM aided MIMO system.

By examining the various schemes investigated throughout Chapter 3 to Chapter 6, our five-step guidelines conceived for the design of closed-loop MIMO systems using limited feedback are summarised as follows. The first step is to design appropriate transmit preprocessing schemes under the assumption of having perfect CSIT. Then, the second step is to determine the specific type of the required feedback information, whose entropy has to be as low as possible. Next we design an efficient quantiser based on the statistical properties of the required feedback information. The distortion metric of the quantiser may be the conventional MSE metric, but the employment of a direct data-link-performance related metric is preferable. Moreover, the fourth step is to improve the efficiency and robustness of the quantiser by employing conventional source compression. Finally, the fifth step is the joint optimisation of the data transmission link and the CSI feedback link based on the ultimate target performance metric.

This thesis is concentrated on a Frequency Division Duplex (FDD) cellular communication scenario using digitalized feedback information, where the Mobile Terminals (MTs) estimate the Down-Link (DL) channel, quantise and feed back the required information to the Base Station (BS) using a bandwidth-limited feedback link, and the BS reconstructs the received CSI feedback information for the sake of throughput or integrity improving the DL transmission. Moreover, the wireless channels are assumed to be slow frequency-flat/narrow-band Rayleigh fading channels. They are mostly assumed to be spatially independent. The scenario of having spatial correlation and Line Of Sight (LOS) transmissions are also considered. Furthermore, both the achievable capacity and the BER performance are evaluated. Iterative decoding is employed in conjunction with channel coding in order to approach the achievable capacity and improve the BER performance.

Acknowledgement

First of all, I would like to thank my supervisor Prof. Lajos Hanzo for his invaluable guidance, support and encouragement. I am very grateful for his consistent encouragement, as well as patience, which kept me in hope. His loyalty to research and positive attitudes towards life and work will continue to stimulate me to make progress in my future career. Meanwhile, I also would like to thank another supervisor Prof. Lie-liang Yang for his great suggestions and endless patient. His remarkable range of reading and mathematical thinking has provided me valuable guidance whenever I was in confusion. All in all, this thesis would never have gone this far without them.

Moreover, I want to thank my colledges in the Communication Group of University of Southampton, both past and present, for their generouse help through my PhD study. I am indebted to Dr. Nan Wu, Dr Soon Xin Ng (Michael), Dr. Yosef Akhtman (Jos), Dr. Wei Liu, Dr. Chun-Yi Wei, Dr. Rong Zhang, Dr. Nicholas Bonello, Shinya Sugiura, Nasruminallah and Dr. Raja A Riaz, Dr. Li Wang, Lingkun Kong, Wang Yao, Dr. Chong Xu, Jing Zuo and Xinyi Xu. I have enjoyed all the discussions with them, both academic and non-academic.

My grateful thanks got to the Virtual Centre of Excellence in Mobile and Personal Communications Ltd. (Mobile VCE) for their generous financial support.

My personal thanks are due to many friends in Southampton, Pei Zhang, Zifang Luo, Xiaoqian Shi, Dr. Zhiqiang Xu, Dr. Xiaoli Li, Mr. Anthony Robson, Mrs Ela Robson and etc. They have easy and enrich my life in the last four years. Finally, I would like to thank my parents and grandparents for their unconditional love and support.

List of Publications

Journal Papers

1. N. Bonello, **D. Yang**, S. Chen and L. Hanzo“ Generalized MIMO Transmit Preprocessing Using Pilot Symbol Assisted Rateless Codes”, *IEEE Transactions on Wireless Communications*, vol. 9, pp. 754-763, 2010.

2. **D. Yang**, N. Wu, L. L. Yang and L. Hanzo, “Closed-loop Linear Dispersion Coded Eigen-beam Transmission and its Capacity”, *IEE Electronics Letters*, vol. 44, pp. 1144-1146, Sept. 2008.

Conference Papers

1. **D.Yang**, L. L. Yang and L. Hanzo, “DFT-based Beamforming Weight-Vector Codebook Design for Spatially Correlated Channels in the Unitary Precoding Aided Multiuser Downlink”, *IEEE International Conference on Communications*, 23-27 May 2010, Cape Town, South Africa.

2. N. Bonello, **D. Yang**, S. Chen and L. Hanzo, “Generalized MIMO Transmit Preprocessing Using Pilot Symbol Assisted Rateless Codes”, *IEEE Vehicular Technology Conference*, 16-19 May 2010, Taipei, Taiwan.

3. **D. Yang**, L. L. Yang and L. Hanzo, “Imperfect Channel Knowledge Based Ergodic Channel Capacity of Transmit Beamforming”, *IEEE Vehicular Technology Conference*, 20-23 September 2009, Anchorage, Alaska, USA.

4. S. Sugiura, **D. Yang**, L. L. Yang, S. Chen and L. Hanzo, “Effect of Array Geometry on the Capacity of the Turbo-Coded Beamforming Aided Uplink”, *IEEE Vehicular Technology Conference*, 20-23 September 2009, Anchorage, Alaska, USA.

5. **D.Yang**, Nasruminallah, L. L. Yang and L. Hanzo, “SVD-aided Un-Equal-Protection Spatial Multiplexing for Wireless Video Telehphony”, *IEEE Vehicular Technology Conference*, 26-29 April 2009, Barcelona, Spaina.

6. C.Y. Wei, **D. Yang**, L. L. Yang and L. Hanzo, “Iterative Detection Aided DL SDMA Systems Using Quantized Channel Impulse Response”, *IEEE Vehicular Technology Conference*, 26-29 April 2009, Barcelona, Spaina.

7. **D. Yang**, W. Liu, L. L. Yang and L. Hanzo, “Channel Prediction and Predictive Vector Quantization Aided Channel Impulse Response Feedback for SDMA Downlink Preprocessing”, *IEEE Vehicular Technology Conference*, Canada, September 21-24, 2008.

8. **D. Yang** L. L Yang and L. Hanzo, “Performance of SDMA systems using transmitter preprocessing based on noisy feedback of vector-quantized channel impulse responses”, *IEEE Vehicular Technology Conference*, Dubline, Irland, April, 2007, pp. 2119–2123.

Declaration of Authorship

I, **DU YANG**, declare that the thesis entitled **Closed-Loop Multiple Antenna Aided Wireless Communications Using Limited Feedback** and the work presented in the thesis are both my own, and have been generated by me as the result of my own original research. I confirm that:

- this work was down wholly or mainly while in candidature for the research degree at this University;
- where any part of this thesis has previously been submitted for a degree or any other qualification at this University or any other institution, this has been clearly stated;
- where I have consulted the published work of others, this is always clearly attributed;
- where I have quoted from the work of others, the source is always given. With the exception of such quotations, this thesis is entirely my own work;
- I have acknowledged all main sources of help;
- where the thesis is based on work done by myself jointly with others, I have made clear exactly what was done by others and what I have contributed myself;
- parts of this work have been published.

Signed:.....

Date:.....

Contents

List of Symbols

- **Matrices and vectors** :

$\boldsymbol{a}$	Information bit sequency before channel encoding
$\boldsymbol{a}_{Tx}$	Array steering vector
$\boldsymbol{a}_{Rx}$	Array response vector
$\boldsymbol{A}_i$	The *i*th dispersion matrix of an LDC
$\boldsymbol{b}$	Bit sequence vector
$\boldsymbol{c}$	Information bit sequency after channel encoding
$\boldsymbol{F}$	Discrite Fourior Transform matrix
$\boldsymbol{H}$	Channel impuse response matix
$\boldsymbol{h}_{mean}$	Mean values of the CIR taps of a N_{Tx}-element MISO channel
$\boldsymbol{G}$	i.i.d Grassian distrubted matrix
$\boldsymbol{g}$	i.i.d Grassian distrubted vector
$\boldsymbol{n}$	Gaussian noise vector
$\boldsymbol{P}_{Tx}$	Linear transmit preprocessing matrix
$\boldsymbol{P}_{Rx}$	Linear transmit post-processing matrix
$Q/\boldsymbol{q}/\boldsymbol{Q}$	Quantization codeword in the form of scalar/vector/matrix
$\boldsymbol{R}$	Covariance matrix
$\boldsymbol{R}_{Tx}$	Covariance matrix at the Transmitter
$\boldsymbol{R}_{Rx}$	Covariance matrix at the Reciever
$\boldsymbol{R}_x$	Covariance matrix of the transmit signal $\boldsymbol{x}$
$\boldsymbol{s}$	Information signal vector before transmit preprocessing
$\hat{\boldsymbol{s}}$	Decision variables vector at the receiver side
$\boldsymbol{U}$	Left-hand-side unitary matrix
$\boldsymbol{V}$	Right-hand-side unitary matrix
$\boldsymbol{\Lambda}$	Diagonal matrix consisting of eigen-values
$\boldsymbol{\Omega}$	Coupling matrix
$\boldsymbol{x}$	Transmit signal vector after transmit preprocessing
$\mathrm{x}/\mathbf{x}/\mathbf{X}$	General representation of quantizer input in the form of scalar/vector/matrix
$\boldsymbol{y}$	Received signal vector
$\boldsymbol{\chi}$	Dispersion Character Matrix of an LDC

- **Variables** :

A	Rician factor
B_C	Coherent bandwidth
B_S	Signal bandwidth
b	Number of feedback bits
$\mathfrak{C}_i$	The *i*-th quantization cell
C_{open}	Channel capacity of an open-loop system
C_{closed}	Channel capacity of a closed-oop system
ΔC	Achievable capacity gain
d_{Tx}	Distance between adjacent transmit antennas

d_{Rx} Distance between adjacent receive antennas

d_{Tx}^{APM} The Euclidean distance of the APM modulated symbols before transmission

d_{Rx}^{APM} The Euclidean distance of the APM modulated symbols after transmission over a noise-free fading channel

d_{Rx}^{SSK} The Euclidean distance of the SSK modulated symbols after transmission over a noise-free fading channel

d_v The degree of a variable node for rateless code

d_c The degree of a check node for rateless code

D_c Maximal check degree

E_{Tx} Transmit energy

E_b Energy ber bit

E_s Energy ber symbol

$|E|$ The number of edges of a rateless code

f_c Carrier frequency

f_{dm} Maximum Doppler frequency

$f_{dm-norm}$ Normalized maximum Doppler frequency

F Number of legitimate combination of an LDC coded transmission signal vector

h Channel impulse response

$|h|$ Channel envelope

I_{max} The maximum number of decoder iterations

I_{avg} The averaged number of iterations required

K Total number of users

M Modulation level

N_{Tx} Number of transmit antennas

N_{Rx} Number of receive antennas

N_s Number of independent data streams

N_0 Variance of Gaussian noise

N_p Number of pilot symbols

N_a Number of input information bits

N_c Number of channel encoded information bits

N_E Number of non-zero power allocation values

N_{ts} Number of symbol intervals in an observed transmission block

N_Q Number of quantizers employed

p_{ij} Pilot symbol

$\mathcal{Q}$ Quantization codebook

$|\mathcal{Q}|$ Quantization codebook size, the total number of codewords

R_s Symbol rate in Bound

R_b Bit rate in bit/second

r_c Channel coding rate

R_f Frame rate in frame/second

T_C Coherent time

T_S Signal symbol duration

T_p	The duration of a pilot symbol interval
T_d	Total duration of data-transmission symbol intervals between two pilot symbols
T_{sample}	Time duration between two pilot symbols
φ	Channel phase
κ	Conditional number of a Matrix
ρ	Correlation coefficient
λ	Eigen-value of an Hermitian matrix
$\lambda^{\frac{1}{2}}$	Singular value of a matrix
α_k	Power normalization factor for the k-th user
$\xi_{\mathcal{Q}}$	The quantization error using codebook $\mathcal{Q}$
$\phi_{Tx,p}$	Angle of departure of the p-th path
$\phi_{Rx,p}$	Angle of arrival of the p-th path
Θ	Hermition angle between two complex-valued unitary vectors
β	Psedo-angle between two complex-valued unitary vectors
σ	Standard deviation of a random variable
η_p	Pilot signalling overhead in percentage
η_f	Feedback signalling overhead in percentage
η_r	Normalized overhead reduction ratio
Π_p	Pilot position interleaver of the proposed PSAR
δ_1	The fraction of degree-one nodes
δ_1^p	The fraction of degree-one nodes corresponding to pilot bits
$\delta_1^{\bar{p}}$	The fraction of degree-one nodes corresponding to information bits

- **Mathematical operations** :

$E[\cdot]$	Statistical expectation
$vec(\cdot)$	Stacks the columns of a matrix into one tall vector
$(\cdot)^H$	Conjugate matrix transpose
$(\cdot)^T$	Matrix transpose
$(\cdot)^*$	Complex conjugate
$\odot$	Element-wise product of two matrices
$\mathtt{tr}\,(\cdot)$	Sum the diagonal elements of a matrix
$(\cdot)^\dagger$	The pseudoinverse of a matrix
$J_0(\cdot)$	Bassel Function of the zero-order first kind
$\mathsf{Q}(\cdot)$	Quantization
$\mathsf{Q}^{-1}(\cdot)$	Inverse of quantization
$(\cdot)_q$	Quantised result of $(\cdot)$
$\hat{(\cdot)}$	Estimation of $(\cdot)$
$(\cdot)_e$	Error of $(\cdot)$
$\tilde{(\cdot)}$	Reconstruction of $(\cdot)$
$(\cdot)^{(f)}$	Signal $(\cdot)$ transmitted through the feedback channel

- **Functions** :

$\delta(x)$	Check node degree distribution for a rateless code

$v(x)$	Variable node degree distribution for a rateless code
$\delta_{LT}(x)$	Degree distribution for a rateless code
$T_I(I_{in})$	Inner decoder's EXIT function
$T_b(I_{in})$	Inner decoder's EXIT function using quantized CIRs

- **Symbols** :

$\mathbb{R}$	Real value
$\mathbb{C}$	Complex value
$\mathbb{N}$	Natrual value
$\mathcal{N}$	Real-valued Normal distribution
$\mathcal{CN}$	Complex-valued Normal distribution
$\mathcal{G}(m,n)$	Grassmannian space

Chapter 1

Introduction

Multiple-Input-Multiple-Output (MIMO) systems facilitate a linear increase of the achievable transmission rate with the minimum of the number of transmit and receive antennas [1]. They also enhance the link's reliability and improve the cellular coverage [2]. Moreover, the closed-loop MIMO system, where the transmitter adapts the transmitted signal according to the avaliable Channel State Information (CSI), may yield further potential improvements [3]. Closed-loop MIMOs are entering next generation cellular products [4] with the promise of widespread adoption in the near future.

In this introduction, a brief review of MIMO techniques is provided in Section 1.1, with special emphasis on closed-loop MIMO techniques. Then the scope of the thesis is specified in Section 1.2, while Section 1.3 outlines the focus of each chapter. Finally, the novel contribution of the thesis are described in Section 1.4.

1.1 Historical Overview

1.1.1 MIMO Techniques

A major technological breakthrough in improving the transmission reliability of wireless links was facilitated by the employment of multiple antennas at the transmitter and receiver. Typically, wireless systems equipped with multiple antennas at both sides are referred to as MIMO systems in contrast to Single-Input Single-Output (SISO) systems, where the latter rely on a single transmit and receive antenna. The concept of employing multiple antenna was first proposed in [1,5], which demonstrated a significant increase of the achievable capacity without requiring any extra bandwidth or power. Compared to SISO systems, MIMO systems are capable of combating the deleterious effects of multipath fading, which is one of the main challenges in the design of wireless communication systems. They outperform single-antenna aided systems both in terms of their system capacity [6] and Bit-Error-Ratio (BER) performance.

MIMO systems may be classified into different groups according to a range of different criteria. Based on the number of antennas employed, a system having a single transmit antenna and several receive antennas is referred to as a Single-Input Multiple-Output (SIMO) system, while having several transmit antennas and a single receive antenna results in a Multiple-Input-Single-Output (MISO) system. The

MIMO system is the most general construction, which subsumes SISO, SIMO, MISO systems as special cases. Moreover, MIMO systems may be also divided into co-located [1, 5–7] and distributed [8–10] MIMO systems. In a co-located MIMO system, the transmit and receive antennas are a part of an antenna array, which are colocated for example of a Base Station (BS) or at a single Mobile Terminal (MT). By contrast, in a distributed MIMO system, the transmit/receive antenna elements of a virtual MIMO may be installed in different equipment and distributed to form a virtual antenna array. Furthermore, according to the system scale, MIMO arrangements may be categorised into single-user [11], multi-user [12] and multi-cell [13] MIMO systems, whose communication model evolves from point-to-point (e.g. a single MT communicates with a single BS), to point-to-multipoint (e.g. a single BS broadcasting to multiple MTs through the Down-Link (DL) channel) and multipoint-to-point (e.g. multiple MTs transmitting signals to one BS using the Up-Link (UL) channel), and finally to multipoint-to-multipoint (e.g. multiple MTs communicating with multiple BSs).

It is essential to employ MIMO techniques both at the transmitter and the receiver for any of the aforementioned MIMO systems to exploit the benefits of having multiple antennas. MIMO techniques may be classified into the following five categories according to their functions.

- Spatial Multiplexing
  N_s independent information data streams are transmitted with the aid of N_{Tx} $(N_s \leq N_{Tx})$ transmit antennas simultaneously, without requiring any extra bandwidth or power, hence the overall data rate becomes N_s times the data rate of using a single transmit antenna. A typical application of spatial multiplexing is constituted by the Vertical Bell-Labs Layered Space-Time Architecture (V-BLAST) [5].

- Spatial Diversity
  In contrast to spatial multiplexing, spatial diversity schemes transmit replicas of the same data stream over N_{Tx} transmit antennas. The attainable diversity gain depends on the similarity of these channels. If these channels are correlated, i.e. fade together, the achievable diversity gain becomes zero. However, if they are independent of each other, the diversity gain becomes $N_{Tx}N_{Rx}$, where N_{Rx} represents the number of receive antennas. The achievable diversity gain in practice is usually between these two values. This transmission scheme has introduced some redundancy in the spatial domain, which is similar to the effects of channel coding. A specific algorithm which exploits the spatial diversity is constituted by Space-Time Coding (STC) [14].

- Beamforming
  Beamforming exploits the CSI at the transmitter/receiver in order to form an angularly selective beam pattern, which steers the transmit/receive beam in a certain desired direction, and suppresses the signal in other directions. It may be viewed as a kind of spatial signal processing scheme, which is applicable for both spatially independent and correlated channels. The research of beamforming schemes is characterized for example in [15–17].

- Space-Division Multiple Access (SDMA)
  SDMA techniques take advantage of the unique user-specific Channel Impulse Responses (CIR) of the MIMO elements, in order to pre-cancel/cancel the inter-user interference at the transmitter/receiver, so as to enable multiple users to communicate in the same time- or frequency-slots, provided that their CIRs are known at the transmitter/receiver. The key challenge of SDMA system

is the design of Multi-User Detectors (MUD) [18–22] and of Multi-User Transmitters (MUT) [12, 23–26].

- Spatial Modulation (SM)
  Spatial modulation activates a single transmit antenna at every transmission instant according to the input information. More explicitly, the information bits are conveyed by the indices of the transmit antenna by exploiting the relative independence of the channel fading associated with the different transmit antennas. Although the achievable throughput increases only logarithmically with the number of transmit antennas, spatial modulation is capable of reducing the complexity of both the transmitter and receiver, as well as achieving a high energy efficiency with the aid of a sufficient high number of antennas. Research ideas on spatial modulation can be perused in [7, 27, 28].

MIMO techniques have been designed for achieving one of above-mentioned functions. For instance, the Alamouti scheme [14] was designed for achieving transmit diversity. However, sophisticated MIMO techniques are capable of supporting more than one functions. For example, the Linear Dispersion Code (LDC) proposed in [29] is capable of achieving both a spatial multiplexing gain as well as a spatial diversity gain. Another example is the multi-functional MIMO detailed in [2], where a combination of the MIMO techniques is employed based on exploiting the prevalent channel properties and system requirements.

Alternatively, the MIMO techniques may divided into the following two categories, namely open-loop and closed-loop MIMOs, based on the availability of the CSI at the Transmitter (CSIT).

- Open-loop MIMOs: CSIT is not available
  In an open-loop MIMO system, the transmitter has no channel knowledge. The CSI may be extracted at the receiver with the aide of pilot-assisted [30], semi-blind [31, 32] or totally blind [33] channel estimation techniques. Alternatively, the channel estimation may be avoided at the receiver with the aid of differential detection techniques [34, 35]. In this case, non-coherent MIMO techniques are available for achieving a spatial multiplexing gain [5], transmit diversity gain [14], receive diversity gain [36] and receive beamforming gain [15]. The open-loop SDMA uplink [37] and open-loop spatial modulation are also implementable.

- Closed-loop MIMOs: CSIT is available
  In a closed-loop MIMO system, the CSI is known both by the transmitter and the receiver. Aided with CSIT, it becomes possible to achieve a transmit beamforming gain [38, 39] and to construct a SDMA DL system [12, 40]. Moreover, the performance of the open-loop MIMO schemes [41], such as spatial multiplexing using the V-BLAST arrangement will be improved by taking the CSIT into design consideration [42].

It is evident that in the presence of perfect CSIT, the closed-loop MIMO arrangement achieves a better performance than open-loop arrangements in terms of almost all performance metrics [3, 43]. Motivated by the potential benefits, substantial research efforts have been dedicated to the design of efficient closed-loop MIMO schemes, which will be reviewed in Section 1.1.2.

1.1.2 Closed-loop MIMO Techniques

The history of closed-loop communication system design may be traced back to Shannon [44, 45]. A typical example of closed-loop design is constituted by adaptive modulation [46] invoked for SISO systems, where the number of modulation levels or the Forward Error Correction (FEC) code rate may be varied based upon the instantaneous channel quality. With the aid of multiple antenna, another signal dimension - namely the spatial dimension - can be exploited by adaptive signalling, which results in further performance improvements [6, 47]. In this section, the classification of closed-loop MIMO systems is provided first, followed by the literature review of transmit preprocessing techniques, the CSI quantization design, and the CSI reconstruction.

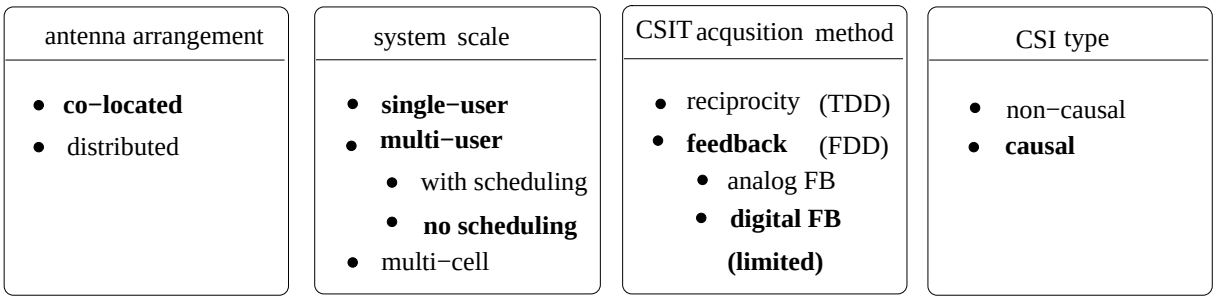

Figure 1.1: The classification of closed-loop MIMO systems according to 1) antenna arrangement; 2) system scale; 3) CSIT acquisition method; and 4) CSI type.

Following the classification of MIMO systems, closed-loop MIMO systems may also be classified into co-located [11] and distributed [48] closed-loop MIMO systems based on the antenna arrangements. Alternatively, they may be categorised into the following three groups, namely single-user [41], multi-user [49] and multi-cell [50] closed-loop MIMO systems. The family of multi-user closed-loop MIMO systems may be further categorised into two types, depending on whether the scheduling techniques [51] are employed for the sake of achieving multi-user diversity [52]. Moreover, closed-loop MIMO systems have their own unique classifications. For example, closed-loop MIMO systems may be categorized according to their CSIT acquisition methods. More explicitly, the CSIT may be obtained by exploiting the reciprocity [53, 54] of the UL and DL channel in a Time Division Duplex (TDD) system, where the UL and DL channel occupy the same frequency band and hence may fade together in the absence of frequency-selective fading. Otherwise, the CSIT may be obtained from a specific feedback channel [3] from the receiver to the transmitter in a Frequency Division Duplex (FDD) system, where the UL and DL channel occupy different frequency band and hence are expected to have different CIRs. For the class of systems using feedback information, the CSI may be fed back using an analog signal [55]. For example, in [55] the signal received by the MTs was directly transmitted back to the BSs. Alternatively, the CSI may be estimated at the receiver, quantised, encoded and then fed back to the BS, which is termed as digital feedback or limited feedback [3]. Another classification of the closed-loop MIMO system is based on the CSI types including non-causal CSI [56] and causal CSI [57]. Non-causal CSI refers to the long-term statistical channel information, such as the CIR taps' mean value and covariance matrix. This type of information is usually measured once before transmission and does not require frequent updates after the initial signalling. By contrast, causal CSI refers to the instantaneous channel information [58], for example the instantaneous CIRs. This kind of information is time-variant and has to be periodically fed back to the transmitter. Employing causal CSI generally achieves a better performance than non-

causal information, but also imposes a higher signalling overhead and signal processing complexity [59]. In addition, **we define the terminology CSI as any information related to both statistical as well as to instantaneous channel states**, which includes not only the CIRs, but also the channel's covariance matrix, the transmit beamforming vector, the appropriate modulation scheme according to the current channel quality, etc.

The benefits of having CSIT is exploited by the transmit preprocessing techniques. A succinct literature review of transmit preprocessing techniques is illustrated in Table 1.1. Based on the algorithm itself, the transmit preprocessing techniques may be categorised into linear and non-linear ones. Transmit antenna selection [72], Tansmit Eigen-Beamforming (TxEBF) [73], Transmit Zero Forcing (TxZF), Transmit Minimum Mean Square Error (TxMMSE) [26] and Transmit Block-Diagonalization (TxBD) [64] belong to the linear transmit preprocessing techniques. By contrast, Dirty Paper Coding (DPC) [24, 74], Vector Precoding (VP) [65] etc. belong to the class of non-linear transmission arrangements. Linear transmit preprocessing techniques have a lower computational complexity than the non-linear ones, but the former ones are inferior to the non-linear ones in terms of their achievable throughput and BER performance. However, recent research of multi-user systems demonstrated that in conjunction with beneficial scheduling schemes, the performance of linear transmit preprocessing may approach that of the non-linear ones [75]. Moreover, when relying on the MIMO functions listed in Section 1.1.1, the transmit preprocessing techniques may also be classified according to their functions, which includes transmit preprocessing schemes designed for improving the spatial multiplexing [42, 76], the spatial diversity [66, 77], the transmit beamforming gain [78], for SDMA DL system [40], and for improving the performance of spatial modulation schemes, as detailed in Chapter 6.

In addition to the transmit preprocessing techniques, another key component of a closed-loop MIMO system using limited back is the CSI quantizer. The literature review of CSI quantisers is provided in Table 1.2. The design principles of conventional source quantisers, such as speech/audio/video codec may be applied to the design of CSI quantisers. For example, it is widely recognized that an efficient audio quantiser must be designed by exploiting the statistical properties of the audio source signal [91]. Similarly, an efficient CSI quantiser must be designed based on the unquantised CSI characteristics, which depends on the specific transmit preprocessing scheme employed [57, 80] and on the MIMO channel used [87]. Another example is the employment of Vector Quantisers (VQ) [91] for MIMO CSI quantisation [79], since it is demonstrated by the conventional source quantiser theory that a VQ, which jointly quantized all the elements of a multi-dimensional source, outperforms the corresponding Scalar Quantizer (SQ) conceived for quantising every source sample separately. Moreover, some algorithms designed for conventional source quantisers, such as the codebook generation algorithm referred to as the Linde-Buzo-Gray (LBG) algorithm [91], are also widely applied for the design of CSI quantisers. However, the ultimate design objective of the CSI quantiser is however different from that of the conventional source quantizer. More explicitly, the design objective of the conventional source quantiser is to reconstruct the input speech/audio/video source signal with minimum distortion. As a result, the quantiser's performance is typically evaluated by the Euclidean distance between the unquantised and quantised source samples. By contrast, the ultimate objective of a CSI quantiser is to improve the system's performance in terms of the attainable throughput and BER. Although this goal could be achieved by minimising the quantisation error in terms of the classic Euclidean distance, further research demonstrated that other distortion metrics, such as the chordal distance [80] and Fubini-Study distance [57], provide a superior performance. Furthermore, the feedback channel is usually bandwidth-limited, error-contaminated and

Table 1.1: Major contributions addressing transmit preprocessing schemes.

Author(s)	Contribution
[60] Costa 1983	proposed the concept of dirty paper coding.
[61] Negiand *et. al.* 2002	combined transmit beamforming with space-time coding in order to increase the received SNR value.
[62] Zhuang *et. al.* 2003	combined the transmit antenna selection with power and rate control, so as to enhance a V-BLAST system's throughput.
[63] Molisch and Win 2004	presented an overview of antenna selection.
[64] Choi and Murch 2004	proposed the Transmit Block Diagonalisation (TxBD) algorithm for a multi-user MIMO downlink system.
[26] Joham *et. al.* 2005	compared three linear transmit preprocessing schemes, namely the TxMF, TxZF and TxMMSE.
[24] Jindal and Goldsmith 2005	compared the sum-capacity of dirty-paper coding to that of TDMA for the Gaussian MIMO broadcast channel.
[65] Hochwald *et. al.* 2005	proposed a vector-perturbation technique for near-capacity multiantenna multiuser communication.
[51] Ajib and Haccoun 2005	provided an overview of scheduling algorithms designed for MIMO-based cellular wireless communication systems.
[66] Celebi *et. al.* 2006	conceived a balanced space-time block code, which increases transmit diversity by using one or two feedback bits.
[11] Vu and Paulraj 2007	provided a tutorial on linear transmit preprocessing.
[49] Zhang and Letaief 2007	investigated multiuser scheduling relying on limited feedback of the CSI in MIMO broadcast channels.
[67] Santoso *et. al.* 2008	designed a transmit power allocation scheme for a STTC-aided MIMO system relying on limited feedback.
[68] Bizaki and Falahati 2008	investigated the non-linear transmit proprocessing scheme termed as Tomlinson-Harashima precoding using imperfect CSI.
[50] Somekh *et. al.* 2009	examined the TxZF algorithm in a multicell scenario, where the BSs cooperated with each other.
[69] Chang *et. al.* 2009	proposed a low-complexity multicell OFDMA DL channel assignment method.
[70] Meri *et. al.* 2010	advocated a novel beamforming and power control algorithm for the MIMO OFDM downlink, which requires 1-bit feedback.
[71] Huang *et. al.* 2010	proposed a precoding design for a dual-hop downlink combined with MIMO amplify-and-forward relaying.

Table 1.2: Major contributions addressing CSI quantiser design.

Author(s)	Contribution
[79] Narula *et. al.* 1998	employed vector quantization for the beamformer weight vector.
[80] Love *et. al.* 2003	proposed the Grassmannian line-packing quantizer.
[81] Santipach and Honig 2003	proposed the Random Vector Quantisation (RVQ) scheme to maximise the achievable throughput.
[82] Love and Heath 2003	conceived DFT-based phase information quantiser in order to achieve the maximum attaninable diversity advantage.
[83] Banister and Zeidler 2003	advocated an improved codebook for beamforming weight vectors by exploiting the channel's temporal correlations.
[57] Love and Heath 2005	proposed the Grassmannian subspace-packing quantiser for a unitary precoding matrix.
[84] Choi and Heath 2005	invented a scheme that combines beamforming weight vector quantization and vector interpolation for an OFDM system.
[85] Zhou and Li 2006	proposed a new precoder selection criterion directly based on the BER and developed a precoder codebook construction method.
[86] Roh and Rao 2006	suggested a maximised-capacity quantizer design criterion and develop the corresponding iterative VQ design algorithm.
[87] Raghavan *et. al.* 2007	proposed a systematic codebook design for correlated channels.
[88] Wu and Lau 2008	introduced a robust joint rate, power and precoder design for slow fading MIMO channels relying on noisy limited feedback.
[89] Ryan *et. al.* 2009	proposed a beamforming codebook based on QAM and PSK constellations, which eliminates the storage of the codebook.
[90] Kim and Beaulieu 2010	propose the Hadamard-matrix based codebook design for beamforming systems.

delayed, which imposes additional requirements on the CSI quantiser design. The channel's correlation in the spatial [79], temporal [83] as well as frequency [84] domain is exploited in order to reduce the feedback signalling overhead. For the sake of minimising the distortion imposed by the transmission errors of the feedback loops, the concepts of designing a robust quantiser and inverse quantiser for multi-media transmissions via error-infested noisy channels [92] may also be employed for robust CSI quantiser design [88]. Last but not least, the closed-loop MIMO system are often combined with other sophisticated techniques, such as long-term channel prediction [93] for the sake of mitigating the influence of the feedback delay imposed [94, 95].

1.2 Scope of the Thesis

This thesis is focused on co-located single-user and multi-user closed-loop MIMO systems, which are highlighted in Fig. 1.1 of Section 1.1.2. The associated multi-user scheduling techniques are beyond the

scope of this thesis. Moreover, we focus our attention on a FDD system, which employs linear transmit preprocessing techniques at the BS in order to exploit the quantised causal CSIs periodically fed back from the MTs through a bandwidth-limited as well as possibly error-contaminated and delayed feedback channel. The performance of the proposed algorithms was evaluated mainly using the following metrics:

- *Continuous-input Continuous-output Memoryless Channel's (CCMC) ergodic capacity*, which represents the upper-bound of the achievable throughput, while maintaining an infinitesimally low BER under the assumption of having a zero-mean, unit-variance Gaussian random input, perfect channel coding and infinite codeword length;
- *Discrete-input Continuous-output Memoryless Channel's (DCMC) ergodic capacity*, which constitutes the upper-bound of the throughput at an infinitesimally low BER under the assumption of using a realistic modulation scheme, perfect channel coding and an infinite codeword length;
- *Throughput*, which represents the realistic number of bits/symbol under the assumption of using a practical modulation scheme, practical channel coding and a finite coding length.
- *Uncoded and coded BER*, which represents the reliability of the system under the assumption of employing a realistic modulation scheme, practical channel coding and a finite codeword length.

Various channel coding schemes are employed in the thesis, including Recursive Systematic Convolutional (RSC) codes, rateless codes, Unit-Rate Codes (URC) and Turbo codes [96, 97]. The popular schemes of iterative channel decoding and iterative detection [98] are also employed for enhancing the attainable BER performance. Several other performance metric are employed, which include the decoder's computational complexity in Chapter 3, the Peak-Signal-to-Noise-Ratio (PSNR) of the decoded video in Chapter 4, as well as the required number of feedback bits and the reconstructed CSI's mean square error in Chapter 5.

1.3 Outline of the Thesis

Having reviewed the literature of MIMO techniques in Section 1.1, and having defined the scope of the thesis in Section 1.2, let us now outline its organisation.

- **Chapter 2:** Three key topics of a closed-loop MIMO system using limited feedback are detailed in this chapter. More explicitly, wireless MIMO channel modelling is discussed in Section 2.1. Then five linear transmit preprocessing algorithms are discussed in Section 2.2. Moreover, three different CSI quantisers are analysed in Section 2.3. Finally, a summary of the chapter is provided in Section 2.4.
- **Chapter 3:** The design of a Transmit Matched Filter (TxMF) aided closed-loop single-user MISO system is investigated in this chapter. The achievable ergodic channel capacity using quantized CSI is investigated in Section 3.1. In Section 3.2, the achievable ergodic channel capacity is further investigated, while considering the effects of both the channel estimation errors and the CSI signalling overhead. Then, a pilot reduction signalling scheme designed for rapidly fading channels is detailed in Section 3.3 and a pilot symbol assisted rateless code is discussed in Section 3.4. Finally, the summary of this chapter is provided in Section 3.5.

- **Chapter 4:** The design of a Transmit Eigen-Beamforming (TxEBF) aided closed-loop single-user MIMO system is investigated in this chapter. The achievable ergodic CCMC capacity using quantized CSI is investigated in Section 4.1. Then, a LDC aided TxEBF scheme is illustrated in Section 4.2, and a TxEBF aided video transmission scheme is detailed in Section 4.3. Finally, the chapter is summarised in Section 4.4.

- **Chapter 5:** The design of the linear Multi-User Transmitter (MUT) aided closed-loop SDMA downlink is discussed in this chapter. First of all, the EXtrinsic Information Transfer Chart (EXIT-Chart) optimised CIR quantiser algorithm is introduced in Section 5.1. Then the soft-decoder assisted CIR recovery scheme is discussed in Section 5.2, followed by the channel prediction and PVQ regime detailed in Section 5.3. Finally, the chapter is summarised in Section 5.4.

- **Chapter 6:** The design of Spatial Modulation (SM) aided open-loop and closed-loop single-user MIMO systems is investigated in this chapter. An overview of the spatial modulation scheme is provided in Section 6.1. Then, three schemes including the open-loop Space Time Space Shift Keying (ST-SSK) designed for systems having more than two transmit antennas, the closed-loop feedback aided phase rotation conceived for systems having two transmit antennas and the closed-loop feedback assisted power allocation are discussed in Section 6.2. Moreover, transmit diversity assisted spatial modulation is discussed in Section 6.3, where diagonal linear dispersion codes are introduced and combined with the ST-SSK scheme. Finally, the summary of this chapter is provided in Section 6.4.

- **Chapter 7:** This chapter summarises the key contents and contributions of each chapter and presents their most salient conclusions in Section 7.1. Our suggestions for future research are outlined thereafter in Section 7.3.

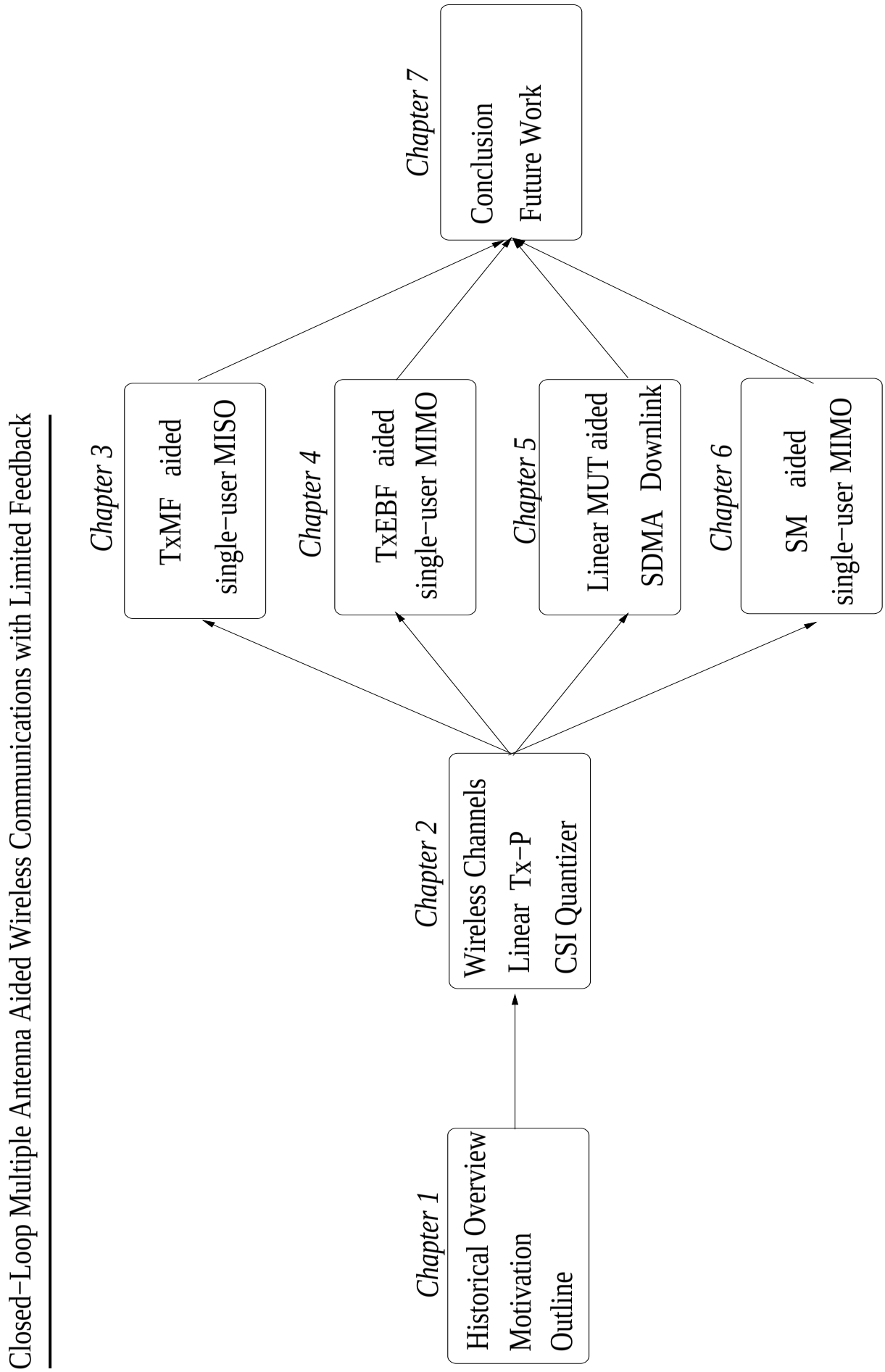

Figure 1.2: Thesis outline.

1.4 Novel Contributions

The thesis is based on the publications and manuscripts submissions of [99–106]. The novel contributions of this thesis include the following:

- In Chapter 3, the lower ergodic channel capacity bound of a TxMF aided closed-loop single-user MISO system scheme is derived [104], when considering the effects of channel estimation errors, quantization errors, the effective capacity loss caused by pilot symbols and that imposed by the channel information feedback bits. Moreover, an improved pilot signalling overhead reduction scheme is proposed for rapidly fading channels [104]. Furthermore, a novel technique, hereby referred to as pilot symbol assisted rateless (PSAR) coding is proposed [105, 106], which significantly reduces the computational complexity of the rateless channel decoder.

- In Chapter 4, a flexible closed-loop MIMO system amalgamating Linear Dispersion Codes (LDCs) and eigen-beam transmission is proposed [101] that achieves a higher capacity than the equivalent open-loop scheme, at the cost of feeding back a modest number of feedback bits from the mobile to the base station using Grassmannian beamforming-vector quantization. Moreover, a TxEBF aided closed-loop MIMO system is employed for video transmission in [103], which is capable of achieving a high bandwidth efficiency, and providing unequal error protection for video bits having different error sensitivities.

- In Chapter 5, a novel concept, referred to as the EXIT-Chart Optimised CSI Quantization (ECO-CQ) is proposed, which is capable of maintaining the lowest possible CSI feedback overhead, while ensuring an infinitesimally low BER [102]. Moreover, a CIR feedback scheme combined with vector quantisation and soft decoding is proposed [99], which is capable of minimising the distortion imposed by the error-contaminated feedback channel. Furthermoare, a periodical CIR update scheme employing a channel predictor at the DL transmitter for predicting the CIR taps for each future symbol transmission instant and hence to mitigate the performance degradation imposed by the associated signalling delays in [100]. A Predictive Vector Quantizer (PVQ) is used at the MTs for compressing the CIRs before their uplink transmission, which is capable of significantly reducing the CIR feedback overhead compared to a conventional VQ.

- In Chapter 6, three novel schemes, namely the open-loop ST-SSK scheme, the feedback-aided phase rotaion scheme and the feedback-aided power allocation schemes are proposed in order to achieve transmit diversity for a SSK aided MIMO system. Moreover, a novel diagonal linear dispersion code is proposed, which is capable of achieving the maximum attainable transmit diversity gain or multiplexing gain, while obeying the diversity versus multiplexing gain trade-off. Furthermore, a transmit diversity aided spatial modulation scheme is proposed, which is a combination of the diagonal LDC and the ST-SSK scheme.

Chapter 2

Key Topics in Closed-loop MIMO Communication

Compared to the family of open-loop MIMO systems, a closed-loop MIMO system has two distinctive components, which are the DL transmit preprocessing at the BS's transmitter side and the CSI quantizer at the MT's receiver as illustrated in Fig. 2.1. Moreover, the design of these two components depends on the underlying channel properties. In this section, these three key topics, namely the wireless MIMO channel model, the linear transmit preprocessing and the CSI quantization are discussed in detail.

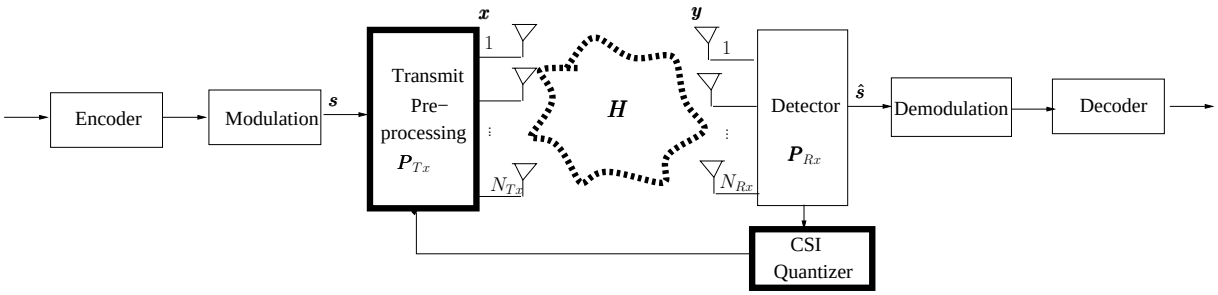

Figure 2.1: System model of a closed-loop MIMO communication system.

For any radio systems, the achievable performance and the appropriate signalling methods are closely related to the properties of the underlying wireless channel. For example, the channel capacity of spatially correlated channels is lower than that of spatially independent channels [107, 108]. Correspondingly, virtually all MIMO techniques are more appropriate for transmission over spatially independent channels than for spatially correlated channels. As a result, a realistic channel model becomes the foundation of system development and verification. In Section 2.1, the channel models employed in the rest of the thesis are described in detail.

A broad literature review of transmit preprocessing algorithms has been provided in Section 1.1.2. In Section 2.2, we focus our attention on the class of the linear transmit preprocessing schemes, including Transmit Matched Filter (TxMF), Transmit Eigen-Beamforming (TxEBF), Transmit Zero-Forcing (TxZF), Transmit Minimum Mean Square Error (TxMMSE) and Transmit Block Diagonalization (TxBD) for both single-user and multi-user scenarios. Apart from introducing these transmit preprocessing algorithms, the feedback information required for each of them is also discussed.

Based on the channel model provided in Section 2.1, three different CSI quantisers are analysed in Section 2.3 in order to effectively quantise the feedback information required for the various transmit pre-processing schemes discussed in Section 2.2. For each quantizer, the generation algorithm, the codebook example and the quantizer's performance quantified in terms of the averaged quantization error versus the number of quantization bits are provided. Finally, a summary of the chapter is provided in Section 2.4.

2.1 Channel Model

In this section, a broad introduction of the wireless channel is given in Section 2.1.1. Then, MIMO channel modelling schemes, including spatial domain and temporal domain models, are discussed in Section 2.1.2, followed by an example of the MIMO channel having two transmit antennas and a single receive antenna in Section 2.1.3.

2.1.1 Wireless Channel

A wireless channel model includes that of multiplicative fading, additive interference and additive noise. The additive noise is usually considered as Gaussian distributed and modelled by a random Gaussian process. The additive interference is modelled by the superposition of the signals transmitted by other users in the multi-user scenario discussed in Chapter 5, which is assumed to be zero in the single-user scenarios of Chapters 3, 4 and 6. The modelling of the multiplicative fading is discussed later in this section. For simplicity, the expression "channel model" refers to the modelling of multiplicative fading only in the rest of the thesis.

From a wave propagation point of view, the strengths of the radio waves decreases as the distance between the transmitter and receiver increases, which is often referred to as *large-scale fading* and is characterized by the *path loss exponent* and *shadowing variance*. Moreover, the radio waves are reflected, diffracted and scattered by the objects (e.g. buildings, hills, vehicles etc.) in the channel and hence arrive at the receiver with different strength at different time instants. The signals received via *multiple paths* are constructively or destructively combined and characterized by the *power delay profile*. Furthermore, since the antennas and the objects in the channel are in motion, the number of multipath components and their relationship varies over time, which results in a rapid fluctuation of the combined received signal over a short period of time and hence this phenomenon is referred to as *small-scale fading*. There are two important channel parameters characterising small-scale fading, namely the *coherence bandwidth* and *coherence time*. The coherence bandwidth denoted as B_C is a statistical measure of the bandwidth over which the channel may be deemed to have an approximately equal gain and linear phase. Assuming that the transmitted signal has a bandwidth of B_S, the channel is considered to be a *frequency-flat* or *narrowband* channel if $B_S \ll B_C$, and to be a *frequency-selective* or *wideband* channel if $B_S > B_C$. The coherence time denoted as T_C represents the time duration over which the channel's envelope is approximately time-invariant. If the transmit signal has a symbol duration T_S, the channel may be considered to be a *slow fading* channel if $T_S \ll T_C$, and to be a *fast fading* channel if $T_S > T_C$. Additionally, when a dominant stationary (nonfading) signal component is present, such as a Line-Of-Sight (LOS) propagation path, the statistical distribution of the fading envelope is *Rician*. Otherwise, the fading envelope of Non-Line-Of-Sight (NLOS) scenarios is considered to obey *Rayleigh* distribution. A more detailed

explanation of the aforementioned terminologies can be found in [109]. In this treatise, we concentrate on *small-scale slow frequency-flat/narrowband NLOS Rayleigh fading* channels.

The radio channel may be modelled by a linear filter associated with a time-variant impulse response. Hence, all characteristics of a radio channel can be represented by this complex-valued time-variant variable referred to as the Channel Impulse Response (CIR). Moreover, the continuous-time CIRs are sampled at a rate equal to the transmit signal's symbol rate for digital signal processing. For the flat fading channels considered in this treatise, the CIR contains a single tap and hence may be described by $h = |h|e^{j\varphi}$, where $|h|$ represents the channel's envelope and φ represents the channel's phase rotation. The statistical properties of CIRs are usually considered to be stationary, which is important in the context of transceiver design aiming for counteracting the long-term channel properties. Moreover, the properties of CIRs substantially vary, depending on the propagation environment and other parameters such as the carrier frequency used and the bandwidth employed. Since characterising every specific propagation scenario is impossible, extensive measurement campaigns have been carried out to capture the channel properties of several typical propagation environments, such as rural, urban, sub-urban, hill terrain etc.. The general objective of channel modelling is to generate CIRs, which capture the radio channel's properties in a specific propagation environment with an adequate grade of realism.

2.1.2 MIMO Channel Modelling

We typically represent the $(N_{Rx} \times N_{Tx})$ CIRs of a MIMO system by a complex-valued matrix, where we have N_{Tx} transmit and N_{Rx} receive antennas, which is formulated as

$$\boldsymbol{H} = \begin{bmatrix} h_{11} & \cdots & h_{1N_{Tx}} \\ \vdots & \ddots & \vdots \\ h_{N_{Rx}1} & \cdots & h_{N_{Rx}N_{Tx}} \end{bmatrix}. \tag{2.1}$$

Every element $h_{ij} = |h_{ij}|e^{j\varphi_{ij}}$ in the matrix represents the CIR spanning from the jth transmit antenna to the ith receive antenna, which are zero-mean unit-variance complex-valued Gaussian variables obeying $h_{ij} \sim \mathcal{CN}(0,1)$, when small-scale narrowband NLOS Rayleigh fading is considered. Moreover, the covariance matrix between two channel samples $\boldsymbol{H}[n]$ and $\boldsymbol{H}[n+m]$ is formulated as

$$\boldsymbol{R}[m] = E_{\boldsymbol{H}}\left[\text{vec}(\boldsymbol{H}[n])\text{vec}(\boldsymbol{H}[n+m])^H\right], \tag{2.2}$$

where $E_{\boldsymbol{H}}[\cdot]$ denotes the statistical expectation over $\boldsymbol{H}$, and the operation $\text{vec}(\cdot)$ stacks the columns of a matrix into one tall vector. The covariance matrix $\boldsymbol{R}[m]$, which is a function of the time difference m due to the channel's stationarity, captures both the channel's spatial and temporal correlations. Based on the premise that the channel's temporal statistics can be the same for all antenna pairs, it may be assumed that the temporal correlation is homogeneous and identical for any channel element h_{ij}. Then, the two correlation effects are separable, and the channel's auto-covariance becomes their product, which is formulated as

$$\boldsymbol{R}[m] = \rho[m]\boldsymbol{R}_0, \tag{2.3}$$

where $\boldsymbol{R}_0 = \boldsymbol{R}[0]$ $(m = 0)$ represents the spatial correlation, while $\rho[m]$ denotes the temporal auto-correlation of a single channel h_{ij}, which is formulated as

$$\rho[m] = E\left[h_{ij}[n]h_{ij}^*[n+m]\right]. \tag{2.4}$$

In the next two sections, the model of the time-domain and spatial-domain correlation is described in detail.

2.1.2.1 Spatial Domain

A substaintial body of research has been reported regarding SISO channel modelling [110, 111]. If the MIMO channels considerred are spatially independent, which corresponds to a rich scattering scenario, the modelling methods proposed for SISO channels may be readily extended to MIMO channels. However, since typical propagation environments often result in spatial correlation, physically meaningful yet easy-to-use methods are required to mimic the channel's spatial characteristics. The methods proposed in the open literature can be categorised into two classes, namely *physical models* and *analytical models*. The difference between these two approaches are described as follows.

1. Physical models [112–116] explicitly model the specific propagation environment (e.g. the location of the scatters) and wave propagation parameters. Physical models allow for an accurate reproduction of radio propagation. The disadvantage of physical models is that they are propagation environment dependent and computationally demanding.

2. Analytical models [117–119] characterize the CIR in a mathematical/analytical way without explicitly accounting for wave propagation. They are often favoured in the context of system development and verification owing to their appealing simplicity. However, they might be oversimplified and hence might fail to represent some properties of the realistic channel.

Besides, some standard models [120–122] have been proposed by various standard organisation. These models are usually a combination of physical models and analytical models. For example, the Spatial Channel Model (SCM) proposed by the 3rd Generation Partnership Project (3GPP) employs the Kronecker model [117] to generate over-simplified channel models for the purpose of quickly checking the validity of algorithms, and also employs physical models to generate specific channel models in various environment for the purpose of performance evaluation [4]. The classification of the MIMO channel spatial models is illustrated in Fig. 2.2. A survey of wireless MIMO channel models can be found in [123] and [124] for example. Moreover, the major contribution on MIMO channel modelling are summarised in Table 2.1.

We employ analytical models in this treatise for its simplicity. Normally, an analytical channel model provides an algorithm to reproduce the CIRs using a limited number of statistical channel parameters measured from the observed real channel. The validity of the channel model algorithm is verified by comparing the observed real channel and the reproduced one in terms of a certain metric, such as the ergodic mutual information. For example, based on the measured channel realizations $\boldsymbol{H}$, the spatial covariance matrix $\boldsymbol{R}_0$ may be readily calculated using Equation (2.2) by setting $m = 0$. Using the knowledge of $\boldsymbol{R}_0$, the realizations of the MIMO channel $\boldsymbol{H}$ may be modelled as

$$\mathrm{vec}(\boldsymbol{H}) = \boldsymbol{R}_0^{\frac{1}{2}}\boldsymbol{g}, \tag{2.5}$$

where $\boldsymbol{R}_0^{\frac{1}{2}}$ denotes the square root of an arbitrary matrix (e.g. any matrix satisfying $\boldsymbol{R}_0^{\frac{1}{2}}\boldsymbol{R}_0^{\frac{H}{2}} = \boldsymbol{R}_0$), and $\boldsymbol{g}$ is an $(N_{Tx}N_{Rx} \times 1)$ vector with independent and identically-distributed (i.i.d.) Gaussian elements, each having a zero mean and a unit variance. However, a significant drawback of this algorithm is the

Table 2.1: Major contributions addressing MIMO wireless channel modelling.

Author(s)	Contribution
[112]Steinbauer *et al.* 2001	introduced the concept of the double-directional mobile radio to describe the angular information at both link ends, which is the foundation of one of the deterministic channel modelling schemes called ray tracing.
[117] Kermoal *et al.* 2002	proposed Kronecker model, which uses the correlation matrices at the link ends to generate spatial correlated MIMO channels.
[118] Sayeed 2002	proposed virtual channel representation, which is restricted to single polarised ULAs.
[113] Molisch *et al* 2003	proposed the so-called Geometry-based Stochastic Channel Model (GSCM), which reduces the complexity compared to ray tracing scheme by using the PDF of the location of the scatterers.
[120] 3GPP 2003	proposed a spatial channel model, which is a combination of physical model and analytical model for various scenarios.
[121] Erceg *et al.* 2004	developed a so-called TGn channel model for indoor environments in 2 GHz and 5 GHz bands, with a focus on MIMO Wireless Local Area Networks (WLANs).
[119] Weichselberger *et al.* 2006	proposed Weichselberger model, which includes both the separate and joint correlation properties at the transmitter and the receiver.
[122] Molisch*et al.* 2006	proposed the pysical directional channel model for various communication scenarios.
[114] Loredo *et al.* 2008	presented a MIMO channel model based on rigorous ray tracing techniques for indoor scenario.
[115] Zajic *et al.* 2009	proposed a MT-to-MT wideband channel model based on the GSCM
[116] Emami-Forooshani and Noghanian 2010	develop a novel semi-deterministic physical channel model called Single Interaction ScatTEring Reflecting (SISTER) which is applicable to arbitrary antennas and is suitable for both indoor and outdoor environments.

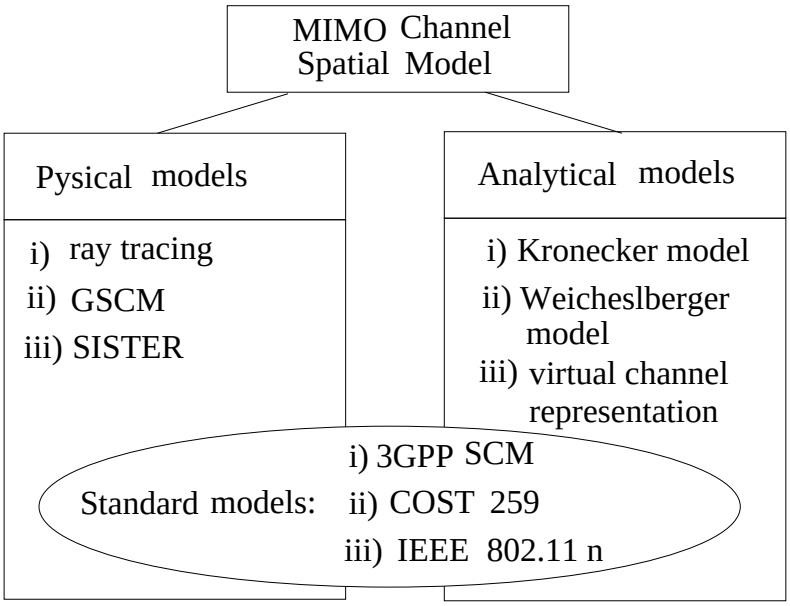

Figure 2.2: Classfication of spatial MIMO channel models.

substaintial size of the spatial correlation matrix $\boldsymbol{R}_0$, when the number of antennas employed becomes relatively high. It requires $(N_{Tx}N_{Rx})^2$ parameters to be fully specified. Moreover, a direct interpretation of the elements of $\boldsymbol{R}_0$ with respect to the physical propagation over the radio channel is challenging. As a result, some more sophisticated channel models were proposed in the open literature, such as the "Kronecker model" [117], the "Virtual Channel Representation" [118] and the "Weichselberger model" [119] .

Kronecker Model [117]

Instead of using the full covariance matrix $\boldsymbol{R}_0$, the Kronecker model employs the one-sided correlation matrix defined as

$$\begin{aligned} \boldsymbol{R}_{Tx} &= E_{\boldsymbol{H}}\left[\boldsymbol{H}^H\boldsymbol{H}\right], \\ \boldsymbol{R}_{Rx} &= E_{\boldsymbol{H}}\left[\boldsymbol{H}\boldsymbol{H}^H\right]. \end{aligned} \tag{2.6}$$

It formulates the channel realization as

$$\boldsymbol{H}_{kron} = \boldsymbol{R}_{Rx}^{\frac{1}{2}}\boldsymbol{G}\boldsymbol{R}_{Tx}^{\frac{H}{2}}, \tag{2.7}$$

where $\boldsymbol{G}$ is a $(N_{Rx} \times N_{Tx})$ complex-valued matrix with elements having i.i.d. zero-mean and unit-variance Gaussian distribution. The channel becomes spatially independent, if $\boldsymbol{R}_{Tx}$ and $\boldsymbol{R}_{Rx}$ are identity matrices. Moreover, the square root matrix $\boldsymbol{R}_{Tx}^{\frac{1}{2}}$ and $\boldsymbol{R}_{Rx}^{\frac{1}{2}}$ may be formulated as

$$\begin{aligned} \boldsymbol{R}_{Tx}^{\frac{1}{2}} &= \boldsymbol{U}_{Tx}\boldsymbol{\Lambda}_{Tx}^{\frac{1}{2}}, \\ \boldsymbol{R}_{Rx}^{\frac{1}{2}} &= \boldsymbol{U}_{Rx}\boldsymbol{\Lambda}_{Rx}^{\frac{1}{2}}, \end{aligned} \tag{2.8}$$

where the unitary matrix $\boldsymbol{U}_{(\cdot)}$ and the diagonal matrix $\boldsymbol{\Lambda}_{(\cdot)} = \mathrm{diag}\,(\lambda_1, \ldots)$ are the eigen-modes and eigen-values of the corresponding covariant matrix $\boldsymbol{R}_{(\cdot)}$, which are calculated through the eigen-

decomposition as follows

$$\begin{aligned} \boldsymbol{R}_{Tx} &= \boldsymbol{U}_{Tx}\Lambda_{Tx}\boldsymbol{U}_{Tx}^{H}, \\ \boldsymbol{R}_{Rx} &= \boldsymbol{U}_{Rx}\Lambda_{Rx}\boldsymbol{U}_{Rx}^{H}. \end{aligned} \tag{2.9}$$

Substitute Equation (2.8) to Equation (2.7), we obtain another expression of the Kronecker model, which is formulated as

$$\boldsymbol{H}_{kron} = \boldsymbol{U}_{Rx}\left(\left(\boldsymbol{\lambda}_{Rx}^{\frac{1}{2}}\boldsymbol{\lambda}_{Tx}^{\frac{T}{2}}\right)\odot \boldsymbol{G}\right)\boldsymbol{U}_{Tx}^{H}, \tag{2.10}$$

where $\odot$ denotes the element-wise product of two matrices.

Virtual Channel Representation [118]

Assuming that Uniform Linear Arrays (ULAs) are employed both at the transmitter and receiver side, and there are P scatters between them, the channel realization $\boldsymbol{H}$ may be written as

$$\boldsymbol{H} = \sum_{p=1}^{P} h_p \boldsymbol{a}_{Rx}(\phi_{Rx}, p)\boldsymbol{a}_{Tx}(\phi_{Tx}, p)^{H}, \tag{2.11}$$

where $h_p = |h_p|e^{j\varphi_p}$ denotes the path gain of the pth scatterer, while $\boldsymbol{a}_{Rx}(\phi_{Rx}, p)$ and $\boldsymbol{a}_{Tx}(\phi_{Tx}, p)$ are the array response and steering vectors for the pth scatterer having an Angle of Arrival (AOA) and Angle of Departure (AOD) of $\phi_{Rx,p}$ and $\phi_{Tx,p}$, respectively. Equation (2.11) may be written in a more compact matrix form as

$$\boldsymbol{H} = \boldsymbol{A}_{Rx}\boldsymbol{H}_P\boldsymbol{A}_{Tx}^{H}, \tag{2.12}$$

where $\boldsymbol{A}_{Rx} = [\boldsymbol{a}(\phi_{Rx,1}), \ldots, \boldsymbol{a}(\phi_{Rx,P})]$ is a $(N_{Rx} \times P)$-element matrix, $\boldsymbol{A}_{Tx} = [\boldsymbol{a}(\phi_{Tx,1}), \ldots, \boldsymbol{a}(\phi_{Tx,P})]$ is a $(N_{Tx} \times P)$-element matrix and $\boldsymbol{H}_p = \text{diag}\,(h_1, \ldots, h_P)$ is a $(P \times P)$ diagonal matrix. Equation (2.12) provides a physical model for reproducing the CIRs, which requires the knowledge of each path's AOA $\boldsymbol{a}_{Rx}(\phi_{Rx}, p)$, AOD $\boldsymbol{a}_{Tx}(\phi_{Tx}, p)$ and that of the path gain h_p.

Furthermore, the array steering and response vectors of ULAs are given by

$$\begin{aligned} \boldsymbol{a}_{Rx}(\phi_{Rx,p}) &= \frac{1}{\sqrt{N_{Rx}}}\left[\begin{array}{cccc} 1 & e^{-j2\pi\cdot 1\cdot d_{Rx}f_c\cos\phi_{Rx,p}} & \ldots & e^{-j2\pi\cdot(N_{Rx}-1)\cdot d_{Rx}f_c\cos\phi_{Rx,p}} \end{array}\right]^{T}, \\ \boldsymbol{a}_{Tx}(\phi_{Rx,p}) &= \frac{1}{\sqrt{N_{Tx}}}\left[\begin{array}{cccc} 1 & e^{-j2\pi\cdot 1\cdot d_{Tx}f_c\cos\phi_{Tx,p}} & \ldots & e^{-j2\pi\cdot(N_{Tx}-1)\cdot d_{Tx}f_c\cos\phi_{Tx,p}} \end{array}\right]^{T}, \end{aligned} \tag{2.13}$$

where f_c is the carrier frequency, while d_{Rx} and d_{Tx} are the antenna spacing at the transmitter and receiver, respectively. They are periodic in $\theta = df_c\cos(\phi)$ with θ period of 1. This implies that scatterers having $\theta = df_c\cos(\phi)$ outside the range of $[-0.5,\ 0.5)$ are reflected back into the principal period of θ. Considering this periodic property, the paths having different AOD and AOAs but producing the same value of θ in the principal period $[-0.5,\ 0.5)$ may be grouped together and hence considered as a single independent path. This idea inspired the invention of virtual channel representation, which is an analytical channel model. More explicitly, we assumed that there are a fixed number of $(N_{Tx} \times N_{Rx})$ virtual paths, which consist of N_{Tx} virtual transmit beams and N_{Rx} virtual receive beams. The corresponding virtual AODs and AOAs are created by uniformly sampling the principal θ period of $[-0.5,\ 0.5)$ using a step-size of $1/N_{Tx}$ and $1/N_{Rx}$, respectively. The resultant matrices $\boldsymbol{A}_{Rx}$ and $\boldsymbol{A}_{Tx}$ using the virtual AOAs

and AODs happen to be the Discrete Fourier Tansform (DFT) matrices $\boldsymbol{F}_{N_{Rx}}$ and $\boldsymbol{F}_{N_{Tx}}$ having a size of $(N_{Rx} \times N_{Rx})$ and $(N_{Tx} \times N_{Tx})$, respectively. Hence, the channel representation of Equation (2.12) may be formulated as

$$\boldsymbol{H}_{virt} = \boldsymbol{F}_{N_{Rx}} \boldsymbol{H}_v \boldsymbol{F}^H_{N_{Tx}}, \tag{2.14}$$

where $\boldsymbol{H}_v$ represents the energy coupling between the N_{Tx} virtual transmit beams and the N_{Rx} virtual receive beams. The matrix $\boldsymbol{H}_v$ is no longer a diagonal matrix and can be further formulated as

$$\boldsymbol{H}_{virt} = \boldsymbol{F}_{N_{Rx}} (\tilde{\boldsymbol{\Omega}}_{virt} \odot \boldsymbol{G}) \boldsymbol{F}^H_{N_{Tx}}, \tag{2.15}$$

where $\tilde{\boldsymbol{\Omega}}_{virt}$ represents the element-wise square-root of the energy coupling matrix $\boldsymbol{\Omega}_{virt}$. Given the measured impulse responses $\boldsymbol{H}$, the energy coupling matrix $\boldsymbol{\Omega}_{virt}$ is formulated as fellows

$$\boldsymbol{\Omega}_{virt} = E_{\boldsymbol{H}} \left[(\boldsymbol{F}_{Rx} \boldsymbol{H} \boldsymbol{F}^*_{Tx}) \odot (\boldsymbol{F}^H_{Rx} \boldsymbol{H}^* \boldsymbol{F}_{Tx}) \right]. \tag{2.16}$$

Having the knowledge of $\boldsymbol{\Omega}_{virt}$, Equation (2.15) provides a scheme, which allows us to reproduce the CIRs for a MIMO channel using ULAs at both the transmit and receive end. If all elements of $\boldsymbol{\Omega}_{virt}$ are identical, the resultant channel matrix is an i.i.d. random matrix.

Weichselberger Model [119]

Given the measured channel realizations, the one-sided correlation matrices $\boldsymbol{R}_{Tx}$ and $\boldsymbol{R}_{Rx}$ may be first calculated using Equation (2.6). Then, eigen-decomposition of the CIR $\boldsymbol{H}$ is applied in order to obtain the eigenbases of both transmitter and receiver as shown in Equation (2.9), where the eigenbases $\boldsymbol{U}_{Tx}$ and $\boldsymbol{U}_{Rx}$, consist of the eigenvectors denoted by $\boldsymbol{u}_{Tx,j}$ $(1 \leq j \leq N_{Tx})$ and $\boldsymbol{u}_{Rx,i}$ $(1 \leq i \leq N_{Rx})$, respectively. Moreover, a so-called coupling matrix denoted as $\boldsymbol{\Omega}$ may be obtained from the measured impulse responses $\boldsymbol{H}$ as follows:

$$\boldsymbol{\Omega} = E_{\boldsymbol{H}} \left[(\boldsymbol{U}_{Rx} \boldsymbol{H} \boldsymbol{U}^*_{Tx}) \odot (\boldsymbol{U}^H_{Rx} \boldsymbol{H}^* \boldsymbol{U}_{Tx}) \right]. \tag{2.17}$$

The coefficients in the coupling matrix specify the average amount of energy that is coupled from the *i*th eigenvector of the receiver side to the *j*th eigenvector of the transmitter side (or vice versa). In other words, it characterises the dependence between the transmitter and the receiver, which is neglected by the Kronecker model. Armed with the knowledge of $\boldsymbol{U}_{Tx}$, $\boldsymbol{U}_{Rx}$ and $\boldsymbol{\Omega}$, the channel realization may be modelled as

$$\boldsymbol{H}_{weich} = \boldsymbol{U}_{Rx} (\tilde{\boldsymbol{\Omega}} \odot \boldsymbol{G}) \boldsymbol{U}^H_{Tx}, \tag{2.18}$$

where $\boldsymbol{G}$ is a $(N_{Rx} \times N_{Tx})$ complex-valued matrix with elements having i.i.d. zero-mean and unit-variance Gaussian distribution, and $\tilde{\boldsymbol{\Omega}}$ is the element-wise square root of the matrix $\boldsymbol{\Omega}$. If all elements of $\boldsymbol{\Omega}$ are exactly identical, the resultant channel matrix is an i.i.d. random matrix, unlike in the Kronecker model.

Summary

Fig. 2.3 illustrates the relationship between the above-mentioned three channel models. More explicitly, the Weichselberger model reduces to the virtual channel representation model, when forcing the eigenbases to be the DFT matrix, and it reduces to the Kronecker model, upon forcing the coupling matrix $\boldsymbol{\Omega}$ to

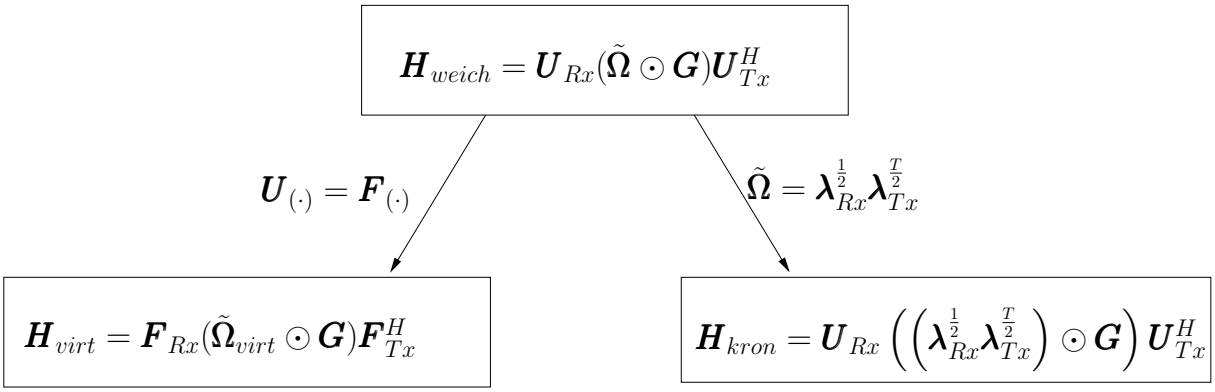

Figure 2.3: Relationships among the three channel models, namely the Weichselberger model [119], the Kronecker model [117] and the virtual channel representation [118].

be the outer product of the two singular vectors $\boldsymbol{\lambda}_{Tx}^{\frac{1}{2}}$ and $\boldsymbol{\lambda}_{Rx}^{\frac{1}{2}}$. It was demonstrated in [118] that the DFT matrices serve as asymptotically optimal eigenbases for the channel matrices using ULAs (when the number of antenna elements tends to infinity). Hence, the employment of the virtual channel representation model is restricted to single polarised ULAs. By contrast, the Kronercker model is suitable for arbitrary antenna configurations. However, by forcing the coupling matrix to assure the form $\tilde{\boldsymbol{\Omega}} = \boldsymbol{\lambda}_{Rx}^{\frac{1}{2}}\boldsymbol{\lambda}_{Tx}^{\frac{T}{2}}$, the dependence between the transmitter and the receiver is neglected. Hence, the Weichselberger model alleviates the restrictions imposed by both the virtual channel representation model as well as by the Kronercker model, and provides a more general and accurate channel model than the other two. It was demonstrated in [119] that the modelled mutual information generated using the Weichselberger model provides the best match of the measured mutual information compared to the other two channel models.

Fig. 2.4 protrays three characteristic structures of the energy coupling matrices and the corresponding physical scenarios with the aid of numerical examples, which further illustrates the physical interpretation of the Weichselberger channel model. The first example represented by $\boldsymbol{\Omega}_1$ shows a fully-loaded structure of the energy coupling matrix. Each transmit eigen-mode is linked with each receive eigen-mode. If all elements of $\boldsymbol{\Omega}_1$ are identical, this scenario corresponds to the spatially white MIMO case. Otherwise, the resultant MIMO channel is spatially correlated. A possible physical scenario leading to such a channel is constituted by rich scattering clusters at both link ends. In this case, the achievable diversity gain contributed by the transmit and receive ends are equal to N_{Tx} and N_{Rx}, respectively, and the attainable multiplexing gains are equal to $\min(N_{Tx}, N_{Rx})$.

The second example represented by $\boldsymbol{\Omega}_2$ of Fig. 2.4 is constituted by the outer product of two fully-loaded energy coupling vectors, which is equivalent to the Kronecker model. Compared to the first example cast in the context of $\boldsymbol{\Omega}_1$, the channel modelled by $\boldsymbol{\Omega}_2$ has similar properties - for example, they both have the same affordable diversity gain and multiplexing gain. However, since the energy coupling between the transmit eigen-mode and the receive eigen-mode is not considered, a corresponding possible physical scenarios is that the scatter clusters around both of the link ends are far apart. Hence the correlation between the transmit beams and receive beams becomes negligible.

The third example constituted by $\boldsymbol{\Omega}_3$ of Fig. 2.4 has significant power values in the first column and negligible power values in the rest of the matrix. The resultant channel matrix is close to modelling a rank-deficient physical scenario, where the elements of the transmit antenna array are so close to each

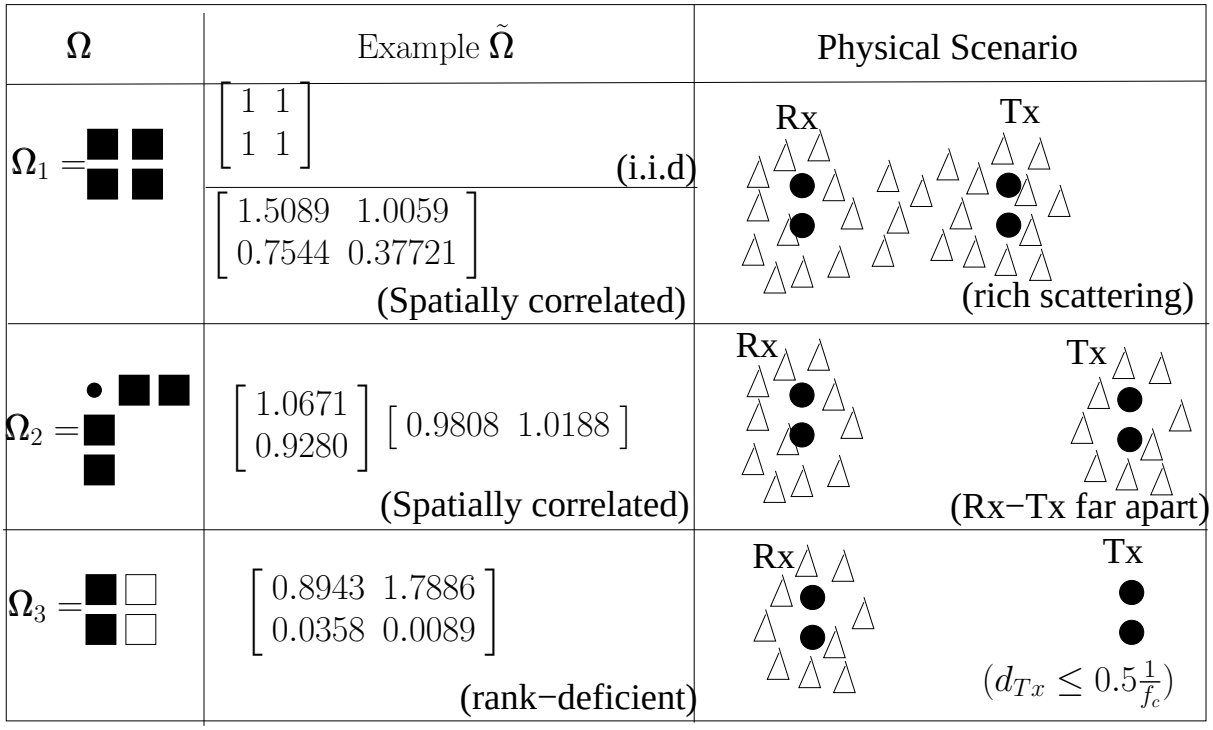

Figure 2.4: Three structures of the energy coupling matrix $\mathbf{\Omega}$ (black squares: significant power; white squares: negligible power; $\mathbf{\Omega}_2$ is the outer product of two vectors), the corresponding examples, and the physical scenarios (black dots: antenna array; white triangles: scatterers) [119]

other that their response to all of the multipath components becomes similar.

In this treatise, we concentrate on the full-rank, spatially white as well as spatially correlated scenarios, and employ the Kronecker model to generate CIRs. The Weichselberger model will not be used, because the energy coupling matrix $\mathbf{\Omega}$ calculated using Equation (2.17) is based on numerous experimentally measured CIRs, which does not conveniently lend itself to simulations. By contrast, the Kronecker model provides a convenient way of generating CIRs for arbitrary one-sided covariance matrices $\boldsymbol{R}_{Tx}$ and $\boldsymbol{R}_{Rx}$ by setting $\tilde{\mathbf{\Omega}} = \boldsymbol{\lambda}_{Rx}^{\frac{1}{2}} \boldsymbol{\lambda}_{Tx}^{\frac{T}{2}}$. Additionally, in order to have a zero-mean, unit-variance Rayleigh channel for each transmit-receive link, the element-wise square root of the energy coupling matrix $\tilde{\mathbf{\Omega}}$ is normalised to satisfy $\mathtt{tr}\left(\tilde{\mathbf{\Omega}}^T \tilde{\mathbf{\Omega}}\right) = N_{Tx} N_{Rx}$.

2.1.2.2 Temporal Domain

According to the Wiener-Khintchine theorem [109], the Power Spectral Density (PSD) is the Fourier transform of the auto-correlation function (ACF), as stated in Equation (2.4)

$$S(f) = \sum_m \rho[m] e^{-j2\pi f m}. \tag{2.19}$$

The frequency range over which $S(f)$ the transmitted signal's PSD is non-zero indicates the Doppler spread. The maximum frequency spread is given by the channel's Doppler spread denoted as f_{dm}. Having a higher mobility in a system results in a proportionately increased Doppler spread. Let us assume that the system is sampled once every transmit symbol duration T_s, and introduce the normalised maximum Doppler spread denoted as $f_{dm-norm} = f_{dm} T_s$, $0 \leq f_{dm-norm} \leq 1$. A popular fast-fading model is that

Table 2.2: Channel Parameters

N_{Tx}	2
N_{Rx}	1
$f_{dm-norm}$	0.1
Scenarios	a) $\boldsymbol{R}_{Tx} = \begin{bmatrix} 1 & 0 \\ 0 & 1 \end{bmatrix}$, $\boldsymbol{R}_{Rx} = 1$
	b) $\boldsymbol{R}_{Tx} = \begin{bmatrix} 1 & 0.93 \\ 0.93 & 1 \end{bmatrix}$, $\boldsymbol{R}_{Rx} = 1$

of Clark which was popularised by Jakes [109], and assumes having uniformly distributed scatterers on a circle around the antenna, which results in the following temporal correlation:

$$\rho[m] = J_0(2\pi f_{dm} m T_s) = J_0(2\pi f_{dm-norm} m), \tag{2.20}$$

where J_0 is the zero-th order Bessel function of the first kind. Having the knowledge of $f_{dm-norm}$, a sequence of time-correlated channel samples may be readily generated using Equation (2.20).

2.1.3 A MIMO Channel Generation Example

In this section, a MIMO channel having two transmit antennas and a single receive antenna associated with the parameters summarised in Table 2.2 is generated as an example. The maximum normalised Doppler frequency is set to 0.1, and the Kronecker model detailed in Section 2.1.2.1 is employed. Two different scenarios are considered, namely a) $\boldsymbol{R}_{Tx} = \begin{bmatrix} 1 & 0 \\ 0 & 1 \end{bmatrix}$, $\boldsymbol{R}_{Rx} = 1$, and b) $\boldsymbol{R}_{Tx} = \begin{bmatrix} 1 & 0.93 \\ 0.93 & 1 \end{bmatrix}$, $\boldsymbol{R}_{Rx} = 1$ in order to represent spatially independent and spatially correlated scenarios, respectively.

Fig. 2.5 illustrates the envelope of the temporal responses h_1 and h_2 of the two channels, where it is clearly seen that the channel samples generated are time-correlated. Moreover, when these two channels are spatially independent i.e. we have $\boldsymbol{R}_{Tx} = \begin{bmatrix} 1 & 0 \\ 0 & 1 \end{bmatrix}$, the envelope of these two channels varies independently, as shown in Fig. 2.5 a). By contrast, when we have $\boldsymbol{R}_{Tx} = \begin{bmatrix} 1 & 0.93 \\ 0.93 & 1 \end{bmatrix}$ for example, the envelopes of these two channels shown in Fig. 2.5 b) have similar values and tend to fluctuate jointly. Utilising the channel realizations generated, three correlation coefficients may be calculated between the two channels, namely those with respect to the complex-valued channel gain, the channel envelope and the channel's phase rotation, as follows

$$\begin{aligned} \rho_{h_1 h_2} &= \frac{E\left[(h_1 - E\left[h_1\right])(h_2 - E\left[h_2\right])\right]}{\sigma_{h_1}\sigma_{h_2}}, \\ \rho_{|h_1||h_2|} &= \frac{E\left[(|h_1| - E\left[|h_1|\right])(|h_2| - E\left[|h_2|\right])\right]}{\sigma_{|h_1|}\sigma_{|h_2|}}, \\ \rho_{\phi_1\phi_2} &= \frac{E\left[(\phi_1 - E\left[\phi_1\right])(\phi_2 - E\left[\phi_2\right])\right]}{\sigma_{\phi_1}\sigma_{\phi_2}}, \end{aligned} \tag{2.21}$$

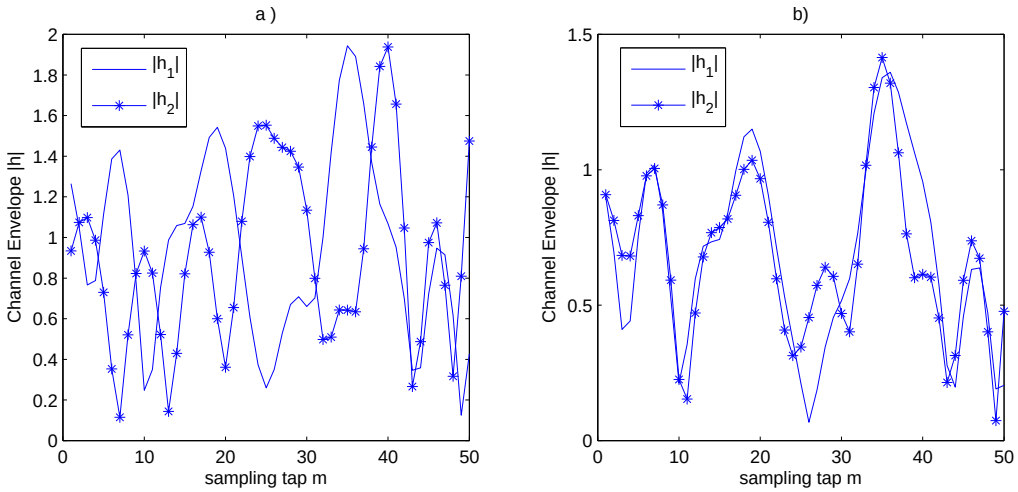

Figure 2.5: Envelope of the temporal channel response of the channels h_1 and h_2, when they are a) spatially independent and b) spatially correlated channels. The covariance matrices $\boldsymbol{R}_{Tx}$ and $\boldsymbol{R}_{Rx}$ are shown in Table 2.2

where σ_x denotes the standard deviation of the random variable x. When the MIMO channel is spatially independent, we have $\rho_{h_1h_2} = \rho_{|h_1||h_2|} = \rho_{\phi_1\phi_2} = 0$. By contrast, when the MIMO channel is spatially correlated, as in scenario b), we may have for example $\rho_{h_1h_2} = 0.93 + 0.0004i$, $\rho_{|h_1||h_2|} = 0.8464$ and $\rho_{\phi_1\phi_2} = 0.6709$. The joint distribution of the two channel envelopes and channel phases is illustrated in Fig. 2.6 and Fig. 2.7 for spatially independent and spatially correlated channels, respectively.

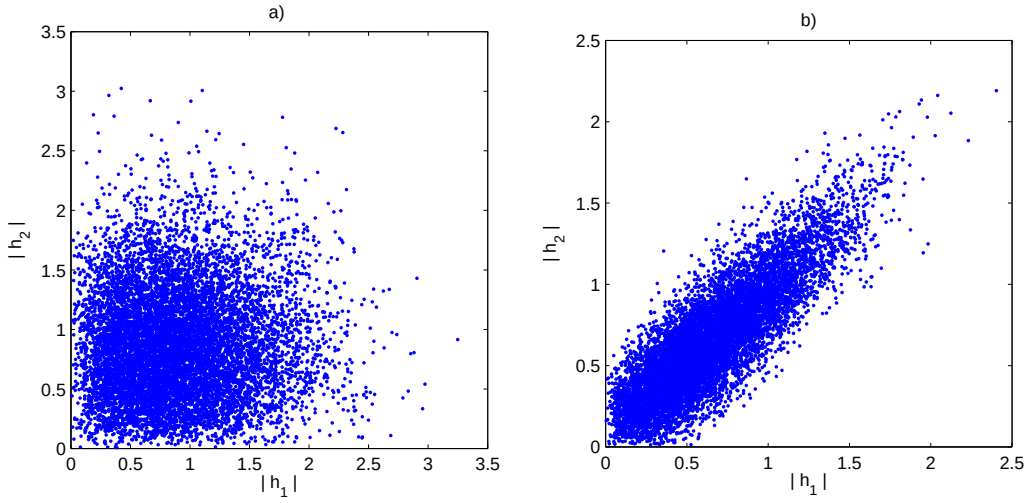

Figure 2.6: Joint distribution of the two channels' envelopes when we have a) spatially independent and b) spatially correlated channels. The covariance matrices $\boldsymbol{R}_{Tx}$ and $\boldsymbol{R}_{Rx}$ are given in Table 2.2

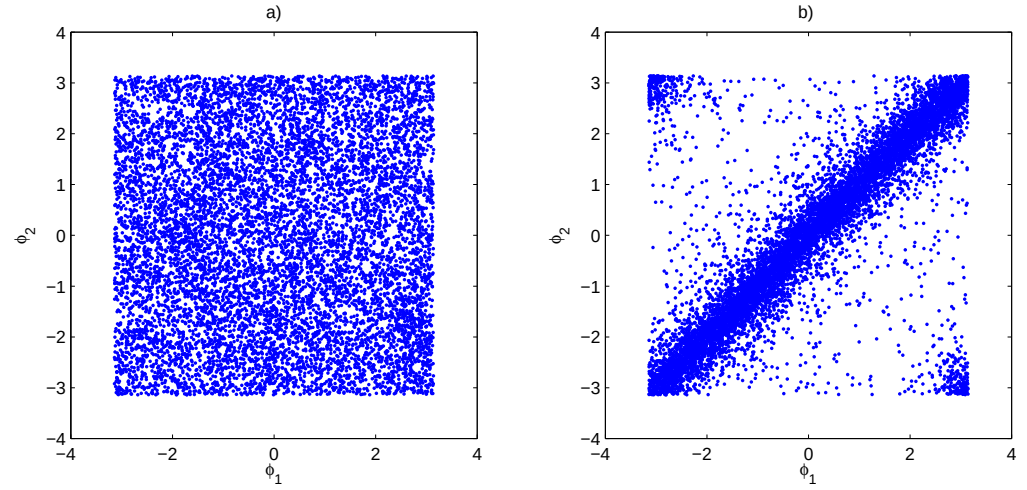

Figure 2.7: Joint distribution of the two channels' phases when we have a) spatially independent and b) spatially correlated channels. The covariance matrices $\boldsymbol{R}_{Tx}$ and $\boldsymbol{R}_{Rx}$ are given in Table 2.2

2.2 Linear Transmit Preprocessing

Having briefly characterized both the family of spatially and temporally correlated MIMO channels, let us now turn our attention to the portrayal of MIMO-aided transmit preprocessing techniques. In Section 1.1.2, the literature review of various transmit preprocessing schemes were provided. In this section, several linear transmit preprocessing algorithms, which may be roughly classified into algorithms for single-user scenarios and multi-user scenarios, are described in detail including every algorithm's derivation, benefits, constraints and the required feedback information.

In this section, perfect channel knowledge is assumed to be availabe both at the transmitter and receiver side. Recall that our generalised MIMO system model having N_{Tx} transmit antennas and N_{Rx} receive antennas was shown in Fig. 2.1. The transmitter preprocessing may be formulated as

$$\hat{\boldsymbol{s}} = \boldsymbol{P}_{Rx}\boldsymbol{y} = \boldsymbol{P}_{Rx}(\boldsymbol{H}\boldsymbol{x} + \boldsymbol{n}) = \boldsymbol{P}_{Rx}(\boldsymbol{H}\boldsymbol{P}_{Tx}\boldsymbol{s} + \boldsymbol{n}), \tag{2.22}$$

where $\hat{\boldsymbol{s}}$ is the estimated symbol obtained in the receiver, $\boldsymbol{s}$ is the symbol to be transmitted before preprocessing, $\boldsymbol{x}$ is the signal to be transmitted after preprocessing, $\boldsymbol{n}$ denotes the noise vector, $\boldsymbol{y}$ is the received signal, $\boldsymbol{P}_{Tx}$ represents the transmit preprocessing matrix and $\boldsymbol{P}_{Rx}$ represents the receive postprocessing matrix. The objective of transmit preprocessing is to exploit the available channel knowledge, and to design an appropriate preprocessing matrix $\boldsymbol{P}_{Tx}$ in order to improve the achievable system performance, such as the throughput and BER. Moreover, the transmit preprocessing matrix $\boldsymbol{P}_{Tx}$ has to satisfy the long-term power constraint of

$$E\left[\|\boldsymbol{x}\|_2^2\right] = E\left[\|\boldsymbol{P}_{Tx}\boldsymbol{x}\|_2^2\right] = \mathtt{tr}\left(\boldsymbol{P}_{Tx}\boldsymbol{R}_S\boldsymbol{P}_{Tx}^H\right) \leq E_{Tx}, \tag{2.23}$$

where $\boldsymbol{R}_S$ represents the covariance matrix of the transmit symbols and E_{Tx} denotes the averaged energy corresponding to the transmit power [26].

2.2.1 Single-user Scenario

The so-called Transmit Matched Filter (TxMF) designed for a MISO channel and the Transmit Eigen-Beamforming (TxEBF) concept conceived for a MIMO channel are introduced in this section. The first one can be considered as a special case of the second one.

2.2.1.1 Transmit Matched Filter for MISO Scenarios

The intuitive idea behind the TxMF concept is that of moving the receiver's matched filter from the receiver to the transmitter, which was proposed in [125]. The resultant TxMF is capable of maximising the power of the desired signal at the respective receiver, while having the same transmit power as the open-loop scheme.

Consider a MISO system, where we have $N_{Tx} > 1$, $N_{Rx} = 1$, $P_{Rx} = 1$. The corresponding transmit preprocessing matrix $\boldsymbol{P}_{Tx}$ of the TxMF scheme may be formulated as

$$\boldsymbol{P}_{Tx} = \frac{\boldsymbol{h}^*}{\|\boldsymbol{h}\|_2}, \tag{2.24}$$

where $\boldsymbol{h}$ represents the $(N_{Tx} \times 1)$-element channel vector. Since $\boldsymbol{P}_{Tx}$ is a complex-valued unitary vector, where we have $\boldsymbol{P}_{Tx}^H \boldsymbol{P}_{Tx} = 1$, the power constraint stated in Equation (2.23) is satisfied.

A particular benefit of using the TxMF is that the received SNR is maximised, yielding $\frac{\|\boldsymbol{h}\|_2 E_{Tx}}{N_0}$. Moreover, if the channel is spatially independent, a transmit diversity order of N_{Tx} as well as a power gain of N_{Tx} are achieved, because the effective channel gain $\|\boldsymbol{h}\|_2$ is given by the sum of N_{Tx} independent Rayleigh distributed variables, which is formulated as $\|\boldsymbol{h}\|_2 = \sqrt{|h_1|^2 + \ldots + |h_{N_{Tx}}|^2}$.

To facilitate the employment of the TxMF at the transmitter side, the receiver could either simply feed back the entire CIR vector $\boldsymbol{h}$, or may calculate the unitary vector $\boldsymbol{P}_{Tx}$ illustrated in Equation (2.24) for feeding it back to the transmitter.

2.2.1.2 Transmit Eigen-beamforming

The capacity of a MIMO channel may be approached by using a combination of Singular Value Decomposition (SVD) and classic water-filling based power allocation [1, 47]. More explicitly, the information is transmitted through the eigen-beams, and the transmit power allocated to each eigen-beam is proportional to its corresponding eigen-value.

The SVD of a MIMO channel $\boldsymbol{H}$ is formulated as

$$\boldsymbol{H} = \boldsymbol{U}_H \boldsymbol{\Lambda}_H^{\frac{1}{2}} \boldsymbol{V}_H^H, \tag{2.25}$$

where $\boldsymbol{U}_H$ is the left-hand-side unitary matrix of the MIMO channel $\boldsymbol{H}$, $\boldsymbol{V}_H$ is the right-hand-side unitary matrix of the MIMO channel $\boldsymbol{H}$, and $\boldsymbol{\Lambda}_H^{\frac{1}{2}}$ consits of $\min(N_{Tx}, N_{Rx})$ number of real positive unitary values $\sqrt{\lambda_i}$ lying on the diagonal line. In fact, $\boldsymbol{U}_H$ and $\boldsymbol{V_H}$ are the eigen-bases of the Hermitian matrices $\boldsymbol{H}\boldsymbol{H}^H$ and $\boldsymbol{H}^H\boldsymbol{H}$, respectively. Moreover, the singular value matrix $\boldsymbol{\Lambda}_H^{\frac{1}{2}}$ is the square root of the eigen value matrix $\boldsymbol{\Lambda}_H$ having $\min(N_{Tx}, N_{Rx})$ non-zero eigen-values λ_i on the diagonal. To approach the channel capacity, the matching postprocessing matrix has to be defined as the left-hand-side unitary matrix given by

$$\boldsymbol{P}_{Rx} = \boldsymbol{U}_H, \tag{2.26}$$

while the preprocessing matrix is formulated as

$$\boldsymbol{P}_{Tx} = \boldsymbol{V}_H \sqrt{\boldsymbol{E}_{Tx}}, \tag{2.27}$$

where $\boldsymbol{E}_{Tx}$ consists of a maximum of $\min(N_{Tx}, N_{Rx})$ number of non-zero diagonal-elements, with E_i representing the power allocated to the corresponding eigen-beams. Using the classic water-filling algorithm, the power allocated to the i-th eigen-beam is calculated as [1, 47]

$$E_i = (\mu - \frac{N_0}{\lambda_i})^+, \tag{2.28}$$

where λ_i is the ith diagonal element of the eigen-value matrix Λ_H, and the function $(\cdot)^+$ represents the value itself inside the parenthesis when this value is positive, and it is set to zero otherwise. Furthermore, E_i must satisfy the total power constraint of

$$\sum_{i=1} E_i \leq E_{Tx}. \tag{2.29}$$

The calculation of E_i is usually carried out in an iterative manner. For example, the value of μ is first initialised as $\mu = \frac{1}{\min(N_{Rx},N_{Tx})}$, and the power allocated to each eigen-beam is calculated using Equation (2.28). If for example we have to allocate zero power to two eigen-beams according to Equation (2.28), then the value of μ becomes $\mu = \frac{1}{\min(N_{Rx},N_{Tx})-2}$ in the next iteration, until the power allocated to all activated eigen-beams becomes non-zero. As a result, the water-filling based power allocation algorithm tends to allocate all the power to the specific eigen-beams having the strongest eigenvalue at low SNRs (e.g. $N_0 \rightarrow +\infty$), and to allocate equal power to all eigen-beams having non-zero eigenvalues at high SNRs (e.g. $N_0 \rightarrow 0$).

The aforementioned algorithm is referred to as transmit eigen-beamforming in this treatise, since the signals are transmitted in the non-zero eigen-directions $\boldsymbol{U}_H$, as viewed from a receiver's perspective. The transmit matched filter designed for the MISO scenario discussed in Section 2.2.1.1 is a special case of transmit eigen-beamforming, where $\boldsymbol{P}_{Rx} = 1$, $\boldsymbol{V}_H$ has only a single eigen-vector $\frac{\boldsymbol{h}^*}{\|\boldsymbol{h}\|_2}$, and all the transmit power is allocated to this single eigen-beam.

Transmit eigen-beamforming essentially decomposes the MIMO channel into several parallel orthogonal sub-channels. Hence, the signal transmitted through these sub-channels becomes interference-free, which is one of the benefits of using transmit eigen-beamforming. Moreover, the channel capacity can be approached when using water-filling based power allocation combined with appropriate modulation and coding schemes for every eigen-beam employed. However, the quality of the resultant orthogonal sub-channels may be very different from each other. Based on the statistical distribution of the eigen-values of a random matrix [126], a diversity order of $(N_{Tx} \times N_{Rx})$ and a beamforming gain of $N_{Tx}N_{Rx}$ are achievable for signals transmitted via the specific eigen-beam having the strongest eigen-value. By contrast, the BER performance of the signals transmitted over the eigen-beam having the weakest eigen-value is typically worse than that experienced for transmission over a Rayleigh channel having no diversity. This property has been exploitted in Section 4.3 to facilitate video transmissions.

Instead of requiring full channel knowledge $\boldsymbol{H}$ at the transmitter side, transmit eigen-beamforming may also be implemented, if only the eigen-vectors in the right-hand-side unitary matrix $\boldsymbol{V}_H$ associated with non-zero transmit power are known at the transmitter side. If water-filling based power allocation is employed in addition, then the singular values or the allocated power calculated at the receiver sided are required to feed back to the transmitter. As a result, the required quantized information is constituted by complex-valued unitary vectors or a unitary matrix, and the power allocated.

2.2.2 Multi-User Scenario

Numerous Multi-User Detection (MUD) algorithms have been proposed in the open literature [127], such as the zero-forcing MUD [128], the Minimum Mean Square Error (MMSE) MUD, the minimum bit-error-rate MUD [129], the sphere-packing MUD [130] and the ant-colony aided MUD [22]. The corresponding transmit preprocessing algorithms do exist for almost every linear MUD scheme [26, 131]. In this treatise, three basic linear transmit preprocessing schemes, namely Transmit Zero-ForcingTxZF [26], TxMMSE [26] and TxBD [64] are considered.

2.2.2.1 Transmit Zero Forcing for MISO Scenarios

When we have $N_{Tx} > 1$ transmit antennas at the BS, $N_{Rx} = 1$ receive antenna at each MT and $K > 1$ active users, the channel matrix $\boldsymbol{H}$ has a size of $(K \times N_{Tx})$, in which the k-th row represents the CIR signature of the kth user. Here we dispense with user-cooperation, hence the postprocessing matrix employed at the MT simply becomes $\boldsymbol{P}_{Rx} = \boldsymbol{I}$. In order to eliminate the inter-user interference at the transmitter, the transmit preprocessing matrix using the TxZF algorithm is formulated as

$$\boldsymbol{P}_{Tx} = \boldsymbol{H}^{\dagger}\alpha = \boldsymbol{H}^{H}(\boldsymbol{H}\boldsymbol{H}^{H})^{-1}\alpha, \tag{2.30}$$

where $(\cdot)^{\dagger}$ represents the pseudoinverse of a matrix, and α is the corresponding power normalisation factor. Assuming that the maximum allowable transmit power of each user is equal to E_{Tx}, the power normalisation factor may be calculated as

$$\alpha = \sqrt{\frac{KE_{Tx}}{\mathtt{tr}\left((\boldsymbol{H}\boldsymbol{H}^{H})^{-1}\right)}}. \tag{2.31}$$

or as

$$\alpha_k = \sqrt{\frac{E_{Tx}}{\boldsymbol{H}^{\dagger H}\boldsymbol{H}^{\dagger}{}_{(k,k)}}},\ \alpha_k \neq \alpha_j,\ k \neq j. \tag{2.32}$$

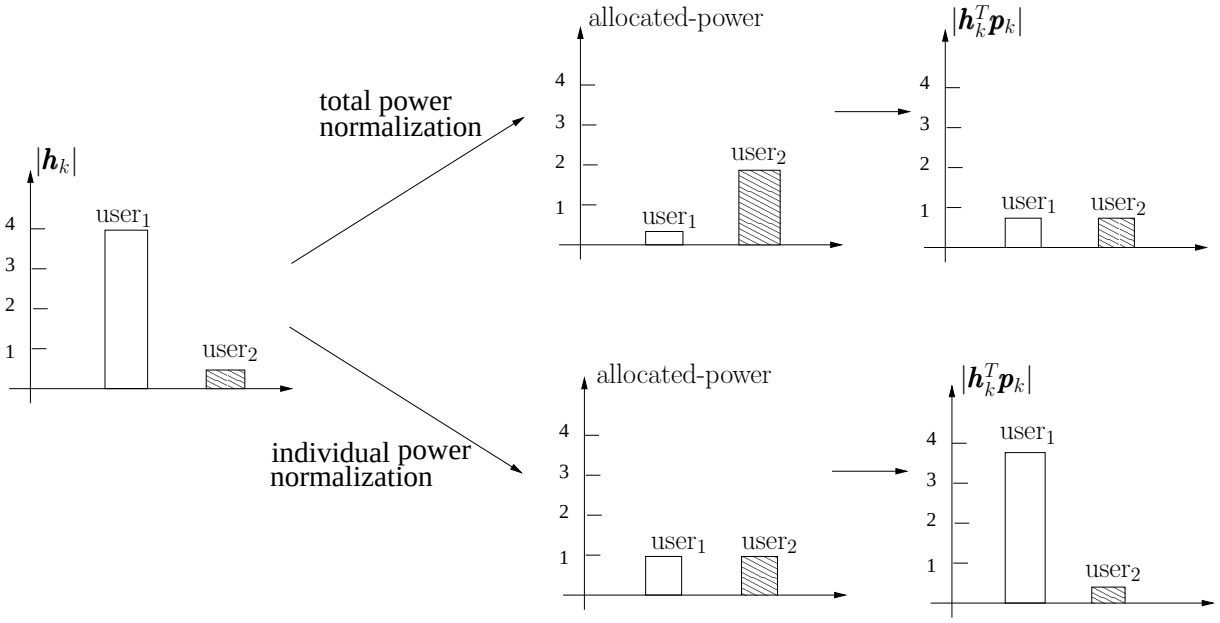

Figure 2.8: Comparison of the total power normalisation and the individual power normalisation regimes of Equations (2.31) an (2.32) using TxZF, when we have $N_{Tx} = 2$, $N_{Rx} = 1$, $K = 2$, and $\|\boldsymbol{h}_1\| = 4$, $\|\boldsymbol{h}_2\| = 0.5$.

These two power normalisation schemes are referred to as *total power normalisation* and *individual power normalisation*, respectively. Using the total power normalisation method presented in Equation (2.31), the allocated power is higher for the users experiencing a deep fade than for those users having a good channel quality. Hence the resultant effective channel gains $|\boldsymbol{h}_k^T\boldsymbol{p}_k|$ becomes equal for all users. By contrast, the power allocated to each user is equal for all users when employing the individual power normalisation method of Equation (2.32). Hence the resultant effective channel gains $|\boldsymbol{h}_k^T\boldsymbol{p}_k|$

become proportional to the users' channel gain $\|\boldsymbol{h}_k\|$. This is illustrated in Fig. 2.8 when assuming $N_{Tx} = 2$, $N_{Rx} = 1$, $K = 2$, and the channel gain for the two users are equal to $|\boldsymbol{h}_1| = 4$ and $|\boldsymbol{h}_2| = 0.5$, respectively. Supposed that the noise variance for all users are the same, the total power normalisation method provides higher minimum SNRs over all users, and consequently better BER performance if all users have the same data rate. The difference between these two power normalisation methods in terms of resultant BER will be illustrated later in Chapter 5.

A significant advantage of employing TxZF is that, provided that we have perfect CSI for all users, the inter-user interferences are completely eliminated by the preprocessing operated at the transmitter. Hence, the complexity of the DL MT receiver can be dramatically reduced and the employment of DL SDMA becomes realistic. However, a constraint of employing TxZF is that the number of users K must satisfy $K \leq N_{Tx}$. Otherwise, the right-side pseudoinverse of the matrix $\boldsymbol{H}$ in Equation (2.30) does not exist. Furthermore, the TxZF experiences noise amplification, just like the ZF-MUD [26, 131].

Unlike in the single-user scenario discussed in Section 2.2.1.1 and Section 2.2.1.2, where the preprocessing matrix can be calculated at the DL receiver side, the preprocessing matrix is unknown to any of the active users, since none of them have the complete channel knowledge of $\boldsymbol{H}$. To facilitate the implementation of TxZF at the transmitter side, the active users are required to feed back their own CIR signatures $\boldsymbol{h}_k$ to the BS's DL transmitter.

2.2.2.2 Transmit Minimum Mean Square Error for MISO Scenarios

Considerring the same system having $N_{Tx} > 1$ transmit antennas at the BS, $N_{Rx} = 1$ receive antenna at the MT, $K \leq N_{Tx}$ activated users, and $\boldsymbol{P}_{Rx} = \boldsymbol{I}$, the objective function of the TxMMSE algorithm is that of minimising the MSE between the transmitted signal $\boldsymbol{s}$ and the estimated signal $\hat{\boldsymbol{s}}$, which is formulated as

$$\boldsymbol{P}_{Tx} = \arg\min_{\boldsymbol{P}_{Tx}} E\left[\|\boldsymbol{s} - \hat{\boldsymbol{s}}\|_2^2\right], \ s.t. \ E\left[\|\boldsymbol{P}_{Tx}\boldsymbol{s}\|_2^2\right] \leq KE_{Tx}. \tag{2.33}$$

The objective expectation can be rewritten as [26]

$$\begin{aligned} \boldsymbol{R} = E\left[\|\boldsymbol{s} - \hat{\boldsymbol{s}}\|_2^2\right] &= E\left[(\hat{\boldsymbol{s}} - \boldsymbol{H}\boldsymbol{P}_{Tx}\boldsymbol{s})^H(\hat{\boldsymbol{s}} - \boldsymbol{H}\boldsymbol{P}_{Tx}\boldsymbol{s})\right] + E\left[\boldsymbol{n}^H\boldsymbol{n}\right] \\ &= E\left[(\hat{\boldsymbol{s}} - \boldsymbol{H}\boldsymbol{P}_{Tx}\boldsymbol{s})^H(\hat{\boldsymbol{s}} - \boldsymbol{H}\boldsymbol{P}_{Tx}\boldsymbol{s})\right] + \frac{E\left[\boldsymbol{n}^H\boldsymbol{n}\right]}{E\left[\|\boldsymbol{s}\|_2^2\right]} E\left[\|\boldsymbol{P}_{Tx}\boldsymbol{s}\|_2^2\right]. \end{aligned} \tag{2.34}$$

Using $E\left[\|\boldsymbol{s}\|_2^2\right] = E\left[\|\boldsymbol{P}_{Tx}\boldsymbol{s}\|_2^2\right]$, this equation can be modified to

$$\boldsymbol{R} = E\left[(\hat{\boldsymbol{s}} - \boldsymbol{H}\boldsymbol{P}_{Tx}\boldsymbol{s})^H(\hat{\boldsymbol{s}} - \boldsymbol{H}\boldsymbol{P}_{Tx}\boldsymbol{s})\right] + \frac{N_0}{E_{Tx}} E\left[\|\boldsymbol{P}_{Tx}\boldsymbol{s}\|_2^2\right]. \tag{2.35}$$

The value of the expectation stated in Equation (2.34) is minimised by setting the partial derivation of $\boldsymbol{R}$ with respect to $\boldsymbol{P}_{Tx}$ to zero, which can be shown that the resultant transmit preprocessing matrix is formulated as [26]

$$\boldsymbol{P}_{Tx} = \boldsymbol{H}^H(\boldsymbol{H}\boldsymbol{H}^H + \frac{N_0}{E_{Tx}}\boldsymbol{I}_K)^{-1}\boldsymbol{\alpha}, \tag{2.36}$$

where $\boldsymbol{\alpha}$ is a $(N_{Tx} \times N_{Tx})$ diagonal matrix having K non-zero diagonal elements representing the power normalisation factors. Similarly, the power allocation factors α can be calculated as

$$\alpha = \sqrt{\frac{KE_{Tx}}{\mathtt{tr}\left(\boldsymbol{H}\boldsymbol{H}^H(\boldsymbol{H}\boldsymbol{H}^H + \frac{N_0}{E_{Tx}}\boldsymbol{I}_K)^{-2}\right)}}. \tag{2.37}$$

At high SNRs, we have $\frac{N_0}{E_{Tx}} \longrightarrow 0$, hence the transmit preprocessing matrix of TxMMSE shown in Equation (2.36) becomes the same as that of TxZF, as illustrated in Equation (2.30).

Similar to the TxZF algorithm, the TxMMSE scheme removes the inter-user interference at high SNRs, and strikes a tradeoff between the noise amplification and interference mitigation at low SNRs so as to minimise the Mean Square Error (MSE) between the transmitted information and the estimated information. In order to facilitate the implementation of TxMMSE at the transmitter, the MTs are required to feed back their own CIR signature $\boldsymbol{h}_k$. Besides, the knowledge of the average noise variance N_0 is essential as well.

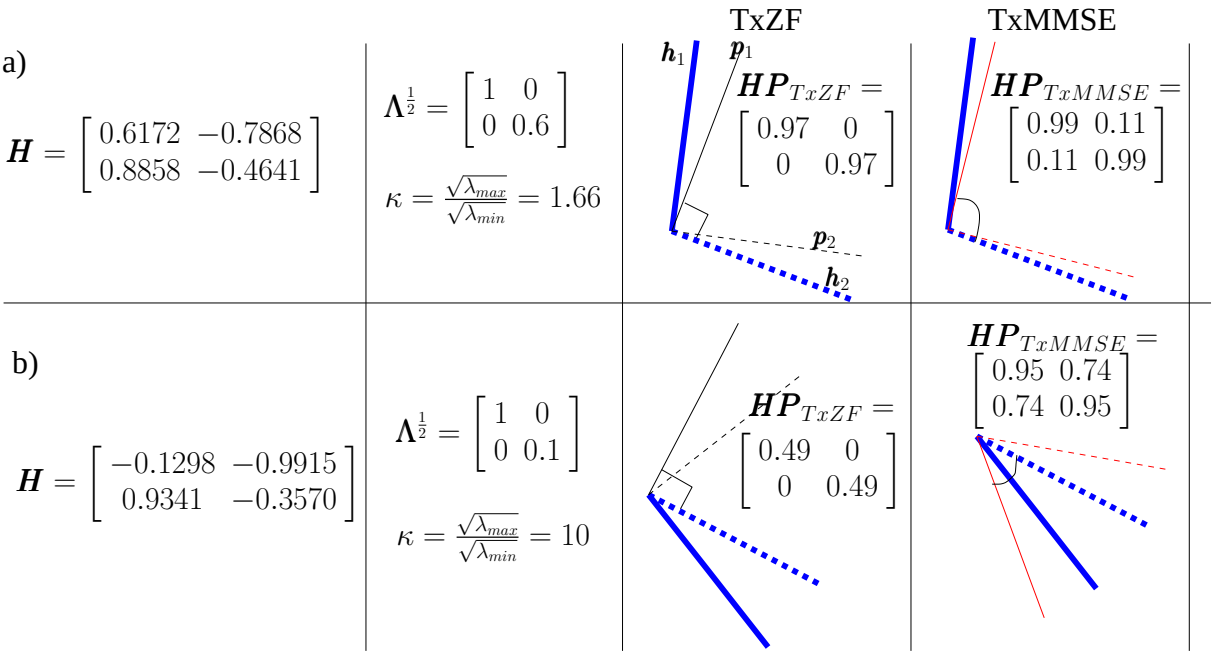

Figure 2.9: Comparison between the TxZF and TxMMSE schemes for $N_{Tx} = 2$, $N_{Rx} = 1$, $K = 2$, $SNR = 6$ dB, using the power normalisation regime of Equation (2.31), and a) $\kappa = 1.66$ b) $\kappa = 10$.

The differences between the TxZF and TxMMSE at low SNRs are further illustrated in Fig. 2.9, where we assumed $N_{Tx} = 2$, $N_{Rx} = 1$, $K = 2$, $SNR = 6$ dB, the power normalisation regime of Equation (2.31) is employed and the corresponding channel matrix $\boldsymbol{H}$ is a) a well-conditioned [1] channel matrix associated with a condition-number of [1] $\kappa = 1$ and b) an ill-conditioned channel matrix associated with a condition-number of $\kappa = 10$. The channel vectors $\boldsymbol{h}_1$ and $\boldsymbol{h}_2$ are represented by the thicker solid and dashed lines, respectively, while the corresponding preprocessing vectors $\boldsymbol{p}_1$ and $\boldsymbol{p}_2$ are represented by the thinner solid and dashed lines, respectively. It becomes plausible from observing the symbols seen

[1]The condition-number κ is defined as the ratio between the maximum singular value and the minimum non-zero singular value formulated as $\kappa = \frac{\sqrt{\lambda_{max}}}{\sqrt{\lambda_{min}}}$. If the condition-number obeys $\kappa \longrightarrow 1$, the corresponding channel matrix $\boldsymbol{H}$ is well-conditional. By contrast, if the condition-number obeys $\kappa \longrightarrow +\infty$, the corresponding channel matrix $\boldsymbol{H}$ is ill-conditional.

in Fig. 2.9 that the preprocessing vectors generated using the TxZF scheme are orthogonal to the corresponding interfering channel i.e. we have $\boldsymbol{p}_1^{\mathbf{ZF}} \perp \boldsymbol{h_2}$ and $\boldsymbol{p}_2^{ZF} \perp \boldsymbol{h}_1$. By contrast, the preprocessing vectors generated by the TxMMSE scheme (e.g. $\boldsymbol{p}_1^{MMSE}$) lies between the orthogonal direction to the interfering channel (e.g. $\mathbf{p}_1^{ZF}$) and the direction of the serving or derived channel (e.g. $\boldsymbol{h}_1$). The difference betwen the effective channel $\boldsymbol{HP}_{Tx}$ using the TxZF scheme and the one using the TxMMSE scheme becomes more significant, when the channel matrix $\boldsymbol{H}$ is ill-conditional, as shown in Fig 2.9 b). More explicitly, the TxMMSE scheme provides a higher receive energy compared to the TxZF scheme. Although it also imposes some inter-user interference, the overall BER performance is expected to be better than that of the TxZF scheme at low SNRs, where the performance is dominated by the noise, rather than by the interference.

2.2.2.3 Transmit Block Diagonization for MIMO Scenarios

The transmit block diagonization technique proposed in [64] may be considered as an extension of the TxZF for the scenario of having more than one receive antennas at the MTs. Having $N_{Tx} > 1$ transmit antennas at the BS, $N_{Rx}^{(k)} > 1$ receive antennas at the k-th MT, while supporting K activated users, the $(\sum_{k=1}^{K} N_{Rx}^{(k)} \times N_{Tx})$ complex-valued channel matrix $\boldsymbol{H}$ is formulated as

$$\boldsymbol{H} = \begin{bmatrix} \boldsymbol{H}^{(1)} \\ \vdots \\ \boldsymbol{H}^{(k)} \\ \vdots \\ \boldsymbol{H}^{(K)} \end{bmatrix}, \tag{2.38}$$

where $\boldsymbol{H}^{(k)}$ represents the $(N_{Rx}^{(k)} \times N_{Tx})$-element channel matrix for the kth user. The DL transmit preprocessing matrix $\boldsymbol{P}_{Tx}^{(k)}$ of the kth user is formulated as

$$\boldsymbol{P}_{Tx}^{(k)} = \boldsymbol{V}^{(k)}, \tag{2.39}$$

where $\boldsymbol{V}^{(k)}$ is a unitary matrix, which constitutes the null-space of other users' channel matrix $\boldsymbol{H}^{(i)}$, $i \neq k$, where we have $\boldsymbol{H}^{(i)}\boldsymbol{V}^{(k)} = \mathbf{0}$. In other words, the transmit preprocessing matrices $\boldsymbol{P}_{Tx}^{(i)}$, $i \neq k$ of the other $(K-1)$ users all constitute the null-space of the kth user's channel matrix $\boldsymbol{H}^{(i)}$, $i \neq k$, yielding $\boldsymbol{H}^{(k)}\boldsymbol{V}^{(i)} = \mathbf{0}$. Hence, the received signal at the kth user becomes

$$\begin{aligned} \boldsymbol{y}^k &= \boldsymbol{H}^{(k)} \sum_{k=1}^{K} \boldsymbol{P}_{Tx}^{(k)} \boldsymbol{s}^{(k)} + \boldsymbol{n}^{(k)} \\ &= \boldsymbol{H}^{(k)} \boldsymbol{P}_{Tx}^{(k)} \boldsymbol{s}^k + \boldsymbol{n}^{(k)} + \boldsymbol{H}^{(k)} \sum_{i=1, i\neq k}^{K} \boldsymbol{P}_{Tx}^{(i)} \boldsymbol{s}^{(i)} \\ &= \boldsymbol{H}^{(k)} \boldsymbol{P}_{Tx}^{(k)} \boldsymbol{s}^k + \boldsymbol{n}^{(k)}, \end{aligned} \tag{2.40}$$

where the inter-user interference has been eliminated. As a result, the entire channel matrix $\boldsymbol{H}$ has been effectively decomposed into K parallel interference-free MIMO channels represented as $\boldsymbol{H}^{(k)}\boldsymbol{P}^{(k)}$. Both open-loop transmission schemes, such as V-BLAST [5], and closed-loop transmission arrangements, such as the eigen-beamforming regime discussed in Section 2.2.1.2 may be employed by the users for information transmission.

The null space $\boldsymbol{V}^{(k)}$ of $\boldsymbol{H}$ can be computed by the SVD [64] as follows

$$\begin{bmatrix} \boldsymbol{H}^{(1)} \\ \vdots \\ \boldsymbol{H}^{(k-1)} \\ \boldsymbol{H}^{(k+1)} \\ \vdots \\ \boldsymbol{H}^{(K)} \end{bmatrix} = \begin{bmatrix} \tilde{\boldsymbol{U}}^{(k)} & \boldsymbol{U}^{(k)} \end{bmatrix} \cdot \begin{bmatrix} \Lambda^{\frac{1}{2}} & \boldsymbol{0} \\ \boldsymbol{0} & \boldsymbol{0} \end{bmatrix} \cdot \begin{bmatrix} \tilde{\boldsymbol{V}}^{(k)H} \\ \boldsymbol{V}^{(k)H} \end{bmatrix}. \tag{2.41}$$

A sufficient condition for ensuring the existence of the null-space matrix $\boldsymbol{V}^{(k)}$ of $\boldsymbol{H}$ is that the channel matrix formulated in Equation (2.41) must be a long rectangular matrix. More tangibly, the number of transmit antennas must be higher than the sum of the number of receive antennas accumulated for the $(K-1)$ interfering users, which may be written as

$$N_{Tx} > \max_k \sum_{i=1, i\neq k}^{K} N_{Rx}^{(i)}, k = 1, 2, \ldots, K. \tag{2.42}$$

Consequently, the size of the null-space matrix $\boldsymbol{V}^{(k)}$ as well as that of the transmit preprocessing matrix $\boldsymbol{P}^{(k)}$ generated for the kth user becomes $\left(N_{Tx} \times (N_{Tx} - \sum_{i=1, i\neq k}^{K} N_{Rx}^{(i)})\right)$.

In fact, the DL TxZF scheme discussed in Section 2.2.2.1 may be viewed as a special case of transmit block diagonalisation [64] where we have $N_{Rx} = 1$ for all users. According to Equation (2.30), we have $\boldsymbol{H}\boldsymbol{P}_{ZF-Tx} = \boldsymbol{\alpha}$, where $\boldsymbol{\alpha}$ is a diagonal matrix, and the preprocessing vector generated for the kth user is orthogonal to all other users' CIR signature $\boldsymbol{h}_i$, $i \neq k$. In other words, the DL preprocessing vector calculated for the kth user $\boldsymbol{p}_k$ constitutes the null space of all other users' channel matrix, which is essentially the same as the result of transmit block diagonalisation [64]. Similar to the DL TxZF and TxMMSE schemes, the channel matrix $\boldsymbol{H}^{(k)}$ estimated at the DL receiver has to be fed back to the BS's DL transmitter in the FDD scenario we considered in this treaties.

2.2.3 Summary

Table 2.3 summerises the above-mentioned five linear transmit preprocessing schemes in terms of their benefits, constraints and the required CSI. The specific type of the required CSI may be classified into the following categories

1. scalar variables, e.g. the noise variance N_0;
2. real-valued vectors, e.g. the eigen-values vector $\boldsymbol{\lambda}$;
3. complex-valued non-unitary vectors, e.g. the MISO CIR $\boldsymbol{h}$;
4. complex-valued non-unitary matrices, e.g. the MIMO CIR $\boldsymbol{H}$;
5. complex-valued unitary vectors, e.g. the TxMF preprocessing vector $\frac{\boldsymbol{h}^*}{|\boldsymbol{h}|}$;
6. complex-valued unitary matrices, e.g. the right-hand-side unitary matrix $\boldsymbol{V}_H$.

In the next section, the quantizers designed for these CSI types will be discussed.

Table 2.3: Summary of various linear transmit preprocessing schemes.

	Benfits	Equaltions and Constraints	Required CSI
TxMF	1) maximised receive SNR; 2) transmit diversity gain; 3) transmit array gain;	$\boldsymbol{P}_{Tx} = \frac{\boldsymbol{h}^*}{\|\boldsymbol{h}\|}$ $N_{Tx} > 1$	unitary vector $\frac{\boldsymbol{h}^*}{\|\boldsymbol{h}\|}$ or CIR $\boldsymbol{h}$
Transmit eigen; beamforming	1) capacity approaching 2) interference-free; 3) parallel sub-channels with different quality.	$\boldsymbol{H} = \boldsymbol{U}_H \boldsymbol{\Lambda}_H^{\frac{1}{2}} \boldsymbol{V}_H^H$ $\boldsymbol{P}_{Tx} = \boldsymbol{V}_H \sqrt{\boldsymbol{E}}, \boldsymbol{P}_{Rx} = \boldsymbol{U}_H$ $E_i = (\mu - \frac{N_0}{\lambda_i})^+$ $N_{Tx} > 1,\ N_{Rx} > 1$	unitary matrix $\boldsymbol{V}_H$; E_i (optional); or $\boldsymbol{\lambda}$ (optional).
TxZF	1) inter-user interference-free; 2) facilitate DL SDMA.	$\boldsymbol{P}_{Tx} = \boldsymbol{H}^H (\boldsymbol{H}\boldsymbol{H}^H)^{-1} \alpha$ $\alpha = \sqrt{\frac{KE_{Tx}}{\mathtt{tr}((\boldsymbol{H}\boldsymbol{H}^H)^{-1})}}$ $N_{Tx} > 1,\ N_{Tx} \leq N_{Rx} K$	$\boldsymbol{h}^{(k)}$.
TxMMSE	1) facilitate DL SDMA; 2) trade-off between inter-user interference and noise.	$\boldsymbol{P}_{Tx} = \boldsymbol{H}^H (\boldsymbol{H}\boldsymbol{H}^H + \frac{N_0}{E_{Tx}} \boldsymbol{I}_K)^{-1} \alpha$ $\alpha = \sqrt{\frac{KE_{Tx}}{\mathtt{tr}\left(HH^H (\boldsymbol{H}\boldsymbol{H}^H + \frac{N_0}{E_{Tx}} \boldsymbol{I}_K)^{-2}\right)}}$ $N_{Tx} > 1$	$\boldsymbol{h}^{(k)}$; and N_0.
Transmit block diagonization	1) inter-user interference-free; 2) facilitate DL SDMA.	$\boldsymbol{P}_{Tx}^{(k)} = \boldsymbol{V}^{(k)}$ $\boldsymbol{H}^{(i)} \boldsymbol{V}^{(k)} = \boldsymbol{0},\ i \neq k$ $N_{Tx} > 1,\ N_{Rx} > 1,$ $K > 1;\ N_{Tx} \leq N_{Rx} K.$	$\boldsymbol{H}^{(k)}$

2.3 CSI Quantization

The required feedback information was discussed in Section 2.2 for each transmit preprocessing scheme considered. In this section, the design of efficient CSI quantisers is discussed, which are capable of achieving a low quantization error at the minimum number of bits, so as to reduce the feedback load and to improve the closed-loop MIMO system's performance.

2.3.1 A General Introduction

Quantization is the process of approximating ("mapping") a continuous range of values (or a very large set of possible discrete values) by a relatively small ("finite") set of discrete values. A plausible example is that of rounding a real number in the interval $[0, 100]$ to an integer $0, 1, 2 \ldots, 100$. This finite set of discrete values is referred to as a *codebook* $\mathcal{Q}$. The elements in a codebook are referred to as *quantization levels* or **codewords** Q_i, where the subscript i is referred to as the *index of a codeword*. The data type of the codewords may be real/complex-valued scalar q_i, vectors $\boldsymbol{q}_i$ and matrices $\boldsymbol{Q}_i$, depending on the unquantized input source X. Here we use the notation Q_i to represent all cases in general. A quantization result or a codeword may then be signalled by using the binary representation of its index. A total of $b = \lceil \log_2 |\mathcal{Q}| \rceil$ bits are required provided that all codewords are equiprobable and when using a codebook having a size of $|\mathcal{Q}| = 2^b$, $\mathcal{Q} = [Q_1, \ \ldots, \ Q_{|\mathcal{Q}|}]$. The quantization error $\xi_{\mathcal{Q}}$ is typically quantified by a distance metric $d(X, \mathsf{Q}(X))$, where $\mathsf{Q}(\cdot)$ represents the quantization process

$Q_i = \mathsf{Q}(X) = \arg\min_{Q_i, 1 \le i \le |\mathcal{Q}|} d(X, Q_i)$.

Given the codebook size $|\mathcal{Q}|$, the design objective when creating a quantizer is to find a codebook, which minimises the average distortion $\bar{\xi}_{\mathcal{Q}} = E_X\left[d(X, \mathsf{Q}(X))|\mathcal{Q}\right]$. The generalised Linde-Buzo-Gray (LBG) algorithm [91, 132] is a widely used codebook design procedure, which is briefly introduced below.

The Linde-Buzo-Gray algorithm [91, 132]:

1. Generate a large number of training samples $\mathsf{X}_1, \mathsf{X}_2, \ldots$ based on the typical input source X to be quantized;

2. Initialise the codebook using $|\mathcal{Q}|$ randomly chosen training samples, and denote this codebook as $\mathcal{Q}_{old}$

3. Find the optimal partition to create quantization intervals or cells, that is, form $|\mathcal{Q}|$ quantization cells C_i satisfying the *Nearest Neighbour Condition* of

$$\mathfrak{C}_i = \{\mathsf{X} : \ d(\mathsf{X}, Q_i) < d(\mathsf{X}, Q_j);\ \forall\, i \neq j,\ i, j \in [1,\ |\mathcal{Q}|]\}. \tag{2.43}$$

   If we have $d(\mathsf{X}, Q_i) = d(\mathsf{X}, Q_j)$ for one or more indices of $i \neq j$, then assign X to the specific set C_j, for which j is the smallest.

4. Compute the average distortion $\bar{\xi}_{\mathcal{Q}_{old}}$ for codebook $\mathcal{Q}_{old}$.

5. Copy codebook $\mathcal{Q}_{old}$ to $\mathcal{Q}_{new}$, where each unquantized value will be represented by the specific *centroid points*, which minimise the average distortion of each quantization cell, which is formulated as

$$Q_i = \arg\min_{Q_i} E\left[d(\mathsf{X}, Q_i), \mathsf{X} \in \mathfrak{C}_i\right]. \tag{2.44}$$

6. Compute the average distortion $\bar{\xi}_{\mathcal{Q}_{new}}$ for the codebook $\mathcal{Q}_{new}$.

7. Compare $\bar{\xi}_{\mathcal{Q}_{old}}$ and $\bar{\xi}_{\mathcal{Q}_{new}}$. If the average distortion improvement of the most recent iteration was sufficiently low, curtail further iterations. Otherwise set $\bar{\xi}_{\mathcal{Q}_{old}} = \bar{\xi}_{\mathcal{Q}_{new}}$, $\mathcal{Q}_{old} = \mathcal{Q}_{new}$ and go to Step 3.

Three issues have to be addressed, when applying the LBG algorithm for CSI quantization codebook design. They are the physical nature of the input source X, the definition of the distance metric $d(\cdot)$ and the algorithm of centroid calculation, given a specific distance metric. In Section 2.2, the required feedback information of each of the preprocessing scheme considered was discussed, which is naturally the content of the input source X as summarised in Section 2.2.3. The training samples of X may be generated using the channel models detailed in Section 2.1, combined with the related algorithms detailed in Section 2.2. The distance metric used for information source quantization (e.g. audio and video) is usually the MSE metric, since the ultimate goal is to reconstruct the original source information. However, the ultimate objective of CSI quantization is to improve the entire closed-loop systems' performance. Although this can be achieved by accurately reconstructing the CSI at the transmitter side, minimising the Euclidean distance between the unquantized CSI and the quantized one may not be the most efficient method of improving the transceiver's overall performance. Hence, apart from the commonly used

MMSE distance metric, we also employ the so-called chordal distance [80, 133], the projection 2-norm distance [57, 133] and the Fubini-Study distance [57, 133] in this treatise. The definition of these distance metrics, the corresponding centroid point calculation methods, the codebook examples, as well as the attainable quantizer performance quantified in terms of the averaged quantization error $\bar{\xi}_{\mathcal{Q}}$ versus the number of quantization bits b, will be detailed in Sections 2.3.2, 2.3.3 and 2.3.4, respectively.

2.3.2 Quantisers Using the Euclidean Distance

With the objective of minimising the Euclidean distance between the input and output of a quantizer, the MSE is formulated as

$$d_{Euclidean}(x, \mathsf{Q}(x)) = \|x - \mathsf{Q}(x)\|_2^2. \tag{2.45}$$

Given the MSE distance metric, the centroids of Equation (2.44) may be explicitly calculated using the numerical average formulated as

$$Q_i = \arg\min_{Q_i} E\left[d(x, Q_i), X \in \mathfrak{C}_i\right] = \frac{\sum^{|\mathfrak{C}_i|} x}{|\mathfrak{C}_i|}, \tag{2.46}$$

where $|\mathfrak{C}_i|$ represents the number of training samples x in the quantization cell $\mathfrak{C}_i$.

This type of quantizer is applicable to all the CSI feedback types summarised in Table 2.3 of Section 2.2.3 such as for example, the scalar noise variance N_0 and the real eigen-value vectors $\boldsymbol{\lambda}$. In this section, we employ the real-valued Rayleigh-faded channel envelope vectors as the input vector to characterise the MSE based quantizer's performance. More explicitly, the quantizer's input source vector $\mathbf{x}$ is formulated as

$$\mathbf{x} = \begin{bmatrix} |h_{11}| \\ \vdots \\ |h_{N_{Rx}N_{Tx}}| \end{bmatrix} \tag{2.47}$$

The elements in $\mathbf{x}$ may be quantized jointly, which is the philosophy of the classic vector quantization scheme [91]; or may be quantized separately, as in the conventional scalar quantization scheme. An advantage of scalar quantization over vector quantization is its smaller codebook size and its low-complexity search process, given the same total number of quantization bits. Hence both of them are employed and compared in this section. Two vector quantization codebooks having a cardinality of $|\mathcal{Q}| = 16$ and generated for the Rayleigh-faded channel envelope's quantization using the above-mentioned scheme are illustrated in Fig. 2.10. The Rayleigh fading channels illustrated in Section 2.1.3, more explicitly, a spatially independent scenario having $N_{Tx} = 2,\ N_{Rx} = 1,\ \rho_{|h_1||h_2|} = 0$, and a spatially correlated scenario associated with $N_{Tx} = 2,\ N_{Rx} = 1,\ \rho_{|h_1||h_2|} = 0.8464$ were considered. By referring to the channel envelope probability distribution exemplified in Fig. 2.6, it is evident that the codewords denoted by the star marks in Fig. 2.10 are distributed accordingly. The codewords of a scalar codebook having a cardinality of $|\mathcal{Q}| = 4$ are also marked in Fig. 2.10, which are those indicated by the circles for comparison. It is clear that for the spatially correlated scenario b), the scalar codebook has allocated a good portion of its codewords to the area where the channel envelope's probability is low, which results in an inefficient design because the high-probability areas remain 'under-represented'. This is further substantiated in Fig. 2.11, which quantifies the average MSE of the Rayleigh-faded channel envelope

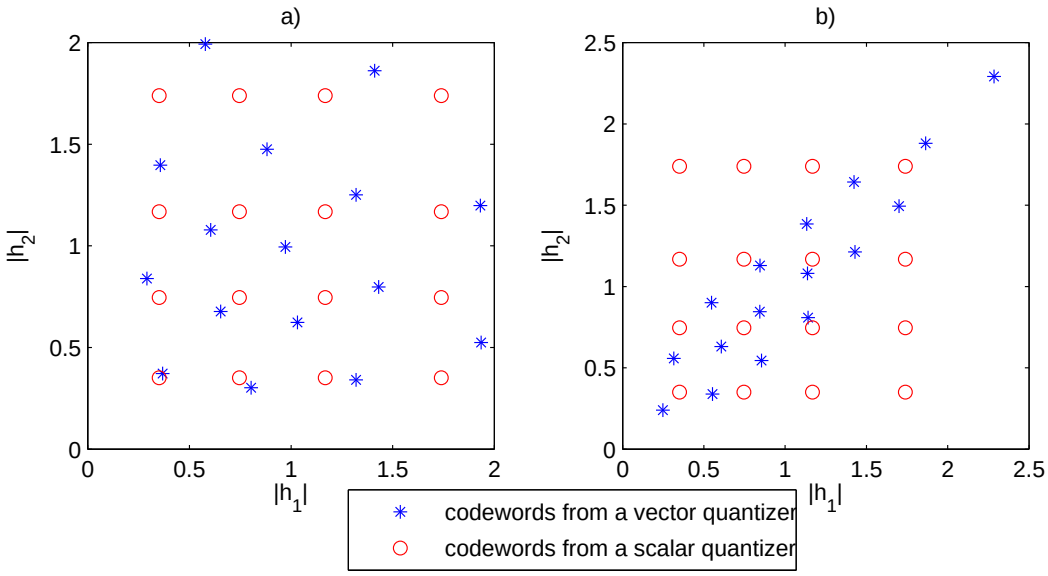

Figure 2.10: Illustrations of the 16 codewords for two Rayleigh-faded channel envelope, where the channels are a) spatially independent and b) spatially correlated having a correlation coefficient of $\rho_{|h_1||h_2|} = 0.8462$. Vector quantization (star markers) and scalar quantization (circle marks) are employed.

quantization error versus the number of quantization bits used. It is demonstrated in Fig. 2.11 that, for the spatially correlated scenario considered, the vector quantizer quantized the two estimated Rayleigh channel envelopes $|h_1|$, $|h_2|$ jointly, and hence achieved a significantly lower quantization error than the scalar quantizer, where $|h_1|$, $|h_2|$ were quantized separately. By contrast, for the spatially independent scenario, the achievable performances of the vector quantizer and of the scalar quantizer are similar to each other.

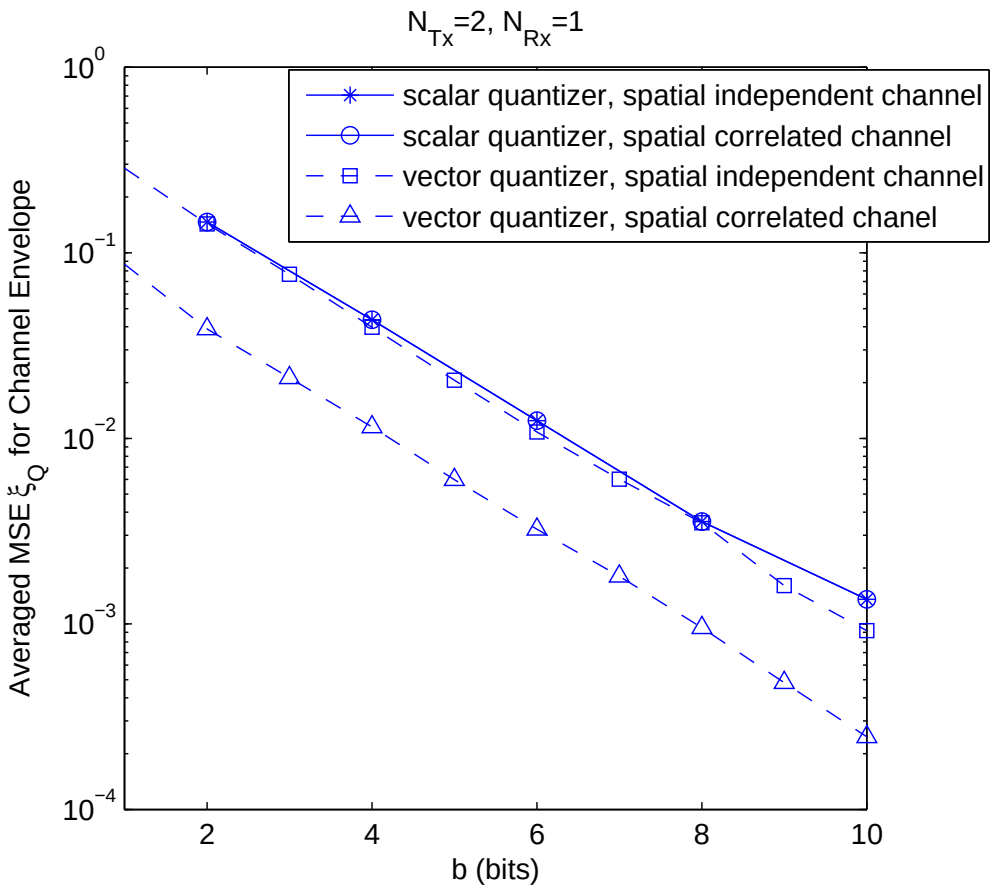

Figure 2.11: The averaged quantization error $\bar{\xi}_{\mathcal{Q}}$ versus the number of quantization bits for Rayleigh-fading channel envelope quantization, when we have $N_{Tx} = 2, N_{Rx} = 1, \rho_{|h_1||h_2|} = 0/0.8462$ using a vector quantizer and a scalar quantizer, respectively.

2.3.3 Unitary Vector Quantizer Using the Chordal Distance

[80] For the TxMF aided MISO system discussed in Section 2.2.1.1, the required feedback information is constituted by the TxMF's weights, which are hosted by a $(N_{Tx} \times 1)$-element complex-valued unitary vector. The chordal distance defined in [80] for quantizer designs is formulated as

$$d_{chor}(\mathbf{x}, \boldsymbol{q}_i) = \sqrt{1 - |\mathbf{x}^H \boldsymbol{q}_i|}, \tag{2.48}$$

where $\boldsymbol{q}_i$ denotes one of the codewords. Since $\mathbf{x}$ and $\boldsymbol{q}_i$ are two complex-valued unitary vectors, we have $\mathbf{x}^H \boldsymbol{q}_i = |\mathbf{x}^H \boldsymbol{q}_i| e^{j\beta}$, where $0 < |\mathbf{x}^H \boldsymbol{q}_i| \leq 1$, which can be represented as $|\mathbf{x}^H \boldsymbol{q}_i| = \cos\Theta$. The phase values Θ and β are defined as the Hermitian angle and the pseudo-angle between two complex-valued unitary vectors, respectively [134]. Minimising the chordal distance between two complex-valued unitary vectors is equivalent to maximising the cosine function of the Hermitian angle between them. Physically, the received SNR represented as $SNR = \frac{|\boldsymbol{h}^T \boldsymbol{q}_i|^2}{N_0} = \frac{|\|\boldsymbol{h}\| \mathbf{x}^H \boldsymbol{q}_i|^2}{N_0}$ is maximised, when $\cos\Theta = |\mathbf{x}^H \boldsymbol{q}_i|$ is maximised, regardless of the pseudo-angle. Compared to the MSE metric, which provides us with a tangible measure of the quantizer's performance, but fail to characterise the performance of the entire system, the chordal distance may be deemed more relevant, since it is directly linked to the achievable system performance by maximising the receiver's SNR. The quantization codebook may be generated

using the LBG algorithm outlined in Section 2.3.1. Since we have $\mathbf{x} = \frac{\boldsymbol{h}^*}{\|\boldsymbol{h}\|}$ as stated in Equation 2.24, the training data $\mathbf{x}$ can be generated using the channel model of Section 2.1. In fact, for spatially independent channels, $\mathbf{x}$ is uniformly distributed in the complex-valued N_{Tx}-dimensional unitary space. By contrast, for spatially correlated channels, $\mathbf{x}$ is only a subset of the complex-valued N_{Tx}-dimensional unitary space. Moreover, the centroid of a given quantization cell may be updated using the following algorithm.

- **Centroid Update Algorithm Using the Chordal Distance:**

  1. Construct a $(|\mathfrak{C}_i| \times N_{Tx})$-element matrix $\boldsymbol{A}$ using all the training vectors belonging to cell $\mathfrak{C}_i$ as the row vectors of matrix $\boldsymbol{A}$. More explicitly, let us construct $\boldsymbol{A} = \begin{bmatrix} \mathbf{x}_1^H \\ \vdots \\ \mathbf{x}_{|\mathfrak{C}_i|}^H \end{bmatrix}$;
  2. Apply SVD to the matrix $\boldsymbol{A}$, yielding $\boldsymbol{A} = \boldsymbol{U}_A \boldsymbol{\Lambda}_A^{\frac{1}{2}} \boldsymbol{V}_A^H$;
  3. Set $\boldsymbol{q}_i = \boldsymbol{v}_{max}$, where $\boldsymbol{v}_{max}$ is one of the columns in the right-hand-side unitary matrix $\boldsymbol{V}_A$ corresponding to the largest singular value.

- **Proof:** Based on the LGB algorithm outlined in Section 2.3.1, the objective function employed for codebook updating can be reformulated as

$$\begin{aligned} \arg\min_{\boldsymbol{q}_i} E\left[d_{chor}(\mathbf{x}_j, \boldsymbol{q}_i), \mathbf{x}_j \in \mathfrak{C}_i\right] &= \arg\min_{\boldsymbol{q}_i} \frac{1}{|\mathfrak{C}_i|} \sum_{j}^{|\mathfrak{C}_i|} d_{chor}(\mathbf{x}_j, \boldsymbol{q}_i) \\ &= \arg\max_{\boldsymbol{q}_i} \sum_{j}^{|\mathfrak{C}_i|} |\mathbf{x}_j^H \boldsymbol{q}_i| \\ &= \arg\max_{\boldsymbol{q}_i} \boldsymbol{q}_i^H \boldsymbol{A}^H \boldsymbol{A} \boldsymbol{q}_i \\ &= \arg\max_{\boldsymbol{q}_i} \boldsymbol{q}_i^H \boldsymbol{V}_A \boldsymbol{\Lambda}_A \boldsymbol{V}_A^H \boldsymbol{q}_i \\ &= \arg\max_{\boldsymbol{q}_i} \left(\lambda_{max} |\boldsymbol{v}_{max}^H \boldsymbol{q}_i|^2 + \ldots + \lambda_{min} |\boldsymbol{v}_{min}^H \boldsymbol{q}_i|^2\right). \end{aligned} \tag{2.49}$$

  Since we have $\lambda_{max} > \ldots > \lambda_{min}$ and $|\boldsymbol{v}_{max}^H \boldsymbol{q}_i|^2 + \ldots + |\boldsymbol{v}_{min}^H \boldsymbol{q}_i|^2 = 1$, the objective function derived in Equation (2.49) is maximised, when we have $|\boldsymbol{v}_{max}^H \boldsymbol{q}_i|^2 = 1$ and $|\boldsymbol{v}_i^H \boldsymbol{q}_i|^2 = 0, \forall \boldsymbol{v}_i \neq \boldsymbol{v}_{max}$. As a result, the updated codeword or centroid of cell $\mathfrak{C}_i$ should be $\boldsymbol{q}_i = \boldsymbol{v}_{max}$.

A codebook example having a size of four codewords generated using the above-mentioned algorithm for a scenario of spatially independently fading MIMO elements is given by

$$\mathcal{Q}_{i.i.d.} = \begin{bmatrix} -0.36 & -0.97 & -0.73 & -0.62 \\ 0.79 + 0.48i & 0.12 + 0.21i & 0.08 - 0.68i & -0.76 + 0.19i \end{bmatrix}, \tag{2.50}$$

and the one for spatially correlated scenario is

$$\mathcal{Q}_{\rho_{h_1 h_2}=0.93} = \begin{bmatrix} -0.62 & -0.65 & -0.76 & 0.78 \\ -0.73 + 0.29i & -0.76 - 0.08i & -0.64 + 0.09i & 0.59 + 0.18i \end{bmatrix}. \tag{2.51}$$

Again, the channel characterized in Section 2.1.3 having $N_{Tx} = 2$, $N_{Rx} = 1$, $\boldsymbol{R}_{Tx} = \boldsymbol{I}$ and $\boldsymbol{R}_{Tx} = \begin{bmatrix} 1 & 0.93 \\ 0.93 & 1 \end{bmatrix}$ was employed. The averaged quantization error $\bar{\xi}_{\mathcal{Q}} = E[d_{chor}]$ versus the number

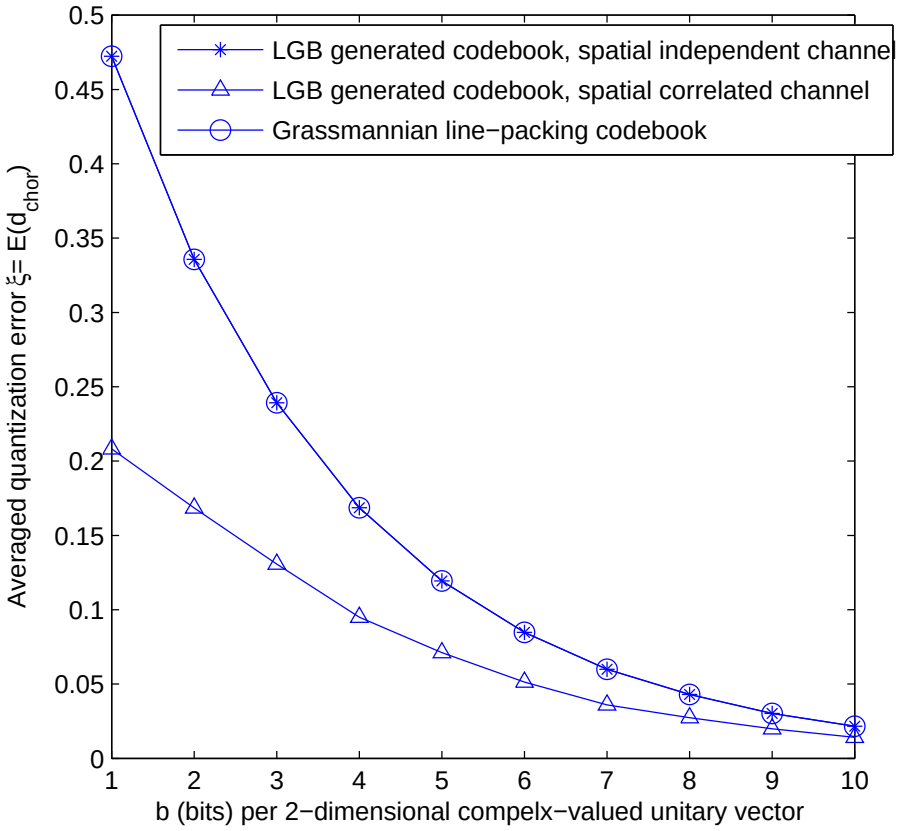

Figure 2.12: The average quantization error $\bar{\xi}_{\mathcal{Q}} = E[d_{chor}]$ versus the number of quantization bits per two-dimensional unitary vector $\boldsymbol{x}$, when we have $N_{Tx} = 2, N_{Rx} = 1, \rho_{h_1 h_2} = 0/0.93$ using the LGB algorithm based beamforming weight-vector quantizer 2.3.2 and the Grassmannian line-packing beamforming weight-vector quantizer of Section 2.3.3, respectively.

of quantization bits per 2-dimensional unitary vector is portrayed in Fig. 2.12. It is demonstrated in Fig. 2.12 that the average quantization error of the spatially correlated scenario is lower than that of the spatial independent scenario, when using the same amount of quantization bits. This is because the unitary vectors $\boldsymbol{x}$ of the spatially independent TxMF scenario spread uniformly across the entire two-dimensional complex-valued unitary space, while that of the spatially correlated TxMF scenario is spread over a limited fraction of the unitary space. Consequently, more quantization bits are required for the spatially independent scenario, since the unquantized unitary vectors in this case contain more information.

Apart from using the LBG algorithm, the TxMF's weight-vector codebooks designed for spatially independently fading MIMO channels can also be generated using the Grassmannian packing theory [133]. Grassmannian space $\mathcal{G}(m,n)$, $(n \leq m)$ is constituted by the set of all n-dimensional subspaces of the m-dimensional space, where we have $n < m$. Again, the packing problem may be stated as follow: given $|\mathcal{Q}|$, n , m, find a set of n-dimensional planes $P_1, \ldots, P_N \in \mathcal{G}(m,n)$ so that $\min_{i \neq j} d(P_i, P_j)$ is as large as possible, where $d(\cdot,\cdot)$ represents metric to be used for quantifying the distance between two planes such as the chordal distance. By setting $n = 1$, $m = N_{Tx}$, the packing problem becomes a Grassmannian line-packing problem, whose results may be readily employed as the TxMF weight vector

codebook for the spatially independently fading TxMF channel considered. A specific codebook example having four codewords for the $m = N_{Tx} = 2$ spatially independently fading TxMF scenario is shown in Equation (2.52).

$$\mathcal{Q} = \begin{bmatrix} -0.16 - 0.73i & -0.08 - 0.32i & -0.24 + 0.59i & -0.95 \\ -0.51 - 0.41i & -0.25 + 0.91i & -0.76 - 0.02i & 0.29 \end{bmatrix}. \tag{2.52}$$

Although the TxMF weight codewords are not the same as those in the codebook generated by the LBG algorithm of Equation (2.50), it is demonstrated in Fig. 2.12 that the average quantization error of the codebook generated by the LBG algorithm and of the one generated by Grassmannian line-packing is virtually identical.

2.3.4 Unitary Matrix Quantizer Using the Project 2-Norm and the Fubini-Study Distance

A specific type of feedback information required by transmit eigen-beamforming which was summarised in Table 2.3 of Section 2.2.3 is constructed by complex-valued unitary matrices. The commonly used distance metrics employed for a unitary matrix quantizer are the project 2-norm distance [133] and the Fubini-Study distance [133], which are defined as

$$d_{proj}(\boldsymbol{X}_1, \boldsymbol{X}_2) = \sqrt{1 - \lambda_{min}(\boldsymbol{X}_1^H \boldsymbol{X}_2)} \tag{2.53}$$

and

$$d_{FS}(\boldsymbol{X}_1, \boldsymbol{X}_2) = \arccos |\det(\boldsymbol{X}_1^H \boldsymbol{X}_2)|, \tag{2.54}$$

respectively. More explicitly, $\lambda_{min}(\boldsymbol{X}_1^H \boldsymbol{X}_2)$ represents the minimum eigen-value of the matrix $(\boldsymbol{X}_1^H \boldsymbol{X}_2)$, while $\det(\boldsymbol{X}_1^H \boldsymbol{X}_2)$ denotes the corresponding determinant. It was demonstrated in [57] that for the transmit eigen-beamforming aided MIMO system discussed in Section 2.2.1.2, the achievable BER performance is optimised using the projection 2-norm distance, while the achievable capacity is maximised, where using the Fubini-Study distance. However, the LBG algorithm outlined in Section 2.3.1 is not applicable to codebook designs using these two distance metrics, because the centroid of a specific cell is difficult to obtain. However, the Grassmannian packing algorithm briefly introduced in Section 2.3.3 is capable of generating an appropriate codebook, as examplified below:

$$\boldsymbol{Q}_1 = \begin{bmatrix} 0.49 & -0.42 \\ -0.14 + 0.22i & 0.60 + 0.39i \\ -0.31 + 0.55i & -0.42 - 0.13i \\ -0.01 - 0.53i & -0.16 - 0.28i \end{bmatrix}, \quad \boldsymbol{Q}_2 = \begin{bmatrix} 0.68 & 0.27 \\ 0.25 + 0.21i & 0.61 - 0.14i \\ 0.58 - 0.24i & -0.33 + 0.51i \\ -0.14 - 0.01i & -0.03 + 0.41i \end{bmatrix}, \tag{2.55}$$

$$\boldsymbol{Q}_3 = \begin{bmatrix} -0.71 & -0.43 \\ 0.12 - 0.48i & -0.17 - 0.19i \\ 0.01 + 0.20i & 0.04 + 0.01i \\ 0.27 - 0.36i & -0.31 + 0.81i \end{bmatrix}, \quad \boldsymbol{Q}_4 = \begin{bmatrix} 0.46 & -0.0655 \\ -0.41 - 0.42i & -0.09 + 0.45i \\ -0.28 - 0.45i & 0.55 - 0.38i \\ -0.38 + 0.01i & -0.45 + 0.34i \end{bmatrix}.$$

For example, the Grassmannian sub-space packing used for the scenario of $m = 4, n = 2$ in order to maximise the minimum Fubini-Study distance between any two sub-spaces may be used to generate the unitary matrix codebook for a transmit eigen-beamforming aided MIMO system associated with $N_{Tx} = 4$, $N_{Rx} = 2$ and communicating over i.i.d. MIMO channels. Such a codebook having four

codewords is illustrated in Equation (2.55). However, the Grassmannian packing results are not available for an arbitrary number of transmit and receive antennas of N_{Tx} and N_{Rx}. In order to circumvent this problem, we may employ a random codebook, where the codewords are randomly generated based on the known statistical distribution of the channel in order to evaluate the corresponding quantization performance bound. The average quantization error measured in terms of a) the project 2-norm distance and b) the Fubini-Study distance versus the number of quantization bits per (4×2)-element unitary matrix $\boldsymbol{X}$ are illustrated in Fig. 2.13, when we have $N_{Tx} = 4, N_{Rx} = 2$ i.i.d. channels, and using the random quantizer and the Grassmannian subspace packing quantizer. It is explicitly demonstrated in Fig. 2.13 that the random quantizer provides a tight performance lower-bound, which is just slightly worse than the performance of the Grassmannian subspace packing quantizer, when the number of quantization bits is low.

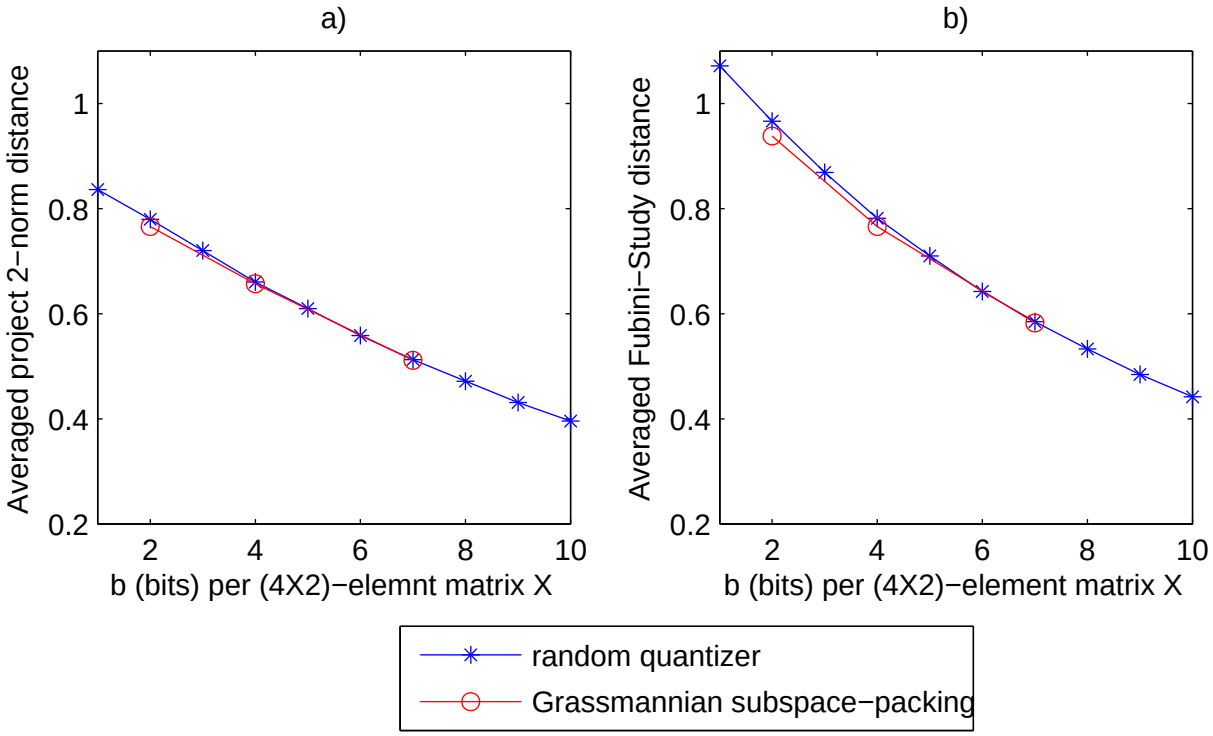

Figure 2.13: The average quantization error a) $\bar{\xi}_{\mathcal{Q}} = E[d_{proj}]$ and b)$\bar{\xi}_{\mathcal{Q}} = E[d_{FS}]$ versus the number of quantization bits per (4×2)-element unitary matrix $\mathbf{X}$, when we have $N_{Tx} = 4, N_{Rx} = 2$ spatially independently fading eigen-beamforming channels, and using the random quantizer as well as the Grassmannian subspace-packing based quantizer, respectively.

2.4 Chapter Summary

In this chapter, three key topics of a closed-loop MIMO communication system were discussed, namely the MIMO wireless channel model, the linear transmit preprocessing philosophy and CSI quantization, as briefly summarised below:

- We concentrated on *small-scale slow frequency-flat/narrowband NLOS Rayleigh fading* channels only. Compared to SISO channel modelling, where only the channel properties exhibited in the

temporal domain have to be considered, the difficulty of MIMO channel modelling lies in the modelling of the saptial domain behaviour. Three channel modelling methods, namely the Kronecker model, the Weichselberger model and the virtual channel representation were introduced in Section 2.1.2.1.

- Linear transmit preprocessing may be characterized by a preprocessing matrix $\boldsymbol{P}_{Tx}$. The linear transmit preprocessing algorithm can be derived as dual pairs of the corresponding MUDs, while satisfying a given transmit power constraint. The feedback information required for single-user MIMO scenarios may be the preprocessing matrix $\boldsymbol{P}_{Tx}$, since the CSI is estimated at the receiver. By contrast, in the case of multi-user MIMO scenarios, each user is required to feed back its own CIR signature to the BS's DL transmitter and the transmit preprocessing matrix can only be generated at the transmitter side, where the CSI of all the users is available.

- The LGB algorithm provides a general method of codebook design, provided that 1) the statistical distribution of the quantizer's input is known; 2) the algorithm for finding the centroid of a partition or cell based on the required distortion metric is available. Three different quantiser optimisation metrics were considered, namely the quantisers using the MSE criterion, the unitary vector quantizer using the chordal distance and the unitary matrix quantizer using the project 2-norm and Fubini-Study distance.

Based on the background provided in this chapter, in the forthcoming chapters, we will incorporate all these three key components along with other essential system components such as modulation and coding into the system designed, in order to evaluate and improve the entire closed-loop system's performance.

Chapter 3

Transmit Matched Filter Aided Closed-loop Single-user MISO System

In this chapter, one of the basic closed-loop systems, namely the Transmit Matched Filter (TxMF) aided closed-loop single-user MISO system as shown in Fig. 3.1 will be investigated. The TxMF algorithm will not be repeated in this chapter since it has been detailed in Section 2.2.1.1. Throughout this chapter, the CCMC ergodic capacity described in Chapter 1, which is the upper-bound of the achievable throughput, is employed in order to evaluate the proposed algorithms.

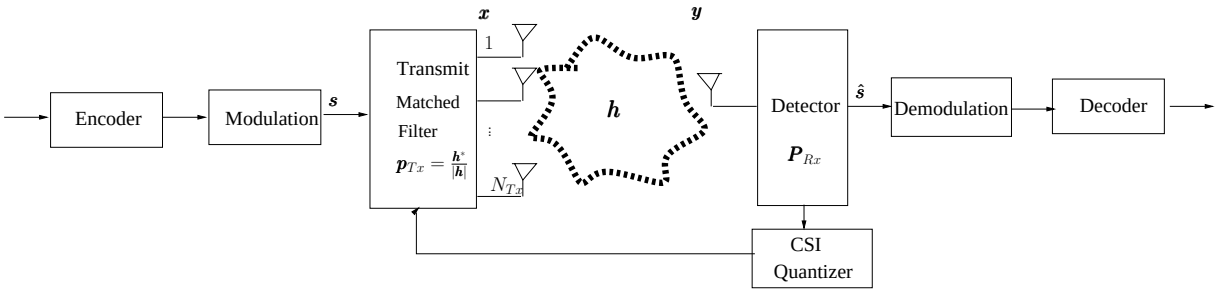

Figure 3.1: System model of a TxMF aided closed-loop single-user MISO system.

The novel contributions of this chapter are:

1. We derive the lower ergodic channel capacity bound of a TxMF aided closed-loop MISO system, when considering the effects of channel estimation errors, quantization errors, the CSI signalling overhead caused by pilot symbols and that imposed by the channel information feedback bits.

2. A novel pilot signalling scheme is proposed, which replaces the consecutive transmission of pilots by their simultaneous transmission, and substantially improves the achievable throughput for systems having a moderate number of transmit antennas, despite encountering rapidly fluctuating channels.

3. We also propose a novel technique, hereby referred to as Pilot Symbol Assisted Rateless (PSAR) coding, where a predetermined fraction of binary pilot symbols is interspersed with the channel-coded bits at the channel coding stage, instead of multiplexing the pilots with the data symbols

at the modulation stage, as in classic Pilot Symbol Assisted Modulation (PSAM). We will subsequently demonstrate that the PSAR code-aided transmit preprocessing scheme succeeds in gleaning more beneficial knowledge from the inserted pilots, because the pilot bits are not only useful for estimating the channel at the receiver, but they are also beneficial in terms of significantly reducing the computational complexity of the rateless channel decoder. Our results suggest that more than a 30% reduction in the decoder's computational complexity can be attained by the proposed system, when compared to a corresponding benchmarker scheme having the same pilot overhead but using the PSAM technique.

This chapter is organised as follows. The achievable ergodic channel capacity using quantized CSI is investigated in Section 3.1, where the different quantisers described in Section 2.3 are compared. In Section 3.2, the achievable ergodic channel capacity is further investigated considering the effect of both the channel estimation errors and the CSI signalling overhead, which demonstrates that a substantial performance degradation is imposed by the pilot signalling overhead. Based on this fact, a novel pilot reduction signalling scheme designed for rapidly fading channels is proposed in Section 3.3, and a pilot symbol assisted rateless code is proposed in Section 3.4. Finally, the summary of this chapter is provided in Section 3.5.

3.1 Achievable Ergodic Channel Capacity Using Quantized CSI

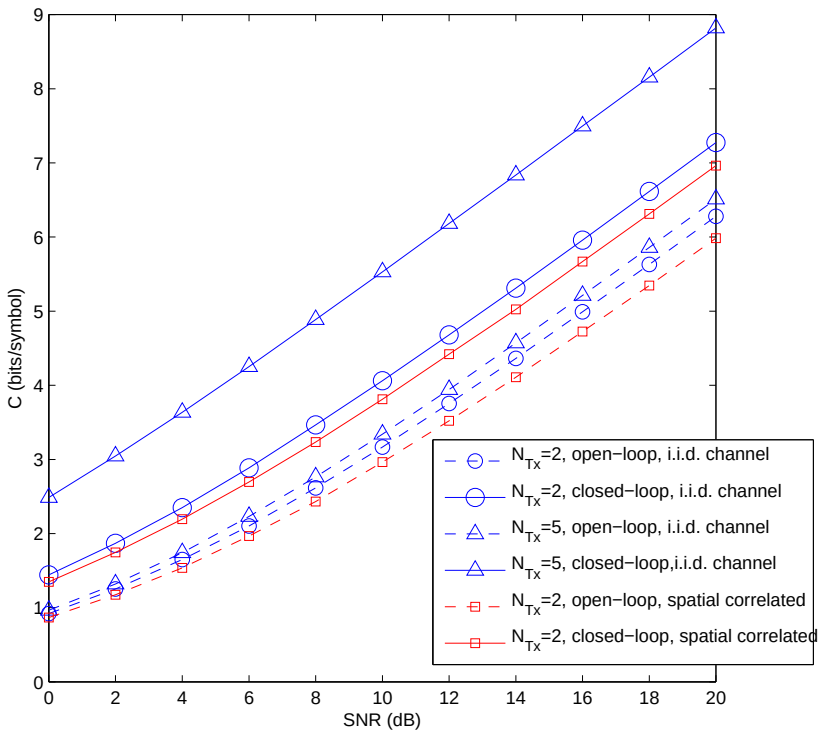

Figure 3.2: Ergodic channel capacity versus SNR for $N_{Tx} = 2, 5$, $N_{Rx} = 1$, when assuming perfect CSIR and CSIT calculated from $C_{open} = E_{\boldsymbol{h}}\left(1 + \frac{||\boldsymbol{h}||^2 E_{Tx}}{N_0 N_{Tx}}\right)$ [52] and $C_{closed} = E_{\boldsymbol{h}}\left(1 + \frac{||\boldsymbol{h}||^2 E_{Tx}}{N_0}\right)$ [52]. Both i.i.d. and spatially correlated Rayleigh fading channels are simulated.

Assuming perfect CSI is available both at the receiver and transmitter side, the ergodic channel ca-

pacity of a MISO system having spatially independent channel and $N_{Tx} = 2, 5$ respectively, is shown in Fig. 3.2, where the closed-loop TxMF aided system provides a substantially higher capacity compared to the corresponding open-loop system having the same antenna configuration. As seen in Fig. 3.2, the closed-loop benefits increase further, when more transmit antennas are employed. By contrast, the achievable ergodic channel capacity remains almost unchanged for the open-loop system upon increasing the number of transmit antennas. These observations are also valid for spatially correlated scenarios. As shown in Fig. 3.2, when the transmit covariance matrix is $\boldsymbol{R}_{Tx} = \begin{bmatrix} 1 & 0.93 \\ 0.93 & 1 \end{bmatrix}$ as the example used in Section 2.1.3, both the open-loop and the closed-loop system achieve a lower capacity than that of the spatially independent channel. Nonetheless, the achievable ergodic channel capacity of a TxMF aided closed-loop system is about 1 (bit/symbol) higher than that of its open-loop counterpart, when the SNR is 20dB.

However, an unrealistic assumption made in Fig. 3.2 is that of having perfect CSIT at our disposal. As we have discussed in the introduction chapter, in a Frequency-Division-Duplex (FDD) system, a widely accepted model of CSIT acquisition is that the CSI is first estimated at the receiver, then quantized based on a pre-defined codebook known by both transmitter and receiver. Will the promised ergodic capacity gain erode because of the loss caused by quantized CSIT? This is the question we intend to answer in this section.

3.1.1 Comparison of the Achievable Ergodic Capacity Using Different Quantisers

In this section, we will employ a TxMF aided closed-loop system communicating over i.i.d channels having two transmit antennas and a single receive antenna as an example, in order to evaluate the achievable ergodic capacity using different quantisers discussed in Section 2.3. More explicitly, four different quantisers are employed, which are described as follows:

1. the Grassmannian line-packing quantiser described in Section 2.3.3, which is employed for quantising the unitary pre-processing vector $\frac{\boldsymbol{h}^*}{|\boldsymbol{h}|}$, and uses the chordal distance as its distance metric;

2. the random quantiser, which is also employed for quantising the unitary pre-processing vector $\frac{\boldsymbol{h}^*}{|\boldsymbol{h}|}$, and uses the chordal distance as its distance metric. Unlike the Grassmannian line-packing quantiser of Section 2.3.3, whose codewords are specifically optimised, the codewords of a random quantiser are generated randomly from a N_{Tx}-dimensional i.i.d. normal distribution. This random quantiser concept was mentioned in Section 2.3.4.

3. the MSE-based complex-valued quantiser described in Section 2.3.2, which is employed for quantising the CIR $\boldsymbol{h}$ and uses the MSE as its distance metric;

4. the MSE-based real-valued quantiser described also in Section 2.3.2, which is employed for quantising the CIR's envelope vector and channel phase rotation vector separately, and uses the MSE distance as its metric.

The corresponding simulation results are shown in Fig. 3.3. When using the Grassmannian line-packing quantiser of Section 2.3.3 in conjuction with a single-bit feedback, the performance of a TxMF aided closed-loop MISO system becomes better than that of its open-loop counterpart. When using a 10-bit

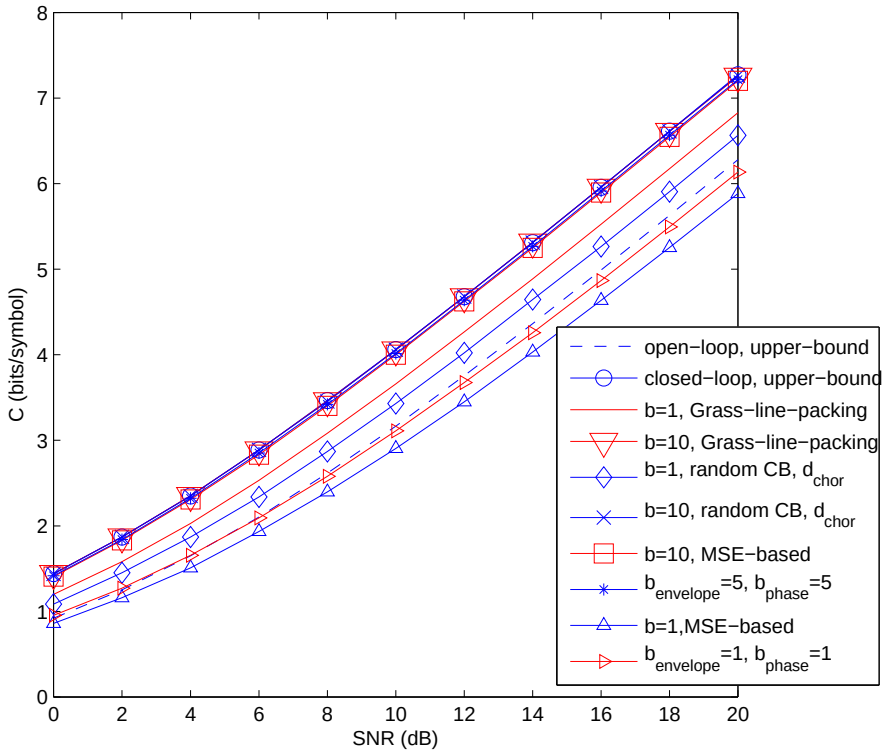

Figure 3.3: The achievable ergodic channel capacity of a TxMF aided closed-loop MISO system in conjunction with quantized CSIT versus SNR, when we have two transmit antennas and using various quantisers. The upper-bound ergodic channel capacity in conjunction with perfect CSIR and perfect CSIT are also plotted for comparison.

feedback, the upper-bound of the ergodic channel capacity associated with assuming perfect CSIT may be closely approached in the $N_{Tx} = 2$ scenario. The random quantiser using the chordal distance metric of Section 2.3.3 is seen to be inferior in Fig. 3.3 in comparison to the Grassmannian line-packing quantiser, when the number of feedback bits is limited. For example, when we have $b = 1$, the achievable capacity using the random quantiser is about 0.1 bit/symbol lower than that of the corresponding Grassmannian line-packing quantiser, as evidenced by Fig. 3.3. However, when the number of feedback bits is sufficiently high, for example $b = 10$ bits, observe in Fig. 3.3 that the performances of these two quantisers become comparable. Similarly, observe in Fig. 3.3 that the MSE-based quantiser, both the complex-valued one and the real-valued one designed for feeding back the entire CIR vector, achieve a similar performance for $b = 10$ bits. However, they are inefficient compared to the chordal-distance-based designs, when b is small. In the rest of this section, the Grassmannian line-packing quantiser of Section 2.3.3 will be employed as a benefit of its efficiency.

3.1.2 Capacity Gain of the Grassmannian Line-Packing Quantiser

Fig. 3.4 illustrates the achievable ergodic channel capacity gain ΔC versus the number of feedback bits b, when we have $N_{Tx} = 2; SNR = 0, 10$-dB, upon communicating over a) an i.i.d channel, and b) a spatially correlated channel, respectively. The achievable ergodic channel capacity gain ΔC is defined as the difference between $C_{closed-\boldsymbol{h}_q}$ and C_{open}, more explicitly we have $\Delta C = C_{closed-\boldsymbol{h}_q} - C_{open}$. The notation $C_{closed-\boldsymbol{h}_q}$ represents the achievable ergodic channel capacity in conjunction with quantized CSIT

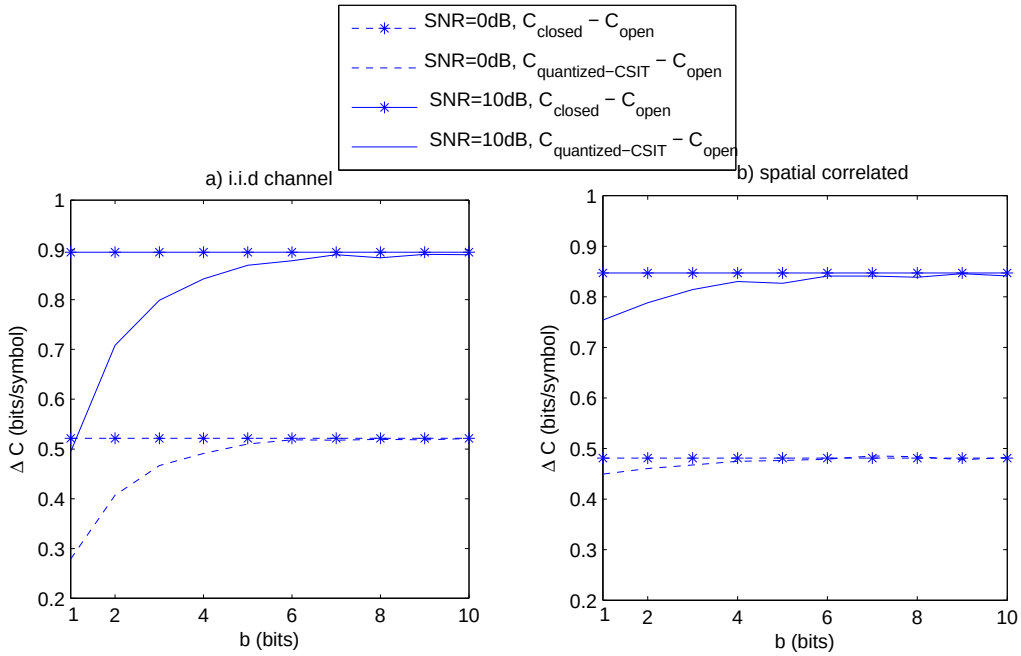

Figure 3.4: The achievable ergodic channel capacity gain $\Delta C = (C_{closed-\boldsymbol{h}_q} - C_{open})$ versus the number of feedback bits b, when we have $N_{Tx} = 2, SNR = 0, 10$ (dB) and having a) an i.i.d channel, and b) a spatially correlated channel, respectively. The upper-bound ergodic channel capacity gain defined as $C_{closed} - C_{open}$ in conjunction with perfect CSIR and perfect CSIT are also plotted for comparison.

$\boldsymbol{h}_q$, and the notation C_{open} represents the upper-bound of the open-loop channel capacity assuming perfect CSIR. The upper-bound of the ergodic channel capacity gain defined as $(C_{closed} - C_{open})$ in conjunction with perfect CSIR and perfect CSIT are also plotted for comparison. Moreover, Fig. 3.5 illustrates the achievable ergodic channel capacity gain ΔC versus the number of feedback bits for transmission over an i.i.d channel, when we have $SNR = 0$ and 10 dB, but in conjunction with an increased number of transmit antennas $N_{Tx} = 5$. These two figures demonstrated that

1. As seen in Fig. 3.4 and 3.5, substantial gains are obtained upon increasing the number of feedback bits from $b = 1$ bit to $b = 3$ bits. Increasing the number of feedback bits from $b = 5$ to $b = 10$ is capable of improving the achievable channel capacity. However, the attainable performance improvement is much smaller than that achieved upon increasing b from 1bit to 3bits.

2. It may be inferred from Fig. 3.4 that the required amount of feedback information is much lower for spatially correlated channels than that observed for spatially independent channels. Using a single bit feedback, nearly 80% of the promised capacity gain is achieved for spatially correlated channels.

3. The channel capacity gain ΔC of a TxMF aided closed-loop MISO system observed in Fig. 3.4a and 3.5 increases with both the SNR value and with the number of transmit antennas N_{Tx}. For example, as seen in Fig. 3.4a, the upper-bound of the channel capacity gain of the $N_{Tx} = 2$ scenario increases from 0.5 bits/symbol to 0.9 bits/symbol when the corresponding SNR value increases from 0dB to 10dB. Moreover, when we have $SNR = 10$dB, the upper-bound of the channel capacity gain increases from 0.9 bits/symbol to 2.3 bits/symbol, when the number of transmit antennas N_{Tx}

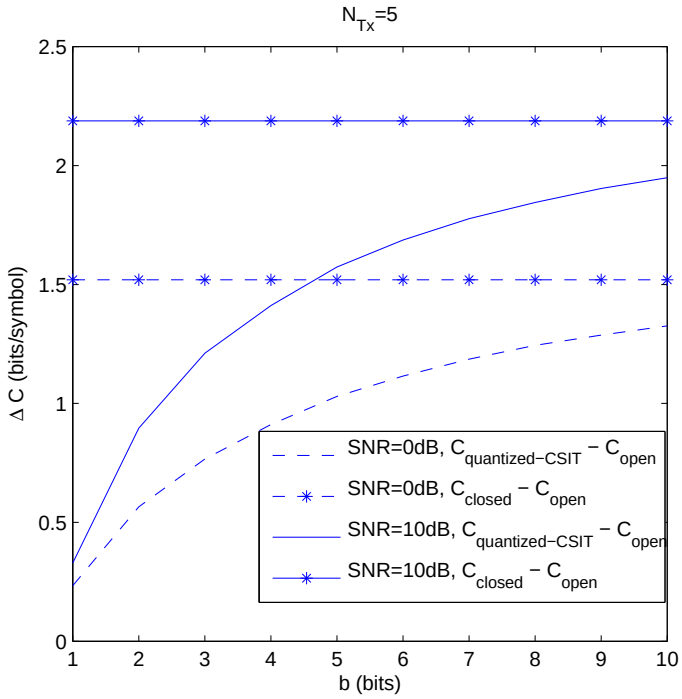

Figure 3.5: The achievable ergodic channel capacity gain $\Delta C = (C_{closed-\boldsymbol{h}_q} - C_{open})$ versus the number of feedback bits b, when we have $N_{Tx} = 5, SNR = 0, 10$ (dB), respectively. The upper-bound of the ergodic channel capacity gain defined as $(C_{closed} - C_{open})$ in conjunction with perfect CSIR and perfect CSIT are also plotted for comparison.

increases from 2 to 5.

4. Observe in Fig. 3.4a and 3.5 that the required number of feedback bits increases with the number of transmit antennas employed, when we aim for approaching the upper-bound of the channel capacity gain. For example, when we have $N_{Tx} = 2, SNR = 0$dB, observe in Fig. 3.4a that using $b = 5$ bits is capable of closely approaching the upper-bound of the channel capacity gain. By contrast, it may be seen in Fig. 3.5 that when N_{Tx} increases to 5 and the SNR remains 10dB, the achievable channel capacity gain ΔC is about 0.3 bits/symbol lower than its associated upper-bound even for using as many as $b = 10$ bits.

In summary, when assuming perfect CSIR, the achievable ergodic channel capacity of a TxMF aided closed-loop MISO system using even 1-bit quantized CSIT is always higher than that of its open-loop counterpart. This achievable channel capacity gain versus the number of feedback bits initially increases rapidly, but the improvements become more modest, when the value of b becomes higher.

3.2 Investigation of the CSI Signalling Overhead

In Section 3.1, we have assumed that the CSI is perfectly known at the receiver and then evaluated the achievable ergodic channel capacity using quantized CSIT for every channel realization $\boldsymbol{h}$. The CSI signalling overheads, including the pilot symbols signalled to the receiver for channel estimation, and the feedback bits signalled to the BS's downlink transmitter, were ignored in Section 3.1 and hence

will be investigated in this section. We will first introduce the pilot assisted channel estimation scheme in Section 3.2.1. Then the achievable ergodic channel capacity of an open-loop MISO system using estimated CSIR is derived to demonstrate the effect of channel estimation error in Section 3.2.2. Then, the achievable ergodic channel capacity of a TxMF aided closed-loop MISO system is also derived in Section 3.2.2 considering the channel estimation error, pilot signalling overhead and feedback overhead. We assume that the feedback channel is both error-free and delay-free, and set aside the study of the effects of channel-induced feedback errors and delays for our future research.

3.2.1 Pilot-Assisted Channel Estimation

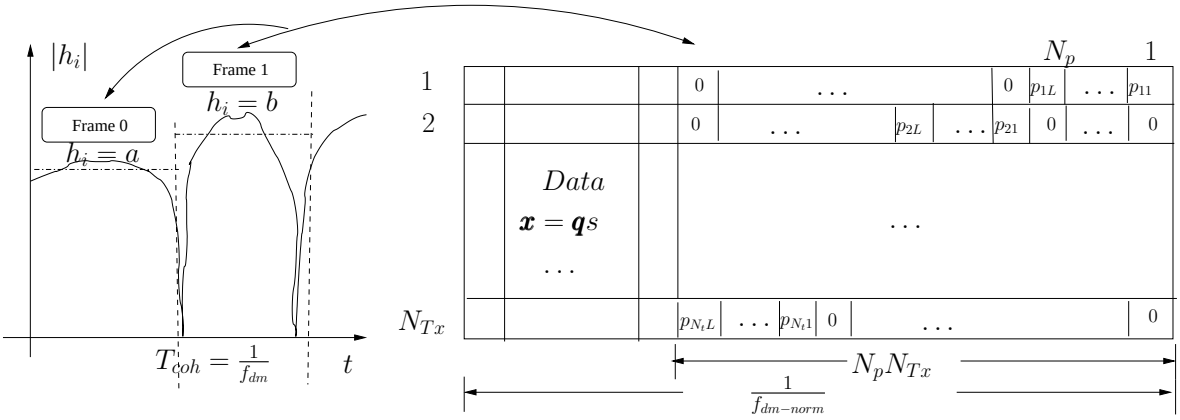

Figure 3.6: Transmission frame structure of the N_{Tx} transmit antennas consisting of $N_p N_{Tx}$ pilots and $(\frac{1}{f_{dm-norm}} - N_p N_{Tx})$ data symbols.

In practice, the channel realizations $\boldsymbol{h}$ varied over time, and the speed of its variation is described by the channel's Dopper frequency as detailed in Section 2.1.2.2. It is common to model the channel by block fading, where the channel realization $\boldsymbol{h}$ is kept constant during a channel coherence period T_{coh} and faded at the end of it. Assuming $T_{coh} \approx \frac{1}{f_{dm}}$ [109], a transmission frame consisting of $\frac{1}{f_{dm-norm}}$ symbols, where $f_{dm-norm}$ denotes the normalized Doppler frequency shift, is transmitted within the channel's coherence period, and its structure is illustrated in Fig. 3.6. The pilot symbols p_{ij}, $|p_{ij}|^2 = 1$ are allocated in the first $N_p N_{Tx}$ symbols in a time-orthogonal manner for channel estimation in order to ensure that they would not cause interference with each other [30]. Hence, each channel h_i is estimated using N_p pilots. Due to the time-orthogonality of the pilots seen in Fig. 3.6, each channel $h_i, i \in [1, N_{Tx}]$ is estimated separately. The estimation is based on averaging the projections of the received signal on p_{ij} as

$$\hat{h}_i = \frac{1}{N_p} \sum_{j=1}^{N_p} p_{ij}^* y_j = h_i + h_e, \tag{3.1}$$

$$h_e = \frac{1}{N_p} \sum_{j=1}^{N_p} p_{ij}^* n_j \sim \mathcal{CN}(0, \frac{1}{N_p} N_0), \tag{3.2}$$

where $\hat{h}_i$ is the estimate of h_i, and the estimation error h_e is a random variable with zero-mean and a variance of $\frac{N_0}{N_p}$. Since the estimation of each channel h_i is independent of the others, the estimation error vector $\boldsymbol{h}_e$ satisfies the distribution $\mathcal{CN}(0, \frac{N_0}{N_p} \boldsymbol{I}_{N_t})$, and the estimated channel vector obeys $\hat{\boldsymbol{h}} = \boldsymbol{h} + \boldsymbol{h}_e$.

3.2.2 Deviation of the Channel Capacity

For an open-loop MISO system, the receiver estimates the CIR vector $\hat{\boldsymbol{h}}$, and considerrs it as the true CIR. Naturally, the received signal y will be rewritten as

$$y = \hat{\boldsymbol{h}}^T \boldsymbol{x} + (n - \boldsymbol{h}_e^T \boldsymbol{x}) = \hat{\boldsymbol{h}}^T \boldsymbol{x} + n'. \tag{3.3}$$

$$E(|n'|^2|\hat{\boldsymbol{h}}) = E(|n'|^2) = E(nn^*) + E(\boldsymbol{h}_e^H \boldsymbol{x}\boldsymbol{x}^H \boldsymbol{h}_e) = N_0 + \frac{N_0}{N_p} \tag{3.4}$$
$$n' \sim \mathcal{CN}(0, N_0 + \frac{N_0}{N_p}),$$

where we have assumed that the transmit power is unity $E[\boldsymbol{x}\boldsymbol{x}^H] = E_{Tx} = 1$, and the equivalent noise n' is a complex-valued Gaussian distributed random variable with the same mean and variance for different CIR vectors $\boldsymbol{h}$. Hence, the capacity is represented as [30]

$$C_{open-\hat{\boldsymbol{h}}} = (1 - \eta_p) E_{\hat{\boldsymbol{h}}} \left(log_2 \left(1 + \frac{1}{\left(N_0 + \frac{N_0}{N_p} \right) N_{Tx}} \|\hat{\boldsymbol{h}}\|^2 \right) \right), \tag{3.5}$$

where $\eta_p = N_p N_{Tx} f_{dm-norm}$, $0 \leq \eta_p \leq 1$ represents the pilot signalling overhead. Equation (3.5) only represents the case, when the CIR estimate $\hat{\boldsymbol{h}}$ is directely derived from the embedded pilot symbols. If more sophisticated channel estimation methods are used, such for example decision-directed channel estimation [135], it is possible to decrease the noise variance $E(n'n'^*)$ without causing any further pilot signalling overhead (i.e. maintaining a constant η_p) so as to improve the ergodic channel capacity. However, the variance of $\boldsymbol{h'}_e$ is difficult to analyse because of the potential error propagation effects caused by sophisticated decision-directed channel estimation algorithms. We will focus our attention purely on the pilot-assisted system analysis in our study.

Similarly, for a TxMF aided closed-loop MISO system, we assumed that the CSI is estimated at the receiver side as $\hat{\boldsymbol{h}} = \boldsymbol{h} + \boldsymbol{h}_e$, where we have $\boldsymbol{h}_e \sim \mathcal{CN}(0, \frac{N_0}{N_p} \boldsymbol{I}_{N_{Tx}})$. The preprocessing vector $\boldsymbol{q}$ is selected from a codebook $\mathcal{Q}$ having $|\mathcal{Q}| = 2^b$ cardinalities based on the estimated CIR knowledge $\hat{\boldsymbol{h}}$. Assuming that the b feedback bits are both delay-free and error-free, the received signal y will be rewritten as

$$\begin{aligned} y &= \boldsymbol{h}^T \boldsymbol{q} s + n = \hat{\boldsymbol{h}}^T \boldsymbol{q} s + n', \\ n' &= n - \boldsymbol{h}_e^T \boldsymbol{q} s. \end{aligned} \tag{3.6}$$

Since $\boldsymbol{q}$ is a unitary vector, we define $\boldsymbol{h}_e^T \boldsymbol{q} = \|\boldsymbol{h}_e\| \cos\Theta e^{j\beta}$, where Θ, $\beta \in [-\pi, \pi]$ are the Hermition angle and the Pseudo-angle between $\boldsymbol{h}_e$ and $\boldsymbol{q}$ as defined in Section 2.3.3. For a given $\hat{\boldsymbol{h}}$, the variance of the equivalent noise n' is

$$\begin{aligned} E(n'n'^*|\hat{\boldsymbol{h}}) &= E(nn^*) + E(\cos^2\Theta \|\boldsymbol{h}_e\|^2 s s^H |\hat{\boldsymbol{h}}) \\ &= N_0 + E(\cos^2\Theta \|\boldsymbol{h}_e\|^2 |\hat{\boldsymbol{h}}). \end{aligned} \tag{3.7}$$

We infer from Equation (3.6) that n' is not a Gaussian variable. However, assuming that n' is Gaussian distributed, we can derive the lower bound of the ergodic channel capacity in the form of

$$C_{closed-\hat{\boldsymbol{h}}-\boldsymbol{h}_q} = (1 - \eta_p) E_{\hat{\boldsymbol{h}}} \left(log_2 \left(1 + \frac{|\hat{\boldsymbol{h}}^T \boldsymbol{q}|^2}{N_0 + E(\cos^2\Theta \|\boldsymbol{h}_e\|^2 |\hat{\boldsymbol{h}})} \right) \right) - b f_{dm-norm}, \tag{3.8}$$

where $\eta_p = N_p N_{Tx} f_{dm-norm}$ represents the pilot signalling overhead in percentage. and $bf_{dm-norm}$ represents the CSI feedback signalling overhead in (bits/symbol). The CSI feedback signalling overhead in percentage should be formulated as $\eta_f = \frac{bf_{dm-norm}}{C'}$, where C' is equal to the achievable ergodic capacity without considering the pilot overhead $C' = E_{\hat{\boldsymbol{h}}}\left(log_2\left(1 + \frac{|\hat{\boldsymbol{h}}^T \boldsymbol{q}|^2}{N_0 + E(\cos^2\Theta \|\boldsymbol{h}_e\|^2 | \hat{\boldsymbol{h}})}\right)\right)$.

3.2.3 Simulation Results

Three typical values of Doppler shifts defined in the Long-Term-Evolution (LTE) Orthogonal-Frequency-Division-Multiplexing-Access (OFDMA) DL system [136] are $f_{dm} = 5$ Hz, 70 Hz, and 300 Hz, which correspond roughly to mobile velocities of 2 (pedestrian), 30 (vehicular) and 130 (vehicular) km/h, respectively. The signal bandwidth of each subcarrier is defined as 15 KHz, which is significantly lower than the channel's coherence bandwidth. Hence, the fading is non-frequency selective. Assuming a maximum achievable symbol rate of $R_s = 15$K symbol/s, the normalised Doppler frequencies are $f_{dm-norm} = 0.2,\ 0.04$ and 0.003, respectively. To simplify our future calculation, we employed $f_{dm-norm} = 0.1,\ 0.01$ and 0.001 in our simulations to represent these three typical scenarios.

Based on the aforementioned analysis in Section 3.2.2, there are four parameters which affect the achievable capacity, namely the normalised Doppler frequency $f_{dm-norm}$, the number of pilot symbols per transmit antenna within the channel's coherence time N_p, the number of transmit antennas N_{Tx} and the number of feedback bits per CIR tap b. The effect of $f_{dm-norm}$ on the achievable capacity can be readily seen from Equation (3.8). When the other three parameters are fixed, for $f_{dm-norm} \to 0$, which corresponds to a time-invariant channel, yielding $(1 - \eta_p) \to 1$ and $bf_{dm-norm} \to 0$, the capacity loss will approach zero. In other words, the achievable ergodic capacity is higher for channels having a low Doppler frequency than for channels having a high Doppler frequency.

However, the effect of the other three parameters N_p, b and N_{Tx} are more complicated. Here we opt for $f_{dm-norm} = 0.1$ and $f_{dm-norm} = 0.001$, representing a rapidly fluctuating channel as well as a slowly varying channel, respectively, and investigate the effect of the pilot-based signalling overhead of $\eta_p = N_{Tx} N_p f_{dm-norm}$ and that of the feedback signalling overhead of $\eta_f = \frac{bf_{dm-norm}}{C'}$ on the achievable capacity.

We observe in Equation (3.8), upon increasing the pilot overhead, the achievable capacity can be improved by increasing the channel estimation accuracy according to $\|\boldsymbol{h}_e\|^2 \to 0$, but imposing an increased capacity loss yielding $(1 - \eta_p) \to 0$. Fig. 3.7 illustrates the achievable ergodic capacity $C_{closed-\hat{\boldsymbol{h}}-\boldsymbol{h}_q}$ of a TxMF aided closed-loop MISO system in conjuction with the estimated and quantized CSIT versus the number of pilot symbols per channel coherence time N_p, when we have $N_{Tx} = 2;\ b = 5;\ f_{dm-norm} = 0.1/0.001,\ SNR = 5$dB, respectively. It demonstrates that when the channel's normalised Doppler frequency is as low as $f_{dm-norm} = 0.001$, a moderate factor of pilot overhead is capable of increasing the achievable capacity by providing a more accurate channel knowledge. However, when the channel's normalised Doppler frequency is as high as $f_{dm-norm} = 0.1$ or the number of pilot symbols N_p becomes comparable to the total number of symbols $\frac{1}{f_{dm-norm}}$, the effect of pilot signalling overhead induced capacity loss becomes dominant, and increasing N_p will decrease the achievable capacity dramatically. Naturally, the capacity degradation imposed by the pilot signalling overhead is more substantial for systems having a large number of transmit antennas, since η_p increases linearly with N_{Tx}.

Similarly, a trade-off between limiting the feedback overhead η_f and having a sufficiently accurate

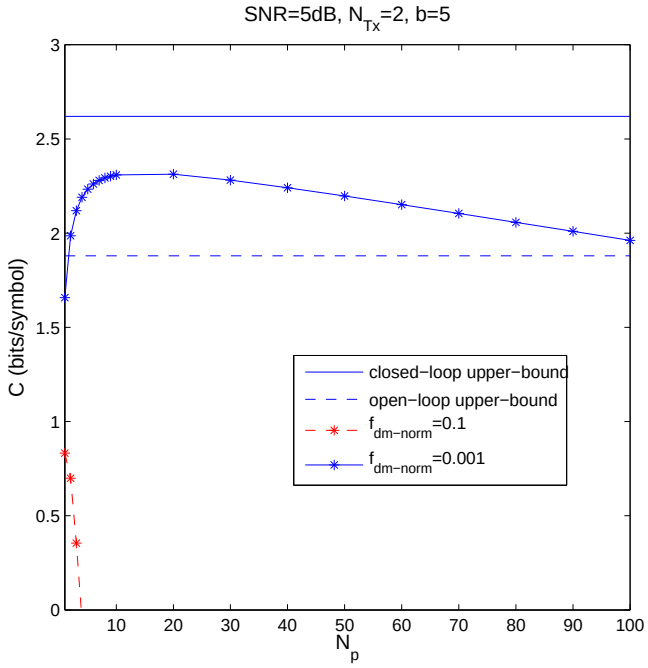

Figure 3.7: The achievable ergodic capacity of a TxMF aided closed-loop MISO system in conjuction with estimated and quantized CSIT $C_{closed-\hat{\boldsymbol{h}}-\boldsymbol{h}_q}$ versus the number of pilot symbols per channel's coherence time N_p, when we have $N_{Tx} = 2$; $b = 5$; $f_{dm-norm} = 0.1/0.001$, $SNR = 5$dB, respectively. The results were plotted from Equation (3.8). The upper-bound ergodic channel capacity in conjunction with perfect CSIR and perfect CSIT are also plotted for comparison.

CSIT is required. Fortunately, the analysis provided in Section 3.1 demonstrates that having a large number of feedback bits is not necessary, since most of the attainable capacity gain may be achieved by using a limited number of feedback bits. Moreover, the feedback overhead η_f is proportional to $\frac{1}{C'}$. This relationship indicates that the feedback overhead required decreases at high SNRs, where the capacity C' increases; secondly, the feedback overhead required may not increase dramatically for systems having a large number of transmit antennas, since the number of feedback bits required for achieving a certain feedback error b and the capacity C' will both increase. Hence, compared to the feedback overhead, the degradation imposed by the pilot symbol overhead analysed in the last paragraph may be more dominant. More explicitly, Fig. 3.7 illustrates the achievable ergodic capacity $C_{closed-\hat{\boldsymbol{h}}-\boldsymbol{h}_q}$ of a TxMF aided closed-loop MISO system in conjuction with the estimated and quantized CSIT versus the number of feedback bits b per CIR tap, when we have $N_{Tx} = 2$; $N_p = 1$; $f_{dm-norm} = 0.1/0.001$, $SNR = 5$dB, respectively. This shows that increasing b is beneficial for channels associated with a low Doppler frequency, such as $f_{dm-norm} = 0.001$, but it is detrimental for channels having a high Dopper frequency, such as $f_{dm-norm} = 0.1$. Moreover, observed in Fig. 3.7 that the attainable improvement is reduced upon increasing the number of feedback bits b.

We jointly consider the effects of N_p, N_{Tx} and $f_{dm-norm}$ in Fig. 3.9, which demonstrates that the achievable ergodic capacity $C_{closed-\hat{\boldsymbol{h}}-\boldsymbol{h}_q}$ of a TxMF aided closed-loop MISO system in conjuction with the estimated and quantized CSIT versus the number of the feedback bits b and pilot overhead η_p, when we have $f_{dm-norm} = 0.001$, $N_{Tx} = 4$, $SNR = 5$dB, respectively. It is shown for a channel having a high coherence time $f_{dm-norm} = 0.001$ that the achievable capacity is maximised by opting for an

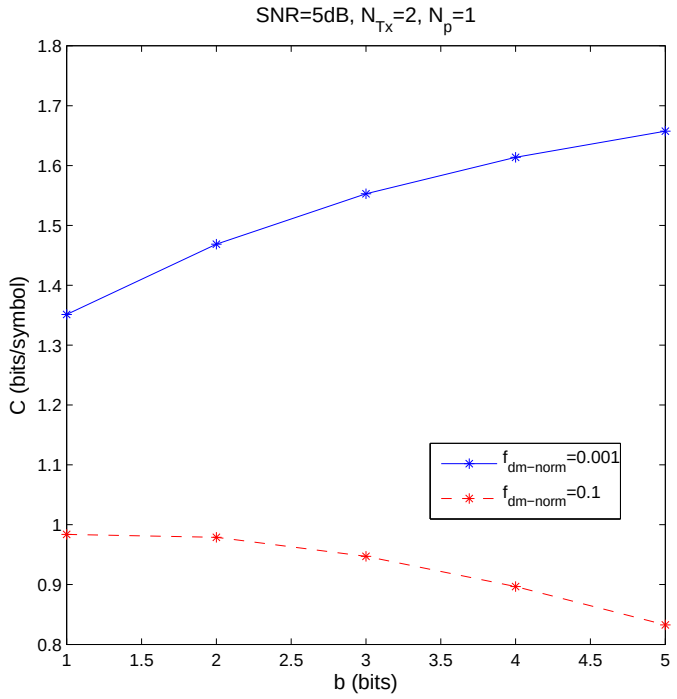

Figure 3.8: The achievable ergodic capacity of a TxMF aided closed-loop MISO system in conjuction with estimated and quantized CSIT $C_{closed-\hat{\boldsymbol{h}}-\boldsymbol{h}_q}$ versus the number of feedback bits b, when we have $N_{Tx} = 2;\ N_p = 1;\ f_{dm-norm} = 0.1/0.001,\ SNR = 5$dB, respectively. The results were plotted from Equation (3.8).

appropriate chosen moderate pilot overhead, when it is beneficial to employ a high number of feedback bits.

3.2.4 Section Summary

In this section, we have derived the achievable channel capacity bound of a TxMF aided closed-loop MISO system, when considering the effects of channel estimation errors, tansmit preprocessing vector quantization errors using Grassmannian-line packing codebook, the effective capacity loss caused by pilot symbols and that imposed by the CSI feedback bits. The simulation results demonstrated that the potential capacity improvements of using a closed-loop design and an increased number of transmit antennas are indeed achieveable for slowly fading channels, but erode for relatively rapidly fading channels. A major reason for this observation is that a large proportion of the channel capacity has to be sacrificed for pilot signalling, especially for systems having a high number of transmit antennas. The feedback overhead also imposes a capacity degradation, but this is less substantial than the effects of the pilot signalling overhead.

3.3 Pilot Overhead Reduction for Rapidly Fading Channels

The analysis provided in Section 3.2 demonstrated that the main reason for the poor performance of a TxMF aided closed-loop MISO system for a channel associated with a low coherence-time is its inability

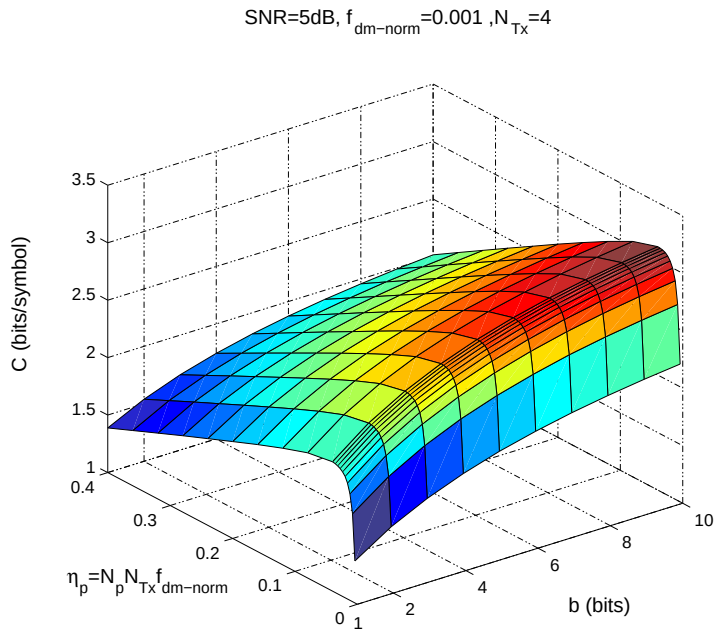

Figure 3.9: The achievable ergodic capacity of a TxMF aided closed-loop MISO system in conjuction with estimated and quantized CSIT $C_{closed-\hat{\boldsymbol{h}}-\tilde{\boldsymbol{h}}}$ versus the number of feedback bits b and pilot overhead η_p, when we have $f_{dm-norm} = 0.001$, $N_{Tx} = 4$, $SNR = 5$dB, respectively. The results were plotted from Equation (3.8).

of affording a sufficiently high number of pilot symbols in order to achieve a sufficiently accurate CSIR knowledge. In this section, we propose a pilot overhead reduction scheme for channels having a low coherence-time.

The simulation results seen in Section 3.1 suggest that as long as a transmitter chooses the right preprocessing vector $\boldsymbol{q}$, even if $\boldsymbol{q}$ represents a coarse CIR estimate since it is from a small codebook having only two codewords, the channel capacity can be improved in comparison to an open-loop design. Using the frame structure shown in Fig. 3.6, the probability of making the right choice for $\boldsymbol{q}$ depends on the quality of the CSIR, namely the CIR estimated at the receiver. However, a substantial simplification becomes possible, since the codebook is already available at the transmitter, and hence the transmitter can subject the pilot symbols to the effects of the legitimate CIRs of the codebook. Accordingly, instead of estimating the true CIR $\boldsymbol{h}$, the receiver simply has to determine which particular $\boldsymbol{q}_i$ vector of the codebook would provide the highest receive energy $E(|y|^2) = E(|\boldsymbol{h}^T\boldsymbol{q}_i|^2 + |n|^2)$, and has to inform the transmitter using $b = log_2|\mathcal{Q}|$ bits. The corresponding new frame structure is shown in Fig. 3.10. The main difference in comparison to that of Fig. 3.6 is that the number of the pilot symbols N_p is independent of the number of transmit antennas N_{Tx}. This will dramatically reduce the capacity loss caused by pilot symbols, especially when the value of N_{Tx} is high, while N_p and $|\mathcal{Q}|$ is limited. For example, if we have $f_{dm-norm} = 0.1, N_{Tx} = 5, N_p = 1, b = 1$, using the frame structure of Fig. 3.6, 50% of the channel capacity loss is imposed by the insertion of pilot symbols. Using the proposed scheme, only 20% of the effective capacity is used for channel estimation. However, if a high-resolution codebook is employed, the number of pilot symbols required increases exponentially, which results in a high effective capacity

loss. Hence, the proposed scheme is no longer beneficial for the case, when a high-resolution codebook is required.

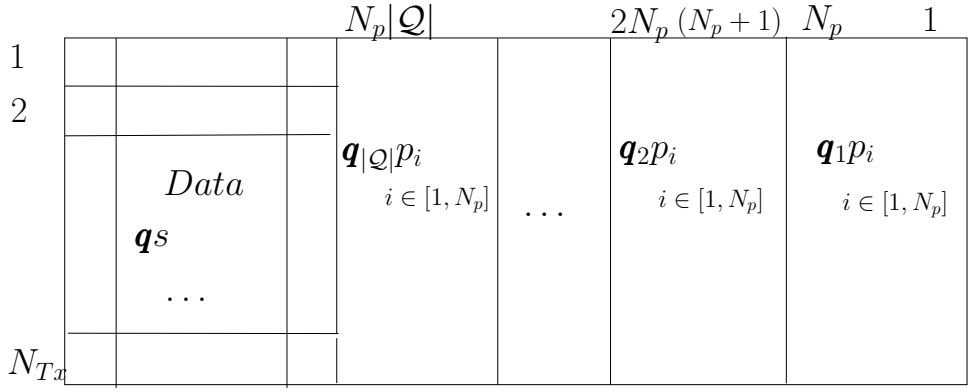

Figure 3.10: The proposed frame structure consisting of $N_p|\mathcal{Q}|$ pilots.

Using the proposed scheme obeying the transmission frame structure shown in Fig. 3.10, the receiver estimates the equivalent channel $h_i'' = \boldsymbol{h}^T \boldsymbol{q}_i, i \in [1, |\mathcal{Q}|]$ by averaging the N_p pilots according to:

$$\hat{h}_i'' = h_i'' + \frac{1}{N_p} \sum_{l=1}^{N_p} n_l = h_i'' + h_e'', \tag{3.9}$$
$$h_e'' \sim \mathcal{CN}(0, \frac{1}{N_p} N_0),$$

where h_e'' represents the CIR estimation error, which is a Gaussian variable with a zero mean and a variance of $\frac{1}{N_p} N_0$. Assuming that the right codeword is chosen by comparing the energy of the estimated equivalent channel $\boldsymbol{q} = \max_{\boldsymbol{q}_i} |\hat{h}_i''|^2$, which is likely to be the case when the noise variance is low, and assuming unit transmit power $E_{Tx} = 1$, the achievable ergodic capacity can be formulated as

$$C_{closed-new-scheme} = (1 - N_p 2^b f_{dm-norm}) E_{\boldsymbol{h}} \left(log_2 \left(1 + \frac{|\boldsymbol{h}^T \boldsymbol{q}|^2}{N_0 + \frac{N_0}{N_p}} \right) \right) - b f_{dm-norm}. \tag{3.10}$$

However at low SNRs, it is possible that the chosen codeword is not the optimal one. For this case, we characterise the lower bound of the achievable performance using random preprocessing, where a random unitary preprocessing vector $\boldsymbol{q}$ is chosen regardless of the current true CIR $\boldsymbol{h}$. Based on Equation (3.10), we quantify the ergodic capacity of a TxMF aided closed-loop MISO system having parameters of $N_{Tx} = 2, 5$; $f_{dm-norm} = 0.1$; $N_p = 1$; $b = 1$ and using the proposed scheme. The results shown in Fig. 3.11 demonstrate that

1. Assuming the right preprocessing vector codeword is chosen from the codebook, the closed-loop system using the proposed pilot overhead signalling reduction scheme outperforms the corresponding old pilot signalling scheme discussed in Section 3.2.2. Moreover, employing more transmit antennas provides a slightly increased capacity. For example, when the number of transmit antennas increases from 2 to 5, the ergodic channel capacity quantified at high SNRs is increased by about 0.5 (bits/symbol);

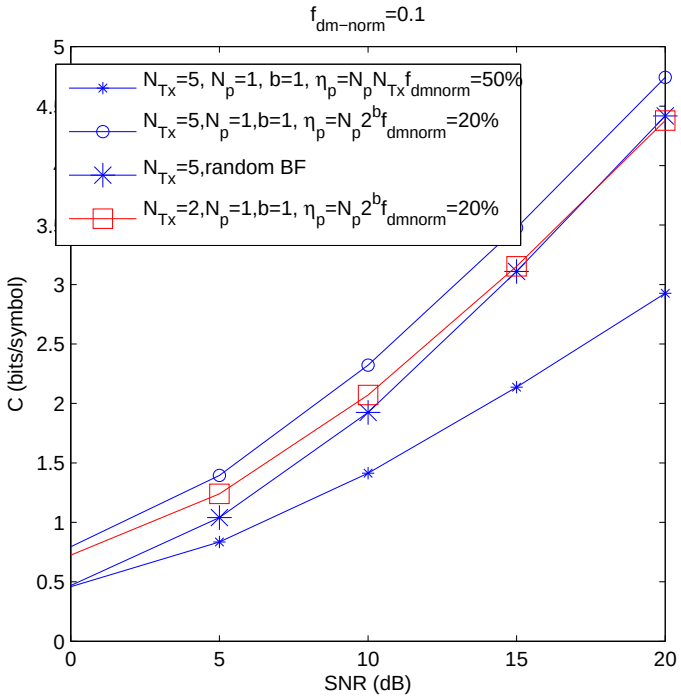

Figure 3.11: The achievable ergodic channel capacity of a TxMF aided closed-loop MISO system in conjunction with estimated and quantized CSIT using the proposed frame structure in Fig. 3.10 namely $C_{closed-new-scheme}$ versus SNR, when we have $N_{Tx} = 2, 5;\ f_{dm-norm} = 0.1;\ N_p = 1;\ b = 1$, respectively. The results were plotted from Equation (3.10).

2. If the preprocessing vector $\boldsymbol{q}$ is chosen randomly, then the performance of a closed-loop system associated with $N_{Tx} = 5$ transmit antenna is still better than that of the corresponding old pilot signalling scheme discussed in Section 3.2.2.

Fig. 3.12 illustrates the ergodic channel capacity of a TxMF aided closed-loop MISO system having parameters of $N_{Tx} = 5;\ f_{dm-norm} = 0.01;\ N_p = 1; b = 1, 5$ and using the proposed scheme. Compared to the performance of using transmission regime of Fig. 3.6, it is clear that for $b = 1$, the performances are quite similar. However, when using a $b = 5$ bit feedback, the performance using the proposed scheme becomes worse than that of the transmission regime of Fig. 3.6 and Section 3.2.2 since the capacity loss caused by the associated high number of pilot symbols is high. As a result, the proposed scheme is deficient for channels having a long coherence time.

In summary, for a channel having a relatively short coherence time, the proposed pilot overhead reduction scheme using a low value of N_p and b is capable of providing a higher ergodic capacity than the open-loop system, especially when the number of transmit antennas is high. However, the benefits of employing closed-loop scheme and a high number of transmit antennas is relatively small. From a robustness point of view, employing a low number of transmit antennas and an open-loop design is more appropriate for channels having a short coherence time.

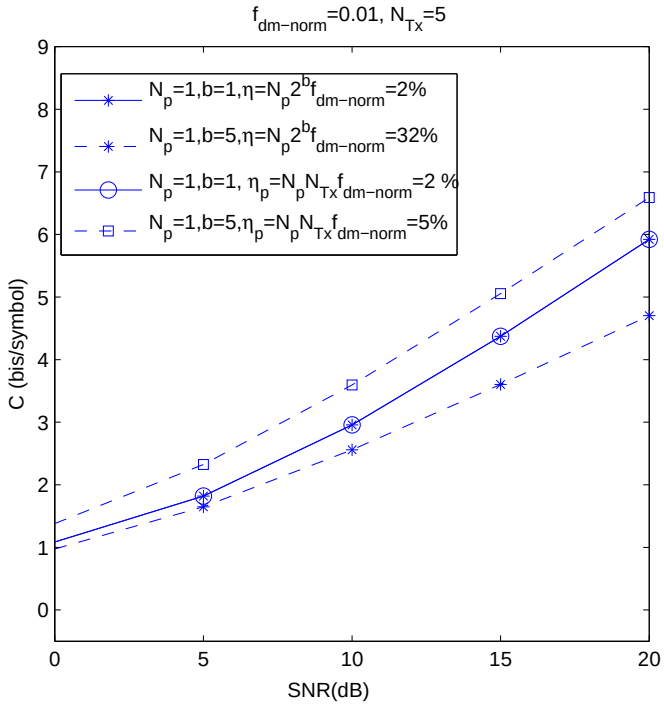

Figure 3.12: The achievable ergodic channel capacity of a TxMF aided closed-loop MISO system in conjunction with estimated and quantized CSIT using the proposed frame structure in Fig. 3.10 namely $C_{closed-new-scheme}$ versus SNR, when we have $N_{Tx} = 5$; $f_{dm-norm} = 0.01$; $N_p = 1$; $b = 1, 5, 10$, respectively, The results were plotted from Equation (3.10).

3.4 Pilot Symbol Assisted Rateless Codes

In Section 3.2 and 3.3, the pilot symbols were multiplexed with the data symbols at the input of the modulation stage, which is referred to as Pilot Symbol Assisted Modulation (PSAM). In this section, we propose a novel technique, hereby referred to as Pilot Symbol Assisted Rateless (PSAR) coding, where a predetermined fraction of binary pilot symbols is interspersed with the information bits at the input of the channel coding stage. We will subsequently demonstrate that the PSAR code-aided transmit preprocessing scheme succeeds in gleaning more beneficial knowledge from the inserted pilots, because the pilot bits are not only useful for estimating the channel at the receiver, but they are also beneficial in terms of significantly reducing the computational complexity of the rateless channel decoder. Our results suggest that more than a 30% reduction in the decoder's computational complexity can be attained by the proposed system, when compared to a corresponding benchmarker scheme having the same pilot overhead, but using the classic PSAM technique. Since the amount of pilot symbols increases with the number of transmit antennas, as demonstrated in Section 3.2 and 3.3, the proposed PSAR scheme is particularly beneficial for employment in multiple antenna assisted systems, rather than in single antenna aided systems. Moreover, the rateless code employed in our system also exploit the knowledge of the CSI at the transmitter by exploiting the inherently flexible nature of a specific family of rateless codes that are capable of modifying both their code-rate as well as their degree distribution based on the CSI, in an attempt to adapt to the time-varying nature of the channel. Using this scheme, the near-capacity performance over a diverse range of channel SNRs rather than at a single SNR value becomes attainable.

A brief introduction to rateless codes is provided in Section 3.4.1. The proposed closed-loop TxMF aided MISO system using PSAR is detailed in Section 3.4.2 with an explicit emphasis on the PSAR encoding/decoding process. Finally, our simulation results are given in Section 3.4.3.

3.4.1 Introducation to Rateless Codes

Unlike the families of the so-called fixed-rate codes such as Hamming codes having a fixed-rate and a rigid construction, the families of rateless codes do not fix their code-rate before transmission. This is essentially the interpretation of the terminology 'rateless'. Luby Transform (LT) codes [137], proposed by Luby in 2002, can be considered as the first practical rateless code family. In this section, we will use LT codes as an example to introduce the encoding and decoding methods of rateless codes as well as their fundamental philosophies.

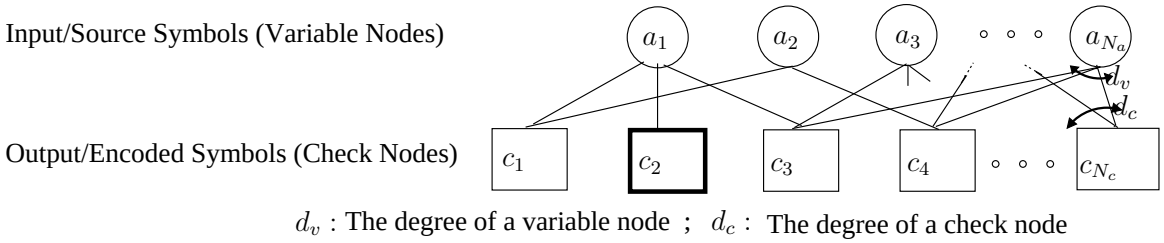

Figure 3.13: A Tanner graph based description of LT codes showing the source symbols (variable nodes) and LT-encoded symbols (check nodes).

The encoding process of a LT code is diagrammatically represented by means of a bipartite graph, commonly referred to as a Tanner graph [138] or a factor graph [139], as shown in Fig. 3.13. Assume a message consisting of N_a input (source) symbols $\boldsymbol{a} = [a_1, a_2, \ldots, a_{N_a}]$, where each symbol contains an arbitrary number of bits (e.g. $a_1 = [010]$). The LT-encoded symbol c_j, $j = 1, \ldots, N_c$, is simply the modulo-2 sum of d_c, $(1 \leq d_c \leq N_a)$ random distinct input symbols. In the context of graph theory, an input source symbol can be treated as a variable node, whilst an LT-encoded symbol can be regarded as a check node. In our discourse, we will interchangeably use the terminology input/output symbols, source/LT-encoded symbols and variable/check nodes. The number of input symbols d_c invoked for producing a check node is referred to as the check node degree. For example, the check node c_2 shown in Fig. 3.13 has a degree of one represented as $d_c^2 = 1$. Correspondingly, the number of output symbols produced by a single variable node is termed as the variable node degree denoted by d_v. For example, observed in Fig. 3.13 that the degree of the first variable node, namely of a_1 is equal to three, which is represented as $d_v^1 = 3$. Given the nature of this encoding scheme, there is no limit on the possible number of encoded symbols that can be produced and for this reason, LT codes do not have a fixed coding rate represented by $r_c = \frac{N_a}{N_c}$, and are referred to as being rateless codes. The philosophy of LT-codes is actually the ideal digital fountain code concept advocated by Byers *et al.* [140]. Metaphorically speaking, a fountain code can be compared to an abundant water supply capable of supplying a potentially unlimited number of encoded packets (water-drops). The receiver is capable of recovering N_a out of N_c transmitted packets on an erasure channel, if N_c is sufficiently larger than N_a.

The hard decoding process as detailed by Luby in [137] commences by locating a self-contained symbol, or the so-called degree-one symbol which is not combined with any other, for example, the output

symbol c_2 shown in Fig. 3.13. The decoder will then add (modulo-2) the value of this symbol to all the LT-encoded symbols relying on it and then removes the corresponding modulo-2 connections. The decoding procedure will continue in an iterative manner, each time commencing from a degree-one symbol and exchanging hard-decision information between the nodes. If no degree-one symbol is present at any point during the decoding process, the decoding operation will abruptly halt. Hence, the performance of a LT code depends on its check node degree and variable degree, which may be characterised by the check node degree distribution $\delta(x)$ and the variable node degree distribution $v(x)$, respectively. A carefully designed degree distribution, such as the robust soliton distribution [137], guarantees that this does not occur more often than a pre-defined probability of decoding failure. Additionally, to implement such a hard decoding scheme, the specific modulo-2 connections between the variable nodes and check nodes do not have to be previously known by both the transmitter and receiver. This may be facilitated by informing both the transmitter and the receiver of the degree distribution $\delta_{LT}(x)$ before transmission, and having synchronised clocks used for the seed of the pseudo-random number generator employed at both link ends.

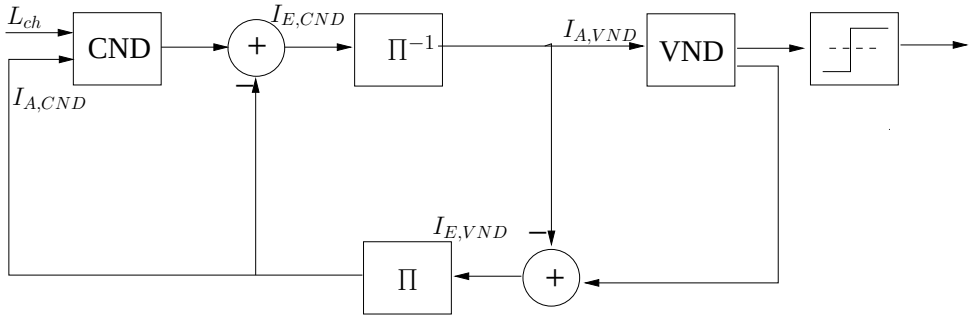

Figure 3.14: Soft decoder structure of an LT code.

The decoding performance of a LT code may be further improved by exchanging soft decisions, rather than hard decisions between nodes in the aforementioned iterations, which is referred to as soft decoding [97]. More explicitly, the re-organised structure of an LT code's soft decoder is illustrated in Fig. 3.14, which is constituted by the serial concatenation of two soft-input-soft-output decoders, namely that of the inner Check Node Decoder (CND) and of the outer Variable Node Decoder (VND). The inner CND receives both channel output values as well as the *a-priori* Log-likelihood Ratio (LLRs) from the VND and then converts them to *a-posteriori* LLRs. The outer VND receives the de-interleaved extrinsic information from the CND. The randomly selected connections between the variable nodes and the check nodes during the encoding process shown in Fig. 3.13 essentially function as an interleaver, which is distinguished by a term inherited from graph theory, namely by the terminology of the "edge interleaver". The extrinsic LLR values are exchanged between these two decoders after passing through the edge interleavers. The decoding performance expected is improved by increasing the number of iterations.

3.4.2 System Model

The system we considered is a TxMF aided closed-loop MISO system having two transmit antennas and a single receive antenna, which is illustrated in Fig. 3.15. The information bits $\boldsymbol{a}$ are first encoded

by a rateless encoder using the degree distribution provided by the Degree Distribution Selector (DDS) at the transmitter. Then the encoded sequence $\boldsymbol{c}$ will pass through an interleaver termed as the "Pilot position interleaver", which is denoted by Π_p in Fig. 3.15. Then, the interleaved encoded bits are BPSK modulated and are preprocessed by the TxMF. At the receiver side, the pilot symbols are used not only for channel estimation but they are also forwarded to the detector of Fig. 3.15. After the pilot position deinterleaver, both the received pilot symbols as well as the received data symbols are forwarded to the rateless decoder of Fig. 3.15. The estimated message $\hat{\boldsymbol{a}}$ is then finally generated by the rateless decoder of Fig. 3.15.

Moving on from providing a general description of the system considered, the components related to the proposed PSAR scheme including the DDS_T, the rateless encoder/decoder and the pilot position de/interleaver, as well as the related signal processing schemes will be detailed below.

3.4.2.1 Transmit Degree Distribution Selector DDS_T

In Section 3.4.1, we have introduced three parameters of a rateless code, namely the flexible coding rate r_c and the two degree distributions $\delta(x)$ and $v(x)$. In the available literature, rateless codes are frequently employed in situations, where the channel statistics are unknown to the transmitter (e.g. open-loop system), and hence the degree distribution of rateless codes is fixed; i.e. the degree distribution used for coining the specific random degree for each transmitted bit is time-invariant and thus channel-independent. Such rateless codes can only control the total number of bits transmitted, i.e. the code-rate, in order to cater for the variations of the channel conditions encountered. In [141], the authors studied the degree distribution of a rateless code, analysed the optimum distribution across a diverse range of channel SNRs and demonstrated that there are substantial differences between these distributions. Consequently, it was argued that rateless codes having a fixed degree distribution are sub-optimal in the sense that they cannot realize codes that operate near to capacity at all possible rates. However, in the specific scenario we are considering here, the rateless encoder is armed with side information. More explicitly, we feed back the channel SNRs and therefore the transmitter becomes capable of calculating the specific degree distribution that results in a performance, which is arbitrarily close to capacity in a near-real time online manner. Moreover, the channel SNR typically varies slower than the CIRs, which does not require a frequent updating.

For every information bit sequence to be encoded, the CSI received via the feedback channel is exploited by what we refer to as the Degree Distribution Selector (DSS)[1] of Fig. 3.15 in order to calculate the required coding rate r_c as well as the corresponding irregular degree (or check node) distribution $\delta(x)$.

[1]We will be referring to the degree distribution selector located at the transmitter by DDS_T.

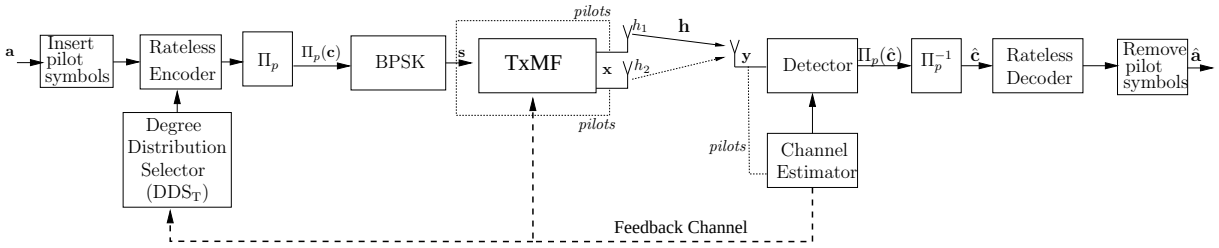

Figure 3.15: The system model of a TxMF aided closed-loop MISO system having two transmit antennas and a single receive antenna, BPSK modulation as well as pilot symbol assisted rateless codes are employed.

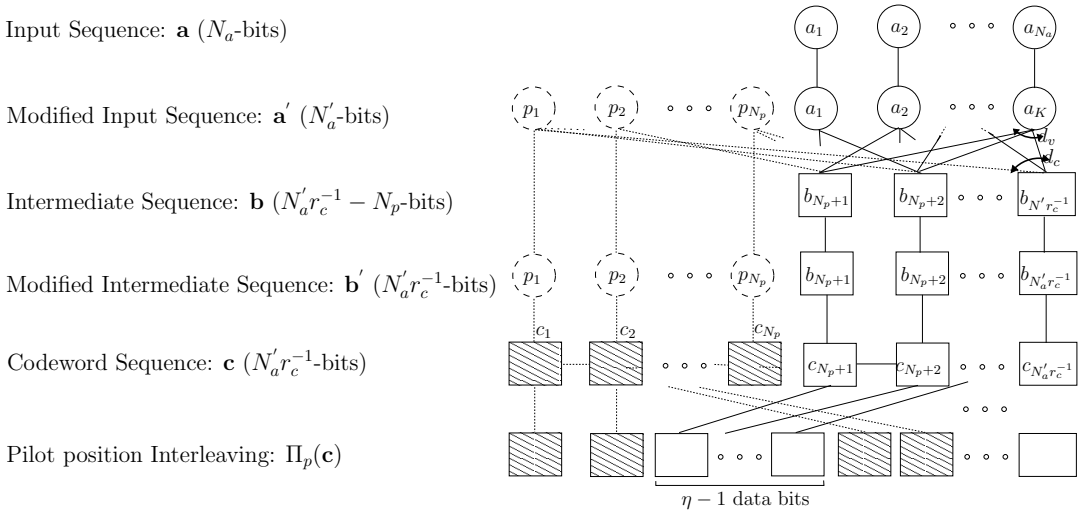

Figure 3.16: The rateless encoder.

The latter can be conveniently represented by means of a polynomial distribution defined by:

$$\delta(x) \quad := \quad \sum_{\forall d_c \in \mathbf{d}} \delta_{d_c} x^{d_c - 1} = \delta_1 + \delta_2 x + \ldots + \delta_{d_c} x^{d_c - 1} + \ldots + \delta_{D_c} x^{D_c - 1}, \tag{3.11}$$

where the positive coefficients δ_{d_c}, $d_c \in \mathbf{d}$ denote the particular fraction of intermediate bits (or check nodes) of degree d_c and $D_c = \max(\mathbf{d})$ is the maximal check (left) degree. The vector $\mathbf{d}$ contains the range of (check) degree values of the degree distribution. In contrast to [141], there is now two different categories of degree-one bits and as a result, the fraction δ_1 of (3.11) can be rewritten as $\delta_1 = \delta_1^p + \delta_1^{\overline{p}}$, where δ_1^p and $\delta_1^{\overline{p}}$ denote the fraction of degree-one nodes corresponding to pilot bits and to information bits, respectively.

The actual design of the degree distributions $\delta(x)$ and $v(x)$ is optimised with the aid of so-called Extrinsic Information Transfer (EXIT) charts [142], which allow us to investigate the convergence properties of iterative decoding schemes without performing bit-by-bit decoding using Monte-Carlo simulations. The details of this optimisation algorithm technique may be found in [105].

3.4.2.2 Pilot Symbol Assisted Rateless Encoder

The rateless encoder of Fig. 3.15 maps a N_a-bit (input) information sequence represented by $\mathbf{a} = [a_1, a_2, \ldots, a_{N_a}]$ into a $(N_a' r_c^{-1})$-bit output sequence $\mathbf{c}$ by performing the steps succinctly described below:

1. *(Modified input bit sequence)* Attach a predetermined pilot-bit sequence $\mathbf{p} = \left[p_1, p_2, \ldots, p_{N_p}\right]$, to the beginning of the N_a-bit input stream $\mathbf{a}$, so that the modified N_a'-bit input sequence becomes equal to $\mathbf{a}' = [\mathbf{p}\ \mathbf{a}]$[2];

2. *(Degree selection)* Randomly choose a degree d_c from a degree distribution $\delta(x) - \delta_1^p$ calculated by the degree distribution selector based upon the received CSI;

3. *(Input bit/s selection)* Randomly choose the previously selected d_c number of bits from $\mathbf{a}'$ having the least number of connections (selections) up to the current transmission instant;

[2] In our case, we have employed a sequence of ones.

4. *(Intermediate bit calculation)* Calculate the value of the intermediate (check) bit $b_i \in \mathbf{b}$ by combining the d_c input bits selected during the previous step using modulo-2 addition. Repeat the last three steps to all the $N_a^{'}$ bits of $\mathbf{a}'$;

5. *(Modified intermediate bit sequence)* Attach again the same pilot bit sequence $\mathbf{p}$ as in the initial step to the beginning of the intermediate bit sequence $\mathbf{b}$ generated in the previous step in order to create $\mathbf{b}' = [\mathbf{p}\ \mathbf{b}]$;

6. *(Codeword bit calculation)* Determine the value of the encoded bit $c_i \in \mathbf{c}$, $i = 1, \ldots, N_a^{'} r_c^{-1}$ by calculating the values of $c_1 = b_1^{'}$ and of $c_i = b_i^{'} \oplus b_{n-1}^{'}$ for $i = 2, \ldots, N_a^{'} r_c^{-1}$, where $b_i^{'} \in \mathbf{b}^{'}$ and $\oplus$ represents the modulo-2 addition operation. The pilot bits in $\mathbf{c}$ correspond to the bits $c_i \in \mathbf{c}$ with $i = 1, \ldots, N_p$.

For clarity, we have also provided a pictorial representation of this rateless encoding process in Fig. 3.16. Compared to the encoding process of a conventional LT code described in Section 3.4.1, our PSAR encoder has two major differences:

1. The pilot sequence p_i is concatenated with the data sequence, and they jointly constitute the rateless check nodes. Moreover, the pilot symbols are constrained to be a specific fraction of the degree-one nodes. Hence, the pilot symbols arrived at after encoding are pre-defined and are known by both the transmitter and the receiver.

2. The employment of a memory-one trellis code was implied in the last step, namely in "Codeword bit calculation". This is because rateless codes were first proposed for transmission over channels imposing symbol erasure (such as the wired Internet). Therefore using rateless codes alone for transmission over noisy wireless channels results in a high error floor [143]. Hence, it is necessary to combine rateless codes with classic Forward Error Correction (FEC) schemes [143] for transmission over noisy wireless channels.

Moreover, the fraction of pilot bits $\delta_1^p = \frac{N_p}{N_c}$ is determined by the channels' Doppler frequency f_{dm}. More explicitly, the channels associated with a high Doppler frequency require a higher value of δ_1^p, since their rapid fluctuation requires frequently updated channel estimates. Otherwise, the fraction of pilot bits required may be quite low for slowly varying channels.

It also follows that the proposed PSAR codes can realize any code rate $r_c = \frac{N_p + N_a}{N_c}$. This implies that whilst other rateless codes such as LT codes [144] are capable of generating codes having an arbitrary rate, PSAR codes can only generate codes having rates that are higher than the fraction of pilots δ_1^p in the code, since we have $r_c = \frac{N_p + N_a}{N_c} > \delta_1^p = \frac{N_p}{N_c}$. At first glance this might appear to be a limitation, however we note that δ_1^p is selected according to the highest expected fading rate, and hence for slow-fading channels PSAR codes can practically realize codes having any rate. Moreover, it is more power-efficient for the transmitter to opt for no transmission when the channel's SNR is very low, instead of transmitting at a very low code-rate.[3]

For clarify, the fraction δ_1^p of pilots is equivalent to the pilot overhead η_p we discussed in Section 3.2. Moreover, we have used N_p in Section 3.2 to represents the number of pilot symbols employed for each

[3]We also point out that this is not the first proposed rateless code with a bounded realizable rate. For instance, Raptor codes [145] cannot realize rates higher than the rate of the outer Low-Density Parity-Check (LDPC) code component of the Raptor code.

transmit antenna during the channel's coherence time. By contrast, the notation N_p used in this section represents a slightly different meaning. More explicitly, it represents the total number of pilot symbols required for assisting a total of N_a data symbols' transmission over a number of coherence intervals.

3.4.2.3 Pilot-Bit Interleaving and Pilot Symbol Transmission

As shown in Figure 3.16, the codeword $\mathbf{c}$ is then interleaved by the pilot position interleaver Π_p, which will position a pair of pilots every $(\eta - 1)$ data bits, where η denotes the pilot spacing. This process represents the effective sampling of the channel's complex-valued envelope at a rate that is higher than the Nyquist rate and thus allowing the receiver to extract the channel attenuation as well as phase rotation estimates for each bit. The data bits are separated by means of a pair of pilot bits (instead of a single pilot), since the channels between the two transmit and a single receive antennas have to be estimated. The interleaved codeword $\Pi_p(\mathbf{c})$ is then BPSK modulated. Then the data symbols are pre-processed by the TxMF represented as $\boldsymbol{x} = \boldsymbol{q}s$, where $\boldsymbol{q}$ is the pre-processing vector obtained from feedback channel. By contrast, the two BPSK modulated pilot symbols will be directly transmitted by the first and second transmit antenna separately in a time-orthogonal manner without TxMF preprocessing, which results the same frame structure as shown in Fig. 3.6.

3.4.2.4 Decoder of Pilot Symbol Assisted Rateless Codes

We denote the pilot bits received on the first and second time-slot by y_1, y_2, respectively. The two pilots bits, periodically occurring every $(\eta - 1)$ data bits, are then passed to the channel estimator (please refer to Figures 3.15), used for generating the corresponding MISO channel vector $\widehat{\mathbf{h}}$ having elements of $\widehat{h}_1$, $\widehat{h}_2$. The channel estimates are then up-sampled and interpolated by means of a low-pass interpolator. Armed with this channel estimate, the received signal is first detected, and then de-interleaved using the pilot position interleaver Π_p described in Section 3.4.2.3, and then passed to the rateless decoder, which estimates the original information bit sequence, i.e. $\widehat{a}$.[4]

The rateless decoder's computational complexity is reduced for the following two resons. Firstly, the number of degree one nodes is increased by interspersing the pilot symbols at the encoding stage. More importantly, the value of the pilot symbols are known inadvance, which produces high-value LLRs in the decoding process. Consequently, the tunnel between the two decoder's EXIT curves is widened hence the converge of the iterative process is accelerated.

3.4.3 Simulation Results

Figures 3.17 and 3.18 illustrate our comparison of the achievable throughput performance as well as the rateless decoder's computational complexity for both the proposed PSAR code-aided close-loop MISO system using TxMF as shown in Fig. 3.15 and for a benchmarker. The benchmarker is the same system, but instead of having a PSAR code, we use a rateless code dispensing with pilots (i.e. we set $\delta_1^p = 0$ at the encoding stage), but then insert the required number of pilots at the modulation stage. In this sense,

[4]It is also implicitly assumed that there is another subsidiary DDS located at the receiver, namely DDS_R (not shown in the figures), that calculates the distributions $\delta(x)$ and $\upsilon(x)$ based on the estimated CSIR and then passes these distributions to the rateless decoder to be described in Section 3.4.1.

we are comparing pilot symbol assisted (rateless) coding with that of pilot symbol assisted modulation in an attempt to verify which of the two techniques offers a better performance (in terms of achievable throughput as well as complexity) for the same amount of pilot overhead.

In order to make a fair comparison, the number of information bits for both scenarios, N_a, was set to 10000 bits and the maximum number of decoder iterations, $I_{\max}$ was fixed to 200 iterations. The normalised Doppler frequency is set to 0.02. The fraction of pilot bits δ_1^p was set to 0.1 for the PSAR code, whilst 10% pilots were inserted at the modulation stage for the benchmarker system. The rateless decoder's computational complexity for both systems was evaluated in terms of the number of message-passing updates per decoded bit, given by $I_{\text{avg}}|E|/N_a$, where I_{avg} represents the average number of iterations required for finding a legitimate codeword at a particular channel SNR value and $|E|$ represents the number of edges in the corresponding Tanner graph.

It can be observed from Figure 3.17 that there is no difference in the throughput performance of the two systems. On the other hand, the proposed PSAR code-aided system offers a considerable reduction in the rateless decoder's computational complexity, as shown in Figure 3.18. It was found that the complexity reduction in this specific scenario is (on average) more than 30%.

Table 3.1: Performance Summary

System Parameter			Comparison Schemes	Pilot-overhead	Throughput at SNR=10dB	Complexity at SNR=10dB
Number of antennas (N_{Tx}, N_{Rx})	(5,1)		Conventional pilot signalling in Fig. 3.6	50%	1.4 (bit/symbol)	—
Normalised Doppler frequency ($f_{dm-norm}$)	0.1					
Number of pilots (N_p)	1		Pilot overhead reduction in Fig. 3.10	20%	2.4 (bit/symbol)	—
Number of feedback bits (b)	1					
Number of antennas (N_{Tx}, N_{Rx})	(2,1)		Conventional PSAM in Figs. 3.6 and 3.10	10%	0.9 (bit/symbol)	550 (message updates/bit)
Normalised Doppler frequency ($f_{dm-norm}$)	0.002					
Modulation (M)	1					
Input frame length (N_a)	10^4		Proposed PSAR shown in Fig. 3.15	10%	0.9 (bit/symbol)	400 (message updates/bit)
Number of Iteration (I_{max})	200					
STBC type	Alamouti					

3.5 Chapter Summary

In this chapter, we have studied the TxMF aided closed-loop MISO system of Fig. 3.1. We have first compared the achievable ergodic channel capacity using various quantisers in Section 3.1, then we have derived the lower ergodic channel capacity bound when considering the effects of channel estimation errors, transmit preprocessing vector quantization errors, the effective CSI signalling overhead caused by pilot symbols and that imposed by the channel information feedback bits in Section 3.2. Our analysis demonstrates that the pilot symbols required for channel estimation result in a significant throughput loss for rapidly fluctuating fading channels, especially when having a moderate high number of transmit antennas. Based on this fact, the novel pilot reduction signalling scheme for rapidly fading channel has been proposed in Section 3.3, which replaces the consecutive transmission of pilots by their simultaneous transmission, which substantially improves the achievable throughput for systems having a moderate number of transmit antennas, despite encountering rapidly fluctuating channels. Moreover, a novel pilot symbol assisted rateless code scheme is proposed in Section 3.4, where a predetermined fraction of binary pilot symbols is interspersed with the channel-coded bits at the channel coding stage, instead of multiplexing the pilots with the data symbols at the modulation stage, as in classic PSAM. The PSAR code-aided transmit preprocessing scheme succeeds in gleaning more beneficial knowledge from the inserted pilots, because the pilot bits are not only useful for estimating the channel at the receiver, but they are also beneficial in terms of significantly reducing the computational complexity of the rateless channel decoder. Our results suggested that more than a 30% reduction in the decoder's computational complexity can be attained by the proposed system, when compared to a corresponding benchmarker scheme having the same pilot overhead but using the PSAM technique. The results shown in this chapter characterized typical systems having the parameters summarised in first two columns of Table 3.1. The corresponding simulation results are also summarised in Table 3.1 and are categorised into two groups of comparisons, which in order to demonstrate the advantages of our proposed schemes1.

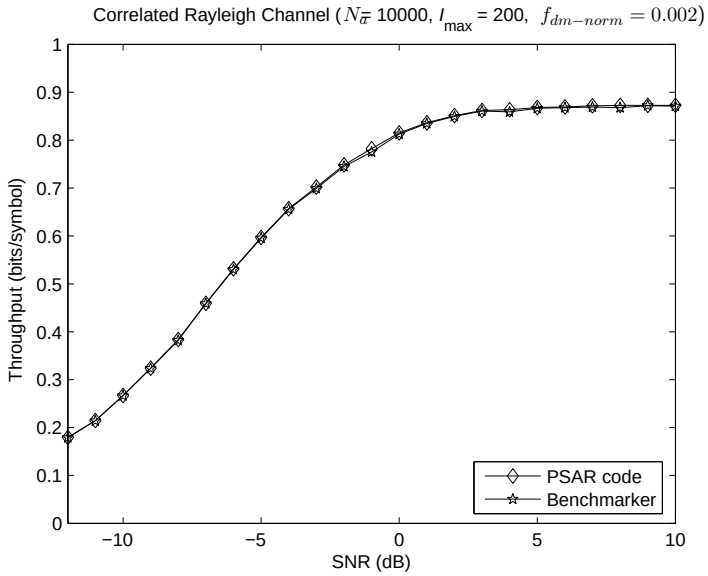

Figure 3.17: A comparison of the achievable average throughput performance (measured in bits/symbol) by the PSAR code and the benchmarker scenario, versus the SNR (in dB), assuming transmission over an Rayleigh channel using BPSK modulation. The benchmarker scenario consists of a rateless code, which is not aided with pilot symbols (i.e. set δ_1^p = 0), and then followed by PSAM with a 10% pilot overhead. The number of information bits for both scenarios, N_a, was set to 10000 bits and the maximum number of decoder iterations, $I_{\max}$ was fixed to 200 iterations. The normalised Doppler frequency is set to $f_{dm-norm} = 0.002$ and the fraction of pilot bits for the PSAR code, δ_1^p, was set to 0.1.

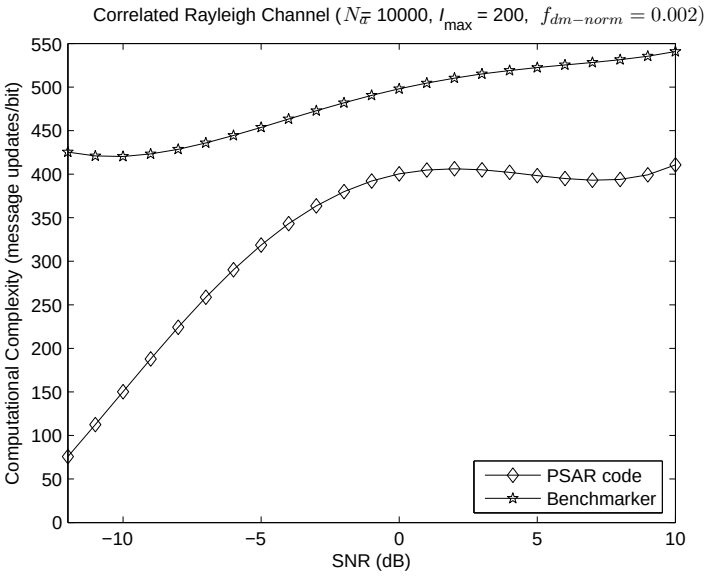

Figure 3.18: A comparison of the rateless decoder's computational complexity (measured in message updates/bit) by the PSAR code and the benchmarker scenario, versus the SNR (in dB), assuming transmission over an Rayleigh channel using BPSK modulation. The benchmarker scenario consists of a rateless code, which is not aided with pilot symbols (i.e. set δ_1^p = 0), and then followed by PSAM with a 10% pilot overhead. The number of information bits for both scenarios, N_a, was set to 10000 bits and the maximum number of decoder iterations, $I_{\max}$ was fixed to 200 iterations. The normalised Doppler frequency is set to $f_{dm-norm} = 0.002$ and the fraction of pilot bits for the PSAR code, δ_1^p, was set to 0.1. It can be verified, that PSAR codes reduces the complexity by more than 30%, when compared with the corresponding benchmarker scenario.

Chapter 4

Transmit Eigen-Beamforming Aided Closed-loop Single-user MIMO System

In this chapter, another single-user closed-loop system, namely the Transmit Eigen-beamforming (TxEBF) aided closed-loop single-user MIMO system will be investigated. The TxEBF algorithm will not be repeated in this chapter since it has been detailed in Section 2.2.1.2. Throughout this chapter, the performance metrics described in Chapter 1 - namely the achievable Continuous-input Continuous-output Memoryless Channel (CCMC) ergodic capacity and the Discrete-input Continuous-output Memoryless Channel (DCMC) ergodic capacity, as well as the BER performance - are employed in order to evaluate the proposed algorithms.

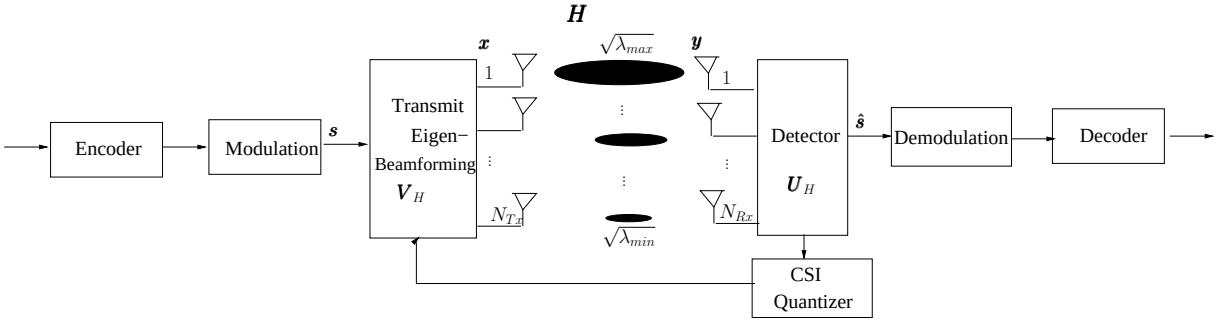

Figure 4.1: System model of a TxEBF aided closed-loop single-user MIMO system.

The novel contributions of this chapter are:

1. A novel Linear Dispersion Code (LDC) aided TxEBF scheme is proposed, which is capable of achieving the maximum attainable diversity gain and the DCMC capacity for an arbitrary number of transmit and receive antennas. Moreover, the proposed scheme is capable of adapting its throughput according to the prevalent SNR.

2. As an application example, a novel TxEBF aided video transmission scheme is proposed, where the encoded video source bits are transmitted through different eigen-beams according to their error sensitivity, so as to improve the decoded video quality at the receiver by providing unequal error protection.

This chapter is organised as follows. The achievable CCMC ergodic capacity using quantized CSI is investigated in Section 4.1, where the different quantisers described in Section 2.3 are compared. Then, a novel LDC aided TxEBF scheme is proposed in Section 4.2, and a TxEBF aided video transmission scheme is detailed in Section 4.3. Finally, the chapter is summarised in Section 4.4.

4.1 Achievable Ergodic Capacity Analysis

Relying to Section 3.1, where the achievable ergodic capacity of a TxMF aided closed-loop single-user MISO system was analysed, the achievable ergodic capacity of a TxEBF aided closed-loop single-user MIMO system is detailed in this section. More explicitly, two different scenarios, namely the CCMC capacity achieved with the aid of perfect CSIR/CSIT, as well as the CCMC capacity associated with perfect CSIR in combination with quantized CSIT are discussed in this section.

4.1.1 The CCMC Capacity with Perfect CSIR/CSIT

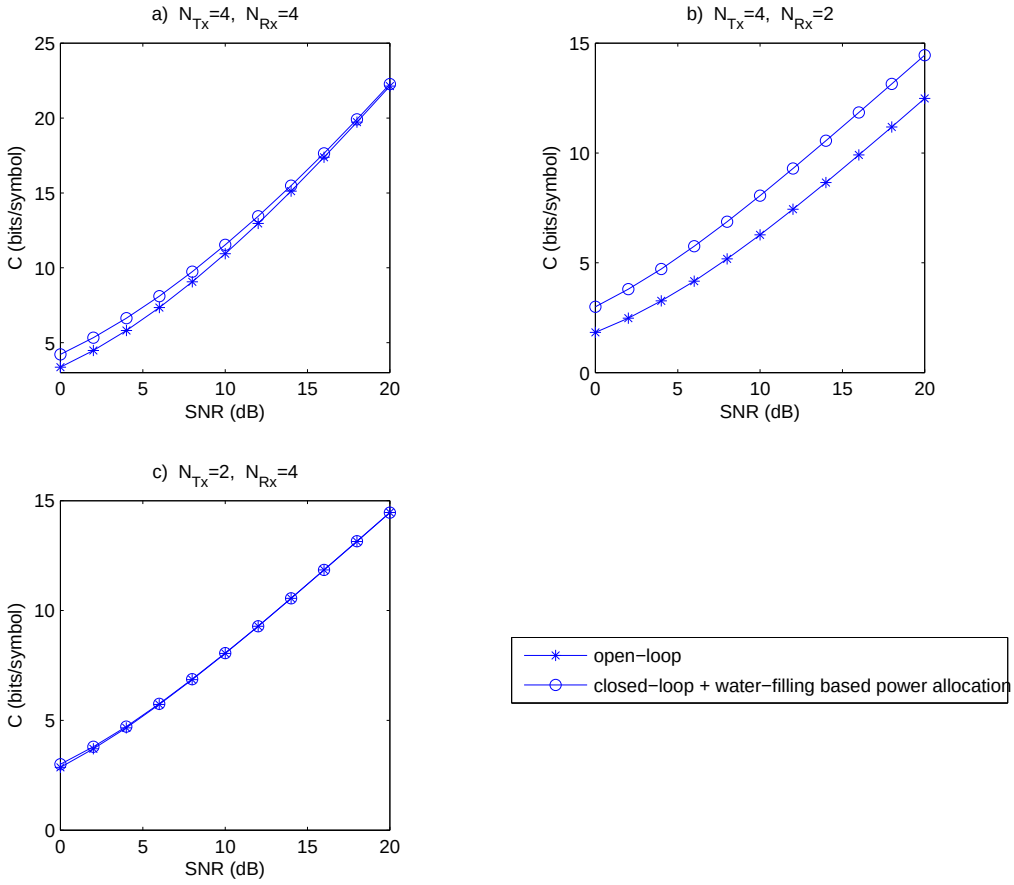

Figure 4.2: Ergodic channel capacity versus SNR for i.i.d Rayleigh fading channels when we have a) $N_{Tx} = 4,\ N_{Rx} = 4$; b) $N_{Tx} = 4,\ N_{Rx} = 2$ and c) $N_{Tx} = 2,\ N_{Rx} = 4$; and assuming perfect CSIR and CSIT calculated from Equations (4.1) and (4.2).

Assuming that perfect CSI is available both at the receiver and transmitter side, the ergodic CCMC capacities of a TxEBF aided closed-loop MIMO system having N_{Tx} transmit and N_{Rx} receive antennas

is formulated as [52]

$$C_{closed} = E_{\boldsymbol{H}} \log \det \left(\boldsymbol{I}_{N_{Rx}} + \frac{\boldsymbol{H}\boldsymbol{R}_x\boldsymbol{H}^H}{N_0} \right), \tag{4.1}$$

where the matrix $\boldsymbol{R}_x$ represents the covariance matrix of the transmitted signal $\boldsymbol{x}$ using transmit eigen-beamforming combined with the water-filling-based power allocation regime described in Section 2.2.1.2. The CCMC capacity of the corresponding open-loop system is formulated as [52]

$$C_{open} = E_{\boldsymbol{H}} \log \det \left(\boldsymbol{I}_{N_{Rx}} + \frac{\boldsymbol{H}^H\boldsymbol{H}}{N_0 N_{Tx}} \right), \tag{4.2}$$

where the covariance matrix $\boldsymbol{R}_x$ is equal to $\frac{1}{N_{Tx}}\boldsymbol{I}_{N_{Tx}}$. Based on these two equations, the CCMC capacity of three MIMO systems communicating over spatially independent channels and associated with a) $N_{Tx} = 4,\ N_{Rx} = 4$; b) $N_{Tx} = 4,\ N_{Rx} = 2$ and c) $N_{Tx} = 2,\ N_{Rx} = 4$ antenna configurations, respectively, are shown in Fig. 4.2. It is demonstrated in Fig. 4.2 that the closed-loop TxEBF aided system provides a substantially higher capacity than the corresponding open-loop system, when we have $N_{Tx} > N_{Rx}$, as for example in the scenario of Fig. 4.2b.

However, the benefits of the TxEBF scheme completely erode at high SNRs, when having the same number of transmit and receive antennas, such as in the scenario of $N_{Tx} = N_{Rx} = 4$ seen in Fig. 4.2a, or when having more receive antennas than transmit antennas, such as in the scenario of Fig. 4.2c. This is because the water-filling-based power allocation scheme described in Section 2.2.1.2 tends to allocate the power equally to all eigen-beams at high SNRs, which results in a covariance matrix of

$$\boldsymbol{R}_x = \begin{bmatrix} \frac{1}{\min(N_{Tx},N_{Rx})}\boldsymbol{I}_{\min(N_{Tx},N_{Rx})} & \boldsymbol{0}_{N_{Tx}-\min(N_{Tx},N_{Rx})} \\ \boldsymbol{0}_{N_{Tx}-\min(N_{Tx},N_{Rx})} & \boldsymbol{0}_{N_{Tx}-\min(N_{Tx},N_{Rx})} \end{bmatrix}. \tag{4.3}$$

When we have $N_{Tx} \leq N_{Rx}$, the covariance matrix $\boldsymbol{R}_x$ converges to $\boldsymbol{R}_x = \frac{1}{N_{Tx}}\boldsymbol{I}_{N_{Tx}}$. Hence, the ergodic CCMC capacity of the TxEBF aided closed-loop MIMO system becomes equivalent to that of its corresponding open-loop system according to Equations (4.1) and (4.2).

By contrast, at low SNRs, the water-filling based power allocation algorithm allocates more power to the specific eigen-beams having higher eigen-values, which results in a covariance matrix $\boldsymbol{R}_x$ approaching $\boldsymbol{R}_x = \begin{bmatrix} 1 & \boldsymbol{0}_{N_{Tx}-1} \\ \boldsymbol{0}_{N_{Tx}-1} & \boldsymbol{0}_{N_{Tx}-1} \end{bmatrix}$. Hence, it is beneficial to employ the closed-loop scheme at low SNRs for any antenna configuration, as demonstrated in Fig. 4.2. To summarise, the TxEBF aided closed-loop scheme is beneficial for MIMO systems having arbitrary antenna configurations at low SNRs by improving the achievable ergodic CCMC capacity. By contrast, it is only worth employing TxEBF for MIMO system having more transmit antennas than receive antennas, when the SNR is sufficiently high.

4.1.2 CCMC Capacity with Perfect CSIR and Quantized CSIT

The feedback information required by a TxEBF aided closed-loop single-user MIMO system includes the unitary matrix $\boldsymbol{V}_H$ of Equation (2.25) and the power allocation vector $[E_1, \ldots, E_{N_E}]$, as we have demonstrated in Section 2.2.1.2 and summarised in Table 2.3. In this section, we will discuss the quantiser design of the power allocation vector and of the unitary matrix $\boldsymbol{V}_H$. Moreover, we will employ a TxEBF aided closed-loop MIMO system communicating over i.i.d. Rayleigh fading channels having four transmit antennas and two receive antennas as an example, in order to evaluate the achievable ergodic capacity using different quantisers.

Power Allocation Vector Quantization

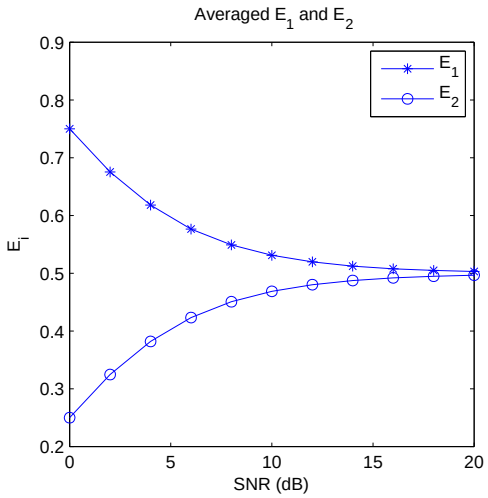

$$E_{\boldsymbol{H}}[E_1, E_2] = \text{Codebook} = \begin{bmatrix} 0.75 & 0.25 \\ 0.68 & 0.32 \\ 0.62 & 0.38 \\ 0.58 & 0.42 \\ 0.55 & 0.45 \\ 0.53 & 0.47 \\ 0.52 & 0.48 \\ 0.50 & 0.50 \\ \vdots & \vdots \\ 0.50 & 0.50 \end{bmatrix}$$

Figure 4.3: The statistical average of the power allocation vector $E_{\boldsymbol{H}}\,[E_1\ E_2]$ versus the SNR for a TxEBF aided closed-loop MIMO system having four transmit antennas, two receive antennas and communicating over an i.i.d Rayleigh fading channel.

First of all, we consider the characteristics of the power allocation vector $[E_1, \ldots, E_{N_E}]$. This vector consists of N_E $(1 \leq N_E \leq \min(N_{Tx}, N_{Rx}))$ number of non-zero real values E_i $(E_i \in [0,\ 1])$. Moreover, we have $\sum_i^{N_E} E_i = E_{Tx}$, and $E_1 \geq E_2 \geq \ldots \geq E_{N_E}$, since the corresponding eigen values have $\lambda_1 \geq \lambda_2 \geq \ldots \geq \lambda_{N_E}$. Without any loss of generality, we assumed the transmit power is unity, hence we have $\sum_i^{N_E} E_i = 1$. Furthermore, this power allocation vector is a function of the SNR, since the noise variance is an input factor of the water-filling based power allocation algorithm described in Section 2.2.1.2. For example, the statistical average of the power allocation vector $E_{\boldsymbol{H}}[E_i]$ of the MIMO system using $N_{Tx} = 4, N_{Rx} = 2$ is portrayed in Fig. 4.3, which varies with the SNR. Moreover, the histograms of the power allocation value E_1 recorded for SNR values of 0dB and 10dB are portrayed in Fig. 4.4a) and b), respectively. It is evident that at low SNRs most of the transmit power is typically allocated to the strongest eigen-beam. By contrast, the transmit power is more or less equally shared by all activated eigen-beams at high SNRs.

A codebook designed for the vector quantization of the power values may be constructed using the statistical average of the power vectors given by $E_{\boldsymbol{H}}[(E_1\ E_2)]$ and shown in Fig. 4.3. Each row-vector in the matrix $E_{\boldsymbol{H}}[(E_1\ E_2)]$ represents the average power at a fixed SNR value. For example, the first row vector $[0.75,\ 0.25]$ is the average power vector at 0dB. Using such a codebook, the statistical average power allocation vector is employed to replace the instantaneous power allocation vectors. For example, the power allocation vector $[E_1\ E_2] = [0.75\ 0.25]$ is used for all CIRs, when the SNR varies between -1dB to 1dB. Assuming that the activated eigen-vectors in the right-hand-side matrix $\boldsymbol{V}_H$ of Equation (2.25) are perfectly known, the achievable ergodic CCMC capacity of the $N_{Tx} = 4, N_{Rx} = 2$ TxEBF aided closed-loop system using the first eight rows of the matrix $E_{\boldsymbol{H}}[(E_1\ E_2)]$ as a codebook is illustrated in

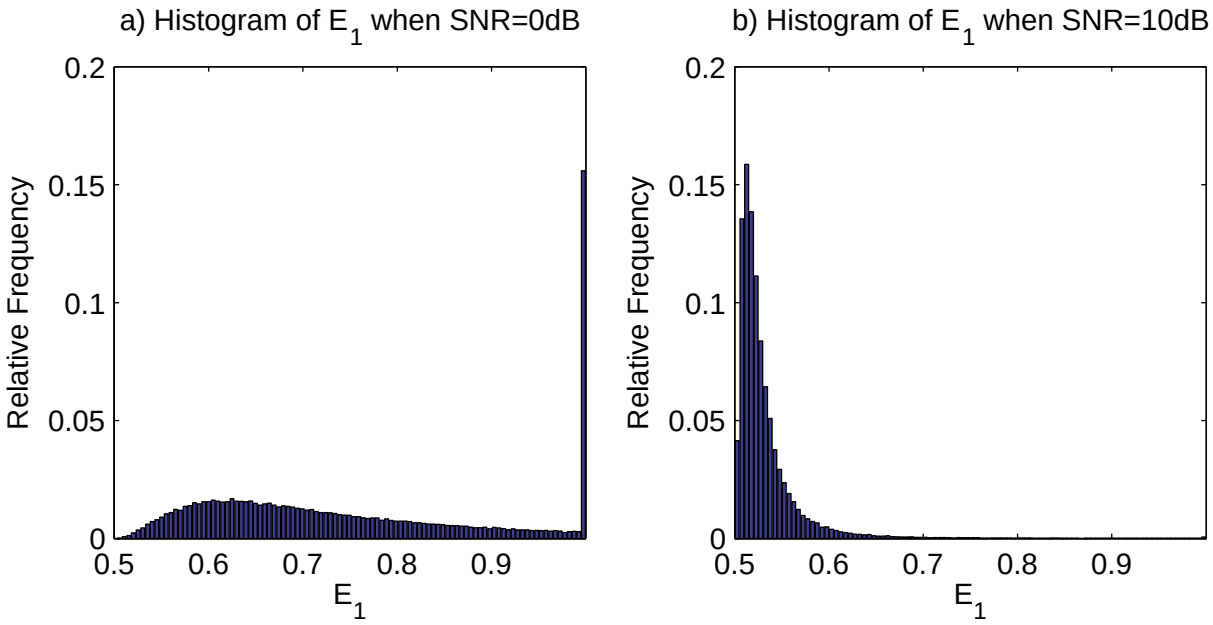

Figure 4.4: Histogram of the power allocation value E_1 of a TxEBF aided closed-loop MIMO system having four transmit antennas, two receive antennas and communicating over an i.i.d Rayleigh fading channel, when the SNR is a) 0dB and b) 10dB, respectively.

Fig. 4.5. It is evident in Fig. 4.5 that the performance degradation imposed by the vector quantization of the power allocation is almost negligible compared to the closed-loop ergodic CCMC capacity upper bound using perfect CSIR/CSIT. In fact, such a codebook consisting of the statistical average power allocation vectors becomes independent of the instantaneous CIRs, it is only related to the SNR value, or to the noise variance N_0. Since the value of N_0 varies significantly slower than the fading CIR taps, the update frequency of the power allocation vector becomes much lower, which results in a low feedback overhead. Moreover, the index of the power allocation vector also implicitly indicates the noise variance N_0. Hence, the family of adaptive modulation and coding schemes, such as the rateless code described in Section 3.4 may invoke this regime in order to accommodate the time-variant SNR fluctuations.

There are a number of methods that may be used to further reduce the feedback overhead. For example, if the SNRs only vary from 0-dB to 8-dB rather than to 20-dB, it is sufficient to employ a reduced-size codebook. As another reduced-overhead feedback technique, it is effective to employ a differential quantiser if the SNRs vary smoothly. More explicitly, it is possible to use a single bit to indicate whether the SNR increased (feed back "1") or decreased (feed back "0"), and then to decode the power allocation vector correspondingly at the receiver. Furthermore, there are also a number of other methods capable of further increasing the accuracy of the quantized power allocation vector. For example, when the SNRs are almost constant, we may generate a codebook using the LGB algorithm detailed in Section 2.3.1 in order to feed back the instantaneous power allocation vectors. In this case, since the power allocation values E_i are correlated with each other (e.g.$\sum_i^{N_E} E_i = 1$), the vector quantiser - which quantises all components of the power allocation vector jointly - is expected to become more efficient than the scalar quantizer, which quantises the power allocation values E_i independently.

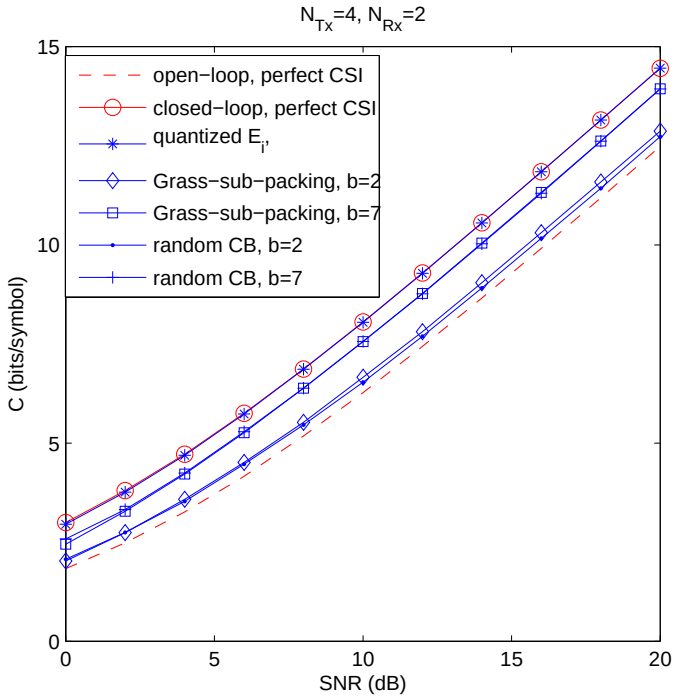

Figure 4.5: The achievable ergodic channel capacity of a closed-loop TxEBF aided system in conjunction with quantized CSIT versus SNR, when we have four transmit and two receive antennas, and using various quantisers. The upper-bound of the ergodic channel capacity received in conjunction with perfect CSIR and perfect CSIT are also plotted for comparison..

Activated Eigen-Beam-Vector Quantization

Having discussed the quantization of the power allocation vectors, the quantization of the activated eigen-vectors in the right-hand-side unitary matrix $\boldsymbol{V}_H$ of Equation (2.25) is discussed as follows. First of all, the eigen-vectors are complex-valued N_{Tx}-dimensional unitary vectors, and the number of activated eigen-vectors required for feedback is determined by the non-zero power allocation values N_E, which is a function of the SNR value. For example, recall from Fig. 4.3 that at low SNRs essentially only the strongest eigen-beam is activated. Hence only a single unitary vector in the matrix $\boldsymbol{V}_H$ has to be fed back, namely the one corresponding to the highest eigen-value. As a result, the Grassmannian line-packing quantizer consisting of unitary vectors using the chordal distance described in Section 2.3.3 becomes an appropriate quantiser. When there are several activated eigen-beams, the required feedback information is constituted by N_E unitary vectors in the matrix $\boldsymbol{V}_H$, which are orthogonal to each other. As a result, the Grassmannian subspace-packing quantiser minimizing the Fubini-Study distance [80] is one of the potential quantiser candidates, whose codewords are orthogonal unitary vectors, as detailed in Section 2.3.4. Alternatively, the random quantiser minimizing the Fubini-Study distance is applicable in this situation, whose codewords are also orthogonal unitary vectors as detailed in Section 2.3.4, especially when the Grassmannian subspace-packing based results are not available for some values of N_{Tx}, N_{Rx} or for an arbitrary codebook size $|\mathsf{Q}|$.

The achievable ergodic CCMC capacities of a TxEBF aided closed-loop system having $N_{Tx} = 4, N_{Rx} = 2$, and using either the Grassmannian subspace packing quantiser or the random quantiser

are compared in Fig. 4.5. The power allocation vectors are also quantized using a small codebook having eight entries, as demonstrated in Fig. 4.3. When a small codebook having $2^b = 4$ codewords is used, the performance of the system using the Grassmannian subspace-packing quantiser of Section 2.3.4 becomes slightly better than that of the random codebook. Nonetheless, they both achieve a higher CCMC capacity than that of the corresponding open-loop system. By contrast, when a sufficiently high number of quantization bits is employed, for example $b = 7$-bits, the achievable CCMC capacity using the aforementioned two quantisers becomes similar. This is consistent with the results shown in Fig. 2.13 of Section 2.3.4, where these two quantisers were compared in terms of their average quantization error quantified in terms of the Fubini-Study distance. It was also demonstrated in Fig. 2.13 that the Grassmannian subspace packing quantiser slightly outperforms the random codebook, when the codebook is small, albeit their performance becomes similar, when the codebook is sufficiently large. Based on these observations, we might conclude that using the random codebook is capable of closely approaching the achievable CCMC capacity.

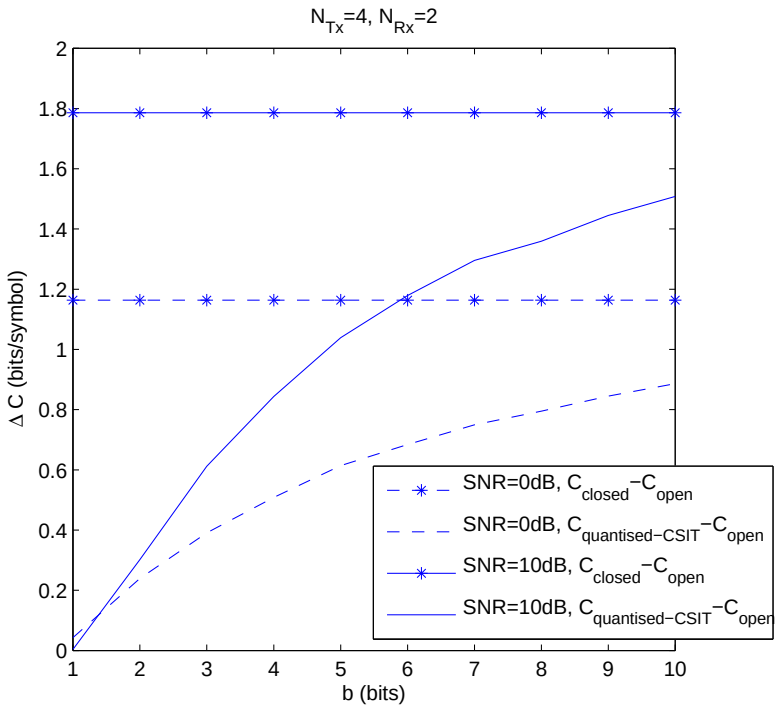

Figure 4.6: The achievable ergodic channel capacity gain $\Delta C = (C_{closed-\boldsymbol{H}_q} - C_{open})$ versus the number of feedback bits b, when we have $N_{Tx} = 4$, $N_{Rx} = 2$, $SNR = 0, 10$-dB, respectively. The upper-bound of the ergodic channel capacity gain defined as $(C_{closed} - C_{open})$ in conjunction with perfect CSIR and perfect CSIT are also plotted for comparison.

Similarly to Fig. 3.5 of Section 3.1.2, where the achievable ergodic channel capacity gain ΔC versus the number of feedback bits b of a TxMF aided closed-loop system was evaluated, Fig. 4.6 illustrates the achievable ergodic channel capacity gain ΔC versus b for a TxEBF aided closed-loop system, when we have $N_{Tx} = 4; N_{Rx} = 2$, $SNR = 0, 10 \sim$ dB, for transmission over an i.i.d Rayleigh fading channel. The achievable ergodic channel capacity gain ΔC is defined as the difference between $C_{closed-\boldsymbol{H}_q}$ and C_{open}, where the notation $C_{closed-\boldsymbol{H}_q}$ represents the achievable ergodic channel capacity in conjunction with the quantized CSIT $\boldsymbol{H}_q$, while C_{open} denotes the upper-bound of the open-loop channel capacity

assuming perfect CSIR. The upper-bound of the ergodic channel capacity gain defined as ($C_{closed} - C_{open}$) in conjunction with perfect CSIR and perfect CSIT is also plotted for comparison. Since the number of bits and the update frequency required for the eigen-vectors' feedback is higher than that required by the power allocation vectors, the number of bits b on the x-axis of Fig. 4.6 only represents the bits employed for feeding back the eigen-vectors using the random quantiser detailed in Section 2.3.4. This figure demonstrates that substantial ΔC gains are obtained upon increasing the number of feedback bits from $b = 1$ to $b = 5$ bits. About 50% of the achievable capacity gain is attained, when using a 5-bit feedback. Moreover, the attainable performance improvement gradually saturates, when the number of feedback bits increases from $b = 5$ to $b = 10$.

4.2 Linear Dispersion Coded Transmit Eigen-beamforming

The TxEBF essentially decomposes the MIMO channel into several parallel orthogonal sub-channels (or eigen-beams), and the quality of the resultant orthogonal subchannels may be very different from each other. In Section 4.1, we have discussed the achievable CCMC capacity, which assumes that the channel's input signal $\boldsymbol{x}$ are Gaussian distributed. When using practical modulation schemes, such as BPSK/QPSK/QAM, we may approach the CCMC capacity upon adaptively activating different modulation and coding schemes for each subchannel according to the subchannels' quality and the noise variance [73, 146].

Another scheme capable of approaching the CCMC capacity is constituted by the employment of "capacity-optimised" space-time coding combined with CSIT-dependent "beamforming" [147], as well as adaptive modulation and coding. This idea has been widely accepted. The research portrayed in [11, 77, 148] demonstrates that the combination of beamforming with Q/OSTBCs is capable of approaching the closed-loop system's capacity. The schematic of such a system is illustrated in Fig. 4.7. The control

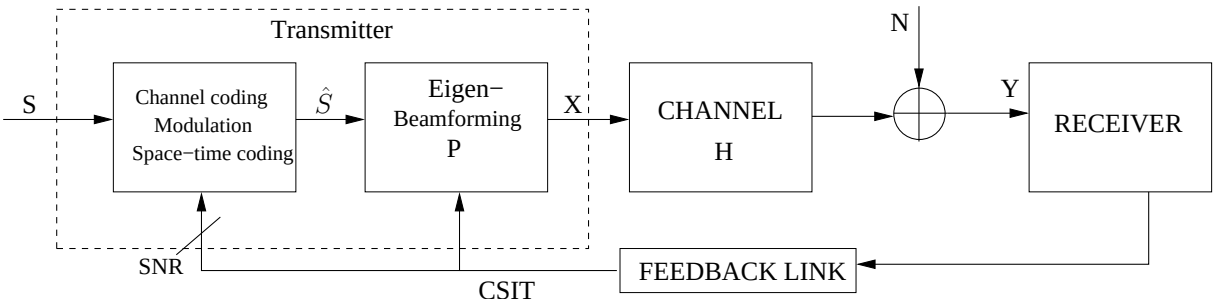

Figure 4.7: Transmitter schematic exploiting the CSIT

of the adaptive modulation and coding modes in the system's schematic shown in Fig. 4.7 is less complex compared to the scheme illustrated in [11, 77, 148]. Our novel contributions are:

1. A group of Linear Dispersion Codes (LDCs) is employed, which are capable of achieving a higher open-loop capacity compared to the Q/OSTBC in prior studies.

2. As a complement to prior ergodic capacity gain studies, our study characterise the closed-loop DCMC MIMO capacity gain in several different system configurations.

3. The Grassmannian line-packing quantizer is employed, which demonstrates that a modest feedback rate requiring a few bits is capable of substantially increasing the attainable capacity.

In fact, employing LDCs in a closed-loop system has been considered in [149–151] by constructing a new multi-mode LDC, which is capable of adapting to the CSIT, where the LDCs are designed off-line based on the channel statistics and stored in both the transmitter and receiver. Whenever the channel changes, a more appropriately LDC may be derived at the receiver and its index will be conveyed back to the transmitter through a feedback channel. Compared to this scheme, the advantage of our proposed scheme to be outlined in Section 4.2.2 is that its specific design ensures maintaining a good performance even when the channel varies too fast to be tracked or the feedback channel is of low quality by simply turning-off transmit eigen-beamforming. However, the overall performance comparison of these two methods require further investigations.

This section is organised as follows. A brief introduction of LDC is given in Section 4.2.1. Then, our system model is described in Section 4.2.2 with the achievable DCMC capacity analysis. Section 4.2.3 provides our simulation results and discussions.

4.2.1 Linear Dispersion Code

The concept of LDCs was first proposed by Hassibi and Hochwald [29], which then attracted substantial research attention [152, 153]. The LDC codeword $\boldsymbol{C}$ is generated as a linear combination of the so-called dispersion matrices and the weight of each LDC component is determined by the modulated symbols. This philosophy can be formulated as:

$$\bar{\boldsymbol{C}} = \sum_{i=1}^{N_s} \boldsymbol{A}_i s_i, \tag{4.4}$$

where $\boldsymbol{A}_i$ is the i-th $(N_{Tx} \times T)$-element complex-valued dispersion matrix and s_i is the i-th of the N_s input symbols to be transmitted. Introducing an operation $vec()$, which is defined as vertical stacking of the columns of an arbitrary matrix, Equation (4.4) can be written as

$$vec(\bar{\boldsymbol{C}}) = \boldsymbol{\chi}\boldsymbol{s}. \tag{4.5}$$

The matrix $\boldsymbol{\chi}$ uniquely and unambiguously characterises an LDC, hence it is referred to as the Dispersion Character Matrix (DCM) and is defined as

$$\boldsymbol{\chi} = [vec(\boldsymbol{A}_1) \quad vec(\boldsymbol{A}_2) \quad \ldots \quad vec(\boldsymbol{A}_{N_s})]. \tag{4.6}$$

Additionally, assuming that the transmit power at each transmission instant is $E_{Tx} = 1$, the DCM $\boldsymbol{\chi}$ should satisfy the following condition in order to maintain a constant power of T for each codeword's transmission,

$$\mathtt{tr}\left(\boldsymbol{\chi}\boldsymbol{\chi}^H\right) = T. \tag{4.7}$$

Apparently, Equation (4.7) can be satisfied if $\boldsymbol{\chi}$ is a unitary matrix. Usually, the design of the matrix $\boldsymbol{\chi}$ is carried out by random search over the set of unitary matrices optimising them according to one or several design criteria, for example, satisfying the full-rank criterion, maximising the determinant of the matrix or the capacity, etc. LDCs can be designed for an arbitrary number of N_{Tx} transmit and N_{Rx}

receiver antennas. The coding rate N_s/T can also be flexibly adjusted. An LDC is described in the form LDC($N_{Tx}N_{Rx}TN_s$)-("modulation-scheme") in this study. For example, the LDC(2221)-QPSK scheme represents an LDC having $N_{Tx} = 2$ transmit antennas, $N_{Rx} = 2$ receive antennas and transmitting $N_s = 1$ QPSK modulated symbol over $T = 2$ time-slot.

Compared to OSTCBs/QOSTBCs [14,46,154], the general LDC construction has the following properties:

1. LDCs are modulation scheme dependent, while OSTBCs and QOSTBCs are independent of the modulation scheme.

2. All the entries in the OSTBC and QOSTBC codewords represent a transformed version of a single modulated symbol in the vector $\boldsymbol{s}$. The Quasi/Orthogoal Space Time Block Codes (Q/OSTBCs) schemes are designed to achieve a certain diversity gain. By contrast, all the entries in the LDC codeword are constituted by a linear combination of all modulated symbols in the vector $\boldsymbol{s}$. We refer to this property as having Non-Separable Transmit Symbols (NSTS), which equips them with the potential of achieving the maximum attainable diversity while maintaining a high data-rate at the same time.

4.2.2 System Model and DCMC Capacity Analysis

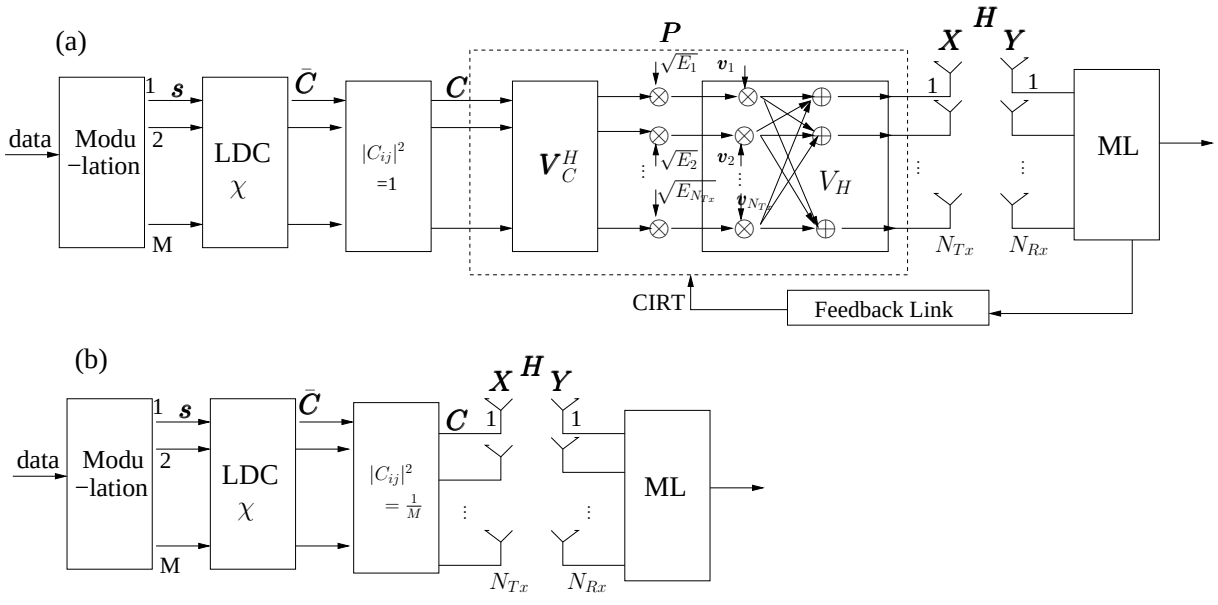

Figure 4.8: Single-user MIMO System Models: a) closed-loop, b) open-loop.

The system we investigated is still a single-user closed-loop MIMO system having N_{Tx} transmit and N_{Rx} receive antennas, as shown in Fig. 4.8 (a), which outlines the structure of Fig. 4.7 in more detail. The CIR is stored in an $(N_{Rx} \times N_{Tx})$-element matrix $\boldsymbol{H}$. Each element in $\boldsymbol{H}$ is an i.d.d. complex-valued Gaussian variable with zero mean and unity variance under the assumption that antennas are spaced sufficiently far apart. Moreover, the CIR is assumed to be constant during an LDC codeword duration of T. The N_s number of modulated symbols constituting an LDC symbol are stored in a vector $\boldsymbol{s}$, which are first passed through an LDC encoder in order to construct an LDC codeword $\boldsymbol{C}$ having a matrix size of

$(N_{Tx} \times T)$ and a unity power for each element. At each transmission instant, one column of the codeword $\boldsymbol{C}$ will be linearly transformed by the transmit eigen-beamforming matrix $\boldsymbol{P}$ and then transmitted. The total transmission power at every instant is normalised to unity $E_{Tx} = 1$ and controlled by the power allocation factor $\sqrt{E_i}$. At the receiver side, a Maximum-likehood (ML) detector is employed. The system's throughput can be easily adapted as a function of the channel quality by varying the modulation schemes or the number of LDC encoded symbols N_s.

The structure of the open-loop benchmark system used for comparison is shown in Fig. 4.8 (b). The transmission power has been equally allocated both over time and space. As a result, at each transmission instant, the total transmit power is unity, treating the combination of the precoder and the channel as the effective channel.

Let us now derive the closed-loop expression of the DCMC capacity of the closed-loop system shown in Fig. 4.8 a. In [155], the authors have provided a method of calculating the open-loop DCMC capacity for the system model of

$$\boldsymbol{y} = \boldsymbol{H}\boldsymbol{s} + \boldsymbol{n}, \tag{4.8}$$

where the $(N_{Rx} \times N_{Tx})$-element matrix $\boldsymbol{H}$ hosts the CIRs, $\mathbf{s}$ is a N_{Tx}-dimensional input vector using M-level modulation and $\boldsymbol{n}$ is a N_{Rx}-dimensional Gaussian noise vector with zero mean. Hence, there are $F = M^{N_{Tx}}$ possible combinations of $\boldsymbol{s}$. Each combination is denoted as $\boldsymbol{s}_f$, $(f = 1, \ldots, F)$. The DCMC capacity is then calculated as [155]:

$$C_{open-loop}^{DCMC} = \frac{1}{T} \max_{p(\boldsymbol{s}_1),\ldots,p(\boldsymbol{s}_F)} \sum_{f=1}^{F} \int_{-\infty}^{\infty} \cdots \int_{-\infty}^{\infty} p(\boldsymbol{y}|\boldsymbol{s}_f) p(\boldsymbol{s}_f) log_2 \left(\frac{p(\boldsymbol{y}|\boldsymbol{s}_f)}{\sum_{g=1}^{F} p(\boldsymbol{y}|\boldsymbol{s}_g) p(\boldsymbol{s}_g)} \right) d\boldsymbol{y} \; (bits/symbol). \tag{4.9}$$

By contrast, the LDC aided closed-loop transmit eigen-beamforming system studied in this contribution is modeled as:

$$\boldsymbol{Y} = \boldsymbol{H}\boldsymbol{P} f_n(\sum_{i=1}^{N_s} \boldsymbol{A}_i s_i) + \boldsymbol{N}, \tag{4.10}$$

where the received signal $\boldsymbol{Y}$ is hosted by an $(N_{Rx} \times T)$-element matrix, the $(N_{Rx} \times N_{Tx})$-element matrix $\boldsymbol{H}$ contains all the CIRs, $\boldsymbol{P}$ is a $(N_{Tx} \times N_{Tx})$-element matrix denoting the transmit beamformer of Fig. 4.8 (a) and the N_s number of modulated symbols are encoded as a $(N_{Tx} \times T)$-element LDC codeword $\bar{\boldsymbol{C}}$. The function $f_n(.)$ denotes the power normalisation function, which transforms the codeword $\bar{\boldsymbol{C}}$ unequal power allocated to its elements to a corresponding codeword $\boldsymbol{C}$ having unity-power elements and the same matrix size. Finally, the $(N_{Tx} \times T)$-element matrix $\boldsymbol{N}$ contains all N_{Rx}-element noise vectors in all T time slots.

Using the DCM matrix $\boldsymbol{\chi}$ and the $vec()$ operation, we have

$$\begin{aligned} \bar{\boldsymbol{H}} &= \boldsymbol{I}_T \otimes (\boldsymbol{H}\boldsymbol{P}), \\ \bar{\boldsymbol{y}} &= vec(\boldsymbol{Y}), \\ \bar{\boldsymbol{c}} &= vec(f_n(\boldsymbol{\chi}\boldsymbol{s})) \\ \bar{\boldsymbol{n}} &= vec(\boldsymbol{N}), \end{aligned} \tag{4.11}$$

where $\bar{\boldsymbol{H}}$ is the Kronecker product of $\boldsymbol{H}$ and an identity matrix $\boldsymbol{I}_T$, while $\bar{\boldsymbol{y}}$ is a $(N_{Rx}T \times 1)$-element vector representing the equivalent receivied signal vector, $\bar{\boldsymbol{c}}$ is a $(N_{Tx}T \times 1)$-element complex-valued vector representing the equivalent LDC encoded transmission signal vector and $\bar{\boldsymbol{n}}$ is a $(N_{Tx}T \times 1)$-element complex-valued vector representing the equivalent noise vector. Then, Equation (4.10) can be reformulated as:

$$\bar{\boldsymbol{y}} = \bar{\boldsymbol{H}}\bar{\boldsymbol{c}} + \bar{\boldsymbol{n}}. \tag{4.12}$$

Furthermore, the vector $\boldsymbol{s}$ has $F = M^{N_s}$ legitimate combinations, if M-level modulation and N_s number of modulated symbols are employed in a LDC. Consequently, the vector $\bar{\boldsymbol{c}}$ also has $F = M^{N_s}$ legitimate combinations, where again each combination is denoted as $\bar{\boldsymbol{c}}_f$, $(f = 1, \ldots, F)$.

It is clear that Equation (4.8) and Equation (4.12) have the same structure. As a result, upon substituting $\bar{\boldsymbol{c}}_f$ and $\bar{\boldsymbol{y}}$ into Equation (4.9), we arrive at the LDC-aided closed-loop system's DCMC capacity of:

$$C^{DCMC}_{closed-loop} = \frac{1}{T} max_{p(\bar{\boldsymbol{c}}_1),\ldots,p(\bar{\boldsymbol{c}}_F)} \sum_{f=1}^{F} \int_{-\infty}^{\infty} \cdots \int_{-\infty}^{\infty} p(\bar{\boldsymbol{y}}|\bar{\boldsymbol{c}}_f) \cdots$$
$$p(\bar{\boldsymbol{c}}_f) log_2 \left(\frac{p(\bar{\boldsymbol{y}}|\bar{\boldsymbol{c}}_f)}{\sum_{g=1}^{F} p(\bar{\boldsymbol{y}}|\bar{\boldsymbol{c}}_g) p(\bar{\boldsymbol{c}}_g)}\right) d\bar{\boldsymbol{y}} \; (bits/symbol). \tag{4.13}$$

4.2.3 Simulation Results and Discussion

Number of transmit antennas (N_{Tx})	2,3,4
Number of receive antennas (N_{Rx})	2,1
Number of time slots used per space-time block (T)	2,8
Number of symbols transmitted per space-time block (N_s)	1,2,3,4
Modulation Level (M)	2 (BPSK), 4 (QPSK)

Table 4.1: Simulation Parameters

Our simulation parameters are summarised in Table 4.1. The channels are assumed to be independent Rayleigh fading both in time as well as space. In the following simulations, four different transmit schemes are considered:

1. Scheme 1: Open-loop equal-power scheme as illustrated in Fig. 4.8 (b), where the total transmit power has been equally allocated over both time and space;

2. Scheme 2: Closed-loop eigen-beamforming scheme as illustrated in Fig. 4.8 (a), where waterfilling-based power allocation is employed, and perfect CSI is assumed to be known by both the transmitter and receiver;

3. Scheme 3: Closed-loop single-beam scheme, where the transmit power has been allocated to the highest-power eigen-beam with perfect CSI;

4. Scheme 4: Closed-loop single-beam scheme using quantized CSIT, where the transmit power has been allocated to the highest-power eigen-beam and the beamforming vector conveyed to the BS with the aid of the MTs' feedback using a Grassmannian line-packing quantizer.

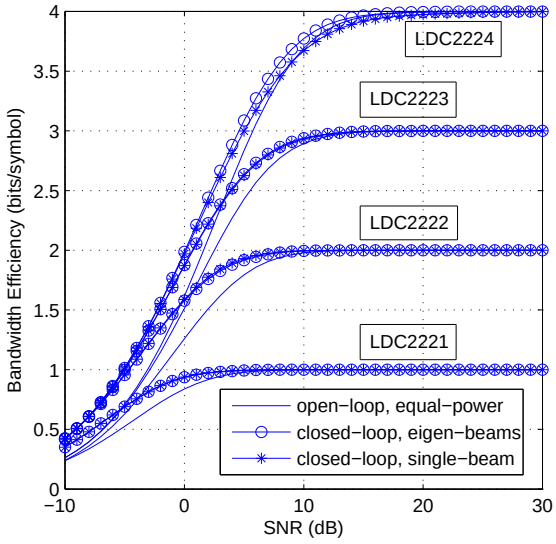

Figure 4.9: DCMC capacity of open-loop and closed-loop system employing LDC(2221)-QPSK, LDC(2222)-QPSK, LDC(2223)-QPSK and LDC(2224)-QPSK schemes, respectively.

Fig. 4.9 illustrates the attainable DCMC capacity of the first three transmission schemes for systems having $N_{Tx} = 2, N_{Rx} = 2$ antennas and using QPSK modulation as well as four different LDC schemes. These three transmit schemes are represented in Fig. 4.9 by the line having no marker, the circle-marker and by the star-marker, respectively. The four LDCs, namely LDC(2221)-, (2222)-, (2223)-, and (2224)-QPSK are employed and illustrated in Fig. 4.9. These results indicate that

1. At low SNRs, employing a closed-loop transmit scheme is capable of providing an approximately 3dB gain. For example, at -10dB, the closed-loop LDC(2224)-QPSK scheme achieves a capacity of 0.438-bits/symbol. To achieve the same capacity value, -7dB is required for the open-loop LDC(2224)-QPSK scheme.

2. For the LDC(2221)-QPSK, (2222)-QPSK and (2223)-QPSK schemes, the performance of employing closed-loop full eigen-beams and single-beam transmission are similar. For the LDC(2224) scheme, the performances of the closed-loop full eigen-beamforming scheme and of the single-beam scheme are almost identical, except for the range of 5dB-15dB where the single-beam system's DCMC capacity is slightly lower than the that of full eigen-beam system. As a result, single-beam transmission allows us to reduce the complexity of power-allocation as well as the required feedback overhead.

Fig. 4.10 illustrates the DCMC MIMO capacity for a $(N_{Tx} = 3, N_{Rx} = 2)$-antenna system using the LDC(3224)-QPSK scheme. When using perfect CSIT, the closed-loop single eigen-beam scheme achieves about 4dB gain over the open-loop scheme, and it performs similarly to the closed-loop full eigen-beam scheme. When using a 3-bit instantaneous beamforming vector feedback generated by a Grassmannian line-packing quantizer through an error-free and delay-free feeback channel as our CSIT, the closed-loop single beam scheme achieves an approximately 2dB gain over the open-loop scheme.

Fig. 4.11 illustrates the achievable BER performance of the same system combining URC [156],

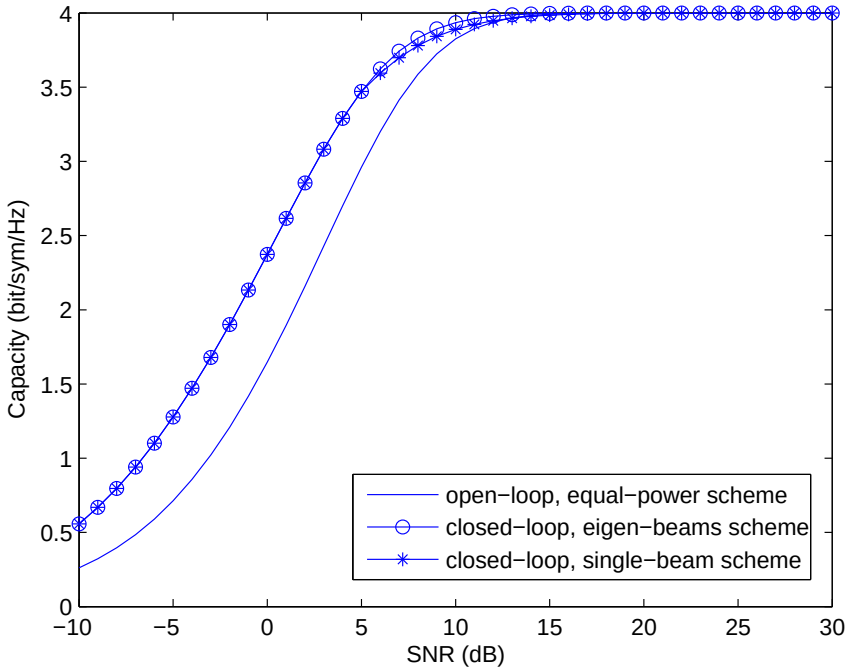

Figure 4.10: DCMC capacity of a $N_{Tx} = 3, N_{Rx} = 2$ system using LDC(3224)-QPSK and different transmission schemes.

a half-rate RSC - RSC(2,1,5)- and a soft-input-soft-output Maximum-Likelihood (ML) detector. The number of detection iterations was set to $I_{URC} = 1$ between the detector and the URC decoder and $I_{RSC} = 5$ between the detector and the RSC decoder. When assuming perfect CSIT, the closed-loop full eigen-beam scheme and the closed-loop single eigen-beam scheme achieve error-free transmission at about 0dB and 1dB, which are 4dB and 3dB lower than the SNR required by the corresponding open-loop scheme, respectively. Using a 3-bit quantized closed-loop single-beam scheme, a 2dB gain is attainable compared to the open-loop benchmark scheme.

4.3 Transmit Eigen-Beamforming for Video Transmission

The popularity of diverse video applications, such as for example video-phones, as well as YouTube- and BBC iplayer-style video streaming stimulates further research on video data transmission. As a result, the provision of high-quality video transmission becomes one of the major requirements imposed on future wireless networks. Although advanced video coding techniques [157] are capable of achieving a high compression ratio, the required bitrates are still typically higher compared to classic voice or text applications. Consequently, employing multiple antennas for video transmissions becomes an attractive solution, since MIMO systems promise a substantial capacity increase without any extra bandwidth requirement by employing spatial multiplexing [135] schemes. Most studies of video coding techniques considered single-antenna aided systems [157]. Nonetheless, some video transmission studies were also dedicated to MIMO systems, but most of them employed diversity-oriented techniques [98] to reduce the SNR requirement, rather than to increase the achievable throughput.

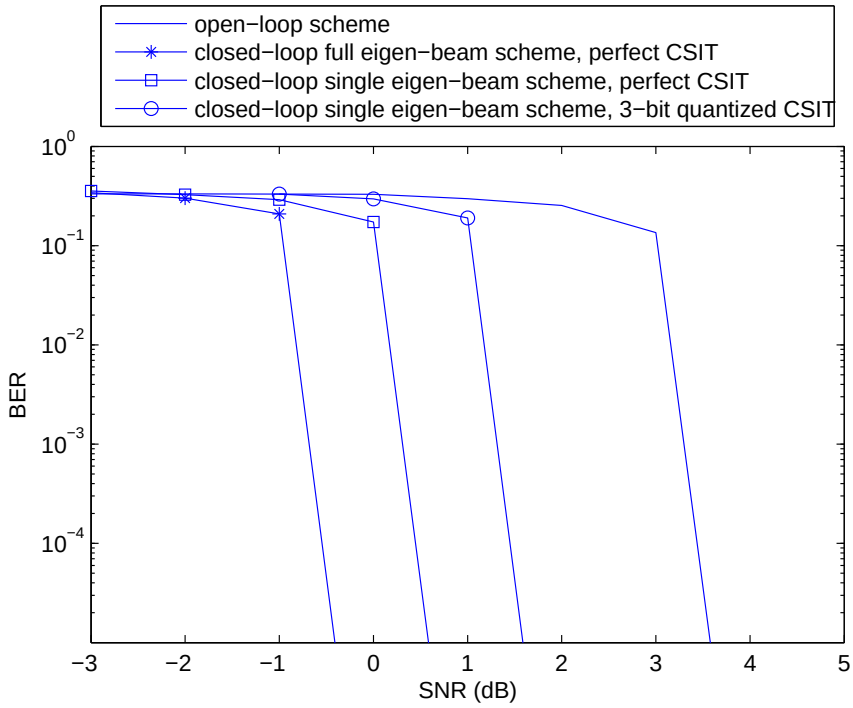

Figure 4.11: BER performance of a $N_{Tx} = 3, N_{Rx} = 2$ system using LDC(3224)-QPSK and different transmission schemes..

In this section, two spatial multiplexing schemes, namely BLAST-type spatial multiplexing [5] and transmit eigen-beamforming aided spatial multiplexing [57], are investigated. We will demonstrate that TxEBF-aided spatial multiplexing is more flexible in terms of providing the required Unequal Error Protection (UEP) for the video streams, hence it is capable of achieving an improved video performance. More explicitly, a widely accepted concept in video streaming is that the source-coded video bits should be unequally protected, where the bits representing more important information, such as the video frame header information for example, should be better protected. By contrast, the bits representing less important information because they only affect a small fraction of a video frame and do not propagate to other frames are capable of tolerating some errors. In the single antenna aided as well as in a BLAST-type spatial multiplexing scenario, video bits having different error sensitivity are transmitted via the same physical channel, exhibiting the same BER. Hence the most natural way to achieve UEP is to employ different-rate channel codes. By contrast, the TxEBF-aided spatial multiplexing decomposes the MIMO channel into orthogonal eigen-beams exhibiting unequal channel gains characterized by their corresponding eigen-values. Consequently, the data transmitted via the different eigen-beams exhibits a different BER. Hence TxEBF-aided UEP video transmission can be achieved in various ways, for example by allocating different error sensitivity bits to different eigen-beams, or by appropriately allocating a different transmit power to each eigen-beam, or classically, by employing different-rate channel codes.

In addition to flexible UEP, another advantage of the TxEBF-aided spatial multiplexing scheme is the ability to simplify the detector compared to that of the BLAST-type spatial multiplexing scheme under the assumption of experiencing a quasi-static or slowly fading channel. Since the eigen-beams are orthogonal to each other, a simple single-stream matched-filter can be used to detect the received signal, instead of employing a complex multi-stream detector. Naturally, the SVD computation has to

be carried out at regular intervals, for example for each new transmission frame, depending on how rapidly the channels fluctuate. By contrast, in the case of the BLAST-type system, a complex multi-stream detector [98] (ML/MMSE) is required to mitigate the inter-stream-interference. Hence, the overall complexity of the TxEBF-aided spatial multiplexing may be derived to be lower than that of the BLAST-type spatial multiplexing, provided that the channel fades slowly. And hence the SVD does not have to be repeated too often. However, a disadvantage of the TxEBF-aided spatial multiplexing is that in the FDD system we considered, the CSI is not avaliable at the transmitter. More explicitly, the Right-hand-side (RHS) singular matrix has to be known to the transmitter and updated, whenever the channel changes. This side-information may occupy a non-negligible fraction of the bandwidth in the reverse link, which otherwise could be used for data transmission. Fortunately, this problem may be solved by employing the efficient RHS singular matrix quantization and feedback technique of Section 4.1, which demonstrates that a low number of feedback bits is sufficient to achieve a performance approaching that attained under the assumption of a perfectly error-free and unquantized feedback channel. In short, we will demonstrate that for a low-Doppler indoor environment the TxEBF-aided spatial multiplexing outperforms the BLAST-type spatial multiplexing.

4.3.1 Introduction to H.264/AVC Video Coding

The H.264/AVC video codec [157] has been employed in this section, which is the most recent block-oriented motion-compensation-based codec standard developed by the ITU-T video coding experts group together with the ISO/IEC moving picture experts group. This standard has been widely used in applications such as Blu-ray Discs, videos from YouTube and the iTunes Store, for terrestrial and satellite DVB television services, for cable television services and for real-time video conferencing.

The H.264/AVC codec constitutes an attractive candidate for wireless video streaming applications owing to its high compression ratio [157]. The H.264/AVC codec employs various Variable Length Coding (VLC) and predictive coding techniques to achieve a high compression efficiency. However, these techniques also make the compressed bit-stream vulnerable to transmission errors. This is because a single bit error in the video stream may render the correct decoding of future codewords impossible. Furthermore, owing to predictive coding the effects of channel errors are likely to be propagated to the neighboring video blocks. Therefore the limited bandwidth and the error-prone nature of wireless transmission systems makes the transmission of compressed video a challenging task.

As a result, in addition to providing a high video compression, the H.264/AVC video codec employs a range of techniques designed for achieving an enhanced error resilience. One of these features is Data Partitioning (DP). In contrast to encoding all video parameters of a Macro-Block (MB) into a single bit-string representing a single video slice, we may generate several bit-strings per slice referred to as partitions, which represent different-sensitivity classes. This allows us to protect the different-sensitivity bits based on their relative importance. In the context of the H.264/AVC scheme we may create three different partitions, namely Partition A, B, and C.

1. Partition A contains the most vulnerable bits representing the slice header information, MB types, quantisation parameters and motion vectors. The bits of an entire video slice, including Partitions B and C are dropped, when Partition A is corrupted. In this scenario the entire slice is marked as corrupted and the decoder will apply error concealment techniques using the corresponding video

segment of the previously decoded frame.

2. Partition B typically contains intra-frame coded MB coefficients and intra-MB Coded Block Pattern (CBP) bits, indicating which blocks within a MB contain non-zero transform coded coefficients. Recovery from error propagation can only be achieved after refreshing the corrupted image regions in the intra-frame mode by switching off inter-frame prediction for certain MBs, when no feedback channel is available. Typically a certain limited fraction of the MBs is encoded in the high-rate, but error-resilient intra-frame coding mode, hence Partition B typically hosts the lowest number of bits in an encoded slice.

3. Partition C carries inter-frame CBP and inter-frame MCER bits for the particular MBs that were encoded using motion compensated prediction. By contrast, when in the intra-frame mode, Partition C carries the intra-frame CBP and intra-frame MCER bits for the MBs coded using the H.264-specific intra-frame prediction mode.

Therefore, in the H.264 video stream, Partition A is the most important one. The specific significance of a Partition B and C is dependent on the importance of the associated Partition A, but they are not decodable in the absence of Partition A. If Partition B of a slice is present along with A, the intra-frame MB update is added to the reconstructed frame, while if Partition C is present, the MCER of a slice is reconstructed and added to the motion compensated slice. As a result, the data of Partition A has to be protected with the highest priority, followed by Partition B and C. Similarly to the scheme proposed for the wavelet video codec, in the TxEBF-aided spatial multiplexing based MIMO system, Partition A should be transmitted via the eigen-beam having the highest-power, while Partition B and C should be transmitted with the aid of the eigen-beams having lower power.

4.3.2 System Model

The BLAST-type spatial multiplexing scheme [5] transmitting independent data streams over different transmit antennas is a widely used method. An attractive design alternative is constituted by the TxEBF-aided spatial multiplexing scheme, provided that CSI is available at the transmitter side. Both system structures are illustrated in Fig. 4.12.

In the BLAST-type spatial multiplexing system shown in Fig 4.12 (a), the video bits are first split into three data streams a_1, a_2 and a_3, depending on their importance. For example, in the context of the H.264/AVC codec of Section 4.3.1, a_1, a_2 and a_3 represent Partitions A, B and C. These data streams are separately channel coded, jointly modulated and transmitted. At the receiver side, a multi-stream detector [135] (e.g. ML/MMSE) is required for separating the different data streams. The BER can be improved by carrying out turbo-detection iterations between the detector and the channel decoder. This system exhibits a similar BER for all transmitted symbols. The classic technique of providing UEP for the different video data streams is by employing different-rate channel codes [98].

In the TxEBF-aided spatial multiplexing system shown in Fig 4.12 (b), the video bits are also split according to their importance. However, the MIMO channel is decomposed into eigen-beams upon multiplying the signal to be transmitted by the Right-Hand-Side (RHS) singular matrix $\boldsymbol{V}$ at the transmitter and upon multiplying the received signal by the Left-Hand-Side (LHS) singular matrix $\boldsymbol{U}^H$ at the receiver. The resultant eigen-beams are orthogonal to each other and exhibit different channel gains, which

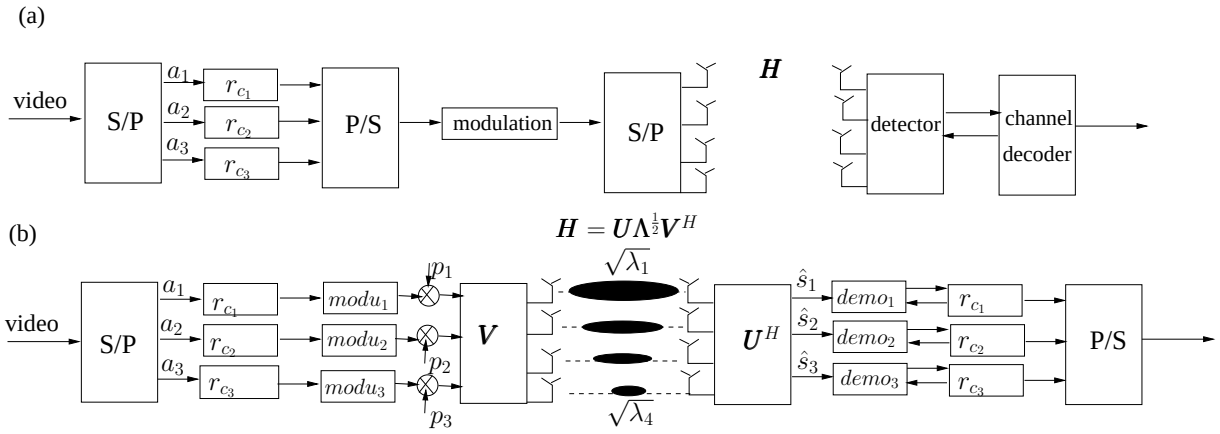

Figure 4.12: System Structure a) BLAST-type spatial multiplexing; b) TxEBF-aided spatial multiplexing.

are characterized by the corresponding eigen-values. As a result, the data transmitted via the different eigen-beams exhibits unequal BERs. Hence UEP video transmission is achieved either by allocating different error sensitivity bits to different eigen-beams, or by appropriately allocating the power to each eigen-beam, or alternatively by employing different-rate channel codes. In order words, the TxEBF-aided spatial multiplexing system is more flexible in terms of providing UEP for the video stream.

4.3.3 Simulation Results

The H.264/AVC JM 13.2 reference codec operated at $R_f = 15$ frames/s using the (176×144)-pixel Quarter Common Intermediate Format (QCIF) "Akiyo" video sequence, encoded at a near-constant bit-rate of $R_b = 64$kbit/s was transmitted through a MIMO system equipped with $N_{Tx} = 4$ transmit and $N_{Rx} = 4$ receive antennas. The half-rate Recursive Systematic Code (RSC) RSC(215) was employed in all system configurations in order to focus our investigations on the UEP performance provided by the TxEBF-aided MIMO channel. Iterative decoding was employed at the receiver side and the number of iterations was set to $I = 2$ for striking a good compromise between enhancing the achievable BER performance and limiting the decoder's complexity.

Let us now continue by addressing our design dilemmas, namely the design of the TxEBF-related parameters for the sake of improving the attainable video performance. The Peak-Signal-to-Noise-Ratio (PSNR) of the luminance (PSNR-Y) [157] is used as our video quality evaluation metric. The video data are first split into two streams according to their error sensitivity. One streams consists of the Partion A and B bits, while the other stream consists of the Partition C bits. The reason for combining the bits of Partion A and B is that on average the total number of Partition A and B bits is similar to the number of Partion C bits. A further split might be needed according to the number of activated eigen-beams. Three TxEBF-aided spatial multiplexing configurations were set up, as illustrated in Table 4.2. Naturally, the more error sensitive bits are transmitted through the eigen-beams having higher power in all configurations. The first two configurations of Table 4.2 activated the three highest-power eigen-beams. However, the first configuration allocated more power to the stronger eigen-beam and less to the weaker eigen-beam. By contrast, the second configuration of Table 4.2 allocated the power the opposite way round. The third configuration activated only the two strongest eigen-beams and allocated

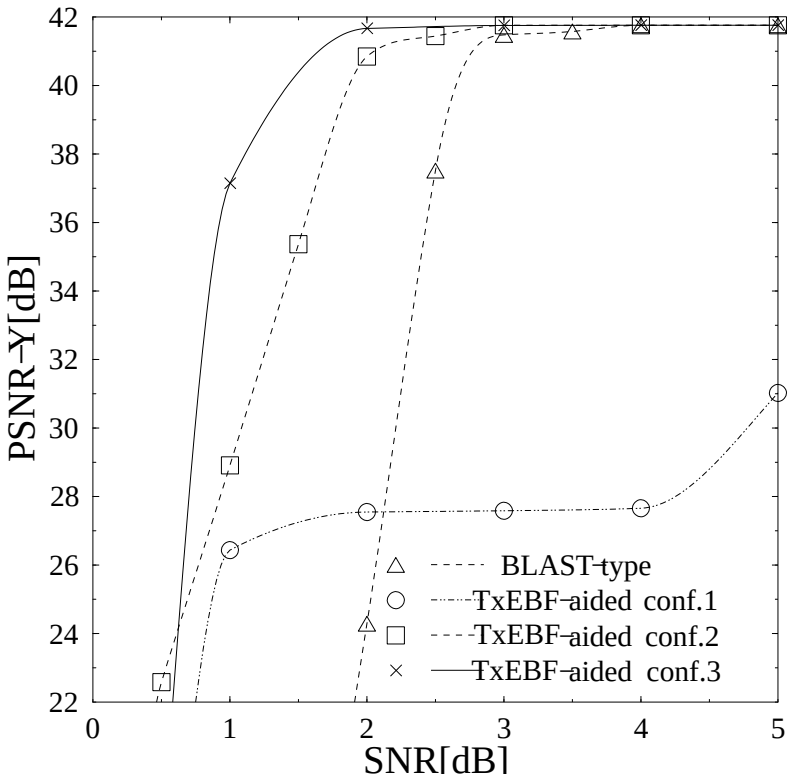

Figure 4.13: PSNR-Y performance versus SNR of the TxEBF-aided spatial multiplexing based video systems using Configurations 1, 2 and 3, as well as of the BLAST-type spatial multiplexing based video system, respectively.

the transmission power to the activated beams equally. Different modulation schemes were employed in the different configurations in a way to ensure that the transmission throughput remained 2 bits/symbol. For comparison, we employed an identical-throughput BLAST-type spatial multiplexing scheme using BPSK modulation, half-rate RSC coding and an MMSE detector as a benchmark. The source-coded video stream was processed on a frame-by-frame basis. As a result, the transmission burst duration was equal to $1/R_f = 66.7$ms and the average number of bits per transmission burst was $R_b/R_f = 4266$bits. Our PSNR performance comparisons are shown in Fig. 4.13, while the BER performance comparisons are illustrated in Fig. 4.14.

The simulation results demonstrated that:

1. As expected, an increased throughput is achieved by employing the proposed TxEBF-aided spatial multiplexing scheme as a result of using multiple antennas.

2. The TxEBF-aided spatial multiplexing scheme provides UEP for the partitioned video bit-stream, while the BLAST-type spatial multiplexing benchmark scheme provides Equal Error Protection (EEP). As a result, observe in Fig. 4.13 that the TxEBF-aided spatial multiplexing system achieved a near-unimpaired video quality associated with PSNR-Y=40dB at 1dB lower SNR than the BLAST-type spatial multiplexing benchmark scheme.

3. Focusing our attention on the PSNR-Y and BER performance of the TxEBF-aided spatial multiplexing system using Configuration 2 of Table 4.2 represented by the line marked by squares in Fig. 4.13 and Fig. 4.14 respectively, it is clear that besides having a low BER ($< 10^{-2}$) for the

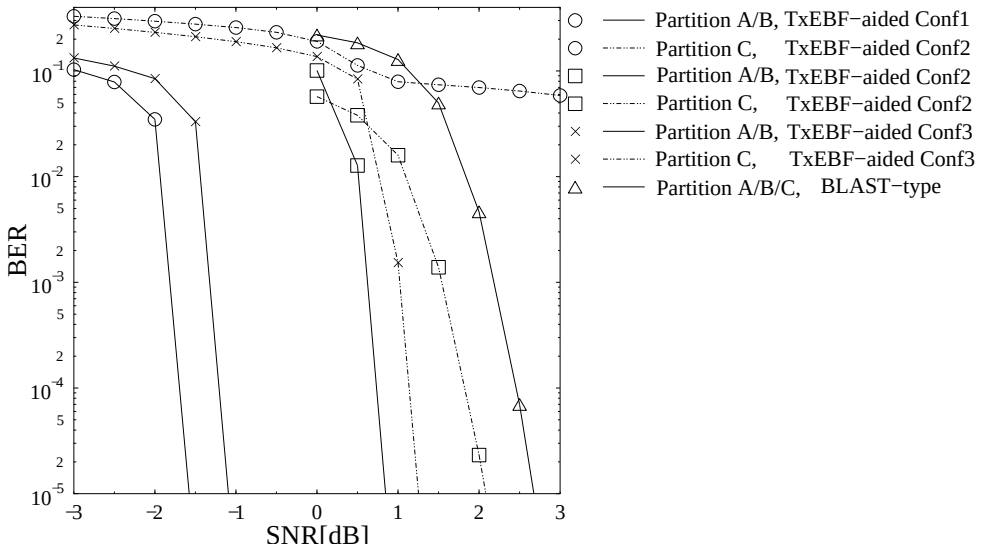

Figure 4.14: BER performance versus SNR of the TxEBF-aided spatial multiplexing system using Configurations 1, 2 and 3 of Table 4.2, as well as of the BLAST-type spatial multiplexing based video system. Two detection iterations were used for exchanging extrinsic information between the detector and the channel decoder in the schematic of Fig. 4.12b.

Partion A and B bits, an acceptable BER performance (< 0.08) is required for Partition C for the sake of reaching a decodable PSNR-Y level. Moreover, when the BER of all the bits is lower than 10^{-4}, the video quality appears subjectively unimpaired and PSNR-Y$\approx$42dB was obtained.

4. As a result, the TxEBF-related parameters should be designed for providing as strong a protection for the sensitive video bits as possible, while maintaining an adequate transmission quality also for the less error-sensitive bits.

Let us now briefly consider the effects of different transmission burst lengths on the achievable video performance. The TxEBF-aided spatial multiplexing system using Configuration 2 of Table 4.2 was used. The PSNR-Y performance of having a transmission burst length of 15 video frames was then evaluated and compared to the results associated with using a single-video-frame transmission burst length. The corresponding results are illustrated in Fig. 4.15. It is shown that the system associated with a longer transmission burst length reaches a near-unimpaired average video performance of PSNR-Y$\approx$42dB at a channel SNR of about 1dB lower than the system having a single-video-frame burst length. This gain accrues from the enhanced error correcting capability of the channel code achieved as a result of its increased codeword length. The price paid for achieving this gain is the 15-fold increased delay of $15 \times 66.7ms = 1s$, which would only be acceptable in a You-Tube-type non-iterative video-streaming.

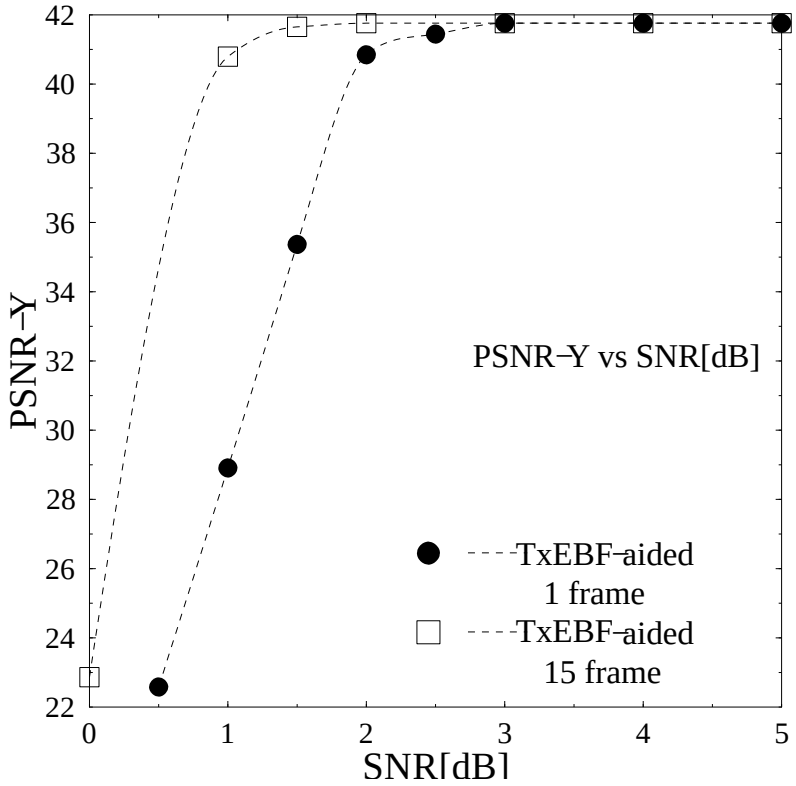

Figure 4.15: PSNR-Y versus channel SNR performance of two system using either a single-frame or 15-frame transmission burst length. The TxEBF-aided spatial multiplexing based video Configuration 2 of Table 4.2 was used.

Source Codec	H.264
Number of transmit antennas (N_{Tx})	4
Number of receive antennas (N_{Rx})	4
Target coded bits transmission rate	2bits/s
Number of Iteration	2
Interleaver length	1000 $\backsim$ 3000
BLAST-type configuration	BPSK RSC(215) MMSE detector
TxEBF-aided, configuration 1 (Configuration 1)	λ_1, QPSK, RSC(215), p_1=0.25, Partition A and Partition B λ_2, BPSK, RSC(215), p_2=0.25, Partition C λ_3, BPSK, RSC(215), p_3=0.5, Partition C $\lambda_1 > \lambda_2 > \lambda_3$
TxEBF-aided, configuration 2 (Configuration 2)	λ_1,QPSK, RSC(215), p_1=0.5, Partition A and Partition B λ_2,QPSK, RSC(215), p_2=0.5, Partition C
TxEBF-aided, configuration 3 (Configuration 3)	λ_1, QPSK, RSC(215), p_1=0.6, Partition A and Partition B λ_2, BPSK, RSC(215), p_2=0.2, Partition C λ_3, BPSK, RSC(215), p_3=0.2, Partition C

Table 4.2: Simulation Parameters

4.4 Chapter Summary

Table 4.3: Simulation Results Summary

System Parameter			Comparison Schemes	DCMC at SNR=5dB	Required SNR when BER$< 10^{-4}$
Number of antennas (N_{Tx}, N_{Rx})	(3,2)		Open-loop scheme shown in Fig. 4.8b	3 (bit/symbol)	3.5 dB
LDC ($N_{Tx}N_{Rx}TN_s$)	(3224)				
Modulation	QPSK		LDC aided TxEBF shown in Fig. 4.8a using 3 $\sim$ bits feedback Grassmannian line-packing quantiser in Section 2.3.3	3.5 (bit/symbol)	1.5 dB
Coding rate r_c	0.5				
Channel code	URC RSC(215)				
Detector type	ML				
Number of iteration (I_{URC}, I_{RSC})	(1,5)				
System Parameter			Comparison Schemes	PSNR-Y at SNR=2dB	BER at SNR=2dB
Number of antennas (N_{Tx}, N_{Rx})	(4,4)		V-BLAST spatial multi--plexing shown in Fig. 4.12a	24dB	$4 \cdot 10^{-2}$ for all three partition bits
Modulation	QPSK BPSK				
Coding rate r_c	0.5		TxEBF aided spatial multi--plexing shown in Fig. 4.12b using configuration 3 detailed in Table 4.2	41.5dB	$< 10^{-5}$ for all three partition bits
Channel code	RSC(215)				
Detector type	MMSE				
Number of iterations (I_{RSC})	2				
Video sequence	"Akiyo"				
Video codec	H.264/AVC				

In this chapter, we have studied the TxEBF aided closed-loop MIMO system shown in Fig. 3.1. In Section 3.1 we have first evaluated the achievable ergodic CCMC capacity of a TxEBF aided closed-loop system, where the situation of having perfect CSIR/CSIT and quantized CSIT were considered. Then, we have proposed a novel closed-loop single-user MIMO system combining LDCs and transmit eigen-beamforming in order to achieve a higher DCMC capacity than that of its open-loop counterpart. Our simulation results illustrate that a modest feedback rate is capable of substantially improving the achievable capacity gain. For example, having a 3-bit feedback is capable of approaching the performance of perfect CSIT in the context of having $N_{Tx} = 3$, $N_{Rx} = 2$ antennas. Moreover, the proposed scheme reduced the complexity of adaptive transmissions at the transmitter side compared to traditional adaptive modulation and coding schemes [2, 158], and achieved the maximum attainable diversity as wll as multiplexing gain for arbitrary antenna configurations. Moreover in Section 4.3, we have compared the ability of a BLAST-type spatial multiplexing based arrangement and that of an TxEBF based MIMO system to support video transmissions. The proposed TxEBF aided closed-loop scheme is more flexible in terms of providing UEP for the source-coded video bits, which is achieved by mapping the bits having different error sensitivity to different eigen-beams, or by appropriately a portioning the total transmission power

to each eigen-beam, or naturally, by employing different-rate channel codes. As a result, the quality of the video signal decoded at the receiver side can be substantially improved. The results shown in this chapter characterized two typical systems having the parameters summarised in first two columns of Table 4.3. The corresponding simulation results are also summarised in Table 4.3 and are categorised into two groups of comparisons, which demonstrated the advantages of our proposed schemes.

Chapter 5

Linear Multi-User Transmitter Aided Closed-Loop SDMA Downlink

Invoking Spatial Division Multiple Access (SDMA) in the Down-Link (DL) has the potential of increasing the achievable throughput with the aid of a linear Multi-User Transmitter (MUT), provided that the CIRs of all antenna elements of all users are known at the DL transmitter. The family of linear MUT algorithms, including Transmit Zero-Forcing (TxZF), Transmit Minimum Mean Square Error (TxMMSE) and Transmit Block Diagonalization (TxBD) detailed in Section 2.2.2 is employed in this chapter. The system model of the linear MUT aided closed-loop SDMA-DL is illustrated in Fig. 5.1. In contrast to the

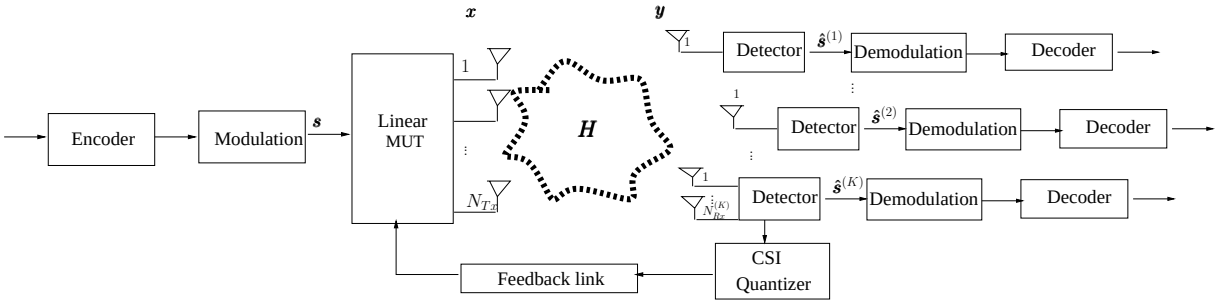

Figure 5.1: System model of a Linear MUT aided closed-loop DL SDMA system.

previous two chapters, where the feedback channel is assumed to be noise-free and delay free, the effects of imperfect feedback channels are investigated in this chapter. The novel contributions of this chapter are:

1. A novel concept, referred to as the EXIT-Chart Optimised CSI Quantizer (ECO-CQ) is proposed. The ECO-CQ scheme assists the system in maintaining the lowest possible CSI feedback overhead, while ensuring that an open EXIT-tunnel is still attainable, which implies maintaining an infinitesimally low BER. Furthermore, we demonstrate that the proposed ECO-CQ may reduce the normalised feedback overhead compared to the conventional Channel Quantizer (CQ). For instance, the ECO-CQ aided iterative DL-SDMA system using an average of $b = 2.7$ quantization bits per CIR coefficient achieves a 10% normalised overhead reduction at $E_b/N_0 = 5$dB, compared to the conventional CQ aided benchmarker system.

2. A soft decoding assisted MIMO CIR recovery scheme is proposed and its performance is evaluated when using a TxZF/TxMMSE assisted MISO multi-user DL-SDMA system. We demonstrate that the CIR reconstructed at the transmitter is constituted by a linear combination of the codebook entries recovered from the error-contaminated received signal. More explicitly, this design does not rely on the straightforward feedback of a specific CIR tap's index or of an entire CIR's index. Our design minimises the distortion imposed by error-prone feedback channels.

3. A periodically activated CIR update scheme is proposed, which employs a channel predictor at the DL transmitter for predicting the CIR taps for each future symbol transmission instant and hence to mitigate the performance degradation imposed by the associated signalling delays. Moreover, a Predictive Vector Quantizer (PVQ) is used at the MTs for compressing the CIRs before their uplink transmission. Compared to a conventional Vector Quantizer (VQ), the PVQ has significantly reduced the CIR feedback bit rate. Hence, with the aid of the same fixed feedback bit rate, the new PVQ scheme can provide more accurate CIR information or support a channel having a higher Doppler frequency in comparison to a conventional VQ.

This chapter is organised as follows. The EXIT-Chart optimized CIR quantiser algorithm is introduced in Section 5.1. The soft decoder assisted CIR recovery scheme is discussed in Section 5.2 in the context of noise-contaminated feedback channels, while the channel prediction and PVQ regime designed for realistic finite-delay feedback channels are detailed in Section 5.3. Finally, the chapter is summarized in Section 5.4.

5.1 EXIT-Chart Optimized CIR Quantizer

In efficient wireless systems, it is essential to minimise the feedback overhead, since the feedback link is often bandwidth limited. In this section, we propose an algorithm, which assists us in exploring the CIR feedback overhead required for maintaining an open EXIT-tunnel for an iterative detection aided system. Therefore, we refer to our CSI quantization algorithm as the EXIT-Chart Optimized CSI Quantizer (ECO-CQ). Although our discussions in this section are concentrated on a TxBD-aided MIMO DL SDMA system using the MMSE-based scalar quantizer introduced in Section 2.3.2, the design principle of the proposed EXIT-Chart optimized CIR quantizer may also be applied for different MUT aided systems and different types of channel quantisers. Below we commence our discourse by summarising the proposed ECO-CQ algorithm in Section 5.1.1. In Section 5.1.2 we outline the system model used. Our EXIT chart analysis is provided in Section 5.1.3, leading to the performance results of Section 5.1.4.

5.1.1 EXIT-Chart Optimized Channel Quantization

Consider the scenario when the BS periodically sends pilots to the DL receivers, so that the MTs may estimate the CIRs and use the allocated feedback channels to periodically feed back the CIRs, as illustrated in Fig. 5.2. The DL channel and the UL feedback channels of the MTs are typically allocated in different bandwidths and the UL feedback information is assumed to be transmitted over the strongly protected UL control channel. Additionally, the BS may avoid the latency involved in awaiting the current CIRs by employing their predicted value generated by the CIR prediction [38] based on the previously received

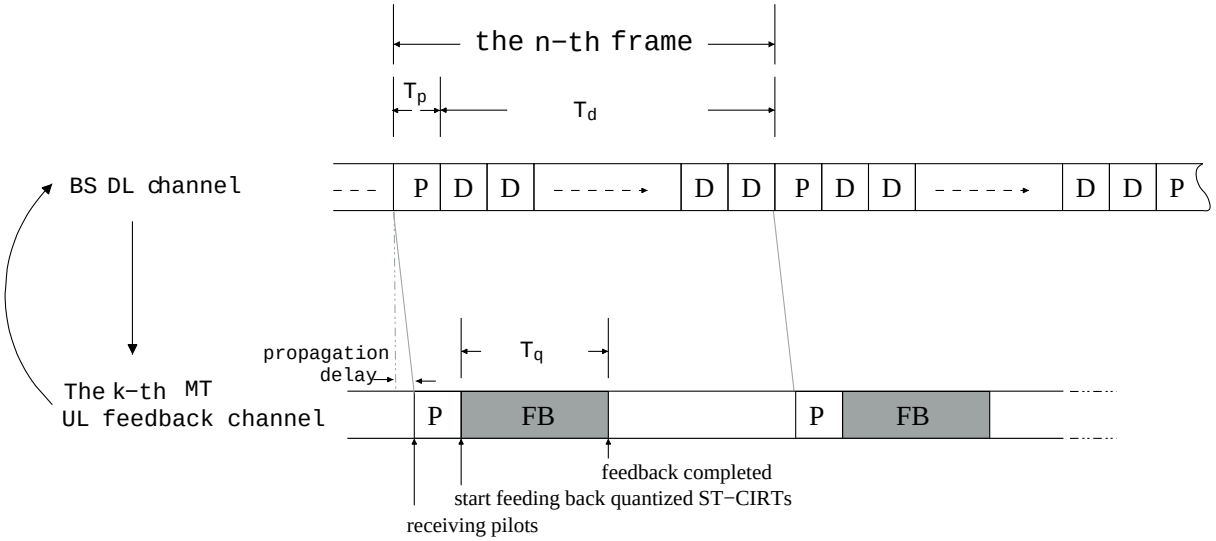

Figure 5.2: The pilot-aided CIR estimation and CIR feedback

quantized CIRs. In this study, we did not take the channel prediction error into account in order to focus our attention on the investigation of the limited CIR feedback. Assuming that the channel prediction is perfect, the CIR coefficients are contaminated by the quantization error only. Hence, at every symbol interval we assume that the BS exploits the current CIR coefficients quantized by using the CQs. Consequently, in our forthcoming discourse the inaccuracy of the CIR employed by the BS will be dominated by the limited CIR feedback bit rate.

Let T_p denote the duration of a pilot symbol interval, which is typically identical to the data symbol interval and T_d denote the total duration of data-transmission symbol intervals between two pilots, as seen in Fig. 5.2. Let us now consider two schemes. First, the MTs employ b_1 bit quantization for each CIR tap to convey the CIR coefficients to the BS, which are subject to a feedback delay duration of T_{b_1}. In the second scheme, the MTs employing b_2-bit quantization to signal the CIR coefficients to the BS and have the corresponding feedback delay duration of T_{b_2}. Then we define *the normalized overhead reduction ratio* η_r associated with using b_2 instead of b_1 bits as

$$\eta_r = \frac{b_1 - b_2}{b_1},\ b_2 < b_1. \tag{5.1}$$

In this section we propose an algorithm, which allows the system to use a different number of quantization bits b in different symbol intervals. The goal is to minimize the average of b over a number of symbol intervals, while maintaining a certain target performance. Let us assume for example that there are 100 symbol intervals. The receiver quantizes the CIRs of 40 symbol intervals using $b = 2$-bit quantization and the rest of the CIRs of 60 symbol intervals using 3-bit quantization. Therefore during the observed 100 symbol intervals, the average number of feedback bits for each sampled CIR conveying both the magnitude and phase is $b = 2 \cdot 0.4 + 3 \cdot 0.6 = 2.6$. The question is now, how to determine the required number of quantization bits b for the sampled CIRs.

In order to resolve this design dilemma, we adopt the design concept of irregular convolution codes [159] and aim to minimize the average number of feedback bits denoted as $\bar{b}$, while assuming that an open EXIT-tunnel is still attainable for the iterative system at a given E_b/N_0 values. More explicitly, we exploit the fact that similarly to having different channel SNRs, the different amount of CIR quanti-

zation noise imposed by varying the number of feedback bits allows us to shape the EXIT-curve of the inner component of our DL-SDMA system. Assume that there are N_{ts} symbol intervals in an observed transmission block and we employ N_Q different number of quantization bits to quantise the CIR. For example, we have $b = \{2,3,4,5\}$ for $N_Q = 4$. The CIRs in the segment of $\alpha_j N_{ts}$ symbol intervals will be quantized by using a specific number of quantization bits b_j, where α_j is a weight, controlling the size of each segment. Then the weighting coefficient α_j has to satisfy:

$$1 = \sum_{j=1}^{N_Q} \alpha_j, \ \bar{b} = \sum_{j=1}^{N_Q} \alpha_j b_j, \text{ and } \alpha_j \in [0,1], \forall j. \tag{5.2}$$

where $\bar{b}$ is an averaged value over the observed transmission block.

According to [159], the corresponding EXIT function $T_I(I_{in})$, which characterises the inner decoder's EXIT-curve in the system, is given by

$$T_I(I_{in}) = \sum_{j=1}^{N_Q} \alpha_j T_{b_j}(I_{in}), \tag{5.3}$$

where $T_{b_j}(I_{in})$ denotes the EXIT function, when the CIRs are quantized by using b_j-bit channel quantization.

5.1.2 System Model

In this section, we outline our system models for both the iterative DL-SDMA arrangement using conventional CQ and for the proposed ECO-CQ. Assume that our system equipped with N_{Tx} transmit antennas at the BS for the sake of supporting K MTs, while each MT employs $N_{Rx}^{(k)}$ receive antennas. We have a $(N_{Rx}^{(k)} \times N_{Tx})$-element channel matrix $\boldsymbol{H}^{(k)}$, which is constituted by the sampled flat-fading CIRs of each Antenna Element (AE) experienced by the k-th user. The elements $[\boldsymbol{H}^{(k)}]_{i,j}$ are i.i.d complex Gaussian random variables with a distribution of $\mathcal{CN}(0,1)$, where we have $1 \leq i \leq N_{Rx}^{(k)}$ and $1 \leq j \leq N_{Tx}$.

5.1.2.1 DL-SDMA MUT Using Conventional CQ and Iterative Detection

Based on the iterative-detection aided DL-SDMA system of [160] in Fig. 5.3, we depicted the architecture of our system using a conventional CQ. The source bits are encoded by the channel encoder as well as by the unity-rate coder[1] [160] and are mapped to the modulated symbols. Let $\mathbf{s}^{(k)} \in \mathbb{C}^{N_s^{(k)} \times 1}$ be a complex-valued column vector, which denotes the data symbol vector to be transmitted to the k-th MT, while $N_s^{(k)}$ represents the number of independent data symbols contained in $\mathbf{s}^{(k)}$. Furthermore, we utilise the Transmit Block Diagonalisation (TxBD) preprocessing matrix $\boldsymbol{P}^{(k)} \in \mathbb{C}^{N_{Tx} \times N_s^{(k)}}$ of [160], which was designed for the sake of eliminating the Multi-user Interference (MUI) by exploiting the knowledge of channel state information at transmitter, as detailed in Section 2.2.2.3. In this thesis, we assume that $\boldsymbol{P}^{(k)}$ is generated based on the quantized CIR fed back from the DL receivers, which is indicated by the notation $\boldsymbol{P}^{(k)}(\boldsymbol{H}_q)$, as shown in Fig. 5.3. After the processing of the TxBD, the K DL signals transmitted to the K MTs will be superimposed and transmitted by the N_{Tx} transmit antennas.

[1]The reason for using an infinite-impulse response URC is because it was demonstrated by Divsalar *et. al* [156] and further detailed in [2] that the employment of a URC allows the system to operate at an infinitesimally low BER.

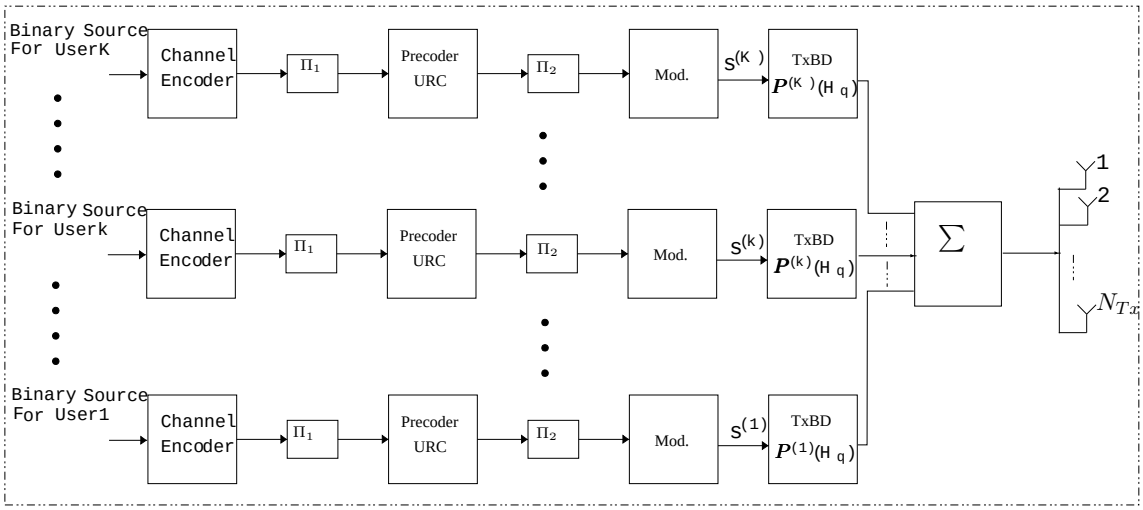

Figure 5.3: The structure of the BS's transmitter in the iterative DL-SDMA system using conventional CQ

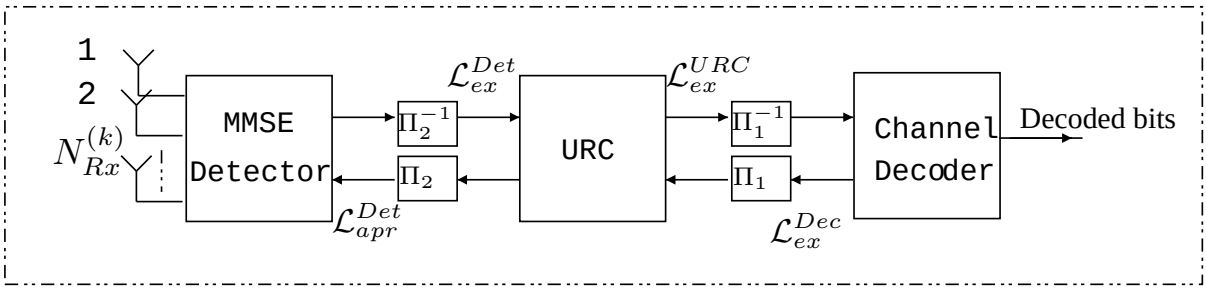

Figure 5.4: The structure of the MT's receiver in the iterative DL-SDMA system using conventional CQ

Fig. 5.4 depicts the structure of the MT's receiver in the iterative DL-SDMA system using conventional CQ. As seen in Fig. 5.4, the MMSE aided SDMA detector constitutes the first stage of the receiver. The iterative decoding process is carried out between the MMSE detector, the URC decoder and the channel decoder, as illustrated in Fig. 5.4[2].

Let $\boldsymbol{y}^{(k)}$ and $\boldsymbol{n}^{(k)}$ be the $N_{Rx}^{(k)}$-element received signal vector and $N_{Rx}^{(k)}$-element noise vector associated with the k-th MT, respectively. If the TxBD matrix $\boldsymbol{P}^{(k)}$ is generated based on perfect CIRs, the MUI can be perfectly eliminated. The received signal vector associated with the k-th MT can be expressed in the following form

$$\boldsymbol{y}^{(k)} = \boldsymbol{H}^{(k)}\boldsymbol{P}^{(k)}\boldsymbol{s}^{(k)} + \boldsymbol{n}^{(k)}, \tag{5.4}$$

where the $(N_{Rx}^{(k)} \times N_s^{(k)})$-dimensional matrix $\boldsymbol{H}^{(k)}\boldsymbol{P}^{(k)}$ characterises the *effective channel* corresponding to the k-th MT.

Naturally, when the TxBD matrix $\boldsymbol{P}^{(k)}$ is generated based on imperfect CIR, the system becomes unable to entirely eliminate the MUI and hence the resultant residual MUI contaminates the received signal of the k-th MT according to

$$\boldsymbol{y}^{(k)} = \boldsymbol{H}^{(k)}\boldsymbol{P}^{(k)}\boldsymbol{s}^{(k)} + \sum_{i=1, i\neq k}^{K} \boldsymbol{H}^{(k)}\boldsymbol{P}^{(i)}\boldsymbol{s}^{(i)} + \boldsymbol{n}^{(k)}, \tag{5.5}$$

[2] $\mathcal{L}_{ex}^{URC}$ denotes the extrinsic information, expressed by using the value of the Log Likelihood Ratio (LLR) [135], provided by URC. Similarly, $\mathcal{L}_{ex}^{Dec}$ is the extrinsic information generated by the channel decoder. $\mathcal{L}_{apr}^{Dec}$ denotes the *a prior* information provided by the detector.

where the second term of Equation (5.5) represents the MUI experienced.

5.1.2.2 DL-SDMA MUT Using ECO-CQ and Iterative Detection

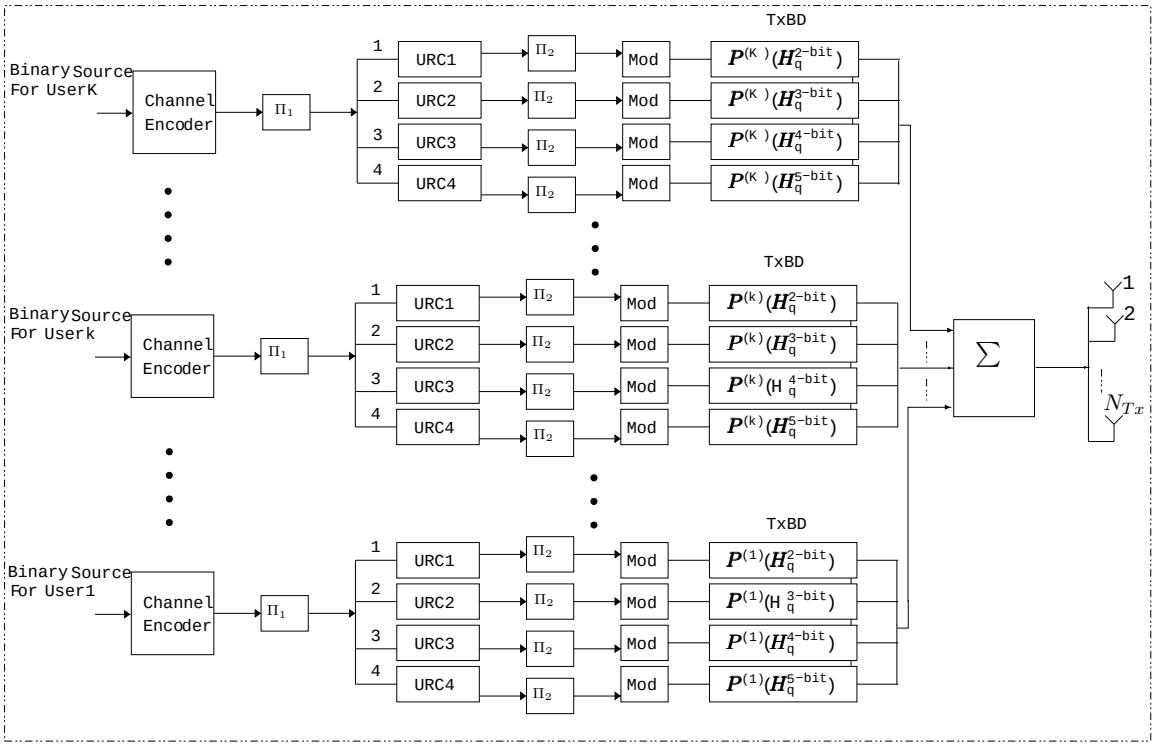

Figure 5.5: The structure of the BS's transmitter in the iterative DL-SDMA system using ECO-CQ

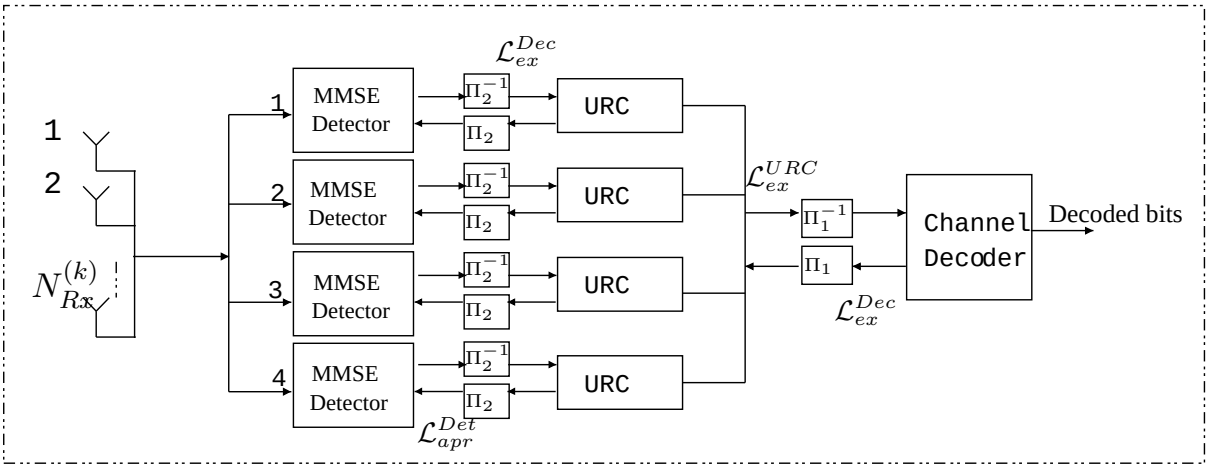

Figure 5.6: The structure of the MT receiver in the iterative DL-SDMA system using ECO-CQ

Certain structural modifications are required by the iterative DL-SDMA system, when it employs an ECO-CQ. Let us utilise four conventional CQs having different number of quantization bits, namely $b = 2, 3, 4$ and 5, to construct an ECO-CQ. As illustrated in Figure 5.5, the data bits encoded by the channel encoder will be partitioned into four segments corresponding to the weighting coefficient vector of $\boldsymbol{\alpha} = [\alpha_1, \alpha_2, \alpha_3, \alpha_4]$. Each of the four segments of the channel-encoded bits will also be encoded by the URC encoder of Figure 5.5 before the modulation stage. For example, for a data block containing N_c

encoded bits, the j-th URC encoder encodes $\alpha_j N_c$ bits. Assuming that m bits per modulated symbol are used for transmission, we have a total of $\alpha_j N_c / m$ transmitted symbols generated by the j-th modulator of Fig. 5.5. Accordingly, as illustrated in Fig. 5.5, the TxBD matrix $\boldsymbol{P}^{(k)}$ will be generated by using the CIRs, which were quantized using four different number of quantization bits per CIR coefficient for the four segments of transmitted symbols. The TxBD matrix $\boldsymbol{P}^{(k)}$ generated by the b-bit quantized CIRs is denoted by $\boldsymbol{P}^{(k)}(\mathbf{H}_q^{b-bit})$, as shown in Fig. 5.5.

Figure 5.6 shows the structure of the iterative DL-SDMA using ECO-CQ. First, the received signal will be partitioned into four segments. Accordingly, for each segment of the received signals, the MMSE detector will generate the soft-bits as the input of the URC decoder. The four segments of the extrinsic information bits generated by the URC decoder will become the *apriori* information bits of the channel decoder of Figure 5.6. As the iterative decoding process is carried out, the extrinsic information bits of the channel decoder will be partitioned into four segments again in order to construct four segments of *apriori* bits of the URC decoder. The four-segment output of the URC decoder will then be forwarded to the MMSE detector for the next iteration of the decoding process.

Again, the specific partitioning of the bits or symbols into segments is carried out according to Equation (5.3), where the transfer functions represent the four segments of soft-bits, i.e. Log Likelihood Ratios (LLR).

5.1.3 EXIT Chart Analysis

In the following discussions, we provide the EXIT chart analysis of our iterative DL-SDMA systems using conventional CQs and the proposed ECO-CQs.

5.1.3.1 Iterative DL-SDMA Systems Using Conventional CQ

Fig. 5.7 illustrates the EXIT chart of the iterative DL-SDMA systems using the conventional CQs in conjunction with different number of quantization bits, b, which is ranging from $b = 2, 3, 4$ to 5. Observe that by reducing the number of quantization bits, the inner EXIT-curves, which characterises the MMSE detector and URC-decoder represented inner systems, are getting closer to the outer EXIT-curve, which characterizes the employed RSC channel decoder, until the open tunnel disappears between them. Based on this EXIT chart, we expect that the system will suffer from a high BER, when using 2-bit CQ at $E_b/N_0 = 6dB$. On the other hand, the system using a 5-bit CQ performs close to the one benefiting from perfect CIR.

5.1.3.2 Iterative DL-SDMA Systems Using ECO-CQ

In Fig. 5.7, we found that the systems using 2-bit CQ are unable to maintain an open EXIT-tunnel for $E_b/N_0 = 6$dB. Therefore, in order to assist the system in maintaining an open EXIT-tunnel at $E_b/N_0 =$ 6dB, we have to increase the number of quantization bits to $b = 3$. However, the EXIT-tunnel of the systems using 3-bit CQ is rather wide. With the aid of the algorithm proposed in Section 5.1.1, and given a certain level of E_b/N_0, we will be able to design the system for maintaining a narrow but still open EXIT-tunnel using an average of less than $b = 3$ bit accuracy quantization. According to Equation (5.2), we can design an ECO-CQ having a low value of b corresponding to the weighting vector $\boldsymbol{\alpha}$. Fig. 5.8(a)

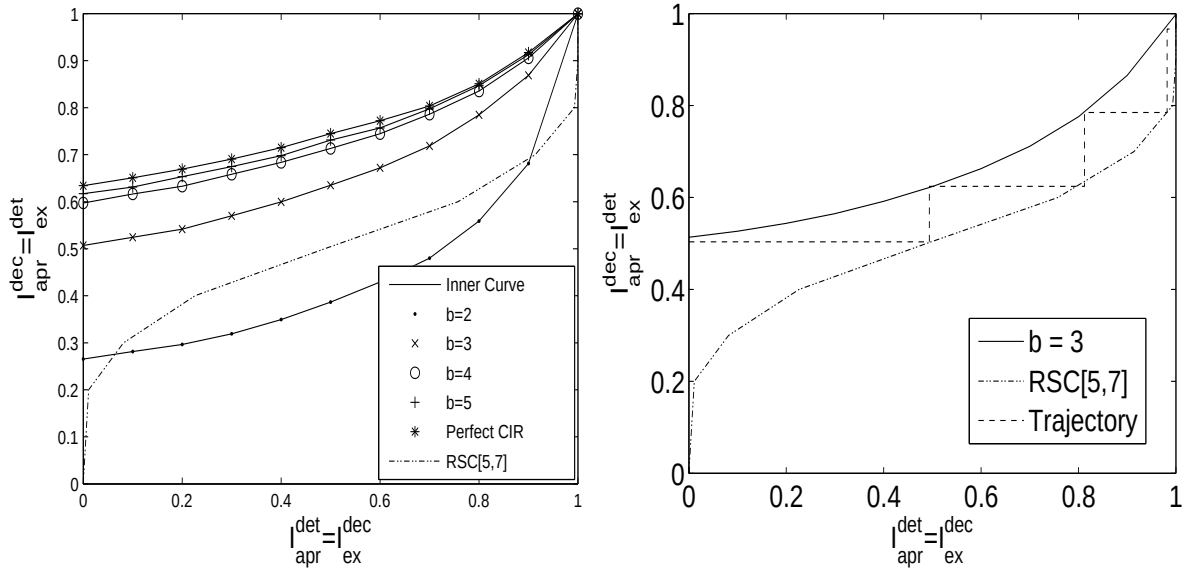

(a) (b)

Figure 5.7: EXIT chart analysis of the iterative DL-SDMA system using a b-bit conventional CQ, where b is ranging from $2, 3, 4$ to 5. The systems are operated at $E_b/N_0 = 6dB$. (a) shows the inner EXIT-curve of the iterative DL-SDMA system using conventional CQ. (b) shows the recorded iterative decoding trajectory of the iterative DL-SDMA system using conventional CQ. A rate-0.5 RSC[5,7] channel coder is employed by the system. The channel model was an uncorrelated flat-fading MIMO channel and the parameters of Table 5.1 were used.

shows the EXIT-curves of the iterative-detection aided DL-SDMA system using ECO-CQ and $b = 2.6$ as well as $\boldsymbol{\alpha} = [0.4, 0.6, 0, 0]$. More explicitly, the weight-vector $\boldsymbol{\alpha}$ indicates that 40% of the CIRs in a transmission block were quantized by the 2 bit CQ, while 60% of the CIRs were quantized with 3 bit CQ accuracy. In this way, we reduced the total number of bits to be fed back to the transmitters. More quantitively, in this example, we reduced the number of feedback bits for each sampled CIR tap's magnitude and phase by 0.4, which represents a reduction of $0.13\%(0.4/3)$ of the overall feedback-rate according to Equation (5.1).

5.1.4 Performance Results

In the section we provide the corresponding BER performance results. The system parameters used are listed in Table 5.1. Figure 5.9 characterizes the BER performance of the iterative DL-SDMA system using a conventional CQ and an ECO-CQ. As illustrated in Fig. 5.9, the iterative-detection aided DL-SDMA systems using ECO-CQ in conjunction with $b = 2.6$ bit per CIR tap are capable of operating at an infinitesimally low BER at $E_b/N_0 = 6$ dB. This confirms the accuracy of the EXIT chart analysis seen in Fig. 5.8. Upon increasing the number of quantisation bits b, we are able to achieve an infinitesimally low BER at lower E_b/N_0 values. The BER performance of the system using a perfect CIR is also provided in Fig. 5.9 as a benchmark. Fig. 5.9 shows that the performance of the system using a 5 bit CQ

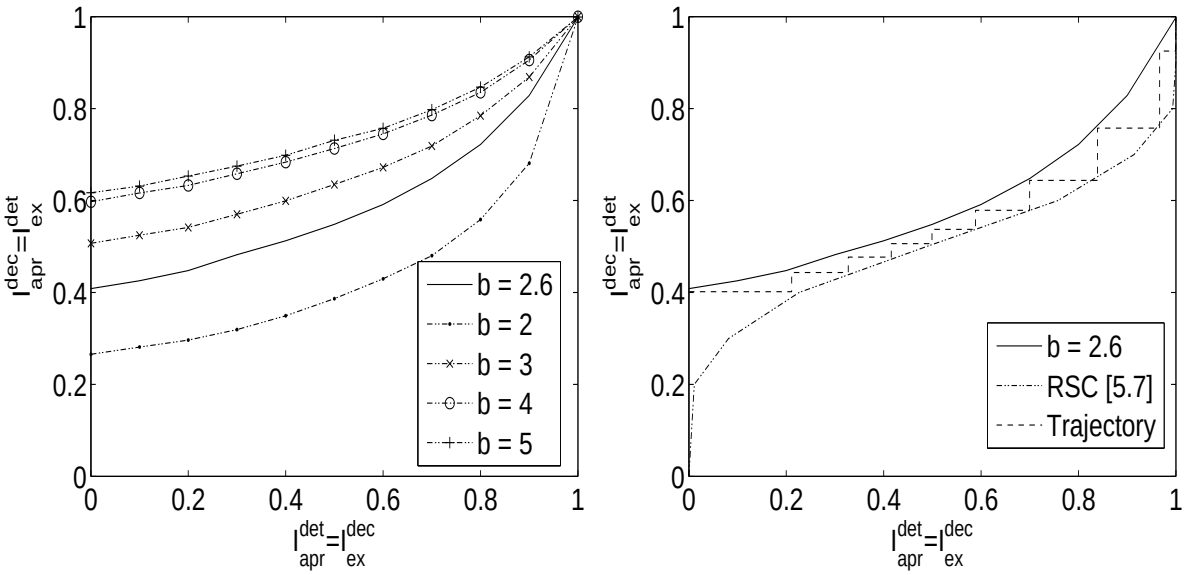

(a) (b)

Figure 5.8: EXIT chart analysis of the iterative DL-SDMA system using ECO-CQ in conjunction with $b = 2.6$ and $\boldsymbol{\alpha} = [0.4, 0.6, 0, 0]$ at $E_b/N_0 = 6$dB. (a) shows the inner EXIT-curve of the iterative DL-SDMA system using ECO-CQ. (b) shows the recorded iterative decoding trajectory of the iterative DL-SDMA system using ECO-CQ. A rate-0.5 RSC[5,7] channel coder is employed for the system. The channel model was an uncorrelated flat-fading MIMO channel and the parameters of Table 5.1 were used.

accuracy is close to the one benefiting from a perfect CIR. Compared to $b = 5$, we are able to save 1.5 quantization bits per CIR sample for both the magnitude and phase quantization by using our ECO-CQ in conjunction with $b = 3.5$ at an E_b/N_0 loss of less than 0.5 dB.

In Table 5.2, we characterized the ECO-CQ aided iterative DL-SDMA system using the minimum required number of quantization bits b for both the magnitude and phase of each CIR coefficient, while maintaining a target BER of 10^{-5}. In order to attain the target BER, the system employing conventional CQ may be required to use a 3-bit CQ to quantize the CIR, when we have $E_b/N_0 \geq 4$dB, as illustrated in Figure 5.9. On the other hand, the ECO-CQ aided system may use a reduced value of b to quantize the CIR, such as 2.9, 2.8, 2.7, and 2.6, while maintaining the same target BER. The corresponding reduced feedback overheads are listed in Table 5.2.

Table 5.1: System Parameters

Channel Encoder	rate-0.5 RSC code
Interleaver length	10^5 bits
Modulation	4QAM
Number of users	$K = 3$
Number of transmit antennas	$N_{Tx} = 6$
Dimension of transmitted signal vector of each user	$N_s^{(k)} = 2$, for $k = 1, 2, 3$.
Number of receive antennas of each MT	$N_{Rx}^{(k)} = 2$, for $k = 1, 2, 3$.

Table 5.2: Reduced feedback overhead of the ECO-CQ aided iterative DL-SDMA systems (extracted from Fig. 5.9)

	E_b/N_0 [dB]	3.5	4.5	5	6
Conv. CQ	Min. required b-bit	3	3	3	3
Conv. CQ	Min. required b-bit	3	3	3	3
	Norm. FB overhead η	1.8%	1.8%	1.8%	1.8%
ECO-CQ	Min. required b-bit	3	2.8	2.7	2.6
ECO-CQ	Min. required b-bit	3	2.8	2.7	2.6
	Norm. FB overhead η	1.8%	1.68%	1.62%	1.56%
Norm. overhead reduction ratio η_r		0	6.7%	10%	13%

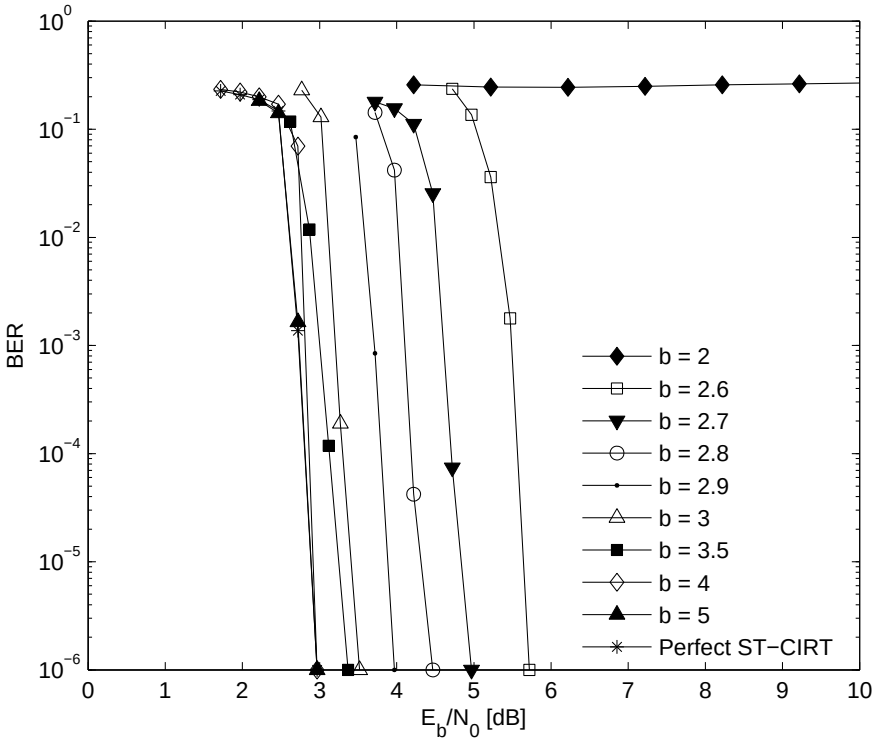

Figure 5.9: BER performance of the iterative DL-SDMA systems using ECO-CQ in conjunction with different values of b, where the $\boldsymbol{\alpha}$ of the ECQ-CQ in association with $b = 2.6, 2.7, 2.8, 2.9$ and 3.5 are $\boldsymbol{\alpha} = [0.4, 0.6, 0, 0]$, $[0.3, 0.7, 0, 0]$, $[0.2, 0.8, 0, 0]$, $[0.1, 0.9, 0, 0]$ and $[0, 0.5, 0.5, 0]$, respectively. The number of decoding iteration is $I = 12$. A rate-0.5 RSC[5,7] channel coder is employed for the system. The channel model was a flat-fading MIMO channel in associated with the normalized Doppler frequency $f_{dm-norm} = 0.001$ and the parameters of Table 5.1 were used.

5.2 Soft-Decoding Assisted MIMO CIR Recovery

Although the feedback information is typically transmitted over the strongly protected UL control channel, it may still become contaminated by transmission errors because of the unavoidable AWGN noise and fading in the wireless propagation environment. When the feedback channel is error-prone, it is important to design efficient inverse quantisers in order to reconstruct the feedback information with the minimum distortion. Hence, we proposed a soft-decoding assisted MIMO CIR recovery scheme and evaluated its performance in a TxZF/TxMMSE assisted MISO multi-user DL-SDMA system. The system model is described in Section 5.2.1. Our VQ soft decoding technique is outlined in Section 5.2.2. Finally, our simulation results are provided in Section 5.2.3.

5.2.1 System Model

In this section, we consider the multi-user DL-SDMA system illustrated in Fig. 5.1. More explicitly, the TxZF and TxMMSE algorithms detailed in Section 2.2.2.1 and 2.2.2.2 are employed as the MUT algorithm at the BS, where N_{Tx} transmit antennas are invoked. A single antenna is installed at all MTs, i.e. we have $N_{Rx}^{(k)} = 1, \forall k$. Moreover, the total number of users K is assumed to be less than the number of transmit antennas N_{Tx}. The system model of the feedback link is illustrated in Fig. 5.10.

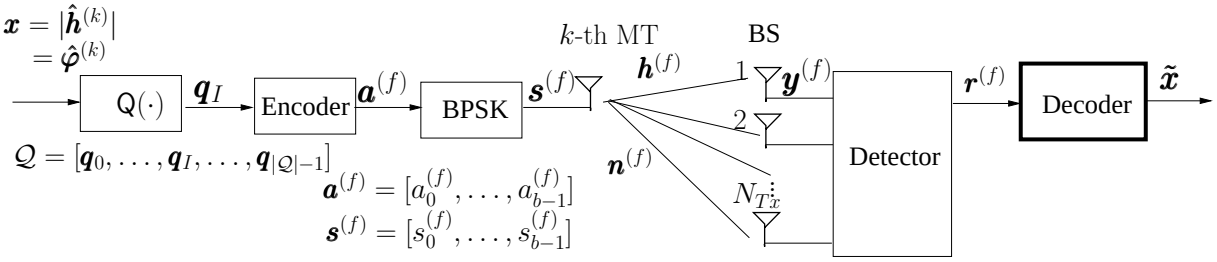

Figure 5.10: System model of the feedback link.

The entire estimated CIR vector $\hat{\boldsymbol{h}}^{(k)}$ is fed into the quantiser. The channel envelope vector $|\hat{\boldsymbol{h}}^{(k)}|$ and the channel phase vector $\hat{\boldsymbol{\varphi}}^{(k)}$ are quantized separately using the real-valued vector quantizer detailed in Section 2.3.2. The quantiser's output is one of the codewords $\boldsymbol{q}_I$ from a pre-defined codebook $\mathcal{Q}$. The index of this codeword I is then encoded into a binary bit sequence $\boldsymbol{a}^{(f)}$ and mapped to the BPSK symbols $\boldsymbol{s}^{(f)}$ ($s_i^{(f)} = \pm 1$). The superscript $(\cdot)^{(f)}$ indicates that it is a signal transmitted through the feedback channel, which distinguishes it from the notations representing the DL signals. Assuming that the codebook size is $|\mathcal{Q}| = 2^b$, a total b BPSK modulated symbols are required to represent a quantizer output. Assuming that the average energy required for feeding back a codeword is E_s, the signal $\boldsymbol{y}^{(f)}$ received at the l-th transmission instant may be formulated as

$$y_l^{(f)} = \sqrt{\frac{E_s}{b}} h_l^{(f)} s_l + n_l^{(f)},\ l = 1, \ldots, b, \tag{5.6}$$

where $h_l^{(f)}$ represents the fading gain, while $n_l^{(f)}$ is the Gaussian noise. Furthermore, provided that the phase associated with a specific fading gain $h_l^{(f)}$ is known, after removing the effects of the phase using

a matched filter detector, Equation (5.6) may be expressed as

$$r_l^{(f)} = \sqrt{\frac{E_s}{b}} |h_l^{(f)}| s_l + n_l^{(f)},\ l = 1, \ldots, b. \tag{5.7}$$

Finally, the detected signal sequence in b time slots $\boldsymbol{r}^{(f)}$ is represented as

$$\boldsymbol{r}^{(f)} = \left\{ r_1^{(f)}, r_2^{(f)}, \ldots, r_b^{(f)} \right\}, \tag{5.8}$$

which is then fed into the inverse VQ. The inverse VQ may also be termed as the VQ decoder that produces the reconstructed signal denoted as $\tilde{\boldsymbol{x}}$.

5.2.2 Hard and Soft VQ Decoder

Given the detected signal sequence $\boldsymbol{r}^{(f)}$, it is straightforward to estimate the encoded bit sequence $\hat{\boldsymbol{a}}^{(f)}$. Then, it is possible to extract the estimated VQ index $\hat{I}$ and to reconstruct the DL CIR vector $\tilde{\boldsymbol{h}}^{(k)}$ as $\boldsymbol{q}_{\hat{I}}$. This decoding method will be referred to as the hard-output VQ decoder. Alternatively, the CIRs of the

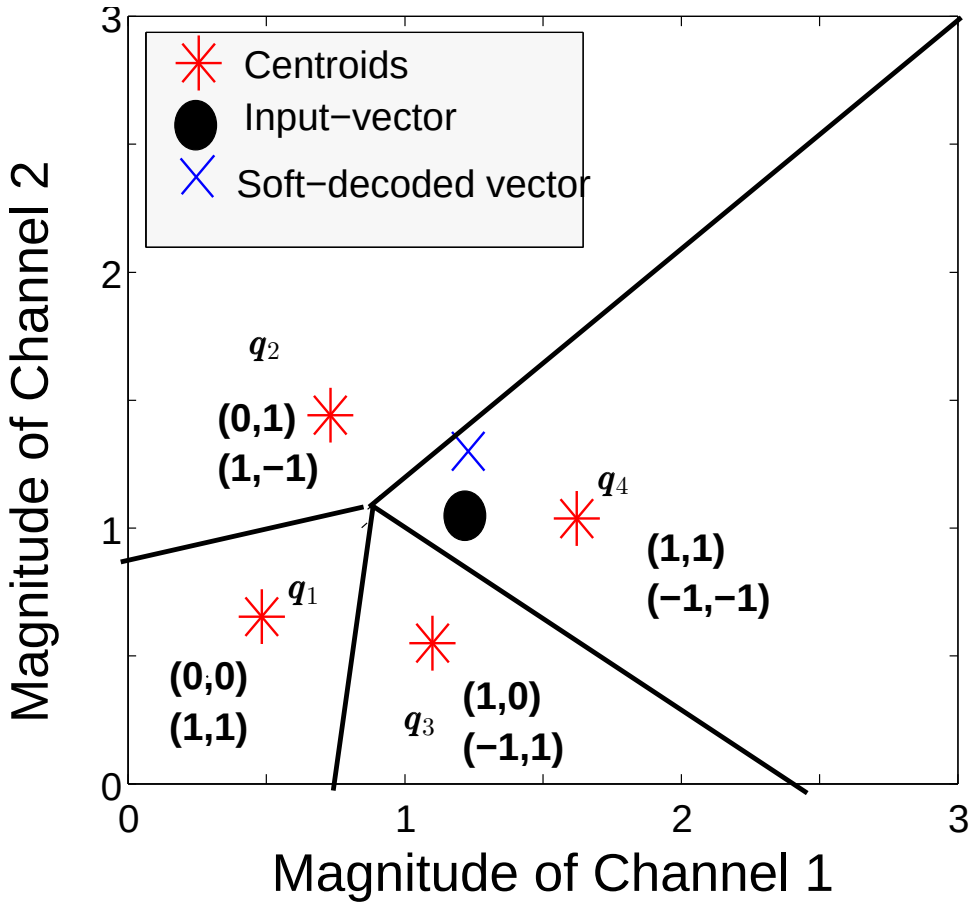

Figure 5.11: An example of soft VQ decoding, when we have $N_{Tx} = 2$, $N_{rx} = 1$, $|\mathcal{Q}| = 4$ and the quantiser's input vector is the CIR magnitude vector of $\boldsymbol{x} = |\boldsymbol{h}|$.

DL MIMO channel signalled back to the MUT may be recovered at the BS with the aid of a soft decoder, which may be carried out by a non-linear MMSE estimator [161]. Let the vector $\boldsymbol{r}^{(f)}$ of Equation (5.8) host the b observations corresponding to $\boldsymbol{x}$. Then, $\boldsymbol{x}$ is reconstructed by the soft VQ decoder as [161]

$$\tilde{\boldsymbol{x}} = \sum_{j=1}^{|\mathcal{Q}|} \boldsymbol{q}_j P\left(I = j | \boldsymbol{r}^{(f)}\right), \tag{5.9}$$

where $\boldsymbol{q}_j$, $j = 1, \ldots, |\mathcal{Q}|$, is the codeword or centroid of the jth VQ partition. In Equation (5.9) $P\left(I = j|\boldsymbol{r}^{(f)}\right)$ represents the *a-posteriori* probability of the VQ codebook index $I = j$, given the observation vector of $\boldsymbol{r}^{(f)}$, which may be expressed as

$$P\left(I = j|\boldsymbol{r}^{(f)}\right) = \frac{P\left[I = j\right] p\left[\boldsymbol{r}^{(f)} \mid I = j\right]}{p\left(\boldsymbol{r}^{(f)}\right)}, \tag{5.10}$$

where $P\left[I = j\right]$ is the *a-priori* probability of having $I = j$, which can be found according to the specific channel statistics encountered, while $p\left[\boldsymbol{r}^{(f)} \mid I = j\right]$ is the Probability Density Function (PDF) of the event, when the natural binary representation of $I = j$ is transmitted over the feedback channel. Assuming that the feedback channel is memoryless, we may have

$$p\left[\boldsymbol{r}^{(f)} \mid I = j\right] = \prod_{l=1}^{b} p\left[r_l^{(f)} \mid s = s_l\right], \tag{5.11}$$

where $p\left[r_l^{(f)} \mid s_l\right]$ is the probability of receiving $r_l^{(f)}$, given that s_l was transmitted, which may be expressed as

$$p\left[r_l^{(f)} \mid s = s_l\right] = \frac{1}{\sqrt{2\pi N_0}} \exp\left(-\frac{\left[r_l^{(f)} - |h_l^{(f)}|s_l\right]^2}{2N_0}\right), \tag{5.12}$$

where N_0 is the variance of the Gaussian noise. Finally, $p\left(\boldsymbol{r}^{(f)}\right)$ in Equation (5.10) is the probability of receiving $\boldsymbol{r}^{(f)}$, which can be expressed as

$$p\left(\boldsymbol{r}^{(f)}\right) = \sum_{j=1}^{|\mathcal{Q}|} P\left[I = j\right] p\left[\boldsymbol{r}^{(f)} \mid I = j\right]. \tag{5.13}$$

The quantizer's input vector $\boldsymbol{x}$ may be reconstructed at the BS by substuiting Equation (5.12) into Equations (5.11) (5.13) and (5.10) and finally into Equation (5.9).

An example of soft VQ decoding is illustrated in Fig. 5.11, when we have $N_{Tx} = 2$, $N_{rx} = 1$, $|\mathcal{Q}| = 4$ and the quantiser's input vector $\boldsymbol{x}$ is the CIR magnitude vector $|\boldsymbol{h}|$. The input vector represented by the black dot is located in the third partition and consequently it is quantized as $\boldsymbol{q}_4$. The index $I = 4$ is then encoded as $\boldsymbol{a}^{(f)} = [1,\ 1]$ using $b = 2$ bits, which is the binary representation of $(I - 1)$. The modulated symbol sequence becomes $\boldsymbol{s}^{(f)} = [-1,\ -1]$ when using BPSK modulation. After transmission over an error-contaminated channel, the signal received at the output of the detector is given by $\boldsymbol{r}^{(f)} = [-0.24 - 0.83]$. Upon using the hard-ouput VQ decoder, the estimated bit sequence $\hat{\boldsymbol{a}}^{(f)}$ and the estimated index VQ $\hat{I}$ are $[1,\ 1]$ and $\hat{I} = 4$, respectively. The resultant reconstructed vector $\tilde{\boldsymbol{x}}$ is $\boldsymbol{q}_4$. By contrast, the soft-output VQ decoder calculates the four probabilities $P\left(I = j|\boldsymbol{r}^{(f)}\right)$ based on the received vector $\boldsymbol{r}^{(f)}$ and reconstructs the quantized vector using Equation (5.9). The resultant reconstructed vector $\tilde{\boldsymbol{x}}$ of this example is illustrated by a cross in Fig. 5.11, which has to be subjected to hard-decision, in order to produce a legitimate codeword in the codebook.

5.2.3 Simulation Results

In the simulations, we have employed a DL-SDMA system having two transmit antennas at the BS, a single receive antenna at the MTs, and two MTs communicated with the BS at the same time. The

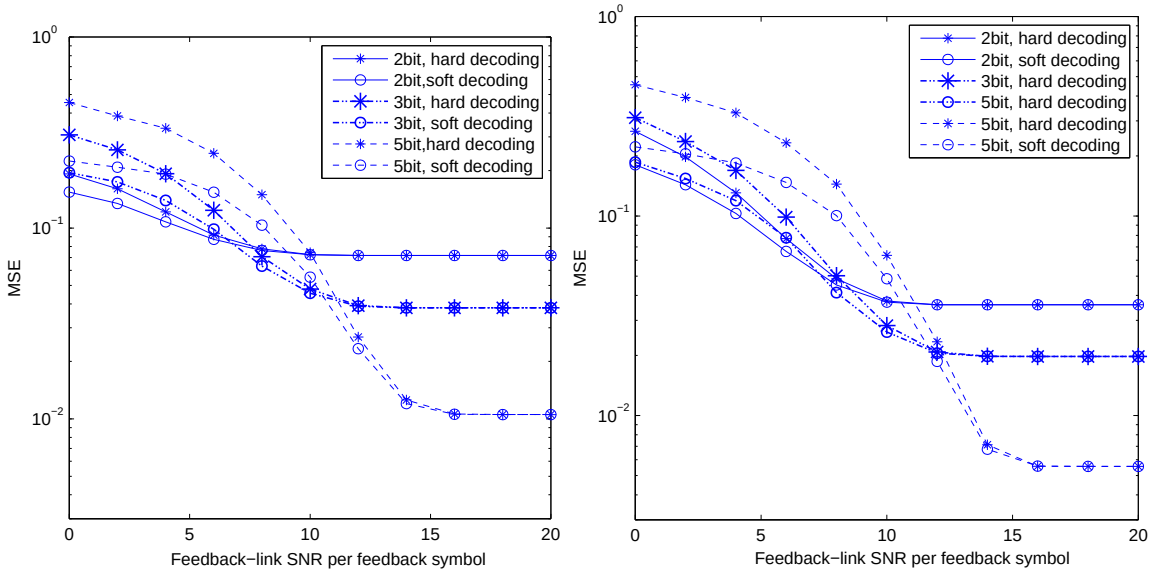

(a) Spatially Independent Channel (b) Spatially Correlated Channel

Figure 5.12: MSE between the quantiser's input $\boldsymbol{x}$, which is the unquantized 2-dimensional channel envelope vector $\boldsymbol{x} = |\boldsymbol{h}^{(k)}|$, and the decoder's output, which is the corresponding reconstructed vector $\tilde{\boldsymbol{x}} = |\tilde{\boldsymbol{h}}^{(k)}|$ for a) i.i.d. channel; b) for spatially correlated channel with a correlation coefficient of $\rho = 0.8$.

TxZF and TxMMSE schemes of Section 2.2 were employed at the BS to pre-eliminate the inter-user interference. The real-valued channel envelope and phase rotation vector quantisers are employed at the MTs to feed back the channel magnitude vector $|\boldsymbol{h}^{(k)}|$ and phase vector $\boldsymbol{\varphi}^{(k)}$ separately. BPSK modulation is used for both the DL data transmission as well as for the feed back CIR transmission. Two scenarios of the feedback link are simulated, in the first one the feedback link is an AWGN channel. In other one the feedback channel is a Rayleigh fading channel plus the ubiquitous AWGN noise. The simulated SNRs of the feedback link varied from 0dB to 20dB.

Fig. 5.12 portrays the MSE between the quantiser's input $\boldsymbol{x}$, which is the unquantized 2-dimensional channel envelope vector $\boldsymbol{x} = |\boldsymbol{h}^{(k)}|$, and the decoder's output, which is the corresponding reconstructed vector $\tilde{\boldsymbol{x}} = |\tilde{\boldsymbol{h}}^{(k)}|$. The DL channel $\boldsymbol{h}^{(k)}$ is either spatially independent as shown in Fig. 5.12(a), or spatial correlated with a correlation coefficient $\rho_{h_1 h_2} = 0.8$ as shown in Fig. 5.12(b). The feedback link is a AWGN channel. Observed in the figures that a lower MSE is achieved by using the soft decoding algorithm than that of the hard decoding scheme, especially when the feedback link's SNR is poor. Moreover, it is more sensible to employ a low feedback rate, for example a 2-bit quantiser, when the feedback link's SNR is low, but to employ more feedback bits when the feedback link SNR is sufficiently high. Furthermore, a lower MSE is achieved for spatially correlated DL channels, when using the same number of quantization bits. This is because vector quantisation becomes more efficient, when the elements of the input vector to be quantized are correlated with each other, as explained in Section 2.1.3.

Fig. 5.13 characterizes the DL BER performance versus a) the DL SNR; and b) the feedback-link SNR at a DL SNR of 14dB, when TxMMSE is employed. The DL channel is an i.i.d. Rayleigh fading channel, while the feedback channel imposes only AWGN. Moreover, the DL channel's phase vector

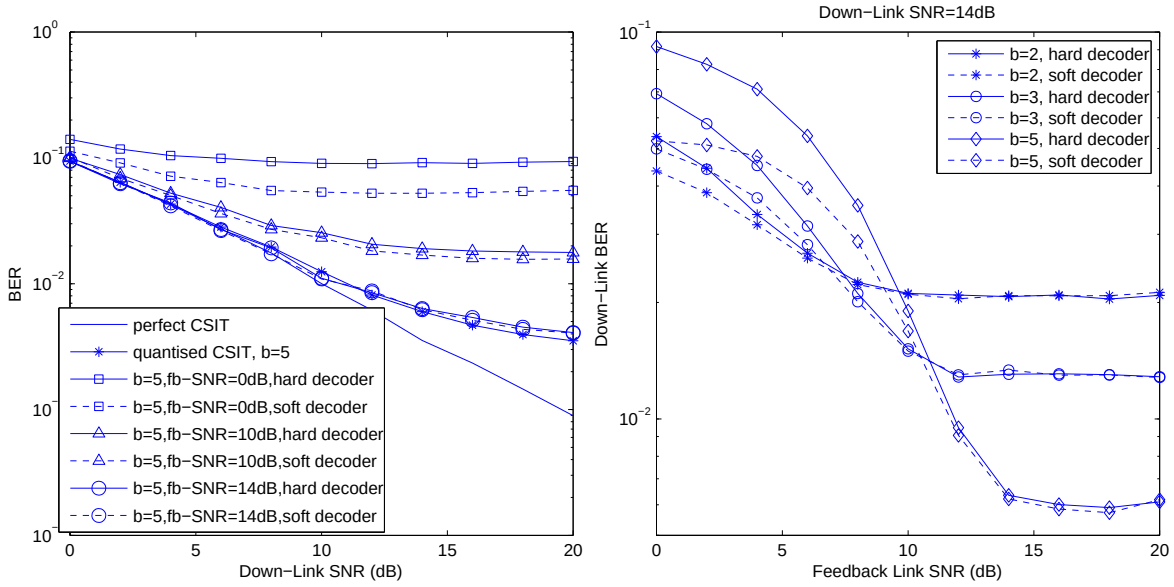

(a) Down-Link BER versus Down-Link SNR (b) Down-Link BER versus Feedback-Link SNR

Figure 5.13: TxMMSE: Down-link BER performance versus a) down-link SNR per bit; b) feedback-link SNR per symbol when the down-link SNR is equal to 14dB for a MIMO channel using two transmit antennas, two receive antennas and supporting two users, when communicating over i.i.d. Rayleigh channels. The channel's phase vector $\boldsymbol{\varphi}$ is assumed to be perfectly known, while the channel's envelope vector $|\boldsymbol{h}|$ is quantised, signalled and then reconstructed at the BS using both the hard and soft VQ decoder.

$\boldsymbol{\varphi}^{(k)}$ is assumed to be perfectly known. The channel's envelope vector $|\boldsymbol{h}^{(k)}|$ is quantised using 5 bits in Fig. 5.13a, and using two, three and five bits in Fig. 5.13b. In Fig. 5.13a, the BER performance associated with perfect CSIT and 5-bit quantised CSIT is also presented for comparison. It is demonstrated in Fig. 5.13a that the benefits of using soft VQ decoding become more obvious, when the feedback-link experiences a low SNR, but they become less obvious as the feedback-link's quality improves. These findings are consistent with the MSE results shown in Fig. 5.12. This is also demonstrated in Fig. 5.13b, where the DL SNR is fixed to 14dB and the AWGN feedback-link SNR increases from 0dB to 20dB. Fig. 5.13 also demonstrated that the best DL performance may be achieved by employing an adaptive feedback scheme. More explicitly, it is beneficial to employ a 2-bit quantiser combined with soft VQ decoding, when the feedback-link SNR is below about 5dB, then switching to a 3-bit quantiser combined with soft decoding until the feedback-link SNR reaches 10dB. When the feedback-link SNR is between 10dB and 15dB, using a 5-bit quantiser combined with soft decoding is capable of providing a slightly reduced DL BER compared to the one using hard VQ decoding. Once the feedback-link SNR becomes higher than 15dB, the benefits of using soft decoding become marginal and hence employing low-complexity hard decoding becomes more attractive owing to its reduced complexity.

Figs. 5.14 shows the BER performance of the same system - $N_{Tx} = 2$, $N_{Rx}^{(k)} = 1$, $K = 2$ - while employing the soft VQ decoding aided CIR recovery for the TxZF based preprocessing schemes, and communicating over correlated Rayleigh fading MIMO channels having a correlation coefficient of $\rho_{h_1 h_2} \approx 0.8$. The results of Figs. 5.14 demonstrate that provided the AWGN feedback-link SNR becomes higher than 5dB in the absence of fading, or becomes higher than 25dB in the presence of Rayleigh fading,

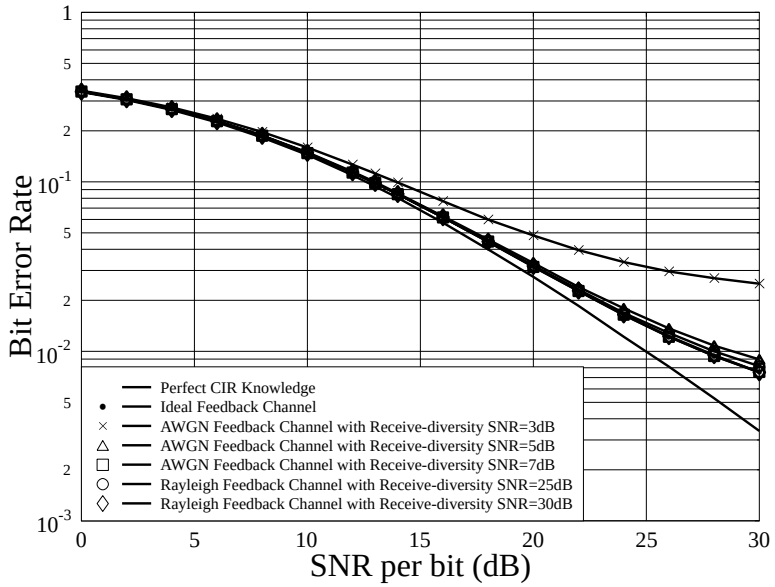

Figure 5.14: TxZF: BER versus SNR per bit performance of a MIMO channel using two transmit antennas, two receive antennas and supporting two users, when communicating over correlated Rayleigh fading channels associated with $\rho \approx 0.8$, where a total of 10-bit are used for quantising every CIR tap of each user.

the performance degradation imposed by the error-contaminated feedback link is negligible compared to the DL BER performance using quantised CSIT.

5.3 Channel Prediction and PVQ for a Realistic Finite-Delay Feedback Channel

The CSI reconstructed at the BS is usually out-dated because of the propagation delay plus the signal processing delay and the control protocol-induced delay as illustrated in Fig. 5.2 of Section 5.1.1. Naturally, channel prediction techniques can be used to mitigate the effect of signalling delay by predicting the channel's envelope into the future [162]. We proposed a periodically operated CIR update scheme employing a channel predictor at the BS, which mitigates the effects of feedback delay. Furthermore, we employed a Predictive Vector Quantizer (PVQ), which exploits both the spatial- and temporal-domain correlation in order to that of significantly reduce the feedback bit rate compared to the conventional VQ. The system model of a TxMMSE aided MISO DL SDMA system having a realistic feedback channel is introduced in Section 5.15. The channel prediction and predictive vector quantization algorithms are introduced in Section 5.3.2 and Section 5.3.3, respectively, while our simulation results are provided in Section 5.3.4.

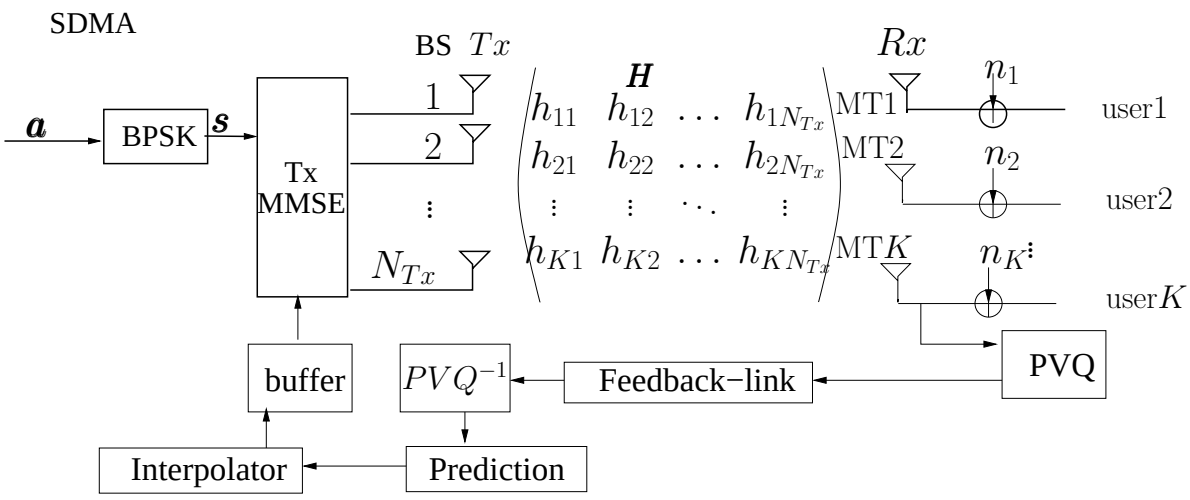

Figure 5.15: Model of a TxMMSE aided MISO multi-user SDMA system using channel prediction and predictive vector quantization for CIR feedback.

5.3.1 System Model

Let us consider a MISO multi-user system employing a total of N_{Tx} DL transmit antennas and a single receive antenna at each MT, as shown in Fig. 5.15. The system's throughput may be increased by a factor of K ($K \leq N_{Tx}$) with the aid of a TxMMSE scheme. In order to provide the CIRs for the BS, the MTs' CIRs $\boldsymbol{h^{(k)}}[n]$ ($N_{Tx} \times 1$) have to be sampled and estimated periodically, which are then forwarded to the quantizer for digitisation. Instead of the quantized CIR $\hat{\boldsymbol{h}}$ itself, the quantized CIR prediction error $\boldsymbol{e}_q$ is represented as a PVQ codeword at the index I_i, which is then fed back to the BS. The PVQ codebook is designed off-line and assumed to be known by both the MTs and BSs. As a result, the BS reconstructs the CIR tap $\tilde{\boldsymbol{h}}^{(k)}[n]$ by inverse quantization. The most recent V number of reconstructed CIR taps are fed into the channel predictor to predict the future CIRs taps. Then an interpolator is invoked to reconstruct the CIR taps. The predicted and interpolated CIR taps will be restored and periodically updated in the BS's DL transmit buffer. This process, as seen in Fig. 5.15, provides the predicted CIRs, which are closer to the actual CIRs than in the absence of prediction.

5.3.2 Channel Predictor

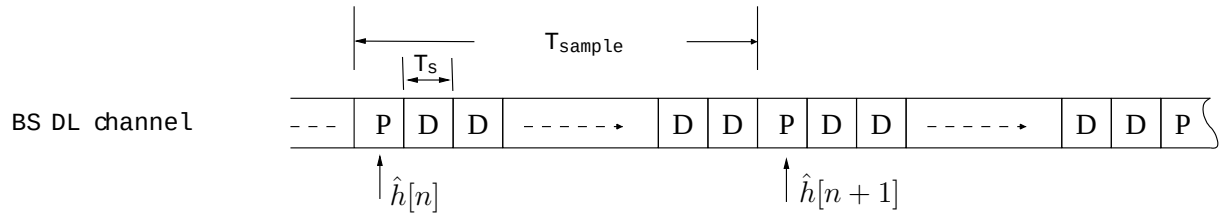

Figure 5.16: The pilot-aided CIR estimation

The DL channel's complex-valued envelope is sampled with the aid of pilot symbols and estimated at every T_{sample} seconds, and it is represented by a sequence $\hat{h}[1],\ \ldots,\ \hat{h}[n],\ \ldots,\ \hat{h}[n+v],\ldots$. The temporal correlation between $h[n]$ and $h[n+v]$ may be characterised by the zero-th order Bessel function

$J_0(\cdot)$ of the first kind, as discussed in Section 2.1.2.2. More explicitly, it is formulated as [93]

$$\rho(v) = J_0(2\pi f_{dm} v T_{sample}), v = 1, 2, \ldots, \tag{5.14}$$

where f_{dm} represents the maximum Doppler frequency shift in Hz. According to the Nyquist theorem [163], the sampling rate $f_{sample} = \frac{1}{T_{sample}}$ must be in excess of $2f_{dm}$. In practice, the channel has to be over-sampled. Hence we define the over-sampling factor β. Then the relationship between f_{sample} and f_{dm} is formulated as $f_{sample} = \beta f_{dm}$. Forthermore, we normalise the sampling rate f_{sample} and the maximum Doppler frequency shift f_{dm} to the data symbol rate, which result in

$$\begin{aligned} f_{dm-norm} &= f_{dm} T_s \\ f_{sample-norm} &= f_{sample} T_s \\ f_{sample-norm} &= \beta f_{dm-norm}. \end{aligned} \tag{5.15}$$

Then, Equation (5.14) may be rewritten as

$$\rho(v) = J_0(2\pi \frac{1}{\beta} f_{dm-norm} v), \; v = 1, 2, \ldots. \tag{5.16}$$

It is evident that the correlation coefficient $\rho(v)$ will increase, when having an increased over-sampling factor β.

According to the autocorrelation coefficient of Equation (5.16), the predicted CIR at the n-th time instant $\hat{h}_p[n]$ may be modelled by the Auto-Regressive (AR) process of [93]

$$h_p[n] = \sum_{v=1}^{V} a[v] \hat{h}[n-v] + n[v], \tag{5.17}$$

where V is the number of previously estimated CIRs, $\hat{h}[n-v]$ represents the CIRs at time instant $[n-v]$, $a[v]$ represents the AR predictor coefficients and $n[v]$ represents the DL Gaussian noise having a variance N_0. The design of $a[v]$ is detailed below.

AR Predictor Coefficient Vector for a SISO Channel

Provided that both the normalised maximum Doppler frequency $f_{dm-norm}$ as well as the number of previous channel taps V and the over-sampling factor β are known, the real-valued predictor coefficient vector $\boldsymbol{a} = (a[1], \ldots, a[V])$ can be derived as follows [93].

1. Calculate

$$\rho(v) = J_0(2\pi \frac{1}{\beta} f_{dm-norm}), v = 0, 1, \ldots, V; \tag{5.18}$$

2. Construct the autocorrelation matrix of the channel:

$$\boldsymbol{R} = \begin{pmatrix} \rho(0) & \rho(1) & \ldots & \rho(V-1) \\ \rho(1) & \rho(0) & \ldots & \rho(V-2) \\ \vdots & \vdots & \ddots & \vdots \\ \rho(V-1) & \rho(V-2) & \ldots & \rho(0) \end{pmatrix}; \tag{5.19}$$

3. Construct the autocorrelation vector of the channel

$$\boldsymbol{\rho} = \begin{pmatrix} \rho(1) \\ \rho(2) \\ \vdots \\ \rho(V) \end{pmatrix}; \tag{5.20}$$

4. Calculate the AR predictor coefficient vector $\boldsymbol{a}$

$$\boldsymbol{a} = (a[1],\ a[2],\ \ldots,\ a[V])^T = \boldsymbol{R^{-1}\rho}. \tag{5.21}$$

AR Predictor Coefficient Matrix for a MISO Channel

Provided that $f_{dm-norm}, V, \beta$ are known, the AR coefficient matrix $\boldsymbol{A}[v],\ v = 1,2,\ldots.V$ can be determined. The CIR vector $\hat{\boldsymbol{h}}[n]$ sampled at time instants n and having N_{Tx} non-zero elements may be predicted according to:

$$\boldsymbol{h}_p[n] = \sum_{v=1}^{V} \boldsymbol{A}[v]\hat{\boldsymbol{h}}[n-v] + \boldsymbol{n}[v], \tag{5.22}$$

where $\boldsymbol{A}[v]$ is a real-valued $(N_{Tx} \times N_{Tx})$ matrix.

1. Calculate

$$\rho(v) = J_0(2\pi\frac{1}{\beta}f_{dm-norm}v), v = 0,1,\ldots,V; \tag{5.23}$$

2. Construct

$$\boldsymbol{R}[ij] = E[\hat{\boldsymbol{h}}[n-i]\hat{\boldsymbol{h}}[n-j]^H] = \rho(|i-j|)\boldsymbol{I}_{N_{Tx}}; \tag{5.24}$$

3. $\boldsymbol{A}[v]$ may be calculated based on the equation:

$$\begin{pmatrix} \boldsymbol{R}[11] & \boldsymbol{R}[12] & \ldots & \boldsymbol{R}[1V] \\ \boldsymbol{R}[21] & \boldsymbol{R}[22] & \ldots & \boldsymbol{R}[2V] \\ \vdots & \vdots & \ddots & \vdots \\ \boldsymbol{R}[V1] & \boldsymbol{R}[V2] & \ldots & \boldsymbol{R}[VV] \end{pmatrix} \begin{pmatrix} \boldsymbol{A}[1]^T \\ \boldsymbol{A}[2]^T \\ \vdots \\ \boldsymbol{A}[V]^T \end{pmatrix} = \begin{pmatrix} \boldsymbol{R}[10] \\ \boldsymbol{R}[20] \\ \vdots \\ \boldsymbol{R}[V0] \end{pmatrix}. \tag{5.25}$$

The accuracy of the prediction is characterised by the MSE between the predicted CIR $\boldsymbol{h}_p[n]$ and the estimated CIR $\hat{\boldsymbol{h}}[n]$, which is formulated as

$$\xi_p = E\left[\|\boldsymbol{h}_p[n] - \hat{\boldsymbol{h}}[n]\|^2\right]. \tag{5.26}$$

The prediction-accuracy is affected by the value of V, by the over-sampling factor β and by the accuracy of the previous estimated CIRs $\hat{\boldsymbol{h}}[n-v]$.

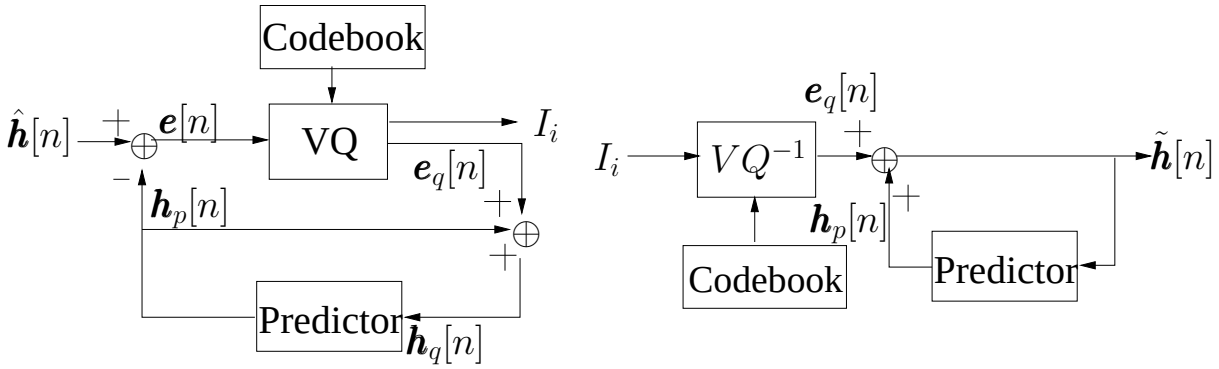

Figure 5.17: Structure of the Predictive Vector Quantizer.

5.3.3 Predictive Vector Quantizer

Fig. 5.17 shows the structure of a PVQ. Although in theory the channel predictor's order p in (5.17) and the PVQ's predictor order in Fig. 5.17 can be chosen to be different, in our design both were fixed to V. Hence the previous V number of quantized CIR taps ($\hat{\boldsymbol{h}}[n-1], \hat{\boldsymbol{h}}[n-2], \ldots, \hat{\boldsymbol{h}}[n-V]$) are used at the MTs to predict the current estimated CIR tap. The predicted value $\boldsymbol{h}_p[n]$ is then subtracted from the current estimated value $\hat{\boldsymbol{h}}[n]$ and the resultant prediction error $\boldsymbol{e}[n]$ is quantized. The quantization result $\hat{\boldsymbol{e}}[n]$ is then added to the prediction result $\boldsymbol{h}_p[n]$ to generate the quantized CIR $\boldsymbol{h}_q[n]$ for future prediction. The reason of using quantized CIRs instead of the unquantized CIRs at the MTs for channel prediction is to avoid using different predictor inputs at the BS and MTs, since at the BS only the knowledge of quantized CIRs is available. At the same time, the index I_i of the codebook representing $\boldsymbol{e}_q[n]$ is fed back to the BS. At the BS, as seen in Fig. 5.17, the PVQ decoder first converts the received codebook index I_i to the corresponding codeword. Simultaneously, an identical predictor invokes the previously reconstructed CIR taps to predict the current CIR taps. The predicted result is then added to the quantized prediction error in order to reconstruct the current CIR tap.

The PVQ quantizes the CIR tap prediction error instead of the channel's envelope or phase vector. It is clear that the former has a reduced input signal range. Based on the theorem stated in [91], the overall reproduction error $E(\|\hat{\boldsymbol{h}}[n] - \tilde{\boldsymbol{h}}[n]\|^2)$ is equal to $E(\|\boldsymbol{e}[n] - \boldsymbol{e}_q[n]\|^2)$. Hence, given a certain feedback rate, the CIR quantization error will be significantly reduced by the PVQ compared to that of the conventional VQ.

The design of the PVQ scheme shown in Fig. 5.17 has already been described in Section 5.3.2. The PVQ codebook used for quantising the prediction error $\boldsymbol{e}[n]$ can be generated using either the open-loop or the closed-loop method. In the open-loop method, the estimated CIRs $\hat{\boldsymbol{h}}[n]$ are employed for channel prediction. The resultant prediction error vectors are used as training data to generate the codebook using the Linde-Buzo-Gray (LBG) algorithm described in Section 2.3.1. The closed-loop method is based on the open-loop method, whose initial codebook is employed to generate the quantized CIRs. The quantized CIRs $\boldsymbol{h}_q[n]$ will then be used for channel prediction, and generate new prediction error vectors as updated training data. A updated closed-loop codebook is obtained using the LBG algorithm and these updated new training data. After several such design iterations, an improved codebook will be generated with the aid of the closed-loop design. When using a large PVQ codebook, the closed-loop design provides only modest improvements, but in case of a less accurate quantizer, closed-loop

design can substantially improve the accuracy of the PVQ. This is illustrated in Table 5.3, in terms of the quantization error variance versus the number of design iterations using the over-sampling rate $\beta = 10$, the quantization bits $b = 5$ and $b = 10$ bits, respectively. It shows that for $b = 5$bits, the quantization error decreases upon employing the closed-loop design, but almost no improvement is obtained, when using $b = 10$bits.

	$\xi_{\mathcal{Q}}$ for $b = 5$	$\xi_{\mathcal{Q}}$ for $b = 10$
Open-loop design	0.3128	5.15×10^{-5}
Closed-loop one iteration	0.0786	5.2×10^{-5}
Closed-loop four iteration	0.0406	5.18×10^{-5}

Table 5.3: Comparison of the quantization error variance for different number of design iterations, when using $f_s = 10 f_{dm}$, $N = 5$ and $N = 10$ bits

5.3.4 Simulation Results and Discussion

Number of BS antennas N_{Tx}	2
Number of MT antennas $N_{Rx}^{(k)}$	1
Number of users K	2
Channel code r_c	Convolutional Code, $r_c = \frac{1}{2}$
DL Modulation scheme	BPSK
MUT scheme	TxMMSE
Predictor type	Linear MMSE
Predictor order V	2
Normalised Doppler Frequency $f_{dm-norm}$	0.01
Up-sampling rate β	10

Table 5.4: System Parameters

The system parameters used in our simulations are summarised in Table 5.4. Moreover, the channels are assumed to be spatially independent flat Rayleigh fading. The interpolation between the predicted CIR taps is assumed to be perfect sinc-interpolation in order to focus our attention on the quantizer and predictor design. The feedback link is also assumed to be error-free.

Fig. 5.18 illustrates the attainable BER versus E_b/N_0 performance. In this example the DL channel estimation is assumed to be perfect and five specific scenarios were investigated concerning the knowledge of the CIR used for transmit preprocessing. The first scenario assumes that the transmitter employs perfect CIR knowledge for preprocessing. The second investigation assumes finite-precision, but zero-delay CIR knowledge provided by a VQ using $b = 8$ bits, while the third one also assumes finite-precision, zero-delay CIR knowledge, which is provided by a PVQ using $b = 6$ bits. The over-sampling factor β is set to 10. The last two scenarios assumed that the feedback delay τ was equal to the sampling interval T_{sample} and that channel prediction was employed. A VQ using $b = 12$ bits, and a PVQ using $b = 10$ bits are employed in the fourth and the fifth scenarios, respectively. The simulation results of

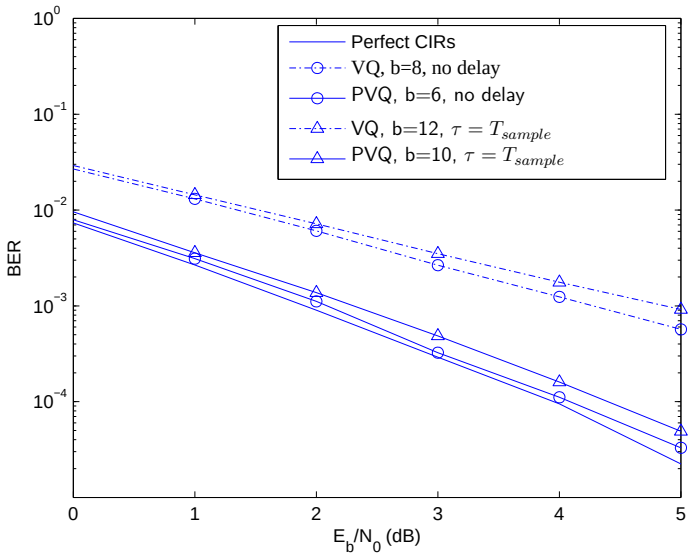

Figure 5.18: BER versus E_b/N_0 with perfect, quantized and predicted CIRs using PVQ or VQ, respectively, assuming perfect DL channel estimation.

Fig. 5.18 indicated that firstly the BER versus SNR performance is about 1dB worse than that of the one having instantaneous CSIT in the situation of having a non-zero feedback delay. Moreover, the performance of PVQ is better than that of the VQ. For example, the BER performance using a $b = 10$-bit PVQ is about 0.8dB better than that using $b = 12$-bit VQ, when having a feedback delay of $\tau = T_{sample}$.

5.4 Chapter Summary

In this chapter, we have studied the linear MUT-aided closed-loop DL SDMA system of Fig. 5.1. Several different MUT algorithms, including the TxBD, TxZF and TxMMSE detailed in Section 2.2.2 are employed in this chapter. Unlike in the previous two chapters, where the feedback channel was assumed to be noise-free and delay-free, the effect of an imperfect AWGN-contanminated feedback channel was investigated in this chapter. More explicitly, we have considered a feedback channel, which is bandwidth limited, noise-contaminated and delayed. To mitigate the degradation caused by the imperfections of the feedback channel, three algorithms were proposed in this chapter. Firstly, we proposed the ECO-CQ scheme of Section 5.1 in order to assist the system in maintaining the lowest possible CSI feedback overhead, while ensuring that an open EXIT-tunnel is still attainable, which implies maintaining an infinitesimally low BER. Secondly, in Section 5.2 we proposed a soft decoding assisted MIMO-CIR recovery scheme, which reconstructed the CIR at the transmitter as a linear combination of all codewords based on the received error-contaminated signal, so as to minimise the distortion due to AWGN-contaminated, error-prone feedback channels. Furthermore, in Section 5.3 we proposed a periodic CIR update scheme employing a channel predictor at the DL transmitter and a PVQ quantizer at the MTs, in order to mitigate the effects of feedback delay as well as to minimise the feedback overhead. The results provided in this chapter characterize three typical systems, whose system parameters are summarised in the first two columns of Table 4.3. The corresponding simulation results are also summarised in Table 4.3 and may be categorised into three groups of comparisons, which demonstrated the advantages of our schemes.

Table 5.5: Simulation Results Summary

System Parameter		Comparison Schemes	BER	Number of Feedback Bits b
Number of antennas $(N_{Tx}, N_{Rx}^{(k)})$	(2,2)	Conventional CQ shown in Fig. 5.3 and 5.4	10^{-6} at SNR=3dB	5
Number of users K	3			
Interleaver length	10^5			
Modulation	4QAM			
Coding rate r_c	0.5	Proposed ECO-CQ shown in Fig. 5.3 and 5.4	10^{-6} at SNR=3dB	3.5
Channel code	URC RSC[5,7]			
Preprocessing	TxBD			
Number of data stream N_s	2			
Number of antennas $(N_{Tx}, N_{Rx}^{(k)})$	(2,1)	Hard Decoder	$5 \cdot 10^{-2}$	5 for vector $\lvert \boldsymbol{h}^{(k)} \rvert$
Number of users K	2			
Modulation	BPSK			
Feedback-link SNR	6dB			
DL channel	i.i.d. Rayleigh	Soft Decoder	$4 \cdot 10^{-2}$	5 for vector $\lvert \boldsymbol{h}^{(k)} \rvert$
Feedback-link channel	AWGN			
Preprocessing	TxMMSE			
Number of antennas $(N_{Tx}, N_{Rx}^{(k)})$	(2,1)	Conventional VQ with channel predictor	$2 \cdot 10^{-3}$ at SNR=3.6dB	12
Number of users K	2			
Modulation	BPSK			
Coding rate r_c	0.5			
Normalised Doppler frequency $f_{dm-norm}$	0.01	Proposed PVQ with channel predictor	$2 \cdot 10^{-3}$ at SNR=3dB	10
Upsampling rate β	10			
Predictor order V	2			
Feedback delay τ	T_{sample}			
Preprocessing	TxMMSE			

Chapter 6

Spatial Modulation Aided Open-Loop and Closed-Loop Single-User MIMO System

In this chapter, a single-user MIMO system using the recently proposed Spatial Modulation (SM) [27] scheme will be investigated, which employs a Space Shift Keying (SSK) scheme [7]. The SSK modulated information bits are conveyed by the indices of the transmit antenna by exploiting the relative independence of the channel fading associated with different transmit antennas. According to the information bits, only one transmit antenna is activated during each time slot, which reduces the complexity both at the transmitter as well as at the receiver.

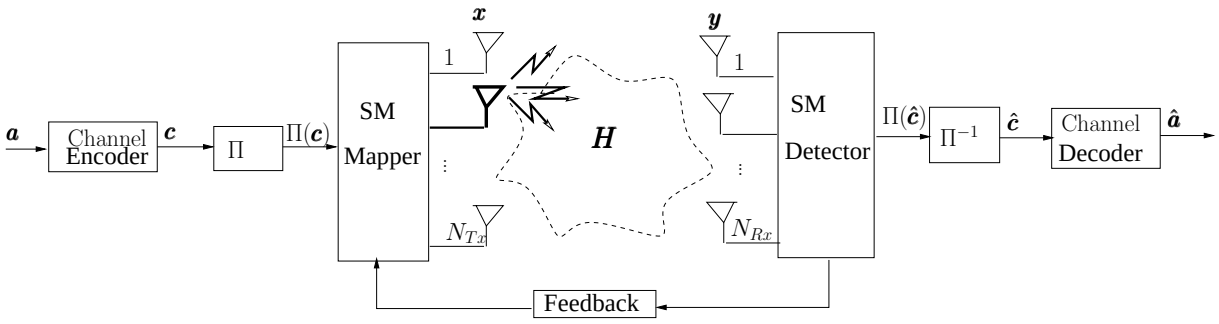

Figure 6.1: System model of a spatial modulation aided closed-loop single-user system.

Unlike in the previous chapters, both open-loop and closed-loop designs will be discussed. The novel contributions of this chapter are:

1. An open-loop Space Time Space Shift Keying (ST-SSK) scheme is proposed for systems having more than two transmit antennas in order to achieve transmit diversity. This scheme is capable of achieving a maximum transmit diversity order of $(N_{Tx} - 1)$ when using $L = (N_{Tx} - 1)$ time slots. Moreover, the proposed scheme is more robust to channel estimation errors than the original SSK modulation [7].

2. A novel closed-loop feedback-aided phase rotation regime is proposed for systems having two transmit antennas, which achieves the maximum attainable second-order transmit diversity and it is resilient to both the spatial correlation of the channels, as well as to channel estimation errors.

It also outperforms the original SSK modulation of [7] in the scenario of having Rician fading channels.

3. A novel closed-loop feedback-aided power allocation regime is proposed, which achieves an additional transmit diversity gain, increases the Euclidean distance between the SSK modulated symbols and enhances the robustness of SSK modulation both to the channel's spatial correlations and to channel estimation errors.

4. A novel diagonal linear dispersion code is proposed, which is capable of achieving the maximum attainable transmit diversity gain or multiplexing gain, while obeying the usual diversity versus multiplexing gain trade-off. Moreover, the proposed scheme eliminates the requirement of synchronisation between transmit antennas and reduces the complexity of the receiver by activating only a single transmit antenna during each transmission time slot.

This chapter is organised as follows. An overview of the spatial modulation scheme is provided in Section 6.1. Then, three novel schemes, namely the open-loop ST-SSK designed for systems having more than two transmit antennas, the closed-loop feedback-aided phase rotation conceived for systems having two transmit antennas and the closed-loop feedback assisted power allocation are proposed in Section 6.2 in order to achieve a useful transmit diversity for SSK modulation. Moreover, transmit diversity assisted spatial modulation is discussed in Section 6.3, where a novel scheme referred to as a diagonal linear dispersion code is proposed and combined with the ST-SSK scheme. Finally, the summary of this chapter is provided in Section 6.4.

6.1 Overview of Spatial Modulation

The main contributions on the subject of spatial modulation are summarised in Table 6.1. The concept of SM may be traced back to [164], which has then been further developed in [165] and [166]. The term of SM has been introduced in [27] by Mesleh and Haas. A comprehensive summary of the research carried out by Mesleh and Haas [169–172] was provided in [28], where several important facets of SM were detailed, including the detector's design, the attainable BER and the receiver's complexity in comparison to other MIMO schemes. Besides Haas and his team, Jeganathan *et al.* [7, 167, 173] pointed out the constraints of the detector schemes advocated in [27, 28], and proposed an optimal detector for SM in [167], complemented by its closed-form BER analysis. Moreover, Jeganathan *et al.* [7, 167, 173] proposed a scheme termed as SSK in [7] and provided its comprehensive analysis, which may be considered as a simplified or special case of SM. Based on the milestone contributions in [7, 28, 167], further research has been dedicated to this scheme, leading to more sophisticated SM schemes in [173–178].

In this section, an overview of the SM scheme is provided. In Section 6.1.1, bit-to-symbol mapping and the detection algorithms are detailed. Then in Section 6.1.2, a comparison of SSK modulation and conventional Amplitude Phase Modulation (APM) is offered in order to provide further insights. Finally, in Section 6.1.3, the performance evaluation of the SM scheme is offered.

Table 6.1: Major contributions addressing spatial modulation.

Author(s)	Contribution
[164] Chau and Yu 2001	proposed the idea of space shift keying and a corresponding transceiver algorithm.
[165] Haas *et al.* 2002	proposed a Walsh matrix aided multiplexing scheme for a system having four transmit antennas, which activated a single transmit antenna each time and employed BPSK modulation.
[166] Mesleh *et al.* 2005	extended the scheme proposed in [165] for QPSK by exploiting the properties of the DFT matrix.
[27] Mesleh *et al.* 2006	proposed the concept of spatial modulation.
[28] Mesleh *et al.* 2008	characterized several important facets of spatial modulation, such as its detector design, its BER and receiver complexity in comparison to other MIMO schemes. The authors also considered the effects of channel imperfections in both uncoded and coded situations.
[167] Jeganathan *et al.* 2008	detailed the constraints imposed by the detector proposed in [27, 28], and conceived an optimal detector in conjunction with its closed-form BER analysis.
[7] Jeganathan *et al.* 2009	restated the concept of space shift keying in conjunction with comprehensive analysis, which is completely different from the one in [164].
[168] Serafimovski *et al.* 2010	proposed the concept of "fractional-bit encoded spatial modulation", which becomes applicable to an arbitrary number of transmit antennas.

6.1.1 System Model

The general system model consists of N_{Tx} transmit and N_{Rx} receive antennas, which is illustrated in Fig. 6.2. A random sequence of independent bits $\boldsymbol{a} = [a_1, \ldots, a_{N_a}]$ enters the channel encoder, which produces the vector $\boldsymbol{c} = [c_1, \ldots, c_{N_c}]$, where N_a and N_c represent the number of channel encoder input and output bits, respectively. The resultant coding rate r_c becomes $r_c = \frac{N_a}{N_c}$. The pseudo-randomly interleaved encoded bits $\Pi(\boldsymbol{c})$ then enter an SM bit-to-symbol mapper, where groups of $m = \log_2(MN_{Tx})$ bits are mapped to a constellation vector formulated as

$$\boldsymbol{x} = \begin{bmatrix} 0 & \ldots & 0 & \underset{\substack{\uparrow \\ j-\text{th position}}}{\sqrt{mE_b}s_i} & 0 & \ldots & 0 \end{bmatrix}^T, \tag{6.1}$$

where E_b represents the average energy of a single bit, and s_i $(1 \leq i \leq M)$ is the j-th element of the transmitted vetor $\boldsymbol{x}$ hosting the modulated symbol using M-level conventional Amplitude Phase Modulation (APM) with unity power. Therefore, the N_{Tx}-element transmitted signal vector $\boldsymbol{x}$ satisfies the power constraint of $E_{\boldsymbol{x}}[\boldsymbol{x}^H\boldsymbol{x}] = mE_b$. The modulated signal is then transmitted over the $(N_{Rx} \times N_{Tx})$-element wireless channel $\boldsymbol{H}$, which is then contaminated by an N_{Rx}-dimensional additive white Gaussian noise

vector $\boldsymbol{n} = [n_1, \ldots, n_{N_{Rx}}]^T, n_j \sim \mathcal{CN}(0, N_0)$, where N_0 represents the noise variance. The received signal is given by $\boldsymbol{y} = \boldsymbol{Hx} + \boldsymbol{n}$. At the receiver side, the SM detector estimates the transmitted bits using the same mapping table as the one employed at the transmitter.

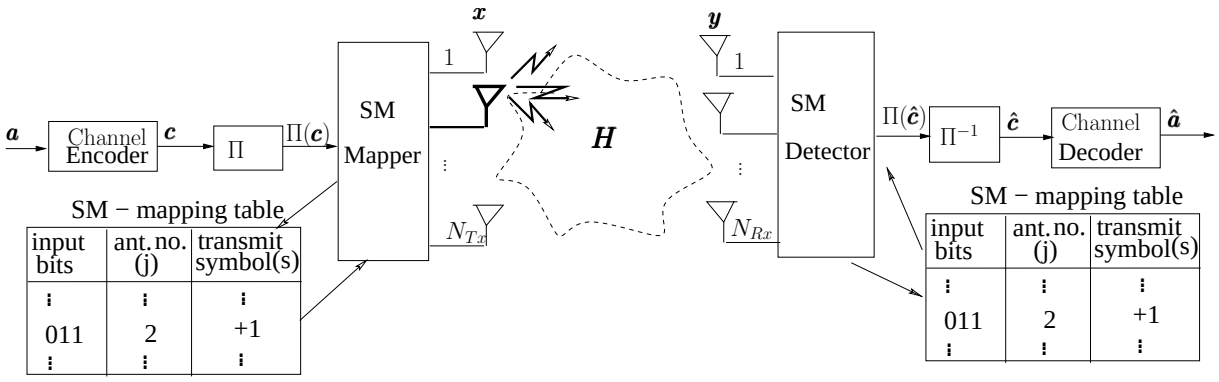

Figure 6.2: A SM aided MIMO system having N_{Tx} transmit and N_{Rx} receiver antennas.

SM Mapping

Spatial modulation consists of a group of m bits that are mapped to a vector $\boldsymbol{x}$ having only a single non-zero element $\sqrt{mE_b}s_i$. Hence, only the j-th transmit antenna will be activated to transmit the modulated signal s_i. The received signal $\boldsymbol{y}$ can be formulated as

$$\boldsymbol{y} = \sqrt{mE_b}\boldsymbol{h}_j s_i + \boldsymbol{n}, \tag{6.2}$$

where $1 \leq j \leq N_{Tx}$, $1 \leq i \leq M$, and $\boldsymbol{h}_j$ represents the j-th column of the channel matrix $\boldsymbol{H}$. Assuming $N_{Tx} = 4$ and that BPSK is employed, the SM mapping rules are illustrated in Table 6.2. When the input bits are "011" for example, the second transmit antenna will be activated, and the transmit symbol is "+1". More generally, the index of the activated transmit antenna is determined by the first two input bits, while the transmitted BPSK symbol depends on the third bit. We may conclude hence that SM essentially divides the input data stream into two sub-streams. The information in one of the sub-streams consists of $m_1 = \log_2 N_{Tx}$ bits/symbol and it is conveyed by the indices of the activated transmit antennas, hence it is SSK modulated [7]. Employing SSK modulation is evidently the key feature of SM, which distinguishes SM from any other MIMO schemes. The other information stream consists of $m_2 = \log_2 M$ bits/symbol which are conveyed using the conventional APM scheme and are transmitted through a $(1 \times N_{Rx})$-element SIMO channel.

SM Detection

The detection of the APM symbols depends on the detection of the SSK modulated symbols, since the activated $(1 \times N_{Rx})$-element SIMO channel is determined by the SSK modulated symbols. This is different from the transmit eigen-beamforming scheme discussed in Chapter 4, where the MIMO channel is decomposed into independent orthogonal subchannels and the BER performances of the subchannels (eigen-beams) are independent of each other. Therefore, the optimal detection algorithm jointly detects the APM symbols and the SSK modulated symbols using the Maximum Likelihood (ML) criterion [167].

Input bits	Activated antenna index	Transmit Symbol
000	1	-1
001	1	+1
010	2	-1
011	2	+1
100	3	-1
101	3	+1
110	4	-1
111	4	+1

Table 6.2: SM Mapping table for a system having $N_{Tx} = 4$ transmit antenna, using BPSK modulation and transmit 3 bits per symbol.

Assuming that the channel matrix $\boldsymbol{H}$ is perfectly known, the index of the activated antenna $\hat{j}$ and the index of the modulated symbol $\hat{i}$ is jointly determined by [167]

$$\begin{aligned}[\hat{j},\ \hat{i}] &= \arg\min_{j,\ i}\left(||\boldsymbol{y} - \sqrt{mE_b}\boldsymbol{h}_j s_i||^2\right) \\ &= \arg\max_{j,\ i}\left(2\sqrt{mE_b}\Re\left(\left(\boldsymbol{h}_j s_i\right)^H \boldsymbol{y}\right) - mE_b||\boldsymbol{h}_i s_i||^2\right).\end{aligned} \tag{6.3}$$

Following SM detection, the signal is demodulated, deinterleaved and decoded correspondingly.

6.1.2 Comparison of SSK Modulation and APM

Understanding the SSK modulation philosophy is the key to the understanding of SM, since the former one is the key component of the latter one. Hence, in this section we compare the M-level SSK modulation scheme to the corresponding conventional M-level APM arrangement from three different perspectives, namely their constellation diagrams, the Euclidean distances between any two modulated symbols and their BER performances. For the sake of their fair comparison, we assumed that the energy of the modulated symbol E_s is unity. Moreover, the APM modulated symbols are transmitted through a $(1 \times N_{Rx})$-element SIMO fading channel $\boldsymbol{h}_j$, while the N_{Tx}-level SSK modulated symbols activates one out of N_{Tx} transmit antennas, and also transmitted through a $1 \times N_{Rx}$-element SIMO fading channel, whose power is normalised by a factor of $\frac{1}{N_{Rx}}$.

For SSK modulation, the modulated symbols are faded according to the different transmit antennas' CIRs denoted as $\boldsymbol{h}_j (1 \leq j \leq N_{Tx})$. For example, the constellation diagram of the SSK modulated symbols is portrayed in Fig. 6.3a, when we have $N_{Tx} = 4,\ N_{Rx} = 1$ and $\boldsymbol{h} = [0.51 + 0.19i,\ \ 0.03 - 0.06i,\ \ -0.39 - 0.69i,\ \ 0.27 - 0.43i]$. The constellation diagram of the 4QAM constellation is also portrayed in Fig. 6.3b for comparison. It is evident that the transmitted constellation points of APM are independent of the channel and are time-invariant, while the transmitted signal constellation points of SSK modulation are channel dependent.

Besides the constellation diagrams, we are also interested in two types of Euclidean distances, namely in the Euclidean distance of the modulated symbols before transmission denoted as d_{Tx}, and in the Euclidean distance of the modulated symbols after transmission over a noise-free fading channel denoted as d_{Rx}. The Euclidean distances d_{Tx} using APM may be formulated as $d_{Tx}^{APM} = |s_i - s_j|$, which is illus-

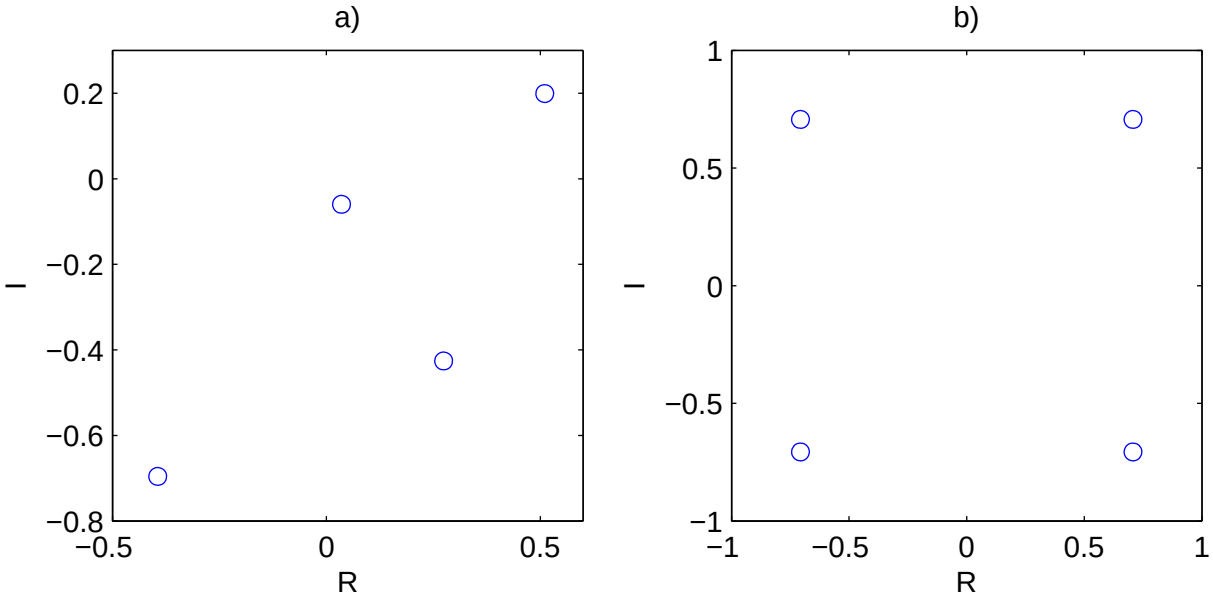

Figure 6.3: Constellation diagrams of a) SSK modulation when we have $N_{Tx} = 4$, $N_{Rx} = 1$ and $\boldsymbol{h} = [0.51 + 0.19i,\ 0.03 - 0.06i,\ -0.39 - 0.69i,\ 0.27 - 0.43i]$; and b) 4QAM modulation, respectively.

trated in Fig. 6.3b. By contrast, there is no modulated symbol for SSK modulation before transmission. Hence, the distance d_{Tx}^{SSK} does not exist. Moreover, the Euclidean distance d_{Rx} using APM over a noise-free SIMO fading channel after RxMF-based detection is formulated as $d_{Rx}^{APM} = |\boldsymbol{h}_j| d_{Tx}^{APM}$. By contrast, the Euclidean distance d_{Rx} using SSK modulation over a noise-free SIMO fading channel is defined as $d_{Rx}^{SSK} = |\boldsymbol{h}_i - \boldsymbol{h}_j| (i \neq j)$. It is evident that both d_{Rx}^{APM} and d_{Rx}^{SSK} are fading-dependent. However, these two distances are quite different, as detailed below.

- The average Euclidean distance between the i-th APM symbol and the j-th APM symbol after detection is denoted as $E_{\boldsymbol{h}}[d_{Rx}^{APM}(i,\ j)]$, which tends to increase upon increasing the number of receive antennas N_{Rx}. The value of $E_{\boldsymbol{h}}[d_{Rx}^{APM}(i,\ j)]$ will converge to $d_{Tx}^{APM}(i,j)$, if the value of N_{Rx} increases to infinity and the power of the channel is normalised by a factor of $\frac{1}{N_{Rx}}$. Similarly, the corresponding average Euclidian distance $E_{\boldsymbol{h}}[d_{Rx}^{SSK}(i,j)]$ using SSK modulation will also increase upon increasing the number of receive antennas N_{Rx}. However, the value of $E_{\boldsymbol{h}}[d_{Rx}^{SSK}(i,j)]$ will converge to $\sqrt{2}$ for any pair of $(i,\ j)$ when the value of N_{Rx} increases to infinity. This is because the CIR vectors $\boldsymbol{h}_i$ become orthogonal to $\boldsymbol{h}_j$, when having an infinite number of dimensions.

- The minimum average Euclidean distance of APM denoted is given by

$$\bar{d}_{min-Rx}^{APM} = \min_{(i,j)} E_{\boldsymbol{h}}[d_{Rx}^{APM}(i,\ j)], \tag{6.4}$$

  which decreases when the number of modulation levels M increases from 4 towards infinity. By contrast, the corresponding minimum average Euclidean distance using SSK denoted as $\bar{d}_{min-Rx}^{SSK}$ may not decrease, when the number of modulation levels M increases. For example, when having an infinite number of receive antennas, the value of $\bar{d}_{min-Rx}^{SSK}$ remains $\sqrt{2}$ for any value of M, which is similar to the related property of Frequency Shift Keying (FSK) modulation [163].

- For APM, increasing the channels' spatial correlation will increase the variance of the modulated signal constellation's distance $d_{Rx}^{APM}(i,\ j)$, but does not affect its mean value. By contrast, for

SSK modulation, increasing the channels' spatial correlation will decrease both the variance and the mean value of the constellation's distance $d_{Rx}^{SSK}(i,\ j)$ between any two symbol i and j. For example, d_{Rx}^{SSK} will tend to 0 with a probability of one, if we have $\boldsymbol{h}_i = \boldsymbol{h}_j$ at any instant.

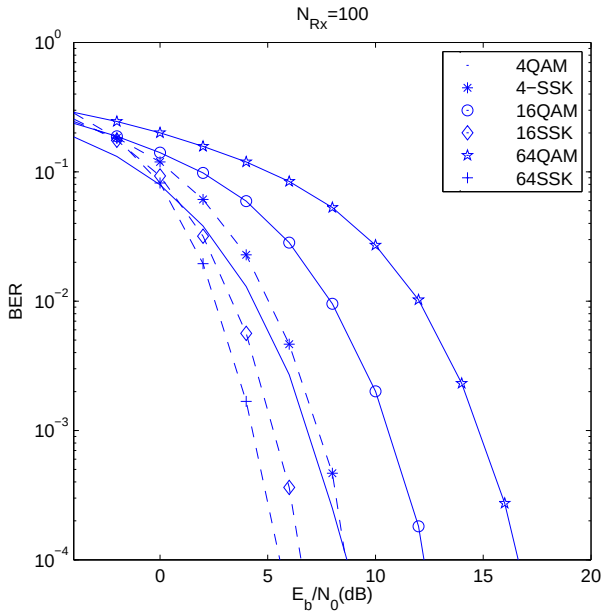

Figure 6.4: BER performance versus E_b/N_0 when using 4QAM, 16QAM, 64QAM, 4-SSK,16-SSK and 64-SSK. The number of receive antennas was $N_{Rx} = 100$, and the SIMO CIRs $\boldsymbol{h}_j$ are normalised by a power scaling factor of $\frac{1}{N_{Rx}}$

The uncoded BER performance can be characterized as a function of the Euclidean distance [163]. Hence, based on the associated Euclidean distance properties, the BER performance of the conventional APM and of the SSK modulation scheme exhibits the following characteristics:

- The BER performance of the conventional APM is proportional to the channel quality quantified in terms of the CIR taps $|\boldsymbol{h}_j|$. By contrast, the BER performance of the SSK modulation is proportional to the difference between the CIR taps associated with the different transmit antennas, namely to $|\boldsymbol{h}_i - \boldsymbol{h}_j|(i \neq j)$;

- The BER performance of the conventional APM improves upon increasing the number of receive antennas, gradually tending to the performance curve of the AWGN channel. Similar BER trends are also observed for SSK modulation. However, the performance of SSK modulation will tend towards to that of the FSK modulation under the asymptotic conditions of having an infinite number of receive antennas. This is demonstrated in Fig. 6.4 for the scenario of having 100 receive antennas[1] each subjected to independently fading, where the BER performances of 4QAM, 4-SSK, 16QAM, 16-SSK, 64QAM and 64-SSK are compared. Fig. 6.4 explicitly demonstrated that the SSK modulation has similar properties to FSK modulation, both of which may be deemed to be energy efficient schemes, provided that the number of receive antennas is sufficiently high;

[1]Naturally, this assumption is unrealistic for practical scenarios, but assists us in characterizing the upper-bound performance of the system.

- The BER performance of BPSK is better than that of 2-SSK, since the former has a higher Euclidian distance of $d_{Rx}^{APM} = 2$ than the $\max(d_{Rx}^{SSK}) = \sqrt{2}$ value of the latter one. For the same reason, the BER performance of QPSK or 4QAM is better than that of 4-SSK, when we have $N_{Rx} < +\infty$;
- The M-level SSK modulation scheme is capable of outperforming the corresponding M-level APM modulation scheme for $M > 8$ and $N_{Rx} > 1$.

In summary, **exploiting the independence of the complex-valued fading of the different antennas is the intrinsic feature of SSK modulation**, which constitutes an energy-efficient modulation scheme. Its BER performance is commensurate with the difference between the CIR taps characterizing the fading associated with the different transmit antennas. SSK may outperform the conventional APM scheme, when the number of modulation levels M becomes higher than eight and the number of receive antennas is higher than one.

6.1.3 Performance Evaluations

The family of SM scheme has a number of advantages. First of all, the uncoded SM scheme is capable of achieving the maximum attainable receive **diversity** order of N_{Rx} [7, 28]. Secondly, random transmit diversity is attainable for a coded SM system, since the specific selection of the transmit antenna to be activated at each time instant is random [28]. Moreover, a beneficial receive antenna **array gain** is achieved, despite employing a low-complexity single-stream ML detector. Furthermore, the transmitter's **complexity** is reduced, since the synchronization of transmit antennas is avoided. The receiver's complexity is also reduced, since the Inter Channel Interference (ICI) is completely avoided. Last but not least, the SSK modulation scheme is **robust** to channel estimation errors [7, 175]. This is partially owing to the reason that the channel estimation error is more influential in determing the actual channel realization encountered than the technique of distinguishing the distance between two columns of the CIR matrix $\boldsymbol{H}$.

Despite the above-mentioned benefits, the SM scheme described in Section 6.1.1 also has a number of disadvantages. First of all, the uncoded SM scheme achieves no transmit diversity [7, 28] and the random transmit diversity-induced gain achieved by the coded SM is quite limited. Secondly, no transmitter array gain is achieved at all. Moreover, the achievable **throughput** is $R = \log_2 N_{Tx} + \log_2 M$, which increases logarithmically with the number of transmit antennas, and this constitutes an inefficient way of exploiting the available transmit antennas.

In order to mitigate or eliminate these disadvantages, more sophisticated SM schemes have also been proposed in the literature [173–178]. For example, a novel scheme termed as time-orthogonal signal design assisted SM was proposed in [178] in order to achieve transmit diversity. The authors of [174] proposed a scheme, which selects a specific beamforming vector instead of activating a particular transmit antenna to convey information. This regime is capable of achieving a valuable fraction of the maximum attainable transmit array gain. In order to increase the achievable throughput, a generalised SSK scheme was proposed in [173], where n_t out of N_{Tx} number of transmit antennas are activated simultaneously in order to represent the information symbols to be transmitted. As a result, the achievable throughput using the generalised SSK scheme increases from $\log_2 N_{Tx}$ to $\log_2 \binom{n_t}{N_{Tx}}$, towards the maximum attainable throughput of $\log_2 \binom{N_{Tx}/2}{N_{Tx}}$. An algorithm optimising the number of simultaneously activated transmit antennas was proposed in [173] in order to minimise the BER.

Naturally, the SSK/SM scheme is not the ultimate winner, when compared to other MIMO schemes in terms of the achievable BER performance. However, it is capable of outperforming other MIMO schemes in certain scenarios. This conclusion may be inferred from the BER performance comparison of SSK and AMP modulation provided in Section 6.1.2. More specifically, in Section 6.1.2, the SSK modulation is equipped with $N_{Tx} > 1$ transmit antennas, while the APM scheme has a single transmit antenna. If they are both equipped with the same number of transmit antennas, the APM arrangement can either achieve a transmit diversity by exploiting the STBC philosophy, or attain a multiplexing gain by creating a V-BLAST scheme, or indeed exploit both the diversity and multiplexing gain using the family of LDC schemes [2]. Here, two design examples are provided, in which the SSK/SM scheme outperforms the STBC scheme and the V-BLAST scheme, respectively.

- **Example 1 (SSK versus STBC):** Let us assume that we have $N_{Tx} = 8$, $N_{Rx} = 8$, a target throughput of $R = 3$ bits/symbol, and investigate an 8-SSK versus a half-rate Orthogonal STBC scheme using 64QAM modulation.
  Analysis: Since the receive diversity order is as high as eight, the benefit of achieving a further transmit diversity gain improvement using the STBC scheme remains limited. The BER performance of 8-SSK having a receive diversity order of eight is expected to be better than that of 64-QAM for transmission over an AWGN channel. As a result, the BER performance of SSK modulation is better than that of the diversity-aided STBC scheme in this scenario.

- **Example 2 (SM versus V-BLAST):** Let us now assume having $N_{Tx} = 4, N_{Rx} = 2$, and a target throughput of $R = 4$ bits/symbol. One of the schemes employed 4-SSK combined with 4QAM, and used the SM scheme's low-complexity ML detector. The other arrangement employed the V-BLAST scheme, which transmits two independent 4QAM data streams and invoked an MMSE detector at the receiver. The reason for employing the MMSE detector is to ensure that the receiver complexity of these two schemes remained comparable.
  Analysis: The V-BLAST scheme transmits two independent 4QAM symbols. The achievable diversity order of the V-BLAST scheme using the MMSE detector is one. The SM scheme employs 4-SSK as well as 4QAM, and achieves a diversity order of two for both the SSK modulated and 4QAM symbols. As a result, the BER performance of the SM scheme is expected to be better than that of the V-BLAST scheme.

Furthermore, the SM/SSK scheme has some unique features, such as for example exhibiting a robustness to channel estimation errors, hence it is capable of outperforming the other MIMO schemes considered.

In summary, the SM scheme is constituted by a combination of SSK modulation and of a $(1 \times N_{Rx})$-element SIMO system using the conventional APM. The intrinsic feature of SSK modulation is that it exploits the independent fading of the different transmit antennas' signals, which allows the system to dispense with transmit antenna synchronisation, while exhibiting a robustness to channel estimation errors. As a result, SM schemes exhibit certain advantages over other MIMO schemes and hence they will be further investigated.

6.2 Transmit Diversity Assisted Space Shift Keying

As discussed in Section 6.1.3, the family of uncoded SSK modulation schemes achieve no transmit diversity. Although employing channel coding is capable of providing some time-diversity gain and space diversity gain owing to the bit-based interleaving, the achievable gain may remain limited. The authors of [178] proposed a novel scheme referred to as time-orthogonal signal design aided SM in order to achieve transmit diversity. However, this scheme is only applicable to systems having two transmit antennas.

Against this background, we intend to design a more diverse range of transmit diversity assisted SSK schemes. Following the philosophy of STBCs, in Section 6.2.1 we first propose an open-loop ST-SSK scheme for scenarios having more than two transmit antennas, which employs multiple transmit time slots for achieving transmit diversity. The unique features of the proposed ST-SSK scheme and its design are discussed. Then in Section 6.2.2, we propose a feedback-aided phase rotation scheme, when relying on two transmit antennas. Moreover, another closed-loop scheme using feedback-aided power allocation is proposed in Section 6.2.3 for systems having an arbitrary number of transmit antennas. Our simulation results are discussed in Section 6.2.4, where the i.i.d. Rayleigh fading channel, the spatial correlated channel, the Rician channel as well as the effects of channel estimation errors are considered. Without any loss of generality, we assume having $N_{Rx} = 1$ throughout this section in order to simplify our discussions.

6.2.1 Open-Loop: Space Time Space Shift Keying for $N_{Tx} > 2$

Following the well-established philosophy of STBCs, we propose a ST-SSK modulation scheme, which uses L time slots to transmit $m_1 = \log_2 N_{Tx}$ bit sequence $\boldsymbol{b}_i$. During each time slot, one out of N_{Tx} antennas is activated according to the bit-to-antenna mapping function of $f(t_l, \boldsymbol{b}_i)$ $(1 \leq f(t_l, \boldsymbol{b}_i) \leq N_{Tx})$. Hence, when $\boldsymbol{b}_i$ is transmitted, the signal received during the L time slots is formulated as

$$\begin{bmatrix} y^{t_1} \\ \vdots \\ y^{t_l} \\ \vdots \\ y^{t_L} \end{bmatrix} = \sqrt{\frac{mE_b}{L}} \begin{bmatrix} h_{f(t_1,\boldsymbol{b}_i)} \\ \vdots \\ h_{f(t_l,\boldsymbol{b}_i)} \\ \vdots \\ h_{f(t_L,\boldsymbol{b}_i)} \end{bmatrix} + \begin{bmatrix} n^{t_1} \\ \vdots \\ n^{t_l} \\ \vdots \\ n^{t_L} \end{bmatrix}, \tag{6.5}$$

where we have $1 \leq l \leq L$, $1 \leq f(t_l, \boldsymbol{b}_i) \leq N_{Tx}$. Upon defining $\boldsymbol{y} = [y^{t_1}, \ldots, y^{t_L}]^T$ and $\boldsymbol{h}_{\boldsymbol{f}(\boldsymbol{b}_i)} = [h_{f(t_1,\boldsymbol{b}_i)}, \ldots, h_{f(t_L,\boldsymbol{b}_i)}]^T$, the transmitted sequence $\hat{\boldsymbol{b}}_i$ is determined at the receiver side according to

$$\begin{aligned} \hat{\boldsymbol{b}}_i &= \arg\min_{\boldsymbol{b}_i} \|\boldsymbol{y} - \sqrt{\frac{mE_b}{L}} \boldsymbol{h}_{\boldsymbol{f}(\boldsymbol{b}_i)}\|_2^2 \\ &= \arg\min_{\boldsymbol{b}_i} \sum_{l}^{L} |y_{t_l} - \sqrt{\frac{mE_b}{L}} h_{f(t_l,\boldsymbol{b}_i)}|^2. \end{aligned} \tag{6.6}$$

Before considering the design of the bit-to-antenna mapping function, let us first prove the following two propositions.

Proposition 1: For a $(N_{Tx} \times 1)$ ST-SSK modulation aided system using L time slots, the transmit

diversity order of L is achieved if and only if for any two bit sequences $\boldsymbol{b}_i$ and $\boldsymbol{b}_j$ ($i \neq j$), and for any two time instances l and n ($l \neq n$), we have

1. the indices of the antennas activated for signalling the bit sequence $\boldsymbol{b}_i$ and $\boldsymbol{b}_j$ are different from each other at any time slot l, which is formulated as $f(t_l, \boldsymbol{b}_i) \neq f(t_l, \boldsymbol{b}_j)$;

2. when transmitting $\boldsymbol{b}_i$ and $\boldsymbol{b}_j$, the difference between the activated channels' CIR taps at the l-th time slot denoted by $\Delta h_{t_l} = h_{f(t_l,\boldsymbol{b}_i)} - h_{f(t_l,\boldsymbol{b}_j)}$ must be a random variable, which is independent of the one during the n-th time slot represented as $\Delta h_{t_n} = h_{f(t_n,\boldsymbol{b}_i)} - h_{f(t_n,\boldsymbol{b}_j)}$.

Proof: Transmitting the bit sequences $\boldsymbol{b}_i$ and $\boldsymbol{b}_j$ ($i \neq j$), the Euclidean distance between the corresponding received signals without noise is formulated as

$$\begin{aligned} d &= \sqrt{\frac{mE_b}{L}} \|\boldsymbol{h}_{\boldsymbol{f}(\boldsymbol{b}_i)} - \boldsymbol{h}_{\boldsymbol{f}(\boldsymbol{b}_j)}\|_F \\ &= \sqrt{\frac{mE_b}{L} \sum_{l}^{L} |h_{f(t_l,\boldsymbol{b}_i)} - h_{f(t_l,\boldsymbol{b}_j)}|^2} \\ &= \sqrt{\frac{mE_b}{L} \sum_{l}^{L} |\Delta h_{t_l}|^2}. \end{aligned} \tag{6.7}$$

A diversity order of L is achieved if and only if Δh_{t_l}, $l \in [1,\ L]$ are independent complex-valued Gaussian variables. As a result, $\forall i \neq j,\ l \neq n,\ i,j \in [1,\ N_{Tx}],\ l,n \in [1,\ L]$, we have $f(t_l, \boldsymbol{b}_i) \neq f(t_l, \boldsymbol{b}_j)$ and $|h_{f(t_l,\boldsymbol{b}_i)} - h_{f(t_l,\boldsymbol{b}_j)}|$ must be independent of $|h_{f(t_n,\boldsymbol{b}_i)} - h_{f(t_m,\boldsymbol{b}_j)}|$.

Proposition 2: For a $(N_{Tx} \times 1)$ ST-SSK modulation aided system, the maximum achievable transmit diversity order cannot be higher than $(N_{Tx} - 1)$.

Proof: Assume that we have $L = N_{Tx}$, when a transmit diversity order of N_{Tx} is achieved. According to Proposition 1, the Euclidean distance d between $\boldsymbol{b}_i$ and $\boldsymbol{b}_j$ is a sum of N_{Tx} independent Δh_{t_l} values. However, for N_{Tx} transmit antennas there are at most $(N_{Tx} - 1)$ independent Δh values. Hence, achieving a diversity order higher than $(N_{Tx} - 1)$ becomes impossible.

Let us now consider the design of the bit-to-antenna mapping function. We propose a shift-mapping function $f_s(t_l, \boldsymbol{b}_i)$ for the scenarios having an even number of transmit antennas; and propose what we refer to as a shift-swap-mapping function $f_{s-w}(t_l, \boldsymbol{b}_i)$ for the scenarios having an odd number of transmit antennas. More explicitly, the algorithms are described as follows.

1. $f_s(t_l, \boldsymbol{b}_i)$ when $N_{Tx} > 2$ and N_{Tx} is an even number:
   - set $\boldsymbol{v} = [1,\ 2, \ldots,\ N_{Tx}]$;
   - set $[f(t_l, \boldsymbol{b}_1),\ f(t_l, \boldsymbol{b}_2), \ldots,\ f(t_l, \boldsymbol{b}_{N_{Tx}})] = \text{Shift}(\boldsymbol{v}, l-1)$, where $\text{Shift}(\boldsymbol{v}, l-1)$ represents a left circular shift of $(l-1)$ positions.

2. $f_{s-w}(t_l, \boldsymbol{b}_i)$ when $N_{Tx} > 2$ and N_{Tx} is an odd number:
   - Create a shift-mapping function following the above-mentioned steps;
   - Randomly group the last $\frac{N_{Tx}}{2}$ bit sequences $(\boldsymbol{b}_{\frac{N_{Tx}}{2}+1}, \ldots, \boldsymbol{b}_{N_{Tx}})$ into $\frac{N_{Tx}}{4}$ pairs;

- Within each pairs, for example $\boldsymbol{b}_{\frac{N_{Tx}}{2}+1}$ and $\boldsymbol{b}_{\frac{N_{Tx}}{2}+2}$ grouped as a pair, swap the mapping results of $f(t_l, \boldsymbol{b}_{\frac{N_{Tx}}{2}+1})$ and $f(t_l, \boldsymbol{b}_{\frac{N_{Tx}}{2}+2})$ for all $l \leq \frac{N_{Tx}}{2}$.

The examples of the activated transmit antenna index for $N_{Tx} = 3$ using the shift-mapping of $f_s(t_l, \boldsymbol{b}_i)$, and for $N_{Tx} = 4$ using the shift-swap bit-to-antenna mapping of $f_{s-w}(t_l, \boldsymbol{b}_i)$ are shown in Table 6.3, respectively. The shift-mapping results for $N_{Tx} = 4$ are also shown in Table 6.3 within the brackets.

Input bits $\boldsymbol{b}_i$	Activated antenna index $f_s(t_l, \boldsymbol{b}_i)$	
	t_1	t_2
0	1	2
1	2	3

(a)

Input bits $\boldsymbol{b}_i$	Activated antenna index $f_{s-w}(t_l, \boldsymbol{b}_i)$ ($f_s(t_l, \boldsymbol{b}_i)$)		
	t_1	t_2	t_3
00	1 (1)	2 (2)	3 (3)
01	2 (2)	3 (3)	4 (4)
10	4 (3)	1 (4)	1 (1)
11	3 (4)	4 (1)	2 (2)

(b)

Table 6.3: Example of the activated transmit antenna when a) $N_{Tx} = 3, N_{Rx} = 1$ using shift bits-to-antenna mapping $f_s(l, \boldsymbol{b}_i)$; b) $N_{Tx} = 4, N_{Rx} = 1$ using shift-swap bits-to-antenna mapping $f_{s-w}(l, \boldsymbol{b}_i)$ and the shift-mapping $f_s(l, \boldsymbol{b}_i)$.

The proposed bit-to-antenna mapping functions have guaranteed that the transmit diversity order of L is achieved if we have $L \leq (N_{Tx} - 1)$, which was shown in Proposition 1. More explicitly, since there is no identical value in the vector $\boldsymbol{v}$, the first requirement stated in Proposition 1, namely that we have $\forall\ i \neq j,\ f(t_l, \boldsymbol{b}_i) \neq f(t_l, \boldsymbol{b}_j)$, is satisfied. This is demonstrated by Table 6.3, where the activated indices in the same column of the l-th time slot are different from each other. Moreover, the proposed mapping function has also guaranteed that $\forall\ l \neq n$, Δh_{t_l} is independent of Δh_{t_n}, which satisfies the second requirement stated in Proposition 1. As a result, when $L \leq (N_{Tx} - 1)$, a transmit diversity order of L is achieved using the proposed mapping functions.

There are two disadvantages of the proposed ST-SSK scheme. Firstly, the receiver's complexity using the single-stream ML detection method will be increased by a factor of L. The other disadvantage is that the achievable throughput is reduced by a factor of L. Since the benefit of increasing the transmit diversity order from one to infinity is the most substantial for low values of L, but becomes more modest for large L, it is worth employing the proposed ST-SSK scheme for low values of L.

6.2.2 Closed-Loop: Feedback-aided Phase Rotation for $N_{Tx} = 2$

Based on Proposition 2, it is plausible now that using the open-loop ST-SSK modulation scheme proposed in Section 6.2.1 we can only achieve a transmit diversity order of one for $N_{Tx} = 2$, since there is only $N_{Tx} - 1 = 1$ independent Δh value. In this section, we propose a scheme specifically for $N_{Tx} = 2$, which feeds back a phase value θ from the receiver to the transmitter so as to maximise the Euclidean distance $d_{min} = d = \sqrt{E_b}\|\boldsymbol{h}_1 - \boldsymbol{h}_2\|$ and hence to achieve transmit diversity. The objective function used for our design may be written as

$$\begin{aligned} \arg\max_{\theta} d_{min}^2 &= \arg\max_{\theta} \|h_1 - h_2 e^{j\theta}\|^2 \\ &= \arg\max_{\theta} \|h_1\|^2 + \|h_2\|^2 - 2\Re\left(h_1^H h_2 e^{j\theta}\right) \\ &= \arg\min_{\theta} \Re\left(h_1^H h_2 e^{j\theta}\right) \\ &= \arg\min_{\theta} \Re\left(|h_1^H h_2| e^{j(\theta+\phi)}\right), \end{aligned} \tag{6.8}$$

where we have $h_1^H h_2 = |h_1^H h_2| e^{j\phi}$. Explicitly, the minimum of Equation (6.8) is achieved for

$$\theta + \phi = (2k+1)\pi, k \in \mathcal{Z}. \tag{6.9}$$

As a result, the Euclidean distance becomes $d = \sqrt{E_b}(|h_1| + |h_2|)$ owing to having two independent channel gains. Hence, a transmit diversity order of two is achieved. In fact, as long as we have $\Re(h_1^H h_2 e^{j\theta}) > 0$, a diversity order of two can be guaranteed. The objective function of Equation (6.8) achieves the minimum BER, in addition to achieving an increased diversity gain. Moreover, since ϕ is a random variable uniformly distributed in $[0,\ 2\pi]$, θ_2 is expected to have the same uniform distribution between 0 and 2π. A scalar quantizer having uniformly distributed quantization levels constitutes an adequate quantizer design.

For the scenario of having more than two transmit antennas, this scheme requires the feedback of the phase vector $\boldsymbol{\theta} = [\theta_1, \ldots, \theta_{N_{Tx}}]$ satisfying $\Re(h_i^H h_p e^{j\theta_i + \theta_p}) > 0, \forall i \neq p$. This optimisation process is computationally demanding and the existence of the solution is not guaranteed. Hence, this feedback scheme is not applicable for scenarios having $N_{Tx} > 2$.

6.2.3 Closed-Loop: Feedback-aided Power Allocation

In this section, we proposed another closed-loop scheme, which exploits the limited feedback information for power allocation. The basic idea is to allocate more power to the specific transmit antenna associated with a higher channel gain, and less power to the transmit antenna associated with a lower channel gain. As a result, the BER performance after power allocation will be improved because the distances between channel's fading coefficients associated with the different transmit antennas are enhanced.

Our proposed feedback-aided power allocation scheme is detailed as follows. First of all, the channel's fading coefficients $|\boldsymbol{h}_j|$ associated with different transmit antennas are estimated at the receiver side. Secondly, the transmit antenna having the lowest channel gain is identified at the receiver, and its index is fed back to the transmitter using $\log_2 N_{Tx}$ bits. For example, two bits $[0\ 0]$ will be fed back to the transmitter, if we have $|h_1| < |h_2| < |h_3| < |h_4|$ for a system having four transmit antennas and a single receive antenna. Upon receiving the feedback information, the transmitter will allocate zero power to the

antenna having the lowest channel gain, and increase the power allocated to other antennas from a value of mE_b to $mE_b + \frac{mE_b}{N_{Tx}-1}$. Using the aforementioned example, the power allocated to the first transmit antenna is zero, and the power allocated to the second, third and fourth antennas are increased from $2E_b$ to $(2+\frac{2}{3})E_b$.

The proposed scheme achieves a certain degree of transmit diversity in a way similar to the conventional antenna selection. The conventional antenna selection activates the transmit antenna associated with the highest channel gain using full transmit power. The resultant effective channels become $\max_j h_j$ instead of h_j, which has a higher mean and a lower variance value. Similarly, the proposed scheme deactivates the transmit antenna associated with the lowest channel gain, and allocates the total transmit power equally to the other transmit antennas, which will also change the statistical properties of the resultant effective channels. Unlike the conventional antenna selection, the performance of a system [2] using the SSK modulation is more dependent on the difference between the resultant effective channel $\Delta h = |h_i - h_j|$ than in the resultant effective channel itself such as $\max h_j$. The reason is that the BER performance of the SSK modulation is proportional to the value of Δh rather than to $|h|$. For a system having two transmit antennas, the proposed scheme is capable of achieving a diversity order of two, since we have $\Delta h = \sqrt{2E_b}\max(|h_1|,|h_2|)$, where h_1 and h_2 represent the two CIRs. For systems having more than two transmit antennas, the determination of the achievable diversity order remains an open problem.

The proposed scheme is capable of improving the attainable BER performance compared to the original SSK modulation scheme described in Section 6.1. A particular reason for this is that a higher transmit diversity order is achieved based on the aforementioned analysis. Another reason is that $\binom{2}{N_{Tx}-1}$ out of $\binom{2}{N_{Tx}}$ Euclidean distances of the SSK modulated symbols at the output of detector becomes higher, when employing the proposed feedback-aided power allocation. Assuming that the channel associated with the k-th transmit antenna has the lowest channel gain, the Euclidean distance of d_{Rx}^{SSK} between the i-th and j-th SSK modulated symbols, which activate the i-th and j-th transmit antennas respectively ($i \neq j \neq k$), is increased from $d_{Rx}^{SSK} = \sqrt{mE_b}|h_i - h_j|$ to $d_{Rx}^{SSK} = \sqrt{(m_1 + \frac{m_1}{N_{Tx}-1})E_b}|h_i - h_j|$, when using the feedback-aided power allocation. Although the Euclidian distances d_{Rx}^{SSK} associated with the k-th antenna, and correspondingly the k-th SSK modulated symbol, do not necessarily increase, the overall BER performance will be improved since the majority of the Euclidean distances d_{Rx}^{SSK} are increased by using the proposed feedback-aided power allocation.

The advantages of the proposed scheme are its low complexity and low feedback overhead. Only low-complexity channel estimation and channel gain comparison are required at the receiver. The transmit power after power allocation is fixed to either $(m_1 + \frac{m_1}{N_{Tx}})E_b$ or to zero. The number of feedback bits is as low as $\log_2 N_{Tx}$. The disadvantages of the proposed scheme manifest themselves in two aspects. Firstly, the proposed scheme might not be the optimal one, and does not achieve the maximum attainable transmit diversity. Moreover, the transmit power after power allocation fluctuates over time, which may impose strong interference on other systems. Hence, the proposed feedback-aided power allocation scheme may suffer from a serious performance degradation in an interference-limited scenario. Nonetheless, the proposed closed-loop feedback-aided power allocation constitutes an effective low complexity scheme, which is capable of achieving a certian degree of transmit diversity, hence improving the BER performance compared to the original open-loop SSK modulation scheme. The BER performance of the

[2] Δh, h_i and h_j are scalar values, since having a single receive antenna associated with $N_{Rx} = 1$ is assumed, as stated at the beginning of this section.

proposed scheme operating in a single-user noise-limited scenario is characterized in Section 6.2.4.

6.2.4 Simulation Results

Number of antennas (N_{Tx}, N_{Rx})	(4,1),(2,1)
Channel Code	Convolutional code
Channel code's constraint length	7
Coding Rate r_c	$\frac{1}{3}$
Interleaver Length	1500
Modulation	2-SSK, 4-SSK
ST-SSK Time Slot	$L = 1, 2, 3$
Channel Spatial Correlation	$\rho_{h_i h_j} = 0, 0.05, \ldots, 0.95$
Rician Factor	$A = 0, 0.5, \ldots, 2$
Channel Estimation Error	$h_e = 0, 0.05, \ldots, 0.2$

Table 6.4: Simulation Parameters

In this section, the achievable performance of the three proposed schemes, namely that of the open-loop ST-SSK scheme of Section 6.2.1, of the closed-loop feedback-aided phase rotation regime invoked for $N_{Tx} = 2$ and detailed in Section 6.2.2, as well as the closed-loop feedback-aided power allocation arrangement described in Section 6.2.3, is characterized and compared to that of the original SSK modulation scheme described in Section 6.1. The communication channels are initially assumed to be i.i.d Rayleigh fading. Then the effects of spatial correlation, Rician channels, and of realistic imperfect channel estimation are discussed, respectively. Both uncoded and coded systems are simulated, where a rate $r_c = \frac{1}{3}$ convolutional code having a constraint length of seven is employed. The length of the interleaver is set to 1500 bits. The simulation parameters are summarised in Table 6.4.

The uncoded BER versus $\frac{E_b}{N_0}$ performance of a system having $N_{Tx} = 4, N_{Rx} = 1$ antennas and using the proposed open-loop ST-SSK modulation scheme discussed in Section 6.2.1 is characterized in Fig. 6.5a. When the transmission time duration L increases from 1 to 3, the achievable throughput decreases from 2 (bits/sym) to $\frac{2}{3}$ (bits/sym). At the same time, the achievable transmit diversity order increases from one to three, which is illustrated in Fig. 6.5a by the increased slope of the BER curves. Moreover, when the number of time slots increases to $L = 4$, the slope of the BER curves remains the same as that of $L = 3$, which demonstrated that the maximum achievable diversity order of a ST-SSK modulation aided system is three $(N_{Tx} - 1 = 3)$. Further BER improvements can be achieved upon combining the ST-SSK scheme with the feedback-aided power allocation of Section 6.2.3. Similar observations are also valid for the coded system, as illustrated in Fig. 6.5b.

Fig. 6.6a characterises the uncoded BER versus $\frac{E_b}{N_0}$ performance for a throughput of $R = 1$ (bits/sym) and $N_{Tx} = 2, N_{Rx} = 1$. The scenarios of a) perfect phase feedback; b) 1-bit feedback-aided phase rotation; c) $1-$bit feedback-aided power allocation; and d) the original open-loop 2-SSK modulation are compared. A diversity order of two results in an approximately 8dB power gain achieved using the first three type of closed-loop schemes of a BER of 10^{-2}. Moreover, using $1-$bit to quantise the feedback phase information imposes a modest performance degradation of about $1-$dB. The achievable BER performances recorded, when using a $1-$bit feedback for either the phase information or for power

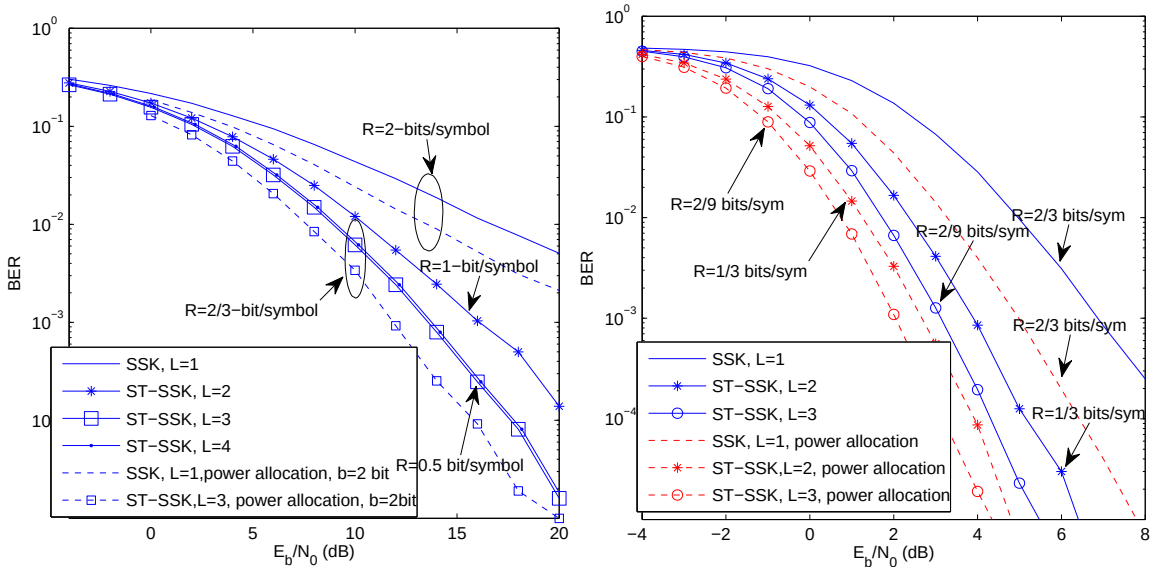

(a) Uncoded (b) Coded

Figure 6.5: Uncoded and coded BER versus $\frac{E}{N_0}$ for $N_{Tx} = 4, N_{Rx} = 1$ for 1) ST-SSK scheme using $L = 1/2/3$, respectively, and using the shift-swap bits-to-antenna mapping f_{s-w} shown in Table 6.3b; 2) ST-SSK scheme combined with feedback-aided power allocation; and 3) the original SSK modulation. All other system parameters are summarized in Table 6.4.

allocation are almost the same. For the coded system characterised in Fig. 6.6b, about 2dB power gain is achieved using the proposed closed-loop schemes at a BER of 10^{-3}.

The attainable performance of the proposed schemes is also investigated when the wireless channels are not i.i.d. Rayleigh fading channels. More explicitly, we investigate the achievable BER versus the channel's spatial correlation coefficient $\rho_{h_i h_j}$, as well as versus the Rician fading factor A and versus the variance of the channel estimation error h_e at a certain SNR per bit value. We opted for recording the SNR per bit value, where a BER of 10^{-3} is achieved for transmission over i.i.d. channels.

The algorithm of generating spatially correlated channels is detailed in Section 2.1.2.1. The format of the transmitter's covariance matrix $\boldsymbol{R}_{Tx}$ employed in our simulations is illustrated in Fig. 6.7a and b for $N_{Tx} = 2$ and $N_{Tx} = 4$, respectively. The transmitter's covariance matrix shown in Fig. 6.7b may be deemed to be representative of the antenna arrangement shown in Fig. 6.7c. More explicitly, the first and third antenna are located sufficiently far away from the second and the fourth antenna to ensure that the channels between them are independent. Moreover, the third and the fourth antenna are gradually moved towards the first and the second antenna, respectively. Hence, the correlation between the CIRs h_1 and h_3, as well as between h_2 and h_4 increases accordingly.

The BER performance versus the spatial correlation coefficient recorded for various transmission schemes are illustrated in Fig. 6.8. It is demonstrated in Fig. 6.8 a and b that when we have $N_{Tx} = 2$, the original open-loop SSK scheme is very sensitive to spatial correlation, especially for a channel coded system. The proposed closed-loop scheme using both feedback-aided phase rotation and feedback-aided power allocation performs better in spatial correlated scenarios. Moreover, the coded BER performance using 1-bit feedback-aided phase rotation is better than that using 1bit feedback-aided power allocation,

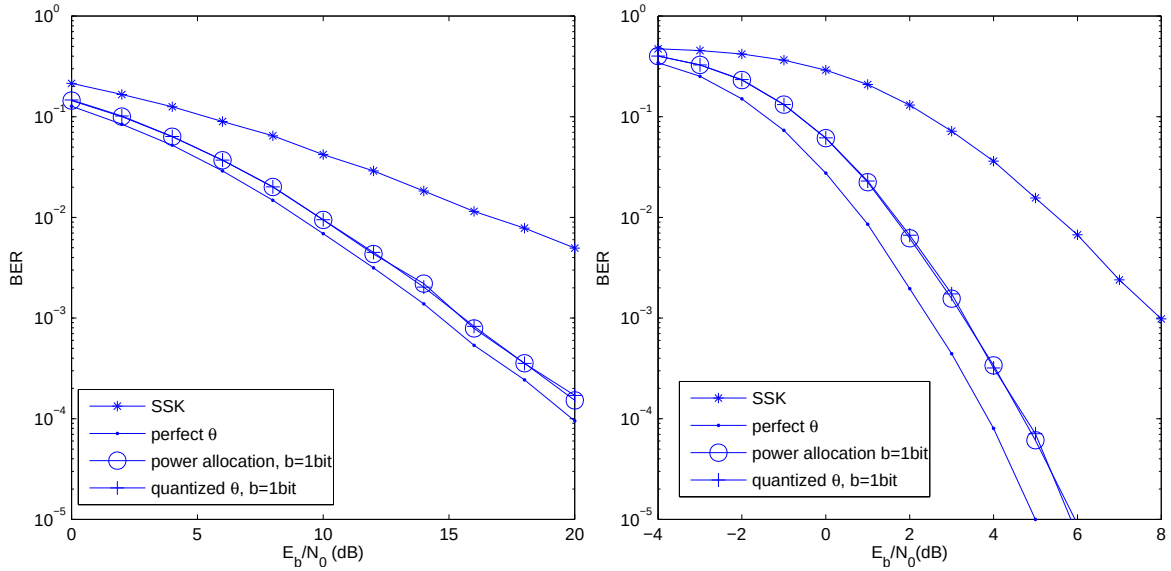

(a) Uncoded (b) Coded

Figure 6.6: Uncoded and coded BER versus $\frac{E_b}{N_0}$ for $N_{Tx} = 2$, $N_{Rx} = 1$ using perfect phase feedback, 1-bit quantized phase feedback and 1-bit power allocation feedback-aided SSK modulation, respectively. The performance of the original open-loop SSK modulation is also included for comparison. All other system parameters are summarized in Table 6.4.

when the spatial correlation coefficient becomes higher than 0.5. These observations may be explained with reference to their associated Euclidean distance Δh. The expression of the Euclidean distance Δh for the original SSK modulation, for the feedback-aided phase rotation scheme and for the feedback-aided power allocation scheme are $\sqrt{E_b}|h_1 - h_2|$, $\sqrt{E_b}(|h_1| + |h_2|)$ and $\sqrt{2E_b}\max(|h_1|, |h_2|)$, respectively. The latter two values will less dramatically decrease if the CIRs h_1 and h_2 are correlated to each other due to spatial correlation. As a result, it is evident that the two closed-loop systems are less sensitive to spatial correlations than the original SSK modulation scheme.

It is also demonstrated in Fig. 6.8c and d that the ST-SSK scheme advocated is sensitive to the spatial correlation, which shows a very similar slope to the uncoded BER curve of the original SSK scheme. For the convolutionally coded system, the sensitivity of the proposed ST-SSK scheme to spatial correlation is slightly less pronounced than that of the original SSK scheme, when the spatial correlation coefficient becomes higher than 0.8. Furthermore, the employment of the proposed feedback-aided power allocation is capable of reducing the system's sensitivity to spatial correlations. The beneficial effect of power allocation is clear for uncoded systems, but becomes less pronounced for coded systems. Again, the reasons for these observations lie in the effect of the resultant CIR tap difference Δh. The value of Δh may be expressed in a common format as for all three schemes as $\sqrt{xE_b}|\boldsymbol{h}_i - \boldsymbol{h}_j|$, where $\boldsymbol{h}_i$ and $\boldsymbol{h}_j$ are L-element vectors for the ST-SSK scheme, while they are scalars for the other two schemes. This Δh quantity is affected by the spatial correlation, regardless whether we use feedback-aided power allocation, whethere we increase the dimension of h_i by using the ST-SSK scheme.

The Rician fading MIMO channel matrix may be modeled as the sum of the matrix representing the

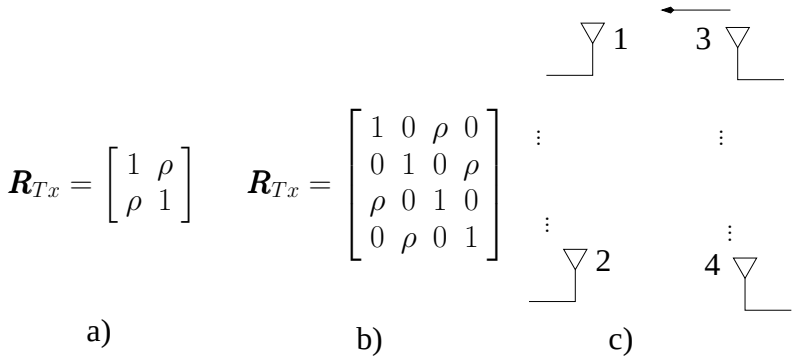

Figure 6.7: The transmit covariance matrix $\boldsymbol{R}_{Tx}$ for a) $N_{Tx} = 2$ and b) $N_{Tx} = 4$. An example of the antenna arrangements corresponding to the transmit covariance b) are also plotted in c).

LOS component and a Rayleigh fading channel matrix as follows [163]:

$$\boldsymbol{h}_{Rician} = \sqrt{\frac{A}{1+A}}\boldsymbol{h}_{mean} + \sqrt{\frac{1}{1+A}}\boldsymbol{h}, \tag{6.10}$$

where the N_{Tx}-element vector $\boldsymbol{h}_{mean}$ host the mean values of the CIR taps of the N_{Tx}-element MISO channel, $\sqrt{\frac{A}{1+A}}\boldsymbol{h}_{mean}$ is the LOS component, $\sqrt{\frac{1}{1+A}}\boldsymbol{h}$ is the fading component and A is the Rician factor. The Rician factor A is defined as the ratio of the LOS and the scatterred power components. Upon increasing the Rician factor A, the channel's spatial correlation increases accordingly, and the channel will eventually tend to an AWGN channel. The LOS component $\boldsymbol{h}_{mean}$ was set to a matrix constituted by unity values in our simulation for simplicity.

The BER performance versus the Rician factor A recorded for the various transmission schemes is illustrated in Fig. 6.9. More explicitly, it is demonstrated in Fig. 6.9a and b that for $N_{Tx} = 2$, the original open-loop SSK scheme is quite sensitive to the Rician factor A, since the resultant channels h_1 and h_2 become correlated with each other. By contrast, the BER performance of the proposed closed-loop scheme using either feedback-aided phase rotation or feedback-aided power allocation improves upon increasing the value of A. It is plausible that Δh of the proposed closed-loop schemes formulated as $\sqrt{E_b}(|h_1| + |h_2|)$ and $\sqrt{2E_b}\max(|h_1|, |h_2|)$ is increased, when having a strong LOS signal. Moreover, the convolutional coded BER performance using 1-bit feedback-aided phase rotation is seen to be better than that using 1-bit feedback-aided power allocation. It is also demonstrated in Fig. 6.9 c and d that the proposed ST-SSK scheme is sensitive to the Rician factor's value, yielding a steeper slope for the uncoded system's BER curve than for the original SSK scheme. Moreover, the employment of the proposed feedback-aided power allocation scheme is capable of reducing the system's sensitivity to the Rician factor A.

Recall that we have discussed the pilot-assisted channel estimation regime in Section 3.2.1. The resultant channel estimation error may be formulated as

$$\hat{\boldsymbol{h}} = \sqrt{h_e}\boldsymbol{g} + \boldsymbol{h}, \tag{6.11}$$

where h_e represents the variance of the channel estimation error, the vector $\boldsymbol{g}$ is constituted by N_{Tx}-dimensional random Gaussian variables having a zero mean and unit variance, while the N_{Tx}-element vector $\boldsymbol{h}$ represents the i.i.d. Rayleigh fading channel.

The BER performance versus the variance h_e of the channel estimation error recorded for the various transmission schemes is illustrated in Fig. 6.10. It is demonstrated in Fig. 6.10 a and b that for $N_{Tx} = 2$ the original open-loop SSK scheme is sensitive to channel estimation errors. The proposed closed-loop scheme using the phase information and the feedback-aided power allocation regimes are both less sensitive to small channel estimation errors, for example to $h_e < 0.05$. However, the sensitivity to high channel estimation errors becomes similar for all three schemes. It is also demonstrated in Fig. 6.10 c and d that for small channel estimation errors, the proposed ST-SSK scheme is significantly less sensitive than the original SSK scheme. Moreover, the employment of the proposed feedback-aided power allocation is capable of reducing the sensitivity to channel estimation errors provided that these errors are confined to relatively small values. However, the sensitivity to high channel estimation errors becomes similar for all three schemes. The resaon for these obervation is that the value of Δh has been increased by using the proposed schemes. As a result, the proposed schemes became robust to small channel estimation errors.

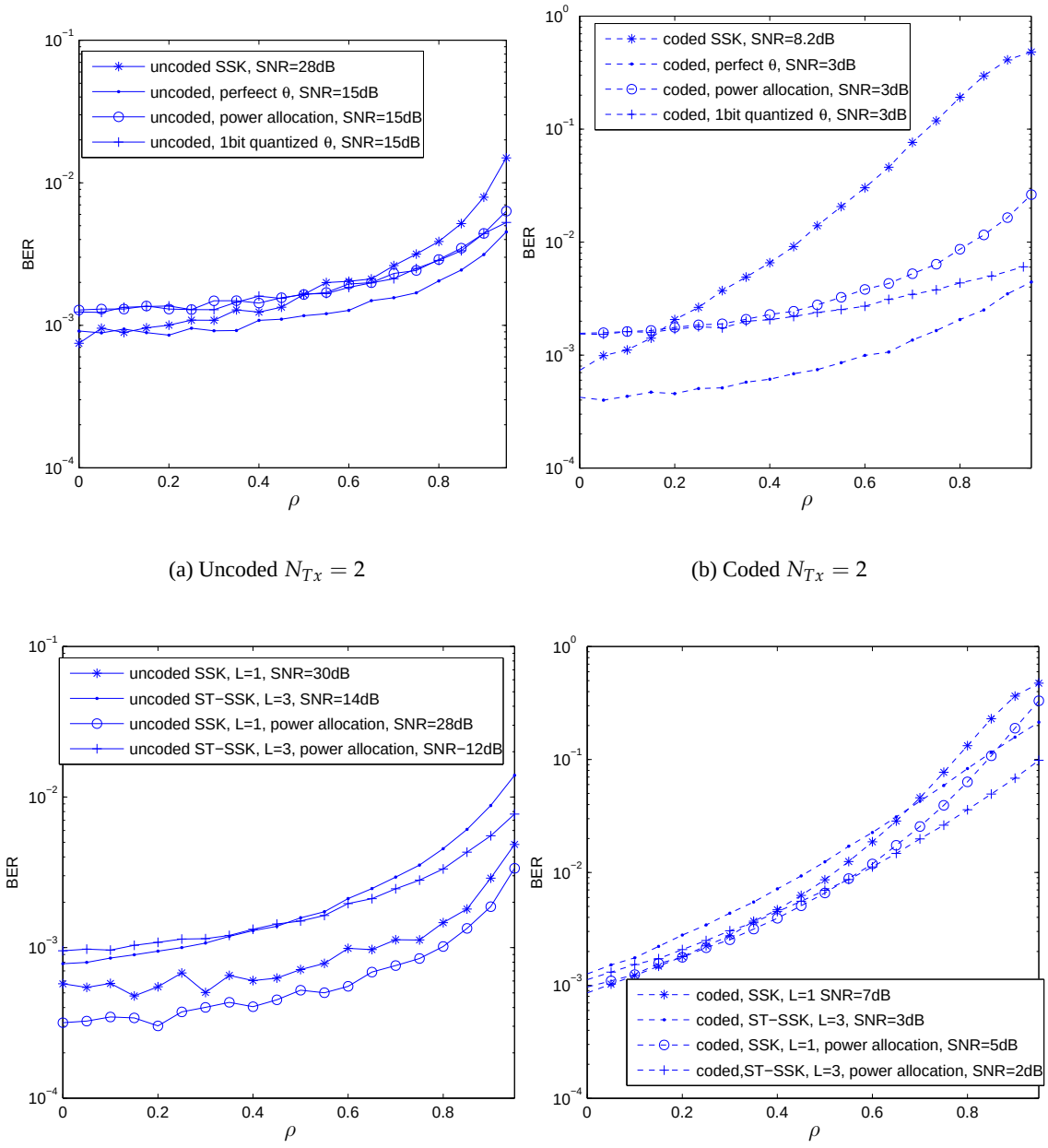

(a) Uncoded $N_{Tx} = 2$

(b) Coded $N_{Tx} = 2$

(c) Uncoded $N_{Tx} = 4$

(d) Coded $N_{Tx} = 4$

Figure 6.8: Uncoded and coded BER performance versus the spatial correlation coefficient $\rho_{h_i h_j}$ at a fixed SNR per bit value using 1) the original open-loop SSK modulation; 2) the proposed closed-loop scheme using perfect and quantized phase feedback for $N_{Tx} = 2$; 3) the proposed feedback-aided power allocation scheme for $N_{Tx} = 2$; 4) the proposed open-loop ST-SSK scheme for $N_{Tx} = 4$; and 5) a combination of ST-SSK and feedback-aided power allocation for $N_{Tx} = 4$. All other system parameters are summarized in Table 6.4.

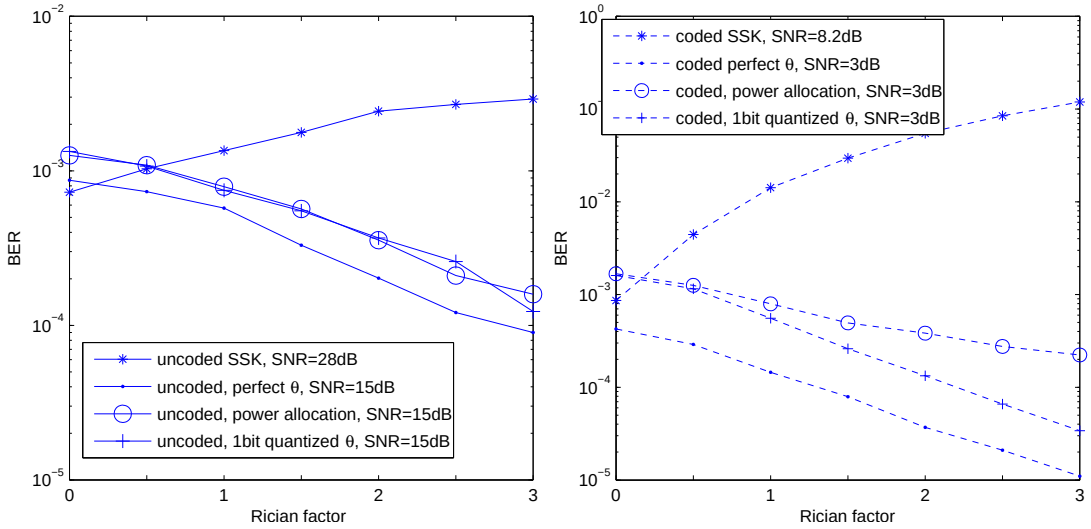

(a) Uncoded $N_{Tx} = 2$

(b) Coded $N_{Tx} = 2$

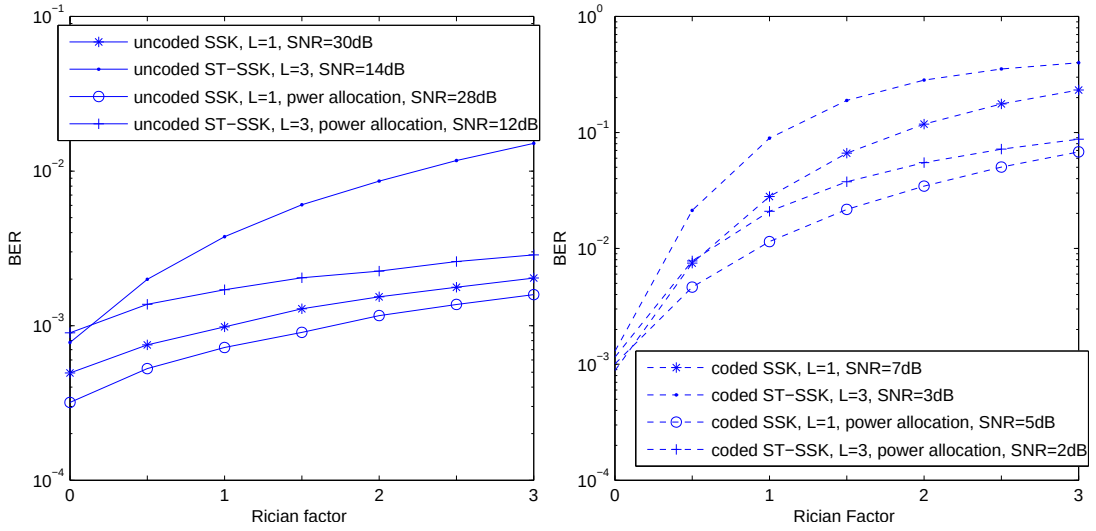

(c) Uncoded $N_{Tx} = 4$

(d) Coded $N_{Tx} = 4$

Figure 6.9: Uncoded and coded BER performance versus the Rician factor A at a fixed SNR per bit value using 1) the original open-loop SSK modulation; 2) the proposed closed-loop scheme using perfect and quantized phase feedback for $N_{Tx} = 2$; 3) the proposed feedback-aided power allocation scheme for $N_{Tx} = 2$; 4) the proposed open-loop ST-SSK scheme for $N_{Tx} = 4$; and 5) a combination of ST-SSK and feedback-aided power allocation for $N_{Tx} = 4$. All other system parameters are summarized in Table 6.4.

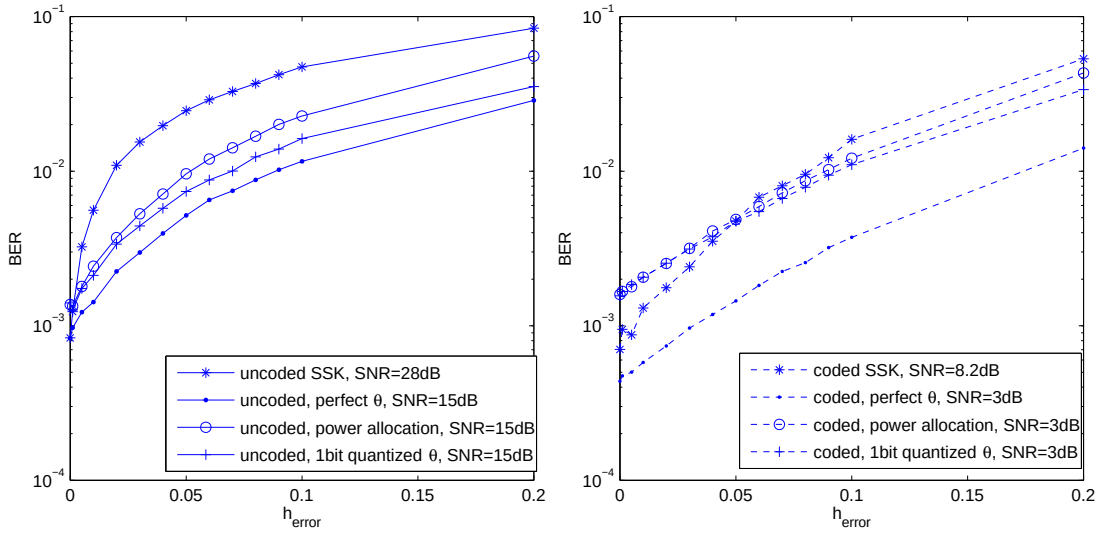

(a) Uncoded $N_{Tx} = 2$ (b) Coded $N_{Tx} = 2$

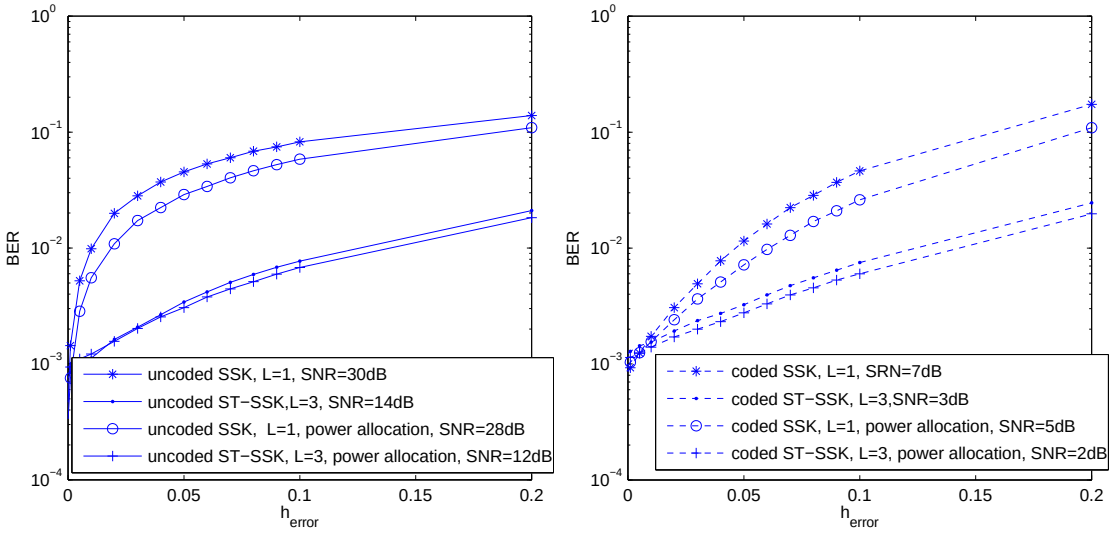

(c) Uncoded $N_{Tx} = 4$ (d) Coded $N_{Tx} = 4$

Figure 6.10: Uncoded and coded BER performance versus the variance of the channel estimation error h_e at a fixed SNR per bit value using 1) the original open-loop SSK modulation; 2) the proposed closed-loop scheme using perfect and quantized phase feedback for $N_{Tx} = 2$; 3) the proposed feedback-aided power allocation scheme for $N_{Tx} = 2$; 4) the proposed open-loop ST-SSK scheme for $N_{Tx} = 4$; and 5) a combination of ST-SSK and feedback-aided power allocation for $N_{Tx} = 4$. All other system parameters are summarized in Table 6.4.

6.3 Transmit Diversity Assisted Spatial Modulation

In Section 6.2, we proposed an open-loop scheme and two closed-loop schemes in order to achieve transmit diversity for a system using SSK modulation. In this section, we propose a transmit diversity aided spatial modulation scheme, which is a combination of the ST-SSK scheme and of the diagonal LDC scheme proposed in Section 6.3.1. The diagonal LDC is capable of achieving the maximum attainable transmit diversity, while activating only a single transmit antenna each time, and hence using a low-complexity single-stream detector. In Section 6.3.2, the diagonal LDC is combined with the ST-SSK schemes proposed in Section 6.2.1, which compensates the throughput loss imposed by the employment of ST-SSK scheme, while providing a flexible transmission arrangement, as demonstrated by the simulation results of Figs. 6.12 and 6.13. For simplicity, the wireless channel considered in this section is an i.i.d. Rayleigh fading channel.

6.3.1 Diagonal LDC

As discussed in Section 6.1.3, one of the major benefits of the SSK/SM modulation is its low complexity. However, the benefit of having a low complexity is not an explicit benefit of the SM scheme, it is rather a result of activating less transmit antennas at each transmission instant. The diagonal LDC scheme proposed in this section is a low-complexity MIMO scheme using the conventional APM, which activates a single transmit antennas at each transmission instant. We will demonstrate that this scheme is capable of achieving the maximum attainable diversity gain as well as multiplexing gain at the same time.

Assuming that M-level QAM modulation is employed, the L-element transmit symbol vector $\boldsymbol{x}$ radiated during L consecutive time slots using the proposed diagonal LDC is formulated as

$$\boldsymbol{x} = \sum_{i=1}^{N_s} \sqrt{m_2 E_b}\boldsymbol{g}_i s_i,\ i = 1, \ldots, N_s, \tag{6.12}$$

where $m_2 = log_2 M$, $\boldsymbol{g}$ represents a L-element unitary vector, s_i represents the QAM modulated symbol having a normalised power, and N_s is the number of multiplexed modulated symbols. Similar to the conventional LDC detailed in Section 4.2.1, the diagonal LDC is defined by its Dispersion Character Matrix $\boldsymbol{\chi}_{diag-LDC}$, which is a $(L \times N_s)$-element complex-valued matrix formulated as

$$\boldsymbol{\chi}_{diag-LDC} = [\boldsymbol{g}_1 \quad \boldsymbol{g}_2 \quad \ldots \quad \boldsymbol{g}_{N_s}]. \tag{6.13}$$

Using this matrix, the L-element transmit symbol vector $\boldsymbol{x}$ may be expressed in a more compact matrix format as

$$\boldsymbol{x} = \boldsymbol{\chi}_{diag-LDC}\boldsymbol{s}, \tag{6.14}$$

where $\boldsymbol{s}$ is a N_s-element vector that consists of N_s modulated symbols. There are a total of M^{N_s} legitimate combinations of $\boldsymbol{s}$ when M-level QAM is employed.

The L elements in the transmit vector $\boldsymbol{x}$ are transmitted one by one using L time slots. A different transmit antenna is activated in each time slot, whose index is denoted as $f(t_l), (1 \leq f(t_l) \leq N_{Tx},\ 1 \leq t_l \leq L)$ and $f(t_l) \neq f(t_n), (l \neq n)$. Consequently, for a system having N_{Tx} transmit antennas and a

single receive antenna, the L-element received signal vector $\boldsymbol{y}$ of the L time slots may be expressed as

$$\begin{bmatrix} y^{t_1} \\ \vdots \\ y^{t_l} \\ \vdots \\ y^{t_L} \end{bmatrix} = \sqrt{\frac{mE_b}{L}} \begin{bmatrix} h_{f(t_1)} & 0 & \dots & \dots & 0 \\ 0 & \ddots & & & \vdots \\ \vdots & & h_{f(t_j)} & & \\ & & & \ddots & 0 \\ 0 & & \dots & 0 & h_{f(t_L)} \end{bmatrix} \begin{bmatrix} g_{11} & g_{12} & \cdots & g_{1N_s} \\ \vdots & \vdots & \vdots & \vdots \\ g_{L1} & g_{L2} & \cdots & g_{LN_s} \end{bmatrix} \begin{bmatrix} s_1 \\ \vdots \\ s_{N_s} \end{bmatrix} + \begin{bmatrix} n^{t_1} \\ \vdots \\ n^{t_l} \\ \vdots \\ n^{t_L} \end{bmatrix}. \tag{6.15}$$

The maximum attainable transmit diversity N_{Tx} is achieved if we have $L = N_{Tx}$. More generally, for a system having N_{Rx} receive antennas, the received signal $\boldsymbol{y}$ of the L time slots is formulated as

$$\begin{bmatrix} y_1^{t_1} \\ y_2^{t_1} \vdots \\ y_{N_{Rx}}^{t_1} \\ \vdots \\ y_1^{t_L} \\ y_2^{t_L} \\ \vdots \\ y_{N_{Rx}}^{t_L} \end{bmatrix} = \sqrt{\frac{mE_b}{L}} \begin{bmatrix} h_{1f(t_1)} & & & \\ h_{2f(t_1)} & & & \\ \vdots & & & \\ h_{N_{Rx}f(t_1)} & & & \\ & \vdots & & \\ & & h_{1f(t_L)} & \\ & & h_{2f(t_L)} & \\ & & \vdots & \\ & & h_{N_{Rx}f(t_L)} & \end{bmatrix} \begin{bmatrix} g_{11} & \cdots & g_{1N_s} \\ \vdots & \vdots & \vdots \\ g_{L1} & \cdots & g_{LN_s} \end{bmatrix} \begin{bmatrix} s_1 \\ \vdots \\ s_{N_s} \end{bmatrix} + \begin{bmatrix} n_1^{t_1} \\ n_2^{t_1} \\ \vdots \\ n_{N_{Rx}}^{t_1} \\ \vdots \\ n_1^{t_L} \\ n_2^{t_L} \\ \vdots \\ n_{N_{Rx}}^{t_L} \end{bmatrix}. \tag{6.16}$$

Alternatively, this transmission regime may be characterised in a more compact format as

$$\bar{\boldsymbol{y}} = \sqrt{\frac{m_2 E_b}{L}} \bar{\boldsymbol{H}} \boldsymbol{\chi}_{diag-LDC} \boldsymbol{s} + \bar{\boldsymbol{n}}, \tag{6.17}$$

where the received signal $\bar{\boldsymbol{y}}$ is a $(N_{Rx}L \times 1)$-element vector, the equivalent channel $\bar{\boldsymbol{H}}$ is a $(N_{Rx}L \times L)$-element matrix, the diagonal LDC's dispersion character matrix $\boldsymbol{\chi}_{diag-LDC}$ is a $(L \times N_s)$-element complex-valued matrix, the signal vector $\boldsymbol{s}$ is a N_s-element vector having M^{N_s} legitimate values and the equivalent noise $\bar{\boldsymbol{n}}$ is a $N_{Rx}L$-element Gaussian variable.

At the receiver, the symbol detection using the ML detector considering M^{N_s} legitimate values may be formulated as

$$\hat{\boldsymbol{s}} = \arg\min_i \|\bar{\boldsymbol{y}} - \bar{\boldsymbol{H}} \boldsymbol{\chi}_{diag-LDC} \boldsymbol{s}_i\|^2. \tag{6.18}$$

If the conventional LDC detailed in Section 4.2.1 is employed, its dispersion character matrix $\boldsymbol{\chi}_{conv-LDC}$ has a larger size of $(N_{Tx}L \times N_s)$, and the corresponding equivalent channel $\bar{\boldsymbol{H}}$ also has a larger size of $(N_{Rx}L \times N_{Tx}L)$ elements. As a result, the complexity of the ML detector using the proposed diagonal LDC is only $1/N_{Tx}$ of that using the conventional LDC. Moreover, the synchronisation between transmit antennas is also avoided by using the diagonal LDC structure, since only a single transmit antenna is activated in each time slot.

The optimization of the dispersion character matrix is essential for both the conventional LDCs [179], as well as for the proposed diagonal LDC. A simple optimisation technique is to generate a large number of $\boldsymbol{\chi}_{diag-LDC}$ matrices consisting of unitary vectors and then choose the particular one offering the

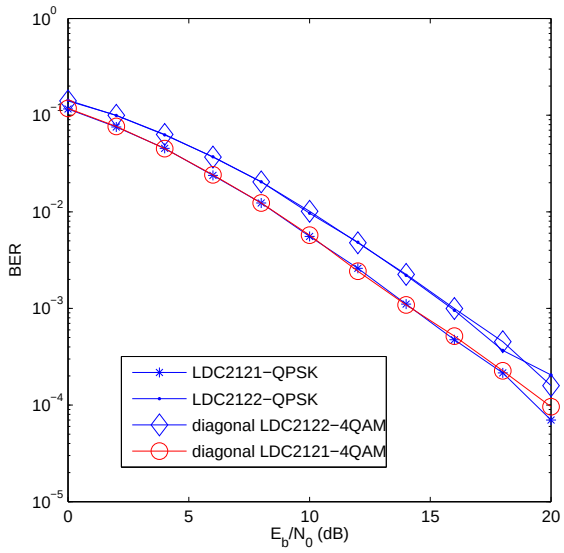

Figure 6.11: BER versus E_b/N_0 for a system having two transmit antennas and a single receive antenna, for the LDC2121-QPSK, LDC2122-QPSK, diagonal LDC2121-4QAM and diagonal LDC2122-4QAM schemes, respectively.

best BER performance at a high SNR value using full search. Two optimal dispersion character matrices have to be derived using this method for a system having two transmit antennas as well as a single receive antenna and transmitting one or two QPSK/4QAM modulated symbols within two time slots. In order to facilitate our further discussion, we refer to the different diagonal LDCs as the "diagonal LDC$N_{Tx}N_{Rx}LN_s$-modulation", similarly to Section 4.2.1 related to conventional LDCs. Hence, the resultant pair of optimal diagonal LDCs are termed as the diagonal LDC2121-4QAM and diagonal LDC2122-4QAM. Their uncoded BER performances are compared to the corresponding conventional LDCs. It is demonstrated in Fig. 6.11 that the diagonal LDC achieves exactly the same uncoded BER performance as the conventional LDCs of Section 4.2.1.

6.3.2 Combination of the ST-SSK and the Diagonal LDC

It is a natural choice to combine the ST-SSK scheme proposed in Section 6.2.1 and the diagonal LDC scheme detailed in Section 6.3.1, so that a transmit diversity gain is achieved for both the SSK as well as the APM and diagonal LDC schemes. Another benefit is that the throughput loss imposed by the ST-SSK scheme might be compensated by increasing the number of modulation levels or the multiplexing order N_s of the diagonal LDC employed.

However, this combination cannot guarantee that a transmit diversity order of $L(L < N_{Tx})$ is achieved for both the SSK modulated and for the diagonal LDC coded information symbols. The index of the activated transmit antennas has to be different from each other for each of the L time slots for the diagonal LDC coded information symbols in order to achieve the maximum attainable the L-th order transmit diversity. By contrast, the same transmit antenna might have to be activated more than once in each of the L time slots for creating L independent Δh values, so that the SSK modulated information symbols benefit from a diversity order of L. For example, the first antenna may be activated in the second

and third time slot, when the bits sequence $[0\ 1]$ is transmitted using the ST-SSK scheme, as shown in Table 6.3b. of Section 6.2.1. By appropriately choosing the activated transmit antennas for each of the L times slots, it is possible to enhance either the SSK modulated or the diagonal LDC coded information symbols.

Configuration	N_{Tx}	N_{Rx}	L	m_1	m_2	N_s	$\boldsymbol{g}$	ML detector complexity
a	8	1	-	3	-	-	-	$4N_{Tx}N_{Rx} = 32$
b	8	1	2	3	3	1	$\sqrt{\frac{1}{L}}[1,\ldots,1]^T$	$4N_{Tx}N_{Rx}ML = 512$
c	8	1	3	3	6	1	$\sqrt{\frac{1}{L}}[1,\ldots,1]^T$	$4N_{Tx}N_{Rx}ML = 6144$
d	4	1	2	2	2	2	$[0,\ldots,0,1_q,0,\ldots,0]^T$	$4N_{Tx}N_{Rx}ML = 126$
e	4	1	2	2	2	2	unitary vector	$4N_{Tx}N_{Rx}M^{N_s}L = 512$
f	4	1	2	-	3	2	unitary vector	$4N_{Rx}M^{N_s}L = 256$
g	4	2	2	2	2	2	unitary vector	$4N_{Tx}N_{Rx}M^{N_s}L = 1024$
h	4	2	2	-	3	2	unitary vector	$4N_{Rx}M^{N_s}L = 512$
i	8	2	3	3	6 (64)	1	$\sqrt{\frac{1}{L}}[1,\ldots,1]^T$	$4N_{Tx}N_{Rx}ML = 12288$

Table 6.5: Computational complexity of the various MIMO systems achieving a thoughput of $R = 3$ (bits/sym), for $m_1 = \log_2 N_{Tx}$ and $m_2 = \log_2 M$.

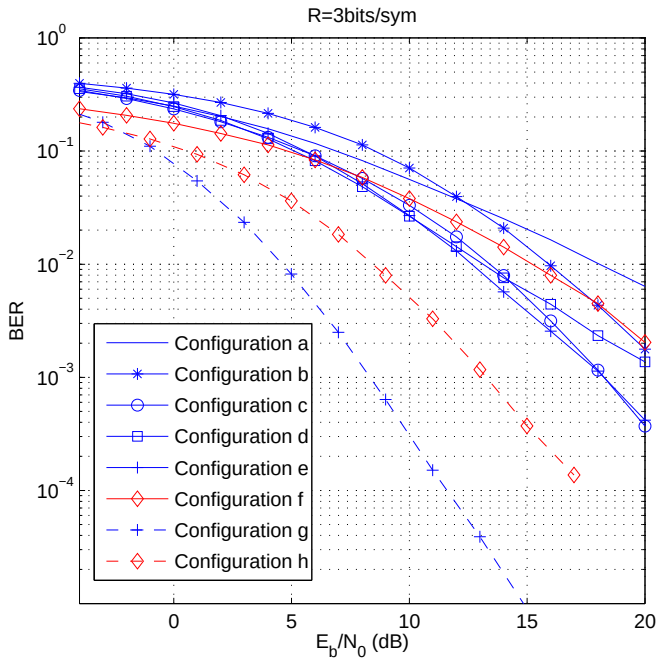

Figure 6.12: BER versus $\frac{\varepsilon_b}{N_0}$ for a system having $N_{Rx} = 1,\ 2$ and a throughput of $R = 3$ (bits/sym) using the various configurations listed in Table 6.5

In Fig. 6.12 and 6.13, the uncoded and coded BER performance of the original SSK scheme, of the diagonal LDC scheme and of the combination of the LDC and ST-SSK schemes is compared. The parameters of eight different configurations are listed in Table 6.5 in conjunction with their complexity when using the ML detector. Each of them achieves a throughput of 3 (bit/symbol). The uncoded BER performances of these eight configurations are characterized in Fig. 6.12, and the corresponding coded

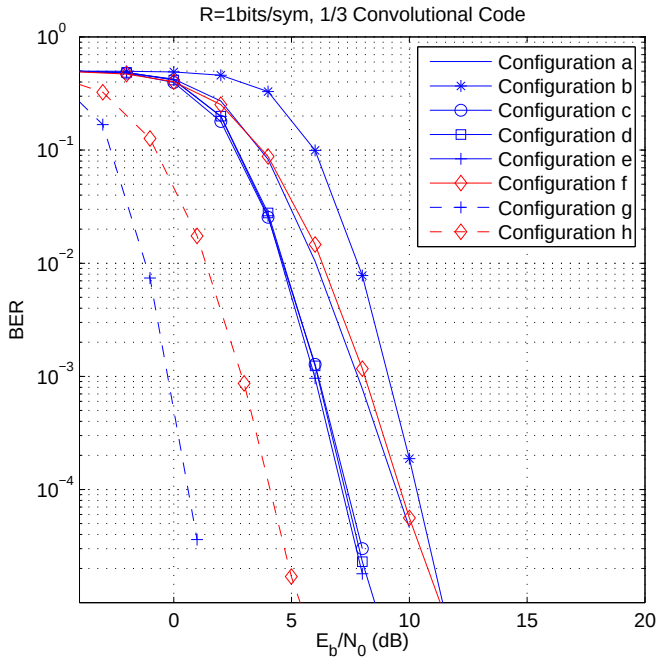

Figure 6.13: BER versus $\frac{\varepsilon_b}{N_0}$ for a coded system having $N_{Rx} = 1, 2$ and a throughput of $R = 1$ (bits/sym) using $\frac{1}{3}$ convolutional codes and the various configurations listed in Table 6.5

BER performance of the $R = 1$ (bits/sym) scheme using a $\frac{1}{3}$-rate convolutional code is illustrated in Fig. 6.13. Configuration (a) utilised $N_{Tx} = 8$ transmit antennas, $N_{Rx} = 1$ receive antenna and the conventional SSK modulation scheme, in order to achieve a throughput of $R = 3$ (bits/sym) and a diversity order of one. Configuration (b) uses two time slots for transmission, and employed $N_s = 1$, as well as $M = 8$-QAM to compensate for the throughput loss. Its uncoded BER performance is worse than that of Configuration (a) at low SNRs because of the increased number of modulation levels, but it becomes better at high SNRs because of the increase in its achievable transmit diversity order. However, the coded performance of Configuration (b) is about 4dB worse than that of Configuration (a) at a BER of 10^{-3}. Configuration (c) further increased the value of L to three, and employed 64QAM for throughput compensation. When achieving a transmit diversity order of three, both the uncoded and coded BER performance improved compared to that of Configuration (a). However, the complexity of the detector has also dramatically increased. Configuration (d) employed $N_{Tx} = 4, N_{Rx} = 1$ antennas, 4-SSK modulation and two time slots to separately transmit two 4-QAM modulated symbols. The achievable uncoded BER performance of Configuration (d) at low and medium SNRs is almost the same as that of Configuration (c), but at a significantly reduced complexity. At high SNRs, the uncoded BER performance of Configuration (d) is worse than that of Configuration (c) because the 4QAM symbols of Configuration (d) benefit from a transmit diversity order of one only. If these two 4QAM symbols are dispersed to two time slots by two complex-valued dispersion vectors, as in Configuration (e), the uncoded BER performance improves at high SNRs at the cost of slightly increasing of the detector's complexity. Nevertheless, the coded BER performance of Configurations (c) (d) and (e) is almost identical since their uncoded BER performances are similar at low and medium SNRs. If the SSK modulation scheme is not employed, as in Configuration (f), the uncoded BER performance improves at low SNRs between -4dB and 5dB, since no error propagation is imposed by the SSK modulated symbols. However, the uncoded

BER performance of Configuration (f) recorded at high SNRs is worse than that of Configuration (c) (d) and (e) because QAM is not a power-efficient scheme. Similar trends may also be observed for the coded scenario. The benefits of using SSK modulation are further demonstrated by comparing the performance of Configuration (g) and (h), where $N_{Rx} = 2$, ST-SM and ST are employed, respectively. As discussed in Section 6.1, the minimum Euclidean distance of the symbols using SSK modulation improves, when N_{Rx} is increased. Hence, the benefits of employing the ST-SM scheme, as in Configuration (g) over the pure STBC scheme of Configuration (h) becomes more substantial.

6.4 Chapter Summary

In this chapter, we have studied various SM aided open-loop and closed-loop MIMO systems obeying the architecture of Fig. 6.1. In Section 6.1, we have first provided an overview of the SM scheme, where the corresponding modulation and detection algorithms were detailed, and a comparison between the SSK and the conventional APM scheme was given. Then, in Section 6.2, we have proposed a novel open-loop scheme termed as ST-SSK and two closed-loop schemes, namely the feedback-aided phase rotation and feedback-aided power allocation regimes designed for achieving transmit diversity for a system using SSK modulation. The simulation results extracted from Fig. 6.5 to Fig. 6.10 demonstrated that in addition to achieving transmit diversity, the proposed scheme also enhances the robustness of the system to channel effects, such as spatial correlation and channel estimation errors. The advocated schemes performe better than the original SSK modulation in the scenario of having Rician fading channels. Moreover, in Section 6.3 a diagonal LDC scheme was proposed, which is capable of striking a flexible trade-off between the maximum attainable diversity as well as multiplexing gain. By activating only a single transmit antenna in each transmission time slot, the proposed diagonal LDC scheme is also capable of dispensing with the synchronization between transmit antennas, as well as reducing the complexity of the receiver by using a single-stream ML detector. Furthermore, a combination of the diagonal LDC and the ST-SSK scheme was proposed in Section 6.3, which provides a transmit diversity gain for both the SSK modulated and LDC coded information bits. The scenarios considered in this chapter may be streamlined into six typical systems, whose parameters are summarised in Table 6.6. The corresponding simulation results are protrayed in Table 6.7, which considers three groups of comparisons quantifying the advantages of the proposed schemes.

Table 6.6: Simulation Parameters

Channel Code		Convolutional code
Coding Rate r_c		$\frac{1}{3}$
Interleaver Length		1500
Channel Spatial Correlation$\rho_{h_i h_j}$		$\rho_{h_i h_j} = 0, 0.05, \ldots, 0.95$
Rician Factor A		$A = 0, 0.5, \ldots, 2$
Channel Estimation Error h_e		$h_e = 0, 0.05, \ldots, 0.2$
System 1	Number of antennas $((N_{Tx},\ N_{Rx}))$	(2,1)
	Modulation	2-SSK
	Quantization bits b	1
System 2	Number of antennas $((N_{Tx},\ N_{Rx}))$	(4,1)
	Modulation	4-SSK
	Quantization bits b	2
System 3	Number of antennas $((N_{Tx},\ N_{Rx}))$	(4,1)
	Modulation	4-SSK
	ST-SSK Time Slot L	3
	Quantization bits b	2
System 4	Number of antennas $((N_{Tx},\ N_{Rx}))$	(8,1)
	Modulation	8-SSK
System 5	Number of antennas $((N_{Tx},\ N_{Rx}))$	(4,1)
	LDC	diagonal LDC4122-8QAM
System 6	Number of antennas $((N_{Tx},\ N_{Rx}))$	(4,1)
	LDC	diagonal LDC4122-4QAM
	SSK	4-SSK
	ST-SSK Time Slot T	2

Table 6.7: Performance Summary

System Parameter	Comparison Schemes	BER Performance (uncoded/coded) SNR=15dB / SNR=4dB	$\rho = 0.8$	$A = 2$	$h_{error} = 0.1$	R (bits /sym)	Detector com--plexity
System 1 in Table 6.6	Conventional SSK	$1.5 \cdot 10^{-2}$ / $4 \cdot 10^{-2}$	$4 \cdot 10^{-3}$ / $2 \cdot 10^{-1}$	$2 \cdot 10^{-3}$ / $5 \cdot 10^{-2}$	$5 \cdot 10^{-2}$ / $1.5 \cdot 10^{-2}$	1 / $\frac{1}{3}$	8 / 8
	Feedback-aided Phase rotation	10^{-3} / $3 \cdot 10^{-3}$	$3 \cdot 10^{-3}$ / $4 \cdot 10^{-3}$	$4 \cdot 10^{-4}$ / 10^{-4}	$1.5 \cdot 10^{-2}$ / 10^{-2}	1 / $\frac{1}{3}$	8 / 8
	Feedback-aided Power allocation	10^{-3} / $3 \cdot 10^{-3}$	$3 \cdot 10^{-3}$ / 10^{-2}	$4 \cdot 10^{-4}$ / $3 \cdot 10^{-4}$	$2 \cdot 10^{-2}$ / 10^{-2}	1 / $\frac{1}{3}$	8 / 8
System 2 in Table 6.6	Conventional SSK	$1.5 \cdot 10^{-2}$ / $3 \cdot 10^{-2}$	$1.5 \cdot 10^{-3}$ / $1.5 \cdot 10^{-1}$	$1.5 \cdot 10^{-3}$ / 10^{-1}	$8 \cdot 1-^{-2}$ / $4 \cdot 10^{-2}$	2 / $\frac{1}{3}$	16 / 16
	Feedback-aided Power allocation	$5 \cdot 10^{-3}$ / $4 \cdot 10^{-3}$	10^{-3} / $8 \cdot 10^{-2}$	10^{-3} / $3 \cdot 10^{-2}$	$7 \cdot 10^{-2}$ / $2 \cdot 10^{-2}$	2 / $\frac{1}{3}$	16 / 16
System 3 in Table 6.6	ST-SSK	$4 \cdot 10^{-4}$ / $2 \cdot 10^{-4}$	$4 \cdot 10^{-3}$ / $9 \cdot 10^{-2}$	$8 \cdot 10^{-2}$ / $3 \cdot 10^{-1}$	$7 \cdot 10^{-3}$ / $6 \cdot 10^{-3}$	$\frac{2}{3}$ / $\frac{2}{9}$	48 / 48
	ST-SSK+ power allocation	10^{-4} / $2 \cdot 10^{-5}$	$3 \cdot 10^{-3}$ / $4 \cdot 10^{-2}$	$2 \cdot 10^{-2}$ / $4 \cdot 10^{-2}$	$6 \cdot 10^{-3}$ / $5 \cdot 10^{-3}$	$\frac{2}{3}$ / $\frac{2}{9}$	48 / 48
System 4 in Table 6.6	Conventional SSK	$2 \cdot 10^{-2}$ / $3 \cdot 10^{-1}$	- / -	- / -	- / -	3 / 1	32 / 32
System 5 in Table 6.6	Diagonal LDC	$3 \cdot 10^{-3}$ / 10^{-1}	- / -	- / -	- / -	3 / 1	256 / 256
System 6 in Table 6.6	Diagonal LDC + ST-SSK	$3 \cdot 10^{-3}$ / $3 \cdot 10^{-2}$	- / -	- / -	- / -	3 / 1	512 / 512

Chapter 7

Conclusions and Future Work

In this treatise, closed-loop multiple antenna aided wireless communications systems using limited feedback is studied, with the goal of improving the efficiency of the CSIT acquisition and exploitation. Four particular applications of closed-loop based MIMO schemes are investigated in this thesis, namely the TxMF aided single-user MISO system of Chapter 3, the TxEBF aided single-user MIMO system of Chapter 4, the linear MUT aided multi-user SDMA downlink discussed in Chapter 5 and the spatial modulation aided single-user MIMO system detailed in Chapter 6. This chapter summarises the key contents and contributions of each chapter and presents their most salient conclusions. Then some design guidlines for closed-loop MIMO system using limited feedback are provided in Section 7.2. Our suggestions for future research are outlined thereafter.

7.1 Chapter Summaries

7.1.1 Chapter 1

Chapter 1 constitutes the general background of our studies throughout this thesis. More specifically, a brief review of MIMO techniques, especially closed-loop MIMO techniques was provided in Section 1.1. Then the scope of this thesis was specified in Section 1.2. Moreover, Section 1.3 outlines the focus of each chapter. Finally, the novel contributions were described in Section 1.4.

7.1.2 Chapter 2

Chapter 2 discussed three key topics in closed-loop MIMO communication, namely the channel model in Section 2.1, the linear transmit preprocessing philosophy in Section 2.2 and the CSI quantisation in Section 2.3. This chapter is the foundation of the entire thesis. The algorithms described in this chapter, including the channel modelling algorithms, the transmit preprocessing algorithms and the CSI quantisation codebook generation algorithms were extensively used in the following four main chapters.

More explicitly, Section 2.1 commenced with a general description of wireless channels in Section 2.1.1, where slow frequency-flat/narrow-band Rayleigh fading channels were considerred. Then the algorithms of MIMO channel modelling were introduced in Section 2.1.2, where the modelling of the

spatial- and of temporal-domain proporties were presented in Section 2.1.2.1 and 2.1.2.2, respectively. Using these modelling algorithms, an example of a MIMO channel having two transmit antennas and a single receive antenna was portrayed in Section 2.1.3. The simulation results shown in Figs. 2.6 and 2.7 demonstrated that the joint distributions of the two channel envelopes and channel phases are different from each other, and vary with the spatial correlation coefficient. Hence, two different CSI quantisers specifically designed for the channel envelope and channel phase vectors were required.

Moreover, Section 2.2 introduced five linear transmit preprocessing algorithms, which are classified into algorithms designed for single-user scenarios, including the Transmit Matched filter (TxMF) and the Transmit Eigen-Beamforming (TxEBF) detailed in Section 2.2.1, as well as the Multi-user Transmitter (MUT) algorithms conceived for multi-user scenarios, including the Transmit Zero-Forcing (TxZF), Transmit Minimum Mean Square Error (TxMMSE) and Transmit Block Diagonalization (TxBD) discussed in Section 2.2.2. Four aspects were highlighted for each transmit preprocessing algorithm, which are the algorithms' derivation, their benefits, constraints and the required feedback information. A summary of these transmit preprocessing schemes was provided in Table 2.3 of Section 2.2.3. The specific type of the required CSI was classified into six categories, which are explicitly listed in Section 2.2.3.

Furthermore, the design of CSI quantisers was presented in Section 2.3. A general introduction to quantization was provided in Section 2.3.1, along with the Linde-Buzo-Gray (LBG) codebook generation algorithm. Then three types of quantisers were introduced, which were classified according to the distance metrics employed for measuring the quantisation error between the unquantised and the corresponding quantised data points. More explicitly, quantisers using the Euclidean distance metric were discussed in Section 2.3.2, which is applicable for arbitrary quantizers such as scalar, vector, matrix, real-valued and complex-valued schemes. The LBG algorithm was employed for generating codebooks having an arbitrary size. The averaged quantisation error versus the number of quantisation bits for 2-dimensional Rayleigh distributed real-value vectors was illustrated in Fig. 2.11. The second type of quantisers using the chordal distance was detailed in Section 2.3.3, which was designed for unitary vectors. The codebook generation using the LBG algorithm was detailed in Section 2.3.3, and the averaged quantization error versus the number of quantization bits was illustrated in Fig. 2.12 for 2-dimensional unitary vectors. The third type of quantisers using the Fubini-Study distance was detailed in Section 2.3.4, which is used for unitary matrices. The corresponding codebook was constructed either using the Grassmannian subspace-packing results available in the open literature [133] or was randomly generated. The averaged quantisation error versus the number of quantisation bits for a (4×2)-element unitary matrix was illustrated in Fig. 2.13.

7.1.3 Chapter 3

Chapter 3 investigated the design of the TxMF aided closed-loop single-user MISO system illustrated in Fig. 3.1. First of all, Section 3.1 commenced with the investigation of the achievable ergodic channel capacity using quantised CSI. Four different quantisers were compared in Section 3.1.1, and the results illustrated in Fig. 3.3 demonstrated that the achievable ergodic channel capacity is maximized by using the Grassmannian line-packing quantiser detailed in Section 2.3.3 and by feeding back the unitary preprocessing vector $\frac{\boldsymbol{h}}{|\boldsymbol{h}|}$. The performance of the Grassmannian line-packing quantiser was further investigated in Section 3.1.2, where both spatially independent and spatially correlated channels were considered. The simulation results portrayed in Fig. 3.4 and 3.5 demonstrated that the achievable ergodic channel

capacity of a TxMF aided closed-loop MISO system using even a single 1-bit quantized CSIT is always higher than that of its open-loop counterpart. The achievable channel capacity gain versus the number of feedback bits initially increases rapidly, but the improvements become more modest, when the value of feedback bits becomes higher.

Moreover, Section 3.2 investigated the achievable ergodic channel capacity in a more realistic scenario, where the channel estimation error, the pilot symbols' signalling overhead, the CSI quantisation error as well as the CSI feedback signalling overhead were all considered. The basic pilot-assisted channel estimation algorithm described in Section 3.2.1 was employed for simplicity. Using the closed-form capacity formula of Equations (3.5) and (3.8) derived in Section 3.2.2, the achievable ergodic capacity of an open-loop and of a TxMF aided closed-loop MISO system are compared in Section 3.2.3 using Mounte-Carlo simulation. The simulation results shown in Figs. 3.7, 3.8 and 3.9 demonstrated that the potential capacity improvements of using a closed-loop design and an increased number of transmit antennas are indeed achieveable for slowly fading channels, but erode for relatively rapidly fading channels. The main reason for this observation is that a large proportion of the channel capacity has to be sacrificed for pilot signalling, especially for systems having a high number of transmit antennas. The feedback overhead also imposes a capacity degradation, but this is less substantial than the effects of the pilot signalling overhead.

Since the investigations of Section 3.2 illustrated that the pilot signalling overhead imposed a serious performance degradation, a novel pilot overhead reduction scheme was proposed in Section 3.4 for rapidly fading channels. The philosophy of our proposed scheme is that the pilot symbols were multiplied with the unitary preprocessing vectors contained in the pre-defined codebook, so as to replace the consecutive transmission of pilots by their simultaneous transmission. The corresponding new frame structure was shown in Fig. 3.10. The main difference in comparison to that of Fig. 3.6 is that the number of the pilot symbols becomes independent of the number of transmit antennas, instead, it is related to the codebook size $|\boldsymbol{Q}|$. This will dramatically reduce the capacity loss caused by pilot symbols, especially when the number of transmit antennas is high, while the codebook size is limited. The simulation results shown in Fig. 3.11 demonstrated that a significant improvement was achieved using the proposed pilot signalling algorithm. For example, if we have a normalised Doppler frequency of $f_{dm-norm} = 0.1$, five transmit antennas, a single receiver antenna and a codebook with two entries, using the conventional pilot signalling scheme of Fig. 3.6, 50% of the channel capacity loss is imposed by the insertion of pilot symbols. By contrast, using the proposed scheme shown in Fig. 3.10, only 20% of the effective capacity is used for pilot invoked for channel estimation.

Furthermore, another novel technique referred to as Pilot Symbol Assisted Rateless (PSAR) coding was proposed in Section 3.4. After briefly introducing the rateless coding philosophy in Section 3.4.1, the system model was presented in Section 3.4.2, where the feedback CSI was used not only for TxBF preprocessing, but also for channel encoding. The philosophy of our proposed PSAR scheme is that a predetermined fraction of binary pilot symbols is interspersed with the channel-coded bits before the channel coding stage, instead of multiplexing the pilots with the data symbols after the FEC stage but before the modulation stage, as in classic Pilot Symbol Assisted Modulation (PSAM) used in previous sections. As a result, the PSAR code-aided transmit preprocessing scheme succeeds in gleaning more beneficial knowledge from the inserted pilots, because the pilot bits are not only useful for estimating the channel at the receiver, but they are also beneficial in terms of significantly reducing the computational

complexity of the rateless channel decoder. The detailed design of the proposed PSAR scheme, including the transmit distribution selector, the encoding process, the transmission and the decoding process were explicitly discussed in Sections 3.4.2.1 to 3.4.2.4. The simulation results shown in Fig. 3.18 demonstrated that a more than 30% decoder complexity reduction can be attained by the proposed system, when compared to the corresponding benchmarker scheme having the same pilot overhead but using the classic PSAM technique.

7.1.4 Chapter 4

Chapter 4 investigated the design of the TxEBF aided closed-loop single-user MISO system. First of all, relying to Section 3.1, where the achievable ergodic capacity of a TxMF aided closed-loop single-user MISO system was analysed, the achievable ergodic capacity of a TxEBF aided closed-loop single-user MIMO system was detailed in Section 3.1. More explicitly, the CCMC capacity achieved with the aid of perfect CSIR/CSIT was detailed in Section 3.1.1, where the upper-bound of the achievable ergodic capacity was provided and illustrated in Fig. 4.2. Then the CCMC capacity associated with perfect CSIR in combination with quantized CSIT was discussed in Section 4.1.2. The required feedback information, namely the power allocation vector and the activated eigen-beam vector, were discussed in Section 4.1.2. The simulation results portrayed in Fig. 4.6 illustrated the achievable ergodic capacity gain versus the number of quantization bits, which demonstrated that the achievable capacity gain may indeed be attained, when using a sufficiently high number of quantization bits.

Given the CSIT, the novel Linear Dispersion Code (LDC) aided TxEBF scheme of Section 4.2 may be invoked. After providing a brief introduction to LDCs in Section 4.2.1, our proposed algorithm of Fig. 4.8 was detailed in Section 4.2.2, along with the derivation of the achievable capacity of the proposed scheme. The philosophy of the scheme advocated is that the modulated symbols are first LDC encoded before preprocessing by the TxEBF weighting vectors. Armed with the LDCs, the proposed scheme is capable of achieving the maximum attainable diversity gain and of approaching the Discrete-Input-Continuous-Output Memoryless Channel's (DCMC) capacity for an arbitrary number of transmit and receive antennas. The simulation results of Figs. 4.9, 4.10 and 4.11 were interpreted in Section 4.2.3 and demonstrated the advantages of the proposed scheme in terms of the achievable DCMC capacity as well as the attainable BER performance.

In contrast to the LDC aided TxEBF scheme discussed in Section 4.2, where the LDCs were employed to eleminate the difference between the decomposed orthogonal eigen-beams, the algorithm proposed in Section 4.3 exploited the different channel quality of the orthogonal eigen-beams for unequal-protection video transmission. A brief introduction to the H.264/AVC video codec was provided in Section 4.3.1, which illustrated that the information bits representing a compressed video source signal have unequal error sensitivity. The philosophy of the proposed scheme is to transmit the more sensitive video bits through the eigen-beam having a higher eigen-value, while transmitting the less sensitive video bits through the eigen-beams corresponding to a lower eigen-value. The system model was detailed in Section 4.3.2. The simulation results of Figs. 4.13 and 4.14 in Section 4.3.3 demonstrated that improved video transmission quality was achieved using the proposed scheme.

7.1.5 Chapter 5

Chapter 5 investigated the design of the linear MUT aided closed-loop SDMA downlink. In contrast to the previous two chapters, where the feedback channel was assumed to be noise-free and delay free, the detrimental effects of imperfect feedback channels were investigated in this chapter. More explicitly, three scenarios of imperfect feedback channels were considered, namely bandwidth-limited, error-contaminated and delayed feedback channel. Three novel feedback schemes were proposed corresponding to the aforementioned three types of imperfect feedback channel.

First of all, the novel concept, of Exit-Chart Optimized CSI Quantization (ECO-CQ) was proposed in Section 5.1. After briefly reviewing the pilot-aided CIR estimation and CIR feedback illustrated in Fig. 5.2, the philosophy of the proposed scheme was detailed in Section 5.1.1, explicitly the ECO-CQ assists the system in maintaining the lowest possible CSI feedback overhead, while ensuring that an open EXIT-tunnel is still attainable so as to achieve an infinitesimally low BER. The proposed scheme was applied in a TxBD aided SDMA downlink system, whose system model was detailed in Section 5.1.2 and the related EXIT-Chart analysis was provided in Section 5.1.3. The simulation results of Fig. 5.9 in Section 5.1.4 demonstrated that the proposed ECO-CQ may reduce the normalised feedback overhead compared to the conventional Channel Quantizer (CQ). For instance, as summarised in Table 5.2, the ECO-CQ aided iterative downlink SDMA system using an average of 2.7 quantization bits per CIR coefficient achieves a 10% normalised overhead reduction at $E_b/N_0 = 5$dB, compared to the conventional CQ aided benchmark system.

Moreover, a soft decoding assisted MIMO CIR recovery scheme was proposed in Section 5.2, which is capable of minimising the distortion imposed by error-prone feedback channels. The proposed scheme was applied in a TxMMSE assisted MISO multi-user SDMA system, which is illustrated by Fig. 5.10 in Section 5.2.1. The soft decoding algorithm was detailed in Section 5.2.2. More explicitly, the CIR reconstructed at the transmitter using the proposed soft VQ decoder is constituted by a linear combination of the codebook entries recovered from the error-contaminated received signal. As a result, this design does not rely on the straightforward feedback of a specific CIR tap's index or of an entire CIR's index. A visualisation of the proposed algorithm was offerred by Fig. 5.11. The simulation results of Figs. 5.12, 5.13 and 5.14 Section 5.2.3 demonstrated that both the average reconstruction error and the achievable BER performance were improved using the proposed soft VQ decoder.

Furthermore, a periodically activated CIR update scheme employing a channel predictor at the DL transmitter for predicting the CIR taps for each future symbol transmission instant was proposed in Section 5.3. Hence this scheme mitigates the performance degradation imposed by the associated signalling delays. The design of long-term channel prediction including both the scalar and vector quantiser was introduced in Section 5.3.1. Then a Predictive Vector Quantizer (PVQ) of Fig. 5.17 was discussed in Section 5.3.2. The simulation results were illustrated in Section 5.3.4. Compared to a conventional Vector Quantizer (VQ), the PVQ has significantly reduced the CIR feedback bit rate. Hence, the new PVQ scheme was capable of providing more accurate CIR information or of supporting a channel having a higher Doppler frequency in comparison to a conventional VQ while using a fixed feedback bit rate.

7.1.6 Chapter 6

Chapter 6 investigated the design of the Spatial Modulation (SM) aided open-loop and closed-loop single-user MIMO. Section 6.1 commenced with a literature review of SM schemes, along with the detailed portrayal of the SM algorithm, and its comparison to the conventional Amplitude and Phase Modulation (APM). It was demonstrated in this section that the SM is constituted by a combination of Space Shift Keying (SSK) modulation and a SIMO system using the conventional APM. The intrinsic feature of the SSK modulation is that it exploits the independent fading of the different transmit antennas signals, which allows the system to dispense with transmit antenna synchronisation, while exhibiting a robustness to channel estimation errors. As a result, the SM scheme exhibit certain advantages over other MIMO schemes.

Moreover, three novel schemes, namely the open-loop Space Time Space Shift Keying (ST-SSK) designed for systems having more than two transmit antennas, the closed-loop feedback aided phase rotation conceived for systems having two transmit antennas and the closed-loop feedback assisted power allocation were proposed in Section 6.2 in order to achieve a useful transmit diversity for SSK modulation. More explicitly, following the philosophy of STBC, the ST-SSK scheme was proposed in Section 6.2.1 for scenarios having more than two transmit antennas, which employs multiple transmit time slots for achieving transmit diversity. Then, in Section 6.2.2, the feedback aided phase rotation scheme was discussed, when relying on two transmit antennas. Another closed-loop scheme using feedback aided power allocation was proposed in Section 6.2.3 for systems having an arbitrary number of transmit antennas. Our simulation results were discussed in Section 6.2.4 using the parameters listed in Table 6.4. The proposed schemes were capable of significantly improving the achievable uncoded BER performance over i.i.d. Rayleigh fading channels as well as over Riacian fading channels, as illustrated in Figs. 6.5, 6.6 and 6.9, respectively. Additionally, the robustness to the spatial correlation and channel estimation errors was also improved by employing the proposed scheme, as illustrated in Figs. 6.8 and 6.10.

Furthermore, a novel transmit diversity aided spatial modulation scheme was proposed in Section 6.3, which is a combination of the ST-SSK scheme and of the novel diagonal LDC scheme. The diagonal LDC detailed in Section 6.3.1 is capable of achieving the maximum attainable transmit diversity, activating only a single transmit antenna at each symbol instant, and reducing the complexity of the detector. Then in Section 6.3.2, the novel diagonal LDC was combined with the ST-SSK schemes proposed in Section 6.2.1, which compensate the throughput loss caused by the employment of ST-SSK scheme. This scheme provided a more flexible transmission arrangement, as demonstrated by the simulation results of Fig. 6.12 and 6.13.

7.2 Design Guidelines

Our guidelines conceived for the design of closed-loop MIMO systems using limited feedback are summarised in this section as illustrated in Fig. 7.1 by examining the various schemes investigated throughout Chapter 3 to Chapter 6. More explicitly, we may formulate the following general design steps in order to acquire and exploit the CSIT, and hence to maximise the benefits of using closed-loop schemes.

1. **Step 1:** Design appropriate transmit preprocessing schemes under the assumption of having perfect CSIT.

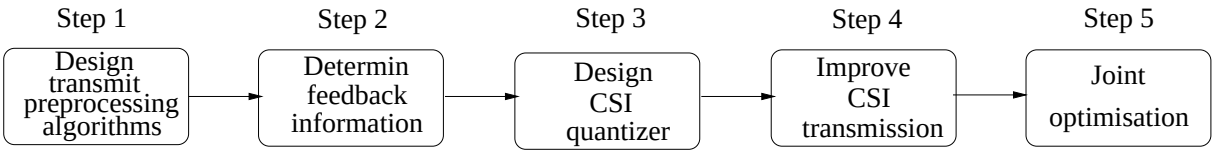

Figure 7.1: Flow chart of the five-steps design procedure.

Example: The transmit preprocessing algorithms detailed in Section 2.2 and employed throughout Chapter 3 to Chapter 5 were derived assuming that perfect CSIT was available. The benefits of these schemes were quantified for example in Fig. 3.2 of Section 3.1 and Fig. 4.2 of Section 4.1.1. The feedback-aided phase rotation scheme of Chapter 6 was also designed assuming the availability of perfect CSIT as illustrated by Equation (6.8).

2. **Step 2:** Determine the specific type of the required feedback information, whose entropy has to be as low as possible.
   Example: It was demonstrated in Fig. 3.3 of Section 3.1.1 that feeding back the unitary beamforming vector is more efficient than that of the entire CIR vector for a TxMF aided closed-loop MISO system, since the former one exhibits a lower entropy than the latter one.

3. **Step 3:** Design an efficient quantiser based on the statistical properties of the required feedback information. The distortion metric of the quantiser may be the conventional MSE metric, but the employment of a direct data-link performance related metric is preferable.
   Example: The different statistical properties of the channel phase vector and channel envelope vector were characterized in Figs. 2.6 and 2.7 of Section 2.1.3, which illustrated the importance of considering the statistical properties of the quantity to be quantized during the quantiser design. The quantisers employed in this thesis included the MSE-based vector quantiser of Section 2.3.2, the Grassmannian quantiser of Section 2.3.3 and 2.3.4 etc. All of the quantisers were designed following this principle. The employment of the MSE metric described in Section 2.3.2 is straightforward, which relies on the employment of the LGB algorithm for codebook generation. However, the chordal distance described in Section 2.3.3 and the Fubini-Study distance of Section 2.3.4 are more favourable, since they are capable of maximizing the data-link's received SNR and achievable mutual capacity, respectively.

4. **Step 4:** Improve the efficiency and robustness of the quantiser by employing conventional source compression.
   Example: The PVQ scheme proposed in Section 5.3 enhanced the efficiency of the quantiser by exploiting the temporal correlation of the MIMO channel. The soft decoding algorithm discussed in Section 5.2 minimised the distortion imposed by the feedback channel. These two approaches are commonly employed in the design of source encoders [91, 92].

5. **Step 5:** Joint optimisation of the data transmission link and the CSI feedback link based on the ultimate target performance metric.
   Example: The ECO-CQ scheme of Section 5.1.1 provided a framework for minimising the feedback overhead based on a specific target BER performance (e.g. an open EXIT-Chart tunnel) of the data-link.

7.3 Future Work

It appears promsing to extend our work reported in this thesis in the following directions.

1. In Chapter 3, we investigated the capacity loss imposed by pilot-assisted channel estimation. It would be interesting to identify the capacity loss imposed by more accurate channel estimation schemes, such as decision-feedback channel estimation [180], in order to minimise the effects of the estimation errors. Alternatively, it would be beneficial to investigate the capacity loss, when using semi-blind [31, 32] or entirely blind [33] channel estimation, where the signalling overhead associated with channel estimation is minimised.

2. In Chapter 4, we demonstrated that the TxEBF is capable of providing unequal error protection to the video stream, hence it is capable of enhancing the video transmission quality. It would be interesting to investigate the optimal combination of the TxEBF and the channel codes for the sake of achieving various Quality of Service (Qos) requirements. This work may also be extended to audio system and 3D video.

3. In Chapter 5, the problem of minimising feedback overhead, minimising the reconstruction error imposed by the error-contaminated feedback channel and of mitigating the feedback delay were treated separately in three distinctive sections. It would be interesting to design a robust system jointly considering all these three aspects, and to evaluate its performance.

4. In Chapter 6, the throughput of SSK modulation increased logarithmically with the number of transmit antennas, which is inefficient. It would be interesting to combine our proposed schemes with the generalised SSK modulation scheme proposed in [173] in order to increase its throughput. Moreover, it would be beneficial to investigate the application of spatial modulation in a multi-user scenario. Since less transmit antennas are activated simultaneously at each symbol interval, the resultant inter-user interference might become quite different from that of the system using traditional MIMO schemes.

5. Scheduling algorithms [51] were not considered in our study. It would be necessary to combine the algorithms proposed in the thesis with user scheduling algorithms operating in multi-user or multi-cell scenarios.

Glossary

3GPP	3rd Generation Partnership Project
ACF	auto-correlation function
AE	Antenna Element
AOA	Angle of Arrival
AOD	Angle of Departure
APM	Amplitude Phase Modulation
AR	Auto-Regressive
BER	Bit-Error-Ratio
BS	Base Station
CBP	Coded Block Pattern
CCMC	Continuous-input Continuous-output Memoryless Channel's
CIR	Channel Impulse Responses
CND	Check Node Decoder
CQ	Channel Quantizer
CSI	Channel State Information
CSIT	CSI at the Transmitter
DCM	Dispersion Character Matrix
DCMC	Discrete-input Continuous-output Memoryless Channel's
DDS	Degree Distribution Selector
DFT	Discrete Fourier Tansform
DL	Down-Link
DP	Data Partitioning
DSS	Degree Distribution Selector
ECO-CQ	EXIT-Chart Optimised CSI Quantizer
EXIT	Extrinsic Information Transfer

FDD Frequency Division Duplex
FEC Forward Error Correction
FSK Frequency Shift Keying

GSCM Geometry-based Stochastic Channel Model

i.i.d. independent and identically-distributed
ICI Inter Channel Interference

LBG Linde-Buzo-Gray
LDC Linear Dispersion Code
LDPC Low-Density Parity-Check
LHS Left-Hand-Side
LLRs Log-likelihood Ratio
LOS Line-Of-Sight
LT Luby Transform
LTE Long-Term-Evolution

MB Macro-Block
MIMO Multiple-Input-Multiple-Output
MISO Multiple-Input-Single-Output
ML Maximum-Likelihood
MMSE Minimum Mean Square Error
MSE Mean Square Error
MT Mobile Terminal
MUD Multi-User Detectors
MUT Multi-User Transmitters

NLOS Non-Line-Of-Sight
NSTS Non-Separable Transmit Symbols

OFDMA Orthogonal-Frequency-Division-Multiplexing-Access

PSAM Pilot Symbol Assisted Modulation
PSAR Pilot Symbol Assisted Rateless
PSD Power Spectral Density
PSNR Peak-Signal-to-Noise-Ratio
PVQ Predictive Vector Quantizer

RHS Right-Hand-Side
RSC Recursive Systematic Convolutional

SCM Spatial Channel Model

SDMA Space-Division Multiple Access
SIMO Single-Input Multiple-Output
SISO Single-Input Single-Output
SISTER Single Interaction ScatTEring Reflecting
SM Spatial Modulation
SSK Space Shift Keying
ST-SSK Space Time Space Shift Keying
SVD Singular Value Decomposition

TDD Time Division Duplex
TxBD Transmit Block Diagonalization
TxEBF Transmit Eigen-Beamforming
TxMF Transmit Matched Filter
TxMMSE Transmit Minimum Mean Square Error
TxZF Transmit Zero-Forcing

UEP Unequal Error Protection
UL Up-Link
ULAs Uniform Linear Arrays
URC Unit-Rate Codes

V-BLAST Vertical Bell-Labs Layered Space-Time Architecture
VLC Variable Length Coding
VND Variable Node Decoder
VQ Vector Quantizer

WLANs Wireless Local Area Networks

Bibliography

[1] E. T. Ar and I. E. Telatar, "Capacity of multi-antenna Gaussian channels," *European Transactions on Telecommunications*, vol. 10, pp. 585–595, 1999.

[2] L. Hanzo, O. lamri, M. El-Hajjar, and N. Wu, *Near-Capacity Multi-Functional MIMO Systems : Sphere-Packing, Iterative Detection and Cooperation*. Wiley-IEEE Press, May 2009.

[3] D. J. Love, R. Heath, V. Lau, D. Gesbert, B. D. Rao, and M. Andrews, "An overview of limited feedback in wireless communication systems," *IEEE Journal on Selected Areas in Communications*, vol. 26, pp. 1341–1365, Oct. 2008.

[4] S. Sesia, I. Toufik, and M. Baker, *LTE: The UMTS Long Term Evolution from Theory to Practice*. John Wiley and Sons Ltd, 2009.

[5] G. J. Foschini, "Layered space-time architecture for wireless communication in fading environments when using multiple antennas," *Bell Labs Technical Journal*, vol. 2, pp. 41–59, 1996.

[6] A. Goldsmith, S. A. Jafar, N. Jindal, and S. Vishwanath, "Capacity limits of MIMO channels," *IEEE Journal on Selected Areas in Communications*, vol. 21, pp. 684–702, June 2003.

[7] J. Jeganathan, A. Ghrayeb, L. Szczecinski, and A. Ceron, "Space shift keying modulation for MIMO channels," *IEEE Transactions on Wireless Communications*, vol. 8, pp. 3692–3703, July 2009.

[8] A. Nosratinia, T. E. Hunter, and A. Hedayat, "Cooperative communication in wireless networks," *IEEE Communications Magazine*, vol. 42, pp. 74–80, Oct. 2004.

[9] Y. Fan and J. Thompson, "MIMO configurations for relay channels: Theory and practice," *IEEE Transactions on Wireless Communications*, vol. 6, pp. 1774–1786, 2007.

[10] C. Li, G. Yue, M. A. Khojastepour, X. Wang, and M. Mohammad, "LDPC-coded cooperative relay systems: performance analysis and code design," *IEEE Transaction on Communications*, vol. 56, pp. 485–496, 2008.

[11] M. Vu and A. Paulraj, "MIMO wireless linear precoding," *IEEE Signal Processing Magazine*, vol. 24, pp. 86–105, Sept. 2007.

[12] Q. H. Spencer, C. B. Peel, A. L. Swindlehurst, and M. Haardt, "An introduction to the multi-user MIMO downlink," *IEEE Communications Magazine*, vol. 42, pp. 60–67, Oct. 2004.

[13] S. Jing, D. N. C. Tse, J. B. Soriaga, J. Hou, J. E. Smee, and R. Padovani, "Multicell downlink capacity with coordinated processing," *EURASIP Journal on Wireless Communications and Networking*, vol. 10, pp. 1–19, 2008.

[14] S. M. Alamouti, "A simple transmit diversity technique for wireless communications," *IEEE Journal on Selected Areas in Communications*, vol. 16, pp. 1451–1458, Oct 1998.

[15] J. S. Blogh and L. Hanzo, *Third Generation Systems and Intelligent Wireless Networking - Smart Antennas and Adaptive Modulation*. John Wiley and IEEE Press, 2002.

[16] S. D. Blostein and H. Leib, "Multiple antenna systems: their role and impact in future wireless access," *IEEE Communications Magazine*, vol. 41, pp. 94–101, July 2003.

[17] D. P. Palomar, J. M. Cioffi, and M. A. Lagunas, "Joint Tx-Rx beamforming design for multicarrier MIMO channels: a unified framework for convex optimization," *IEEE Transactions on Signal Processing,*, vol. 51, pp. 2381–2401, Sept. 2003.

[18] B. Suard, G. Xu, H. Liu, and T. Kailath, "Uplink channel capacity of space-division-multiple-access schemes," *IEEE Transactions on Information Theory*, vol. 44, pp. 1468–1476, July 1998.

[19] X. Wang and H. V. Poor, "Iterative (Turbo) soft interference cancellation and decoding for coded CDMA," *IEEE Transactions on Communications*, vol. 47, pp. 1046–1060, 1999.

[20] A. Tarable, G. Montorsi, and S. Benedetto, "A linear front end for iterative soft interference cancellation and decoding in coded CDMA," *IEEE Transactions on Wireless Communications*, vol. 4, pp. 507–518, 2005.

[21] S. Chen, N. N. Ahmad, and L. Hanzo, "Adaptive minimum bit error rate beamforming," *IEEE Transactions on Wireless Communications*, vol. 4, pp. 341–348, 2005.

[22] C. Xu, B. Hu, L. L. Yang, and L. Hanzo, "Ant-colony-based multiuser detection for multi-functional antenna array assisted MC DS-CDMA systems," *IEEE Transactions on Vehicular Technology*, vol. 57, pp. 658–663, 2008.

[23] A. Callard, A. Khandani, and A. Saleh, "Trellis precoding for the multi-user environment," in *The 40th Annual Conference on Information Sciences and Systems*, (Princeton, NJ), pp. 414–419, Mar. 2006.

[24] N. Jindal and A. Goldsmith, "Dirty-paper coding versus TDMA for MIMO broadcast channels," *IEEE Transactions on Information Theory*, vol. 51, pp. 1783–1794, May 2005.

[25] C. B. Peel, B. M. Hochwald, and A. L. Swindlehurst, "A vector-perturbation technique for near-capacity multiantenna multiuser communication-part I: channel inversion and regularization," *IEEE Transactions on Communications*, vol. 53, pp. 195–202, Jan. 2005.

[26] M. Joham, M. Utschick, and J. A. Nossek, "Linear transmit processing in MIMO communications systems," *IEEE Transaction on Signal Processing*, vol. 53, no. 8, pp. 2700–2712, 2005.

[27] R. Mesleh, H. Haas, C. W. Ahn, and S. Yun, "Spatial modulation - a new low complexity spectral efficiency enhancing technique," in *First International Conference on Communications and Networking in China*, (Beijing), pp. 1–5, Oct. 2006.

[28] R. Y. Mesleh, H. Haas, S. Sinanovic, C. W. Ahn, and S. Yun, "Spatial modulation," *IEEE Transactions on Vehicular Technology*, vol. 57, pp. 2228–2241, July 2008.

[29] B. Hassibi and B. M. Hochwald, "High-rate codes that are linear in space and time," *IEEE Transactions on Information Theory*, vol. 48, pp. 1804–1824, 2002.

[30] D. Samardzija and N. Mandayam, "Pilot-assisted estimation of MIMO fading channel response and achievable data rates," *IEEE Transactions on Signal Processing*, vol. 51, pp. 2882–2890, Nov. 2003.

[31] C. Shin, R. W. Heath, and E. J. Powers, "Non-redundant precoding-based blind and semi-blind channel estimation for MIMO block transmission with a cyclic prefix," *IEEE Transactions on Signal Processing*, vol. 56, no. 6, pp. 2509–2523, 2008.

[32] H. A. Cirpan and M. K. Tsatsanis, "Stochastic maximum likelihood methods for semi-blind channel estimation," *IEEE Signal Processing Letters*, vol. 5, no. 1, pp. 21–24, 1998.

[33] J. K. Tugnait, "Blind spatio-temporal equalization and impulse response estimation for MIMO channels using a Godard cost function," *IEEE Transactions on Signal Processing*, vol. 45, no. 1, pp. 268–271, 1997.

[34] B. L. Hughes, "Differential space-time modulation," *IEEE Transactions on Information Theory*, vol. 46, pp. 2567–2578, 2000.

[35] A. L. Moustakas, S. H. Simon, and T. L. Marzetta, "Capacity of differential versus nondifferential unitary space-time modulation for MIMO channels," *IEEE Transactions on Information Theory*, vol. 52, pp. 3622–3634, Aug. 2006.

[36] L. Hanzo, L. L. Yang, E. L. Kuan, and K. Yen, *Single- and Multi-Carrier DS-CDMA: Multi-User Dection, Space-Time Spreding, Synchronisation, Standards and Networking*. John Wiley and IEEE Press, 2003.

[37] L. Wang, O. Alamri, and L. Hanzo, "Sphere packing modulation in the SDMA uplink using K -best sphere detection," *IEEE Signal Processing Letters*, vol. 16, no. 4, pp. 291–294, 2009.

[38] S. Zhou and G. B. Giannakis, "How accurate channel prediction needs to be for transmit-beamforming with adaptive modulation over rayleigh MIMO channels?," *IEEE Transactions on Wireless Communications*, vol. 3, pp. 1285–1294, July 2004.

[39] D. Avidor, J. Ling, and C. Papadias, "Jointly opportunistic beamforming and scheduling (JOBS) for downlink packet access," in *Communications, 2004 IEEE International Conference on*, vol. 5, pp. 2959–2964, June 2004.

[40] P. Svedman, E. A. Jorswiec, and B. Ottersten, "Reduced feedback SDMA based on subspace packings," *IEEE Transactions on Wireless Communications*, vol. 8, pp. 1329–1339, Mar. 2009.

[41] C. Lin, V. Raghavan, and V. V. Veeravalli, "To code or not to code across time: space-time coding with feedback," *IEEE Journal on Selected Areas in Communications*, vol. 26, pp. 1588–1598, Oct. 2008.

[42] Y. Zhang, "Approaching V-BLAST capacity with adaptive modulation and LDPC encoding," *IEEE Transactions on Communications*, vol. 55, pp. 2261–2269, Dec. 2007.

[43] D. J. Love, R. W. Heath, W. Santipach, and M. L. Honig, "What is the value of limited feedback for MIMO channels?," *IEEE Communications Magazine*, vol. 42, pp. 54–59, Oct. 2004.

[44] C. E. Shannon, "The zero error capacity of a noisy channel," *IRE Transcaction Information Theory*, vol. 2, pp. 8–19, 1956.

[45] C. E. Shannon, "Channels with side information at the transmitter," *IBM Journal Research and Development*, vol. 2, pp. 289–293, 1958.

[46] L. Hanzo, S. X. Ng, T. Keller, and W. Webb, *Quadrature Amplitude Modulation: Single and Multicarrier Quadrature Amplitude Modulation in Turbo-Coded, Turbo-Equalised and Space-Time Coded TDMA, CDMA and OFDM Systems: From Basics to Adaptive Trellis Coded, Turbo Equalised and Space Time Coded OFDM, CDMA and MC CDMA Systems*. John Wiley and Sons Ltd, 2004.

[47] A. J. Goldsmith and P. P. Varaiya, "Capacity of fading channels with channel side information," *IEEE Transactions on Information Theory*, vol. 43, pp. 1986–1992, Nov. 1997.

[48] H. Zhang and H. Dai, "Cochannel interference mitigation and cooperative processing in downlink multicell multiuser MIMO networks," *EURASIP Jounal on Wireless Communications and Networking*, vol. 2, pp. 222–235, 2004.

[49] W. Zhang and K. B. Letaief, "MIMO broadcast scheduling with limited feedback," *IEEE Journal on Selected Areas in Communications*, vol. 25, pp. 1457–1467, Sept. 2007.

[50] O. Somekh, O. Simeone, Y. Bar-Ness, A. M. Haimovich, and S. Shamai, "Cooperative multi-cell zero-forcing beamforming in cellular downlink channels," *IEEE Transactions on Information Theory*, vol. 55, pp. 3206–3219, July 2009.

[51] W. Ajib and D. Haccoun, "An overview of scheduling algorithms in MIMO-based fourth-generation wireless systems," *IEEE Network*, vol. 19, pp. 43–48, 2005.

[52] D. Tse and P. Viswanath, *Fundamentals of Wireless Communication*. Cambridge University Press, 2005.

[53] D. Y. Zeng and R. F. Song, "Elimination of interference non-reciprocity in TDD MIMO-OFDM systems," in *International Conference on Wireless Communications, Networking and Mobile Computing*, (Shanghai), pp. 105–108, Sept. 2007.

[54] L. P. Wither, R. M. Taylor, and D. M. Warme, "Echo-MIMO: A two-way channel training method for matched cooperative beamforming," *IEEE Transactions on Signal Processing*, vol. 56, no. 9, pp. 4419–4432, 2008.

[55] G. Caire, N. Jindal, and M. Kobayashi, "Achievable rates of MIMO downlink beamforming with non-perfect CSI: a comparison between quantized and analog feedback," in *Fortieth Asilomar Conference on Signals, Systems and Computers*, (Pacific Grove, CA), pp. 354–358, Oct. 2006.

[56] C. Farsakh and J. A. Nossek, "Spatial covariance based downlink beamforming in an SDMA mobile radio system," *IEEE Transactions on Communications*, vol. 46, pp. 1497–1506, 1998.

[57] D. J. Love and R. W. Heath, "Limited feedback unitary precoding for spatial multiplexing systems," *IEEE Transactions on Information Theory*, vol. 51, pp. 2967–2976, Aug. 2005.

[58] J. H. Sung and J. R. Barry, "Approaching the zero-outage capacity of MIMO-OFDM without instantaneous water-filling," *IEEE Transactions on Information Theory*, vol. 54, pp. 1423–1436, Apr. 2008.

[59] S. Jafar, "Capacity with causal and noncausal side information: A unified view," *IEEE Transactions on Information Theory*, vol. 52, pp. 5468–5474, Dec. 2006.

[60] M. Costa, "Writing on dirty paper," *IEEE Transactions on Information Theory*, vol. 29, pp. 439–441, May 1983.

[61] R. Negi, A. M. Tehrani, and J. M. Cioffi, "Adaptive antennas for space-time codes in outdoor channels," *IEEE Transactions on Communications*, vol. 50, pp. 1918–1925, 2002.

[62] H. Zhuang, L. Dai, S. Zhou, and Y. Yao, "Low complexity per-antenna rate and power control approach for closed-loop V-BLAST," *IEEE Transactions on Communications*, vol. 51, pp. 1783–1787, Nov. 2003.

[63] A. F. Molisch and M. Z. Win, "MIMO systems with antenna selection," *IEEE Microwave Magazine*, vol. 5, pp. 46–56, Mar. 2004.

[64] L. U. Choi and R. D. Murch, "A transmit preprocessing technique for multiuser MIMO systems using a decomposition approach," *IEEE Transactions on Wireless Communications*, vol. 3, pp. 20–24, Jan. 2004.

[65] B. M. Hochwald, C. B. Peel, and A. L. Swindlehurst, "A vector-perturbation technique for near-capacity multiantenna multiuser communication-part II: perturbation," *IEEE Transactions on Communications*, vol. 53, pp. 537–544, Mar. 2005.

[66] M. E. Celebi, S. Sahin, and U. Aygolu, "Balanced space-time block coding: an efficient way to increase diversity with feedback," *IEE Processings Communications*, vol. 153, pp. 519–524, 2006.

[67] A. Santoso, Y. Li, J. K. A. Allan, and B. Vucetic, "Dynamic transmit power allocation in space-time trellis coded systems," *IEEE Transactions on Wireless Communications*, vol. 7, pp. 3079–3089, Aug. 2008.

[68] H. K. Bizaki and A. Falahati, "Tomlinson-Harashima precoding with imperfect channel state information," *IET Communications*, vol. 2, pp. 151–158, Jan. 2008.

[69] R. Y. Chang, Z. Tao, J. Zhang, and C.-C. J. Kao, "Multicell OFDMA downlink resource allocation using a graphic framework," *IEEE Transactions on Vehicular Technology*, vol. 58, pp. 3494–3507, Sept. 2009.

[70] F. Z. Merli, X. Wang, and G. M. Vitetta, "Low-rate-feedback-assisted beamforming and power control for MIMO-OFDM system," *IEEE Transactions on Vehicular Technology*, vol. 59, pp. 225–234, 2010.

[71] Y. Huang, L. Yang, M. Bengtsson, and B. Ottersten, "A limited feedback joint precoding for amplify-and-forward relaying," *IEEE Transactions on Signal Processing*, vol. 58, pp. 1347–1357, 2010.

[72] R. T. Derryberry, S. D. Gray, D. M. Ionescu, G. Mandyam, and B. Raghothaman, "Transmit diversity in 3G CDMA systems," *IEEE Communications Magazine*, vol. 40, pp. 68–75, Apr. 2002.

[73] A. Ahrens, S. X. Ng, V. Kühn, and L. Hanzo, "Modulation-mode assignment for SVD-aided and BICM-assisted spatial division multiplexing," *Physical Communication*, vol. 1, pp. 60–66, 2008.

[74] J. F. Du, E. G. Larsson, and M. Skoglund, "Costa precoding in one dimension," in *IEEE International Conference on Acoustics, Speech and Signal Processing*, vol. 4, (Toulouse), May 2006.

[75] Z. Lin, T. B. Sorensen, and P. E. Mogensen, "Downlink SINR distribution of linearly precoded multiuser MIMO systems," *IEEE Communications Letters*, vol. 11, pp. 850–852, Nov. 2007.

[76] R. W. Heath and D. J. Love, "Multimode antenna selection for spatial multiplexing systems with linear receivers," *IEEE Transactions on Signal Processing*, vol. 53, pp. 3042–3056, Aug. 2005.

[77] F. Zhu and M. S. Lim, "Combined beamforming with space-time block coding using double antenna array group," *Electronics Letters*, vol. 40, pp. 811–813, June 2004.

[78] S. A. Jafar and S. Srinivasa, "On the optimality of beamforming with quantized feedback," *IEEE Transactions on Communications*, vol. 55, pp. 2288–2302, Dec. 2007.

[79] A. Narula, M. J. Lopez, M. D. Trott, and G. W. Wornell, "Efficient use of side information in multiple-antenna data transmission over fading channels," *IEEE Journal on Selected Areas in Communications*, vol. 16, pp. 1423–1436, Oct. 1998.

[80] D. J. Love, R. W. Heath, and T. Strohmer, "Grassmannian beamforming for multiple-input multiple-output wireless systems," *IEEE Transactions on Information Theory*, vol. 49, pp. 2735–2747, Oct. 2003.

[81] W. Santipach and M. L. Honig, "Asymptotic performance of MIMO wireless channels with limited feedback," in *IEEE Military Communications Conference*, vol. 1, (Boston, MA), pp. 141–146, Oct. 2003.

[82] D. J. Love and R. W. Heath, "Equal gain transmission in multiple-input multiple-output wireless systems," *IEEE Transcations on Communications*, vol. 51, pp. 1102–1110, Nov. 2003.

[83] B. C. Banister and J. R. Zeidler, "Feedback assisted transmission subspace tracking for MIMO systems," *IEEE Journal on Selected Areas in Communications*, vol. 21, pp. 452–463, Apr. 2003.

[84] J. Choi and R. W. Heath, "Interpolation based transmit bemforming for MIMO-OFDM with limited feedback," *IEEE Transcations on Signal Processing*, vol. 53, pp. 4125–4135, 2005.

[85] S. Zhou and B. Li, "BER criterion and codebook construction for finite-rate precoded spatial multiplexing with linear receivers," *IEEE Transcations on Signal Processing*, vol. 54, pp. 1652–1665, 2006.

[86] J. C. Roh and B. D. Rao, "Transmit beamforming in multiple-antenna systems with finite rate feedback: A VQ-based approach," *IEEE Transcations on Information Theory*, vol. 52, pp. 282–292, 2006.

[87] V. Raghavan, R. W. Heath, and A. M. Sayeed, "Systematic codebook designs for quantized beamforming in correlated MIMO channels," *IEEE Journal on Selected Areas in Communications*, vol. 25, pp. 1298–1310, Sept. 2007.

[88] T. Wu and V. K. N. Lau, "Robust rate, power and precoder adaptation for slow fading MIMO channels with noisy limited feedback," *IEEE Transactions on Wireless Communications*, vol. 7, pp. 2360–2367, June 2008.

[89] D. Ryan, I. V. L. Clarkson, I. Collings, D. Guo, and M. Honig, "QAM and PSK codebooks for limited feedback MIMO beamforming," *IEEE Transactions on Communications*, vol. 57, pp. 1184–1196, 2009.

[90] Y. G. Kim and N. C. Beaulieu, "On MIMO beamforming systems using quantized feedback," *IEEE Transactions on Communications*, vol. 58, pp. 820–827, 2010.

[91] A. Gersho and R. M. Gray, *Vector Quantization and Signal Compression*. Kluwer Academic Publishers, 1991.

[92] M. Skoglund and P. Hedelin, "Hadamard-based soft decoding for vector quantization over noisy channels," *IEEE Transactions on Information Theory*, vol. 45, no. 2, pp. 515–532, 1999.

[93] A. Duel-Hallen, S. Hu, and H. Hallen, "Long-range prediction of fading signals," *IEEE Signal Processing Magazine*, vol. 17, pp. 62–75, May 2000.

[94] A. E. Ekpenyong and Y. F. Huang, "Feedback constraints for adaptive transmission," *IEEE Signal Processing Magazine*, vol. 24, pp. 69–78, May 2007.

[95] C. Jonietz, W. Gerstacker, and R. Schober, "Robust transmit processing for frequency-selective fading channels with imperfect channel feedback," *IEEE Transactions on Wireless Communications*, vol. 7, pp. 5356–5368, Dec. 2008.

[96] C. Berrou, A. Glavieux, and P. Thitimajshima., "Near Shannon limit error-correcting coding and decoding: Turbo-codes," in *IEEE International Conference on Communications*, vol. 2, (Geneva), pp. 1064–1070, May 1993.

[97] C. Berrou and A. Glavieux, "Near optimum error correcting coding and decoding: turbo-codes," *IEEE Transactions on Communications*, vol. 44, no. 10, pp. 1261–1271, 1996.

[98] L. Hanzo, T. H. Liew, and B. L. Yeap, *Turbo Coding, Turbo Equalisation, and Space-Time Coding*. John Wiley and Sons, 2002.

[99] D. Yang, L. L. Yang, and L. Hanzo., "Performance of SDMA systems using transmitter preprocessing based on noisy feedback of vector-quantized channel impulse responses," in *IEEE 65th Vehicular Technology Conference, VTC2007-Spring.*, (Dublin), pp. 2119–2123, Apr. 2007.

[100] D. Yang, W. Liu, L. L. Yang, and L. Hanzo, "Channel prediction and predictive vector quantization aided channel impulse response feedback for SDMA downlink preprocessing," in *IEEE 68th Vehicular Technology Conference, VTC-fall*, (Calgary, BC), Sept. 2008.

[101] D. Yang, N. Wu, L. L. Yang, and L. Hanzo, "Closed-loop linear dispersion coded eigen-beam transmission and its capacity," *IEE Electronics Letters*, vol. 44, pp. 1144–1146, Sept. 2008.

[102] C. Y. Wei, D. Yang, L. L. Yang, and L. Hanzo, "Iterative detection aided DL SDMA systems using quantized channel impulse response," in *IEEE 69th Vehicular Technology Conference, VTC-Spring*, (Barcelona), Apr. 2009.

[103] D. Yang, . Nasruminallah, L. L. Yang, and L. Hanzo, "SVD-aided unequal-protection spatial multiplexing for wireless video telephony," in *IEEE 69th Vehicular Technology Conference, 2009. VTC- Spring*, (Barcelona), Apr. 2009.

[104] D. Yang, L. L. Yang, and L. Hanzo, "Imperfect channel knowledge based ergodic channel capacity of transmit beamforming," in *IEEE Vehicular Technology Conference, VTC-Fall*, (Anchorage, Alaska, USA), Sept. 2009.

[105] N. Bonello, D. Yang, S. Chen, and L. Hanzo, "Generalized MIMO transmit preprocessing using pilot symbol assisted rateless codes," *IEEE Transactions on Wireless Communications*, vol. 9, pp. 754–763, 2010.

[106] N. Bonello, D. Yang, S. Chen, and L. Hanzo, "Generalized MIMO transmit preprocessing using pilot symbol assisted rateless codes," in *IEEE Vehicular Technology Conference, VTC-Spring*, (Taipei, Taiwan), May 2010.

[107] C. N. Chuah, D. N. C. Tse, J. M. Kahn, and R. A. Valenzuela, "Capacity scaling in MIMO wireless systems under correlated fading," *IEEE Transactions on Information Theory*, vol. 48, pp. 637–650, Mar. 2002.

[108] D. S. Shiu, G. J. Foschini, M. J. Gans, and J. M. Kahn, "Fading correlation and its effect on the capacity of multielement antenna systems," *IEEE Transactions on Communications*, vol. 48, pp. 502–513, Mar. 2000.

[109] T. S. Rappaport, *Wireless Communications: Principles and Practice*. Prentice Hall PTR, 2nd ed., December 2001.

[110] A. Saleh and R. Valenzuela, "A statistical model for indoor multipath propagation," *IEEE Journal on Selected Areas in Communications*, vol. 5, pp. 128–137, Feb. 1987.

[111] S. J. Howard and K. Pahlavan, "Autoregressive modeling of wide-band indoor radio propagation," *IEEE Transactions on Communications*, vol. 40, pp. 1540–1552, Sept. 1992.

[112] M. Steinbauer, A. F. Molisch, and E. Bonek, "The double-directional radio channel," *IEEE Antennas and Propagation Magazine*, vol. 43, pp. 51–63, Aug. 2001.

[113] A. F. Molisch, A. Kuchar, J. Laurila, K. Hugl, and R. Schmalen-berger, "Geometry-based directional model for mobile radio channels - principles and implementation," *European Transactions on Telecommunications*, vol. 14, pp. 351–359, 2003.

[114] S. Loredo, A. Rodriguez-Alonso, and R. P. Torres, "Indoor MIMO channel modeling by rigorous GO/UTD-based ray tracing," *IEEE Transactions on Vehicular Technology*, vol. 57, pp. 680–692, Mar. 2008.

[115] A. G. Zajic, G. L. Stuber, T. G. Pratt, and S. T. Nguyen, "Wideband MIMO mobile-to-mobile channels: Geometry-based statistical modeling with experimental verification," *IEEE Transactions on Vehicular Technology*, vol. 58, pp. 517–534, Feb. 2009.

[116] A. Emami-Forooshani and S. Noghanian, "Semi-deterministic channel model for multiple input multiple output systems. Part 1: Model development and validation," *IET Microwaves, Antennas & Propagation*, vol. 4, pp. 17–25, Jan. 2010.

[117] J. P. Kermoal, L. Schumacher, K. I. Pedersen, P. E. Mogensen, and F. Frederiksen, "A stochastic MIMO radio channel model with experimental validation," *IEEE Journal on Selected Areas in Communications*, vol. 20, no. 6, pp. 1211–1226, 2002.

[118] A. M. Sayeed, "Deconstructing multiantenna fading channels," *IEEE Transactions on Signal Processing*, vol. 50, no. 10, pp. 2563–2579, 2002.

[119] W. Weichselberger, M. Herdin, H. Özcelik, and E. Bonek, "A stochastic MIMO channel model with joint correlation of both link ends," *IEEE Transactions on Wireless Communications*, vol. 5, pp. 90–99, 2006.

[120] "Spatial channel model for multiple input multiple output (MIMO) simulations (Release 6)," tech. rep., 3GPP Techinical Specification 25.996, 2003.

[121] V. Erceg, L. Schumacher, and P. Kyritsi, "TGn channel models," tech. rep., IEEE P802.11, Wireless LANs, 2004.

[122] A. F. Molisch, H. Asplund, R. Heddergott, M. Steinbauer, and T. Zwick, "The COST 259 directional channel model A: overview and methodology," *IEEE Transactions on Wireless Communications*, vol. 5, pp. 3421–3433, 2006.

[123] K. Yu and B. Ottersten, "Models for MIMO propagation channels: A review," *Wiley Journal on Wireless Communications and Mobile Computing special Issue on Adaptive Antennas and MIMO Systems*, vol. 2, pp. 653–666, 2002.

[124] P. Almers, E. Bonek, A. Burr, N. Czink, M. Debbah, V. Degli-Esposti, H. Hofstetter, P. Kyösti, D. Laurenson, G. Matz, A. F. Molisch, C. Oestges, and H. Özcelik, "Survey of channel and radio propagation models for wireless MIMO systems," *EURASIP Journal on Wireless Communications and Networking*, vol. 2007, pp. 56–75, 2007.

[125] R. Esmailzadeh, E. Sourour, and M. Nakagawa, "Prerake diversity combining in time-division duplex CDMA mobile communications," *IEEE Transactions on Vehicular Technology*, vol. 48, pp. 795–801, 1999.

[126] R. Kwan, C. Leung, and P. Ho, "Distribution of ordered eigenvalues of Wishart matrices," *Electronics Letters*, vol. 43, pp. 31–32, Mar. 2007.

[127] S. Verdú, *Multiuser Detection*. Cambridge University Press, 1998.

[128] D. A. Shnidman, "A generalized Nyquist criterion and an optimal linear receiver for a pulse modulation system," *Bell System Technology Journal*, vol. 46, pp. 2163–2177, 1967.

[129] S. Chen, "Adaptive minimum bit-error-rate filtering," *IEE Proceedings Vision, Image and Signal Processing*, vol. 151, pp. pp. 76–85, 2004.

[130] L. Wang, L. Xu, S. Chen, and L. Hanzo, "Genetic iterative search-centre-shifting K-best sphere detection for rank-deficient SDM-OFDM systems," *Electronics Letters*, vol. 44, pp. 552–553, 2008.

[131] L. L. Yang, "Design linear multiuser transmitters from linear multiuser receivers," in *IEEE International Conference on Communications*, (Glasgow, Scotland.), pp. 5258–5263, 24-28 June 2007.

[132] Y. Linde, A. Buzo, and R. Gray, "An algorithm for vector quantizer design," *IEEE Transactions on Communications*, vol. 28, pp. 84–95, Jan. 1980.

[133] J. H. Conway, R. H. Hardin, and N. J. A. Sloane, "Packing lines, planes, ect.: Packing in Grassmannian spaces," *Experimental Mathematics*, vol. 5, pp. 522–527, 1996.

[134] K. Scharnhorst, "Angles in complex vector spaces," *Acta Applicandae Mathematicae: An International Survey Journal on Applying Mathematics and Mathematical Applications*, vol. 69, pp. 95–103, 2004.

[135] L. Hanzo, M. Munster, B. J. Choi, and T. Keller, *OFDM and MC-CDMA for Broadband Multi-user Communications, WLANs and Broadcasting*. John Wiley and Sons, 2003.

[136] "3GPP TR 36.803V0.2300," tech. rep., 3GPP Techinical Specification, 2007.

[137] M. G. Luby, "LT codes," in *Proceeding of 43rd Annual IEEE Symposium on Foundations of Computer Science*, pp. 271–280, Nov. 16-19 2002.

[138] R. Tanner, "A recursive approach to low complexity codes," *IEEE Transactions on Information Theory*, vol. 27, pp. 533–547, 1981.

[139] F. R. Kschischang, B. Frey, and H. A. Loeliger, "Factor graphs and the sum-product algorithm," *IEEE Transactions on Information Theory*, vol. 47, pp. 489–519, 2001.

[140] J. Byers, M. G. Luby, and M. Mitzenmacher, "A digital fountain approach to asynchronous reliable multicast," *IEEE Journal on Selected Areas in Communications*, vol. 20, pp. 1528–1540, 2002.

[141] N. Bonello, R. Zhang, S. Chen, and L. Hanzo, "Reconfigurable rateless codes," *IEEE Transactions on Wireless Communications*, vol. 8, no. 11, pp. 5592–5600, 2008.

[142] S. ten Brink, "Convergence behavior of iteratively decoded parallel concatenated codes," *IEEE Transaction on Communications*, vol. 49, pp. 1727–1737, 2001.

[143] R. Palanki and J. S. Yedidia, "Rateless codes on noisy channels," in *Proceedings of the IEEE International Symposium on Information Theory*, (Chicago), July 2004.

[144] M. G. Luby, M. Mitzenmacher, M. A. Shokrollahi, and D. A. Spielman, "Efficient erasure correcting codes," *IEEE Transactions on Information Theory*, vol. 47, no. 2, pp. 569–584, 2001.

[145] A. Shokrollahi, "Raptor codes," *IEEE Transactions on Information Theory*, vol. 52, no. 6, pp. 2551–2567, 2006.

[146] Z. Zhou, B. Vucetic, M. Dohler, and Y. Li, "MIMO systems with adaptive modulation," *IEEE Transactions on Vehicular Technology*, vol. 54, no. 5, pp. 1828–1842, 2005.

[147] M. Skoglund and G. Jongren, "On the capacity of a multiple-antenna communication link with channel side information," *IEEE Journal on Selected Areas in Communications*, vol. 21, pp. 395–405, Apr. 2003.

[148] J. Liu and E. Gunawan, "Exact bit-error rate analysis for the combined system of beamforming and Alamouti's space-time block code," *IEEE Microwave and Wireless Components Letters*, vol. 14, pp. 398–400, Aug. 2004.

[149] R. Hayes and J. Caffery, "Dispersive covariance codes for MIMO precoding," in *IEEE Global Telecommunications Conference*, vol. 3, 28th Nov.- 2nd Dec. 2005.

[150] C. Lin, V. Raghavan, and V. V. Veeravalli, "Optimal power allocation for linear dispersion codes over correlated MIMO channels with channel state feedback," in *IEEE Global Telecommunications Conference*, (Washington, DC, USA), pp. 1602–1606, Nov. 2007.

[151] C. Lin and V. V. Veeravalli, "A limited feedback scheme for linear dispersion codes over correlated MIMO channels," in *IEEE International Conference on Acoustics, Speech and Signal Processing*, vol. 3, (Honolulu, HI), Apr. 2007.

[152] N. Wu and L. Hanzo, "Near-capacity irregular precoded linear dispersion codes," in *IEEE International Conference on Communications*, (Beijing, China), May 2008.

[153] N. Wu and L. Hanzo, "Irregular precoder-aided differential linear dispersion codes," in *IEEE 67th Vehicular Technology Conference, VTC-Spring*, (Singapore), May 2008.

[154] H. Jafarkhani, *Space-Time Coding Theory and Practice*. Cambridge Universigy Press, 2005.

[155] S. X. Ng and L. Hanzo, "On the MIMO channel capacity of multi-dimensional signal sets," *IEEE Transactions on Vehicular Technology*, vol. 55, pp. 528–536, Mar. 2006.

[156] D. Divsalar, S. Dolinar, and F. Pollara, "Serial concatenated trellis coded modulation with rate-1 inner code," in *IEEE Global Telecommunications Conference*, vol. 2, (San Francisco, CA), pp. 777–782, Nov./Dec. 2000.

[157] L. Hanzo, P. Cherriman, and J. Streit, *Video Compression and Communications: From Basics to H.261, H.263, MPEG2, MPEG4 for DVB and HSDPA-Style Adaptive Turbo-Transceivers*. Wiley-IEEE Press, 2007.

[158] L. Hanzo, C. Wong, and M. Yee, *Adaptive Wireless Transceivers: Turbo-Coded, Turbo-Equalised and Space-Time Coded TDMA, CDMA and OFDM Systems*. John Wiley & Sons, 2002.

[159] M. Uchler and J. Hagenauer, "EXIT charts of irregular codes," in *Proceedings of Conference Information Sciences and Systems*, (Princeton, USA), Mar. 2002.

[160] C. Y. Wei, J. Akhtman, S. X. Ng, and L. Hanzo, "Iterative near-maximum-likelihood detection in rank-deficient downlink SDMA systems," *IEEE Transactions on Vehicular Technology*, vol. 57, pp. 653 – 657, 2008.

[161] M. Skoglund, "Soft decoding for vector quantization over noisy channels with memory," *IEEE Transaction on Information Theory*, vol. 45, no. 4, pp. 1293–1307, 1999.

[162] K. Kabayashi, T. Ohtsuki, and T. Kaneko, "MIMO systems in the presence of feedback delay," in *IEEE International Conference on Communications*, vol. 9, (Istanbul, Turkey), pp. 4102–4106, Jun 2006.

[163] J. Proakis, *Digital Communications*. McGraw-Hill, 1995.

[164] Y. A. Chau and S. H. Yu, "Space modulation on wireless fading channels," in *IEEE 54th Vehicular Technology Conferencel, VTC-fall*, vol. 3, (Atlantic City, NJ), pp. 1668–1671, Oct. 2001.

[165] H. Haas, E. Costa, and E. Schulz, "Increasing spectral efficiency by data multiplexing using antenna arrays," in *IEEE 13th International Symposium on Personal, Indoor and Mobile Radio Communications*, vol. 2, (Lisboa, Portugal), pp. 610–613, Sept. 2002.

[166] R. Mesleh, H. Haas, Y. Lee, and S. Yun, "Interchannel interference avoidance in MIMO transmission by exploiting spatial information," in *IEEE 16th International Symposium on Personal, Indoor and Mobile Radio Communications*, vol. 1, (Berlin), pp. 141–145, Sept. 2005.

[167] J. Jeganathan, A. Ghrayeb, and L. Szczecinski, "Spatial modulation: optimal detection and performance analysis," *IEEE Communications Letters*, vol. 12, pp. 545–547, Aug. 2008.

[168] N. Serafimovski, M. D. Renzo, S. Sinanovic, R. Y. Mesleh, and H. Haas, "Fractional bit encoded spatial modulation (FBE-SM)," *IEEE Communications Letters*, vol. 14, pp. 428–431, 2010.

[169] R. Mesleh, H. Haas, C. Ahn, and S. Yun, "Spatial modulation - OFDM," in *Proceeding of the 15th International OFDM Workshop*, (Hamburg, Germany), Sept. 2006.

[170] S. Ganesan, R. Mesleh, H. Haas, C. W. Ahn, and S. Yun, "On the performance of spatial modulation OFDM," in *Fortieth Asilomar Conference on Signals, Systems and Computers*, (Pacific Grove, CA), pp. 1825–1829, Oct.-Nov. 2006.

[171] R. Mesleh, S. Ganesan, and H. Haas, "Impact of channel imperfections on spatial modulation OFDM," in *IEEE 18th International Symposium on Personal, Indoor and Mobile Radio Communications*, (Athens), Sept. 2007.

[172] R. Mesleh, S. Engelken, S. Sinanovic, and H. Haas, "Analytical SER calculation of spatial modulation," in *IEEE International Symbosium on Spread Spectrum Techniques and Applications*, (Bologna, Italy), Aug. 2008.

[173] J. Jeganathan, A. Ghrayeb, and L. Szczecinski, "Generalized space shift keying modulation for MIMO channels," in *IEEE 19th International Symposium on Personal, Indoor and Mobile Radio Communications*, (Cannes), Sept. 2008.

[174] T. Handte, A. A. Muller, and J. Speidel, "BER analysis and optimization of generalized spatial modulation in correlated fading channels," in *IEEE 70th Vehicular Technology Conference, VTC-Fall*, (Anchorage, Alaska, USA), Sept. 2009.

[175] M. M. U. Faiz, S. Al-Ghadhban, and A. Zerguine, "Recursive least-squares adaptive channel estimation for spatial modulation systems," in *IEEE 9th Malaysia International Conference on Communications*, (Kuala Lumpur), pp. 785–788, Dec. 2009.

[176] R. Mesleh, R. Mehmood, H. Elgala, and H. Haas, "Indoor mimo optical wireless communication using spatial modulation," in *IEEE International Conference on Communications*, (Cape Town, South Africa), 23–27, May 2010.

[177] M. D. Renzo, R. Y. Mesleh, H. Haas, and P. M. Grant, "Upper bounds for the analysis of Trellis coded spatial modulation over correlated fading channels," in *IEEE 71st Vehicular Technology Conference, VTC-Spring*, (Taipei, Taiwan), 16-19, May 2010.

[178] M. D. Renzo and H. Haas, "Performance comparison of different spatial modulation schemes in correlated fading channels," in *IEEE International Conference on Communications*, (Cape Town, South Africa), 23-27, May 2010.

[179] N. Wu and L. Hanzo, "Near-capacity irregular convolutional-coding aided irregular precoded linear dispersion codes," *IEEE Transactions on Vehicular Technology*, vol. 58, pp. 2863–2871, 2009.

[180] P. Garg, R. K. Mallik, and H. M. Gupta, "An analytical approach to space-time block coding with decision-feedback channel estimation," *IEEE Transactions on Vehicular Technology*, vol. 56, pp. 1442–1447, 2007.

Subject Index

Author Index

I

J

K

L

M

N

O

P

R

S

Z